Timescales of processes controlling water vapour entry to the stratosphere

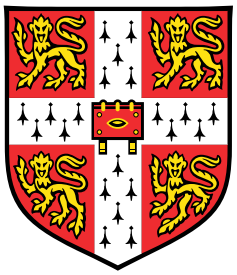

Jacob Willock Smith

Department of Applied Mathematics and Theoretical Physics
University of Cambridge

This dissertation is submitted for the degree of
Doctor of Philosophy

Darwin College

September 2019

Declaration

This thesis is the result of my own work and includes nothing which is the outcome of work done in collaboration except as declared in the Preface and specified in the text. It is not substantially the same as any that I have submitted, or, is being concurrently submitted for a degree or diploma or other qualification at the University of Cambridge or any other University or similar institution except as declared in the Preface and specified in the text. I further state that no substantial part of my thesis has already been submitted, or, is being concurrently submitted for any such degree, diploma or other qualification at the University of Cambridge or any other University or similar institution except as declared in the Preface and specified in the text. It does not exceed the prescribed word limit for the relevant Degree Committee.

Jacob Willock Smith
September 2019

Acknowledgements

Perpetual love and thanks go to my mother, sister and father, as well as Louisiane, who have shaped my perspectives and approaches to all things in life. Without them, I would not find the motivation nor strength to complete such achievements. I am also thankful to Socket, whose purrs and cuddle-seeking in the final months provided welcome relief from writing.

I would also like to acknowledge my colleagues and office-mates, particularly Philip and Alison, who encouraged discussion, critical analysis and far too many tea and coffee breaks.

Not least of all, I am extremely grateful to my supervisors for their thorough support throughout this research. Prof Peter Haynes, Dr Amanda Maycock, Dr Neal Butchart and Dr Andrew Bushell (and Dr Steven Hardiman's early involvement) have keenly supported the development of my scientific thoughts. I am also grateful for collaborating through the Met Office sponsorship, which has invaluably connected my studies to the practical workings of climate model development.

Abstract

This thesis assesses the representation of the key processes determining water vapour entry into the stratosphere in reanalysis and two global climate model configurations. This is done by applying the advection-condensation method and comparing alternative formulations.

In the region of the atmosphere around 15–50 km altitude known as the stratosphere, water vapour is present in concentrations around ten thousand times lower than at the Earth's surface. Yet, water vapour still influences surface warming and stratospheric chemistry due to its radiative and chemical properties. Previous studies have identified low temperatures (more accurately, low saturation mixing ratios) and large-scale transport through the tropical tropopause layer to be the key factors that determine stratospheric water vapour. However, their relative importance at different timescales, and the role of the other influences such as detailed ice microphysics, are not yet well known. It is a crucial priority to improve the generally poor representation of stratospheric water vapour in global climate models for both present and future scenarios.

In the first chapter of results, the representation of the average annual cycle of lower stratospheric water vapour by temperature and large-scale transport is assessed. Model-specific features are reflected in water vapour predictions by the advection-condensation method. Applying a climate model advection scheme to the advection-condensation method, to test sensitivity to transport formulation, finds more similar temporal variability but also affects vertical attenuation of concentrations in the stratosphere. Expanding on earlier studies, the impact of sub-seasonal temperature variability on stratospheric water vapour is quantified in reanalysis and in one global climate model where it is found to be under-represented.

Following on, the next chapter investigates the substantial interannual variability of tropical lower stratospheric water vapour by isolating temperature and transport impacts in reanalysis. The approach asks whether the characteristics of a particular year are obtained by transport through temperatures from another year. Results identify almost total independence from transport variations across years, but important seasonal variability. This agrees with many studies on seasonality of transport, and points squarely to temperatures controlling interannual variability.

The subsequent chapter takes advantage of the complete water budget available in a global climate model to assess the impact of additional processes. Results find the phase change of ice to vapour (sublimation) is a substantial component of the water vapour budget above the tropical tropopause, and convective injection of ice occurs above the vertical minimum in saturation mixing ratio. Results also show that the extent to which advection-condensation calculations are rehydrated by different measures of sublimation depend crucially on their vertical extent.

The final chapter of results analyses the response of advection-condensation and sublimation to climate change scenarios. Increases in transport efficiency through the tropical tropopause agree with well understood aspects of climate change. Convective ice injection is higher but no more intense, whereas sublimation above the vertical dry point has increased. These changes appears to be controlled solely by the elevated and warmer tropopause. The results show that predictions of a wetter model stratosphere, both with and without sublimation, scale similarly with the higher saturation mixing ratios at the tropical tropopause.

Overall, this thesis identifies the relative impact on stratospheric water vapour from temperatures, large-scale transport and ice sublimation in the tropical tropopause on different timescales. Many of the findings are in the context of the global climate models studied, motivating further development to represent more accurately both the present and projections across this century.

Table of contents

Chapter 1

Introduction

1.1 Background

Water vapour in the stratosphere has far-reaching impacts through radiative and chemical interactions. Changes to water vapour concentration in the stratosphere (hereafter H_2O_{strat} when referring to the topic and observations, otherwise q for model calculations) have a radiative impact at the Earth's surface and throughout the atmosphere beneath (Forster and Shine, 1999; Held and Soden, 2000; Maycock et al., 2011). H_2O_{strat} is also a constituent of polar stratospheric clouds which deplete ozone (Solomon, 1999). Variations across seasonal to century-wide timescales in the main source of H_2O_{strat} can be substantial. Causes of the present H_2O_{strat} distribution, and its changes, are therefore important to understand.

The stratosphere, troposphere, and Brewer-Dobson circulation

The lowest $\sim$15 km of the Earth's atmosphere is defined as the troposphere, where temperatures decrease with height (negative gradient) due to solar radiation heating the Earth's surface and the lowest levels where the atmosphere is more dense. Convective mixing re-distributes this energy vertically in the troposphere.

The stratosphere is the name given to the atmospheric region at $\sim$15–50 km altitude which is distinguished for a positive temperature gradient that is controlled primarily by radiation and ozone chemistry. In this region is an overall global-scale circulation pattern called the Brewer-Dobson circulation (BDC), driven by wave activity from the troposphere, which gradually moves air poleward (Brewer, 1949; Butchart, 2014; Haynes, 2005; Plumb, 2002). This is accompanied by upward motion over the equator, and downward motion at the poles.

Descriptions of air motion may also be thought of as the movement of individual air parcels. This approximation helps to distinguish properties of air present in one location from another as well as in situations of movement or mixing. Dividing the atmosphere entirely into fluid parcels to describe a dynamical or chemical property defines a tracer (Andrews et al., 1987, chapter 9).

The stratosphere is, however, very dry — at just below four parts per million parts of air per unit volume (3.7 ppmv) it is about ten thousand times drier than the lowermost atmosphere. Why it is so dry relates to the few processes that introduce water vapour to the region. The two main sources are methane oxidation and transport of air from the humid troposphere in the tropics.

Tropical Tropopause Layer

Between the troposphere and stratosphere is a vertical minimum in temperatures, this vertical cold point is colder and higher in the tropics ($\sim$17 km, compared to extratropics $\sim$11–15 km). The surrounding region is described as the tropical tropopause layer (TTL, Fueglistaler et al., 2009), where there is influence from a number of tropospheric and stratospheric processes. Those relevant to the large-scale transport of water vapour into the stratosphere are presented in the schematic in figure 1.1.

Typically, air parcels are lifted in convective events to levels below or near the tropical tropopause layer (label a in figure 1.1). Outside of these deep convective systems, in the upper troposphere there is general subsidence due to the local balance of radiative heating (b). However, some parcels surpass the level of zero radiative heating (LZRH) and move slowly upwards into the stratosphere.

Dehydration and other processes in the tropical tropopause layer

The concentration of water vapour in air is generally limited by the saturation concentration, defined by air pressure and the Clausius-Clapeyron relation for equilibrium pressure of water vapour over ice. This saturation limit depends on temperatures in a non-linear way, as shown in figure 1.2. As an air parcel cools its saturation limit lowers, and less strongly for successive cooling. As air rises and cools through the tropical tropopause layer, the saturation limit becomes smaller than the water vapour concentration. The air has become saturated, or even supersaturated. This drives a conversion of excess vapour to ice (label c in figure 1.1) by forming new crystals (nucleation) and by depositing onto any ice already present (deposition).

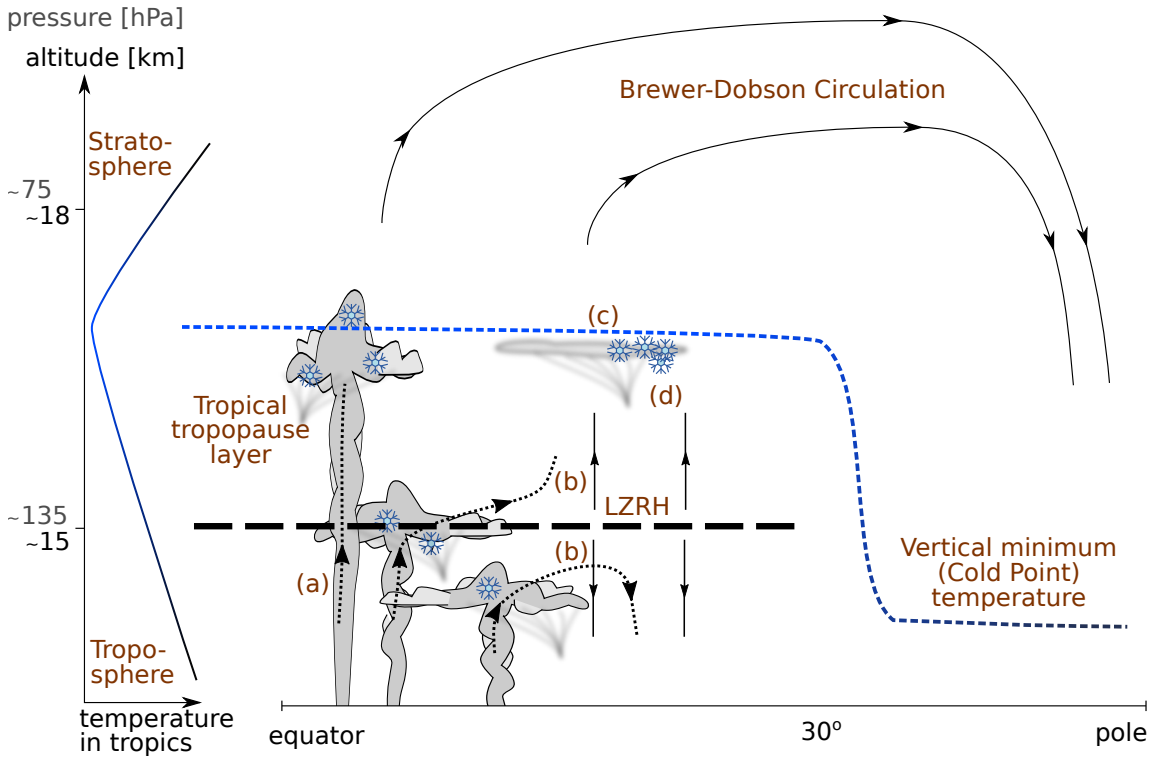

Fig. 1.1 Schematic of key regions and processes associated with the tropical tropopause layer (TTL). The labelled processes are (a) convective injection of tropospheric air including ice, (b) the overall descent below the level of zero radiative heating (LZRH) and ascent above, (c) vapour phase change to ice (deposition) at low temperatures (more widespread than displayed), (d) sedimentation of ice cloud (also more extensive than displayed).

In this way, air transported into the stratosphere through the tropical tropopause layer is strongly dehydrated.

The precise balance and rates of conversion between vapour and ice depend on many fine details. The fate of any ice present in the atmosphere, whether from convection or deposition, is usually to fall under gravity (sedimentation) and to convert back to vapour (sublimation) when encountering air that is sufficiently below saturation (d).

Annual cycles in the TTL and the tape recorder

Variability is substantial at many timescales in the tropical tropopause layer. There is an annual cycle in cold point temperatures which are coldest in boreal winter (hereafter winter unless specified; Fueglistaler et al., 2011; Ming et al., 2017; Reed and Vicek, 1969), which leaves an annual imprint on water vapour (amplitude of about 40 % of time mean concentrations) rising into the stratosphere (the water vapour tape recorder, Mote et al., 1996).

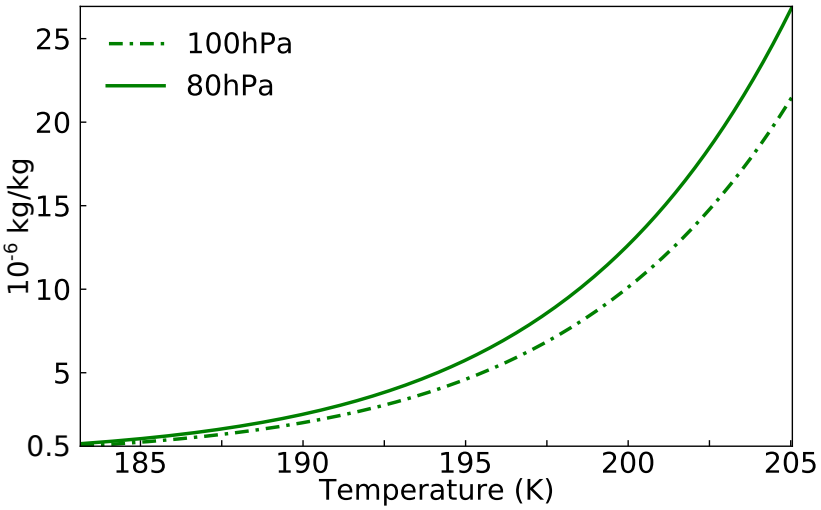

Fig. 1.2 Formulations of the saturation limit over ice ($\mathrm{kg\,kg^{-1}}$) of Wagner et al. (2011) formulation (described in section 2.4.1) at typical pressures of the tropical tropopause layer 100 hPa and 80 hPa.

The vertical propagation speed of the tape recorder is determined by the strength of the Brewer-Dobson circulation and mixing.

The Brewer-Dobson circulation also varies annually, with tropical upwelling weakest in boreal summer (hereafter summer unless specified; Randel et al., 2002). This variation contributes to the annual cycles in tropopause temperatures, the height of the vertical cold point — the base of the tape recorder signal — which is lowest in July-September and highest around January-April (for example, figure 5b of Kim and Son, 2012, showing pressure variation in GPS observations), and the vertical propagation speed.

An average annual cycle is defined by averaging each month over many years, referred to as a climatological annual cycle. The seasonal signatures of these processes are left in H_2O_{strat} which can therefore indicate how they are all represented in any estimates.

Interannual variability in the TTL

Interannual variations are also significant in the tropical tropopause layer, composed of a number of processes which primarily affect temperatures, perturbing H_2O_{strat} concentrations by $\pm 10\,\%$ ($\sim$1 ppmv peak to peak).

The Quasi-Biennial Oscillation (QBO), with a period of roughly 27 months, is a downward-moving signal of winds in the equatorial stratosphere which perturbs the Brewer-Dobson circulation. When the associated temperature perturbations descend to the tropical tropopause, they alter the tape recorder signal.

The El-Niño Southern Oscillation, with ∼2–7 year timescales, is associated with horizontal shifts in deep convection in the west Pacific Ocean and driving of the Brewer-Dobson circulation, both of which affect temperatures and water vapour in the tropical tropopause layer (Konopka et al., 2016).

Other interannual influences on tropical tropopause temperatures with implications for H_2O_{strat} include major sudden stratospheric warmings (occurring roughly every other year, Tao et al., 2015) and strong volcanic injections of aerosols (Fueglistaler and Haynes, 2005; Joshi and Shine, 2003).

The interannual variability that arises from the combination of these different processes may present abrupt deviations, as suggested for the temporary rise and drop in 2015-2016 (Avery et al., 2017; Tweedy et al., 2017), the temporary drop 2011-2012 (Gilford et al., 2016; Urban et al., 2014) and the prolonged drop following 2000 (∼25 % drop over a couple of months, ∼10 % when discounting annual variation) (Fueglistaler, 2012; Randel et al., 2006; Tao et al., 2015).

1.2 Motivation and research questions

Climate models

An essential application of meteorology and climate science are global climate models. These are computational calculations of the leading order processes acting in the atmosphere (and potentially other climate components such as oceans, sea ice and land cover). Their results are approximations of the real atmosphere, and their estimates of H_2O_{strat} will therefore be referred to separately as q. Climate models inform meteorological forecasts and climate projections. Climate models provide confidence in changes that will occur in the atmosphere and ocean this century (Intergovernmental Panel on Climate Change, 2013b), especially when the projections of a diverse set of climate models are consistent.

Kim et al. (2013) have compared temperatures in the tropical tropopause layer in the recent generation of climate models of the CMIP5 project. They have found a trend for lifting and warming of the tropical tropopause. They have also found modelled tropical tropopause temperatures to be very different but systematically warm compared to reanalyses, with implications for q. Gettelman et al. (2010) have reported findings from a multi-model comparison of climate models with interactive chemistry which show a wide spread in present day estimates of q, as well as general moistening of the stratosphere in future scenarios. As

the implementation of current understanding of climate processes, model development is crucial to improve accuracy and confidence in climate projections.

Met Office Unified Model

One particular model, the Met Office Unified Model (UM), has sought to address its tropical tropopause warm and wet biases with extensive physical and numerical development (Hardiman et al., 2015). While the specific process refinements had modified temperatures and q in expected ways, some of which responded consistently with a Clausius-Clapeyron relationship, their combined response has led to only a slight reduction of warm and wet biases. The coupling of temperature and water vapour through the Clausius-Clapeyron relation in the tropical tropopause may therefore not be a very strong constraint. This needs to be confirmed. If so, it remains to be asked what determines the wet bias of the climate model stratosphere. Answers may be completely numerical (relating to computation on the model grid), or relate to mis-representations of the physical processes (perhaps from unexpected behaviour in large-scale transport or the parameterised interactions between phases of modelled water) or contributions from reasonably represented processes like convective injection of ice.

Advection-condensation

The processes described in section 1.1 can affect water vapour rising into the stratosphere in a number of ways. It has been established that the leading controls of variations in H_2O_{strat} are the simple combination of instant dehydration to the saturation limit and large-scale transport (Fueglistaler et al., 2005; Gettelman, 2002; Liu et al., 2010; Schoeberl and Dessler, 2011). The application of this method, recording the pathways of air parcels into the stratosphere and dehydrating instantly according to temperature and pressure, is referred to by many names including Lagrangian dry point calculation, final dehydration and the advection-condensation method to name a few. Where studies account for only this simple combination, interannual variability is well described, but a fixed dry bias persists. The details of ice microphysics (which generally moisten the simple advection-condensation method) are therefore secondary to the dehydrating effect of temperature. But, the temperature field varies substantially both horizontally and temporally. The additional effect of wind variability is then to modify the weighting function of sampled temperatures. Some regions and some time periods of tropical tropopause temperatures may be sampled more often than others.

Aspects worth further study in the advection-condensation method

A first aspect to consider is whether the advection-condensation method provides insight to water vapour calculated by a global climate model. There are several aspects of representation to consider. One is the physical representation of the annual cycles in the tropical tropopause layer and tropical lower stratosphere. The other is to distinguish the differences in the underlying calculations, such as between climate model advection scheme and advection-condensation transport, as well as the timescales of instantaneous dehydration.

Variations in temperatures at sub-seasonal timescales are one important aspect for H_2O_{strat}. Earlier studies have shown that H_2O_{strat} predictions are lower when sub-monthly temperature variance is larger in the tropical tropopause layer (Liu et al., 2010). Sub-seasonal variability has been found to be underestimated in reanalysis compared to observations (Kim and Alexander, 2015). The subsequent impact on tropopause temperatures has been alluded to (figure 5 of Fueglistaler et al., 2013), and Bonazzola and Haynes (2004) have pointed out that loss of sub-daily and $<$90 day temperature variability moistens Lagrangian dry point predictions of the stratosphere. However, it has not been fully investigated how the structure of sub-monthly variability affects dehydration and the transport of water vapour entering the stratosphere. Neither has the impact between reanalysis and climate models been compared.

The impacts of variability from transport alone in the advection-condensation method are less clear. Of particular relevance is the Asian summer monsoon anticyclone, where a significant number of air parcel pathways through the tropical tropopause layer are constrained to the point that they miss the coldest regions (suggested by Bannister et al., 2004; James et al., 2008; Park et al., 2008). However its overall contribution to H_2O_{strat} remains debated (Wright et al., 2011). In particular, Hasebe and Noguchi (2016) have provided evidence that the observed step-wise drop in lower stratospheric water vapour concentrations in the years after 2000 is caused by both tropopause cooling and a weaker monsoon constraint of pathways. The impacts of changes in temperatures and transport may be separated further by investigating how dehydration patterns respond to separately evolving the timeseries of wind and temperature.

Aspects worth further study not in the advection-condensation method

While the simple advection-condensation method has been found to explain variability in H_2O_{strat} (Fueglistaler et al., 2005; Liu et al., 2010), there are aspects not captured by it. Its prediction for average concentrations of water vapour in the lower stratosphere often disagree with observations (Schoeberl and Dessler, 2011). This suggests that the processes neglected

by the method cannot be ignored entirely. To this end, several underlying assumptions of the advection-condensation method have been tested in earlier studies.

For instance, the advection-condensation method takes no account of small-scale mixing processes (Riese et al., 2012), nor the detailed ice microphysics that occur as water vapour is deposited. Many published findings test dehydration with a higher fraction of saturation (allowing supersaturation) leading to wetter estimates for the stratosphere (for example, James et al., 2008; Jensen and Pfister, 2004; Schoeberl and Dessler, 2011). The method also assumes dehydration is instantaneous whereas, in reality, vapour nucleation and deposition have a finite timescale that depends on many aspects of the air and available ice. This aspect has been incorporated into the advection-condensation method in some cases (Bonazzola and Haynes, 2004; Gettelman, 2002; Jensen et al., 2018) also with a moistening effect.

Importantly, sublimation after the final dehydration of air entering the stratosphere may occur, referred to as rehydration. Ice may be present from several processes which may be contained in, or external to, the advection-condensation calculation. For water vapour that has previously deposited, the ice encountered may have formed from earlier dehydration in the same parcel of air, or it could have fallen (sedimented) from above. Various approaches have been taken to incorporate rehydration into the advection-condensation method, including those of Dessler et al. (2016, 2007); Gettelman (2002). The effect of each of these processes suggests that H_2O_{strat} concentrations may be captured if a more realistic and complete set of water phase processes are accounted for in the advection-condensation method.

There may also be an influence on H_2O_{strat} that bypasses the advection-condensation processes, extreme deep convective events may introduce ice directly into the tropical lower stratosphere (convective injection), sublimating and thereby modifying the water vapour budget. Depending on the local saturation limit (hereafter the saturation mixing ratio, SMR) and properties of ice nucleation and deposition, this may hydrate or dehydrate. There is observational evidence for specific cases of deep convective events to cause dehydration (Kim et al., 2018) and increases in water vapour (Corti et al., 2008; Danielsen, 1993; Khaykin et al., 2009). Both effects are supported by modelling studies (Schoeberl and Dessler, 2011; Schoeberl et al., 2019; Ueyama et al., 2018, 2015). The overall impact on H_2O_{strat} is sensitive to the relative humidity and dehydration efficiency where ice is injected (Jensen et al., 2007; Rollins et al., 2016), and is therefore currently uncertain. Clarity on the involvement of convectively injected ice in the water budget of the tropical tropopause layer may begin to constrain its role in estimates of H_2O_{strat}.

Climate change impacts

Separate to the insight provided by processes contained and neglected by the advection-condensation method is the question of climate change impacts. In response to higher carbon dioxide concentrations, the Brewer-Dobson circulation is predicted to strengthen (Butchart, 2014). The tropopause is expected to lift and warm, but is sensitive to each climate model in which it is simulated. This is expected to drive long-term increases in H_2O_{strat} (Gettelman et al., 2010), delivering an amplifying effect on surface temperatures. Changes to variability of temperatures and transport, and their informing processes may yet exert as much influence. With the incomplete understanding of H_2O_{strat} control in the present climate, the relative role of different processes may be inaccurately represented in estimates of H_2O_{strat}. While trends in methane oxidation are not expected to cause leading-order changes to H_2O_{strat} (Revell et al., 2016), if the influence of convection is strong (whether dehydrating or rehyrating overall) future predictions for H_2O_{strat} remain uncertain. Therefore, characterising processes determining H_2O_{strat} is important to improve projections.

A calculation by Dessler et al. (2016) has sought to characterise H_2O_{strat} trends over the 21^{st} century in two climate models, accounting for advection-condensation and convective injection. Such a result would address a number of the challenges detailed above, specifically the characteristics of moisture sources in the stratosphere not from advection-condensation. However, several aspects of their method are unclear and lack justification. For example, their work has pointed out that, at fixed pressure levels near the tropopause, convectively lofted ice increases over the century. But, the tropopause is projected to lift, distorting what is being compared at fixed pressure levels. Therefore, this does not clearly identify trends affecting the atmosphere above the tropopause. They have concluded that sublimation of convectively lofted ice is necessary to derive sufficient absolute increases in H_2O_{strat}. Several aspects are therefore to be questioned: the characteristics of ice in the tropical lower stratosphere, its trends, its variability, and the details of ice rehydration parameterisation on the advection-condensation method.

1.3 Outline of thesis

Several points worthy of investigation have been raised, and will be distilled in this section. It will also outline how and where this thesis aims to address these questions.

The data sources and general methods applied in this thesis will be provided in chapter 2, and some specific details follow in each chapter where relevant.

Chapter 3 will begin the investigation of processes affecting H_2O_{strat} in climate models. To do so, results of the advection-condensation method in reanalysis and two different climate models will assess influences on annual cycles in the tropical tropopause layer and lower stratosphere. As part of this, it will seek to uncover the transport differences between the climate model and the advection-condensation calculations, and to address the impact and structure of sub-monthly temperatures on H_2O_{strat} in reanalysis and climate models.

Chapter 4 will draw further insight from the advection-condensation method by introducing a novel method to quantify the control of temperatures and winds separately on variability of H_2O_{strat} on interannual and seasonal timescales. The bulk of the study is conducted in reanalysis to assess the relationship of temperature and wind variability in the historical timeseries. The conclusions are briefly confirmed for a global climate model.

Chapter 5 will provide, to my knowledge, the first comprehensive breakdown of processes contributing to the water budget of the tropical tropopause layer on the timesteps of a climate model. This chapter will then quantify the impact of ice rehydration on H_2O_{strat} from process-specific parameters. The results of ice penetration will be contrasted with local saturation mixing ratios, and make a suggestion to investigate a potentially observation-based treatment of ice microphysics in the advection-condensation method.

The final topic to be investigated will be the contributions to climate model trends of H_2O_{strat} across the 21^{st} century. The advection-condensation method will yield a process-based description of the primary changes. More specifically, the projected changes to convective injection and its influence on H_2O_{strat} need to be determined to provide crucial clarification of trends in modelled H_2O_{strat}. Chapter 6 will build on the previous chapter's water budget analysis to investigate the role of model processes in climate forcing scenarios. In particular the results provide insight to the make-up of stratospheric water vapour trends, and how convective influence changes in the climate model studied.

Bringing together this investigation of water vapour entering the stratosphere, the conclusions and overall contributions of this thesis will be discussed in chapter 7.

Chapter 2

Methods and data sources

The goal of this thesis is to understand better the processes controlling water vapour entry to the stratosphere. Advection-condensation calculations are an established method to determine the key influences in reanalysis, however it may be utilised to uncover aspects affecting stratospheric water vapour in global climate models. Study of its elements in this thesis will include the relative role of temperature and transport in variability, the effect of different sub-seasonal timescales of the temperature field in reanalysis and climate models, model process indications of ice rehydrating the tropical lower stratosphere, and the characteristics of their response to climate forcing scenarios.

To achieve these goals, the advection-condensation method of Lagrangian dry points will be qualified in the climate models that will be studied. The direct observations that will be used to evaluate model representation of H_2O_{strat} will be described in section 2.1. Following this will be details of observation-assimilated climate models, reanalysis datasets, in section 2.2. Methods to estimate H_2O_{strat} will then be described, including global climate models in section 2.3 and the Lagrangian advection-condensation approach in section 2.4. An implementation of the advection-condensation method to a tracer advected by a climate model is developed in section 2.5. Experiments in each chapter will also modify the basic Lagrangian dry point method, simplifying some aspects and expanding on others.

To be clear, the topic of stratospheric water vapour and its observational records will be referred to as H_2O_{strat}. Estimates of H_2O_{strat} from global climate models will be referred to as q. Alternative calculations will show a relevant suffix, such as q_{LDP} for Lagrangian dry point calculations, and will be introduced in the appropriate section.

2.1 Observation datasets

2.1.1 Stratospheric water vapour

Records of stratospheric variables are available from some balloon and rocket-sondes and from satellites. These two approaches provide complementary performance in horizontal coverage and vertical resolution. For water vapour, sondes offer very detailed vertical profiles but require extensive and sustained campaigns to offer a global long-term view. Meanwhile satellite-borne measurements sample almost all latitudes and longitudes but resolve vertical regions no more precisely than 1–4 km (Damadeo et al., 2013; Harries et al., 1996; Lambert et al., 2007; Thomason et al., 2010).

It is therefore challenging to accurately observe the strong vertical gradients in water vapour near the tropical tropopause layer. The large atmospheric variability combined with the multitude of processes acting make it difficult to constrain climate models in this region.

A second challenge to useful stratospheric water vapour records is achieving sufficient sampling over a long time. Many sites reporting stratospheric sonde data do not provide regular observations over many years. Some such radiosonde stations have been operating over many decades (for example at Boulder, USA, since 1980 Hurst et al., 2011; Oltmans et al., 2000) however they have been difficult to reconcile with satellite records (Hegglin et al., 2014; Lossow et al., 2018). Satellite-based observations are also intermittent because of limited instrument lifetimes (ranging up to two decades).

There has been a recent effort to merge overlapping satellite observations into a single useful timeseries, called SWOOSH (Stratospheric Water and Ozone Satellite Homogenized database Davis et al., 2016). For water vapour, this timeseries starts from 1986. The dataset is constructed by merging satellite datasets onto a regular grid. This involves grouping individual vertical retrievals into gridded regions and performing an average over them all (that is, each satellite contribution is weighted by its number of observations in that gridbox). This is performed for each month for a sufficient number of retrievals in each gridbox. Any gridboxes lacking sufficient satellite records are treated as empty. SWOOSH can also provide an estimate for these empty gridboxes from the climatological average annual cycle.

This thesis will study the period 1999–2009 in which there are two distinct periods of satellite coverage which necessitate use of a merged satellite record. Before 2006, available satellite records of H_2O_{strat} include HALOE, and SAGE-II, whereas from mid-2004 Aura MLS (Livesey et al., 2011) is incorporated. The SWOOSH dataset will be used as a source of homogenised satellite data as a best-observed state of stratospheric water vapour for comparison with global-scale results in the same time period.

A systematic difference exists between HALOE and MLS records of water vapour. For the purposes of interannual variability where the deseasonalised timeseries is of interest, not the time mean, the difference is usually dealt with by applying a constant offset to one of these two timeseries (for example, as done by Fueglistaler et al., 2013; Randel, 2010). To account for such systematic differences, the SWOOSH methodology determines measurements between one satellite and the reference record from MLS that are approximately collocated. It then calculates and applies a mean offset as a function of latitude and altitude for each non-reference record. The combined monthly mean can then be determined (see Davis et al., 2016, for further details). This minimises the systematic differences and also provides a useful time mean estimate for comparisons in this thesis.

2.1.2 Deep convection

As a proxy for the spatial distribution of deep convective activity, outgoing long-wave radiation (OLR) will be compared. The record from the High-Resolution Infrared Radiation Sounder (HIRS) (Schreck et al., 2018) will be used for this purpose. Aboard the same set of NOAA satellites as its well-used predecessor, this record set implements a number of modifications to provide a more 'climate-quality homogeneous dataset'. Two key changes are an improved estimate of the OLR diurnal cycle, and the incorporation of sounding channels detecting water to provide a more accurate OLR dataset.

2.2 Reanalysis datasets

A reanalysis dataset provides a consistent system of assimilating observations into a specific global climate model over a historical period. The same techniques are applied as in climate analysis datasets for meteorological forecasting, but instead of focusing on present day records it is applied to historical data to produce a consistent timeseries (in that sense, re-analysing past records). Such datasets generally offer the best estimate of the atmosphere as the physical understanding built into climate models is combined with what observations are available.

However, the reliability of a reanalysis extends only as far as the records that are assimilated (usually temperatures, horizontal winds, surface pressure, and humidity in the troposphere), and model implementation. For example, many current reanalyses have simple parameterisations for the impact of methane oxidation on stratospheric water vapour, and older reanalyses take no account of this process at all. Additional complications arise from

the assimilation process, such as discontinuities in long timeseries where new (and often more accurate or detailed) observational records are incorporated.

In particular, stratospheric water vapour calculations in reanalysis are limited as there are no direct observations to inform them. Instead, it is determined from the driving climate models. The recent and comprehensive comparison of H_2O_{strat} in reanalyses by the S-RIP project (Davis et al., 2017) show poor agreement with observations and advise against their use in scientific studies.

However, the dynamical fields of winds and temperatures in reanalysis find good agreement (Long et al. 2017, particularly Figures 8 and 9; Abalos et al. 2015; Boothe and Homeyer 2017; Kim et al. 2019), and have been used extensively to drive Lagrangian transport studies of water vapour entering the stratosphere (Fueglistaler et al., 2013; Kremser et al., 2009; Liu et al., 2010; Poshyvailo et al., 2018; Schoeberl et al., 2012; Tao et al., 2019). ERA-Interim (ERA-I) is one of the commonly used reanalyses for such studies. Transport is also more consistent between kinematic and diabatic vertical winds (Liu et al., 2010). For these reasons, ERA-I (Dee et al., 2011) is studied in this thesis.

It should be noted that the ERA-I reanalysis product has reached the end of its operational life (its timeseries was discontinued on 31st August 2019). Its replacement, ERA5 is available (Copernicus Climate Change Service (C3S), 2017) but will not be studied in this thesis. The reanalysis dataset offers vast increases in resolution as well as developments to its climate model and assimilation system, but it has not yet been studied for basic characteristics of stratospheric water vapour.

2.3 Global climate models

Global climate models incorporate the fundamental leading-order processes that control the Earth's climate. This Earth-system approach attempts to depict the known process that may be relevant for answering questions relating to historical climate interactions, present day numerical weather prediction, and future climate projections.

For the atmosphere, this involves coupling the fluid dynamical equations to schemes of radiation, moisture and convection. Boundary and forcing conditions include insolation, chemical composition (for example, carbon dioxide and aerosols), sea surface temperatures, sea ice extent, land surface roughness (vegetation types), orography and volcanic injection. Many of these may instead be represented through coupling to further physical models of features such as oceans, sea ice, vegetation and atmospheric chemistry.

Stratospheric water vapour is highly dependent on all of these schemes, necessitating full global atmosphere models for its representation. With direct observations of tropical tropopause processes incomplete, H_2O_{strat} can arguably be examined in more detail in climate models where complete diagnostic approaches can be used. Complete water budgets on model grids can show explicitly the involvement of each process. With this information, extensive model evaluation is possible. Constraining these processes is dependent on the availability of suitable observations.

2.3.1 Met Office Unified Model

The climate model experiments in this thesis are based upon configurations of the Met Office Global Atmosphere model, collectively referred to as the Unified Model (UM).

The model has a hybrid height vertical grid (terrain following bottom level, adjusting back to geopotential height until 18 km altitude). It advects with a semi-implicit semi-Lagrangian scheme; the latest-timestep gridpoint values are determined from a Lagrangian determination of their location at the previous timestep. This demands interpolation calculations and conservation corrections. Another aspect imposed for numerical reasons is minimum concentrations throughout the atmosphere; tracer values must be positive-definite (greater than zero) and the minimum permitted specific humidity is $10^{-8}\,\mathrm{kg\,kg^{-1}}$.

In this thesis, two model configurations will be utilised that build on the configurations and simulations that support two SPARC activities: an assessment report on ozone depleting substances (Ko et al., 2013), and QBOi (Butchart et al., 2018). The experiment of the first configuration was conducted by Dr Amanda Maycock. The experiments in the second configuration were initially conducted by Dr Andrew Bushell and I re-ran them for additional diagnostics relating to Lagrangian and water budget analyses that appear in each chapter, as well as to develop the tracer subjected to instantaneous dehydration in section 3.3.

The first UM version is configured with interactive chemistry (Morgenstern et al., 2009) – importantly for H_2O_{strat} and the tropical tropopause this configuration enables ozone interaction with dynamics – and is referred to as UM-UKCA. Its specific model version is HadGEM3 vn7.3 GA6. It has 96×72 gridpoints longitude$\times$latitude with 60 vertical levels extending to 84 km altitude.

In the second UM configuration chemistry (and ozone) is prescribed. It is also a later model version, HadGEM3 vn10.4 GA7, and so is referred to as UM10.4. A number of changes have been made to numerical and physical schemes (both formulations and parameterisations), targeting several known model deficiencies (see Walters et al., 2019, for

Table 2.1 Description of Unified Model configurations used in experiments. (*) Difference of UM-UKCA and CONTROL of table 2.2 10 °N–S zonal mean 100 hPa 10 year mean from ERA-I 96 hPa 1999-2009 mean.

Description	UM(GA) version	TTL temperature bias *	Interactive chemistry	Resolution (lon × lat × ht)	levels in 15–19 km
UM-UKCA	HadGEM3 vn7.3 GA6	5.8 K	yes	$96 \times 72 \times 60$	15.7, 16.8, 18.0
UM10.4	HadGEM3 vn10.4 GA7	2.6 K	no	$192 \times 144 \times 85$	15.4, 16.0, 16.7, 17.4, 18.0, 18.8

further details). The principal implication of the later model version for H_2O_{strat} is a reduced warm bias in the model's tropical tropopause layer and a slightly smaller wet bias in the stratosphere. The resolution is also higher, 192×144 with 85 vertical levels extending to 85 km altitude. The main configuration details, and estimates of tropical tropopause layer temperature bias are provided in table 2.1.

Interactive chemistry has two impacts on the simulation of stratospheric water vapour. One is its direct increase from methane oxidation which is otherwise parameterised. Being a generally slow process in a relatively steady part of the atmosphere, this is expected to make little difference in present day scenarios. The other impact is indirect, as interactive ozone can respond to dynamical variability in the tropical tropopause layer. It amplifies the effect of cooling processes (notably the Brewer-Dobson circulation) on tropopause temperatures (Fueglistaler et al., 2011; Randel et al., 2006), thereby amplifying variations in final dehydration. The difference due to interactive chemistry is anticipated to be slightly increased variability of tropopause temperatures and water vapour.

Following a ten year spin-up period from initial state, the UM-UKCA is forced by year 2000 conditions (sea surface temperatures, insolation, sea ice and aerosol forcing) for 50 years. For the UM10.4, three forcing scenarios are carried out. Its CONTROL case repeats year 2002 forcing conditions for 42 years, the other cases multiply CO_2 concentrations and increment sea surface temperatures. The model configuration details are also provided in table 2.1, and experiment-specific configurations are provided in table 2.2

These model configurations have been chosen to provide similar forcing conditions but contrasting simulations of the present day tropical tropopause. By analysing these scenarios for processes relevant to stratospheric water vapour, conclusions about their relative role may be argued to span the recent UM representations of this part of the atmosphere. The climate forcing scenarios also provide a view of projections from one model, with a complementary

Table 2.2 Description of Unified Model experiments analysed. (*) I re-ran these experiments to obtain additional diagnostics for analysis of water budgets, Lagrangian dehydration, and development of tracer subjected to instantaneous-dehydration.

UM configuration	Experiment description	Forcing scenario year repeated	Designed by	Conducted by
UM-UKCA	UM-UKCA	CCMVal REF-B2 year 2000	Eyring et al. (2010)	Dr A. Maycock
UM10.4	CONTROL	year 2002	Butchart et al. (2018)	Dr A. Bushell*
UM10.4	$CO_2 \times 2$,SST+2 K	year 2002	Butchart et al. (2018)	Dr A. Bushell*
GCM	$CO_2 \times 4$,SST+4 K	year 2002	Butchart et al. (2018)	Dr A. Bushell*

multi-model analysis soon available for context from the QBOi project (Bushell et al., 2019; Holt et al., 2019; Richter et al., 2019).

To determine saturation limits for water vapour, the UM implementation of saturation vapour pressure over ice and liquid water follows the Goff-Gratch formulation (UMDP29, 2018). It is provided as a look-up table of temperatures every 0.1 K between 183.16 K and 338.16 K. Interpolation is applied to obtain the exact temperature in each calculation. It will be compared with other commonly used formulations of the saturation vapour pressure in section 2.4.1.

Further details of how the UM schemes are calculated in a model timestep, with particular focus on modifiers of ice and water vapour in the tropical tropopause, will be provided in section 5.2 before the relevant analysis.

The UM has been included in many multi-model intercomparison studies (including comparisons of climate chemistry and stratosphere dynamics, Butchart et al., 2018; Eyring et al., 2016; Kim et al., 2013; Morgenstern et al., 2017; Taylor et al., 2012). It also shares the same shortcomings. Of the CMIP5 generation models studied by Kim et al. (2013), they have shown tropical tropopause mean temperature to be 1.8 K too warm compared to reanalysis (their table 2). So too have all historical versions of the UM which results in a stratosphere that is too wet (Hardiman et al., 2015).

2.4 Lagrangian advection-condensation method

As described in section 1.1, stratospheric water vapour is closely constrained by the low saturation limits experienced by air being transported through the tropical tropopause layer. As such, H_2O_{strat} can be simply represented by calculating only the advection and condensation of pathways entering the stratosphere.

For situations where a variable is strongly linked to transport, a Lagrangian method has advantages. This is because the large variations from advecting a quantity between fixed points are removed from the calculation, thereby reducing residual errors. However, uncertainty remains in the representation of transport, as well as a lack of small-scale mixing.

An offline transport scheme makes use of vector wind fields, $\mathbf{u}(\mathbf{x},t)$, a function of spatial position and time provided from a separate calculation. These could be from reanalysis, a global climate model, or some artificially generated field. From an initial set of particle positions $\mathbf{x}(t_0)$, the particles evolve according to:

$$d\mathbf{x} = \mathbf{u}\, dt \tag{2.1}$$

The Lagrangian trajectory code utilised in this thesis is called OFFLINE (Liu, 2009; Methven, 1997), which has been widely used in the past to study transport in the tropical tropopause layer (for example, Bonazzola and Haynes, 2004; Fueglistaler et al., 2005; Fueglistaler and Haynes, 2005; Fueglistaler et al., 2013). OFFLINE employs procedures for fourth-order Runge-Kutta timestepping and polynomial interpolation (Press et al., 1992, sections 3.1 and 16.1) which is linear in the horizontal and cubic in the vertical. It also records fields of interest such as temperature at each point along trajectory pathways with the same interpolation procedure. Additionally, the scheme contains a procedure by which the vertical advection coordinate can be different from the grid of the input data. The rest of the transport scheme works on the input grid, so only the vertical advection step is performed using a transformed grid.

I have implemented additional functionality in OFFLINE. The code now allows vertical advection on any vertical grid that is different from the vertical structure of input fields (provided the vertical advection grid is provided on the input grid). There is also the option to record a second temperature field from an alternative file stream. Additionally, Prof Peter Haynes has provided a modified copy of OFFLINE that records a second temperature field along pre-calculated trajectories.

The instantaneous-dehydration method to estimate H_2O_{strat} from a set of trajectory pathways requires a few more steps. First, the trajectory pathways originating in the troposphere

that reach the stratosphere must be selected. Secondly, the saturation mixing ratio must be determined using the pressure and temperature record along the trajectory path. Implementing the instantaneous dehydration approximation, and assuming a wet troposphere and no rehydrating processes in the lower stratosphere, the final trajectory concentration of water vapour will be determined by the pathway's minimum saturation mixing ratio. Where this occurs is referred to as the Lagrangian dry point (LDP). Using the history of temperature, pressure and wind velocities in this way obtains details of final dehydration characteristics and an estimate of H_2O_{strat} for the point of trajectory release. The average across an ensemble of trajectories released on a horizontal surface in the tropics and at a single time provides an estimate of H_2O_{strat} entering the tropical stratosphere (the estimate will be referred to as q_{LDP} or SMR_{LDP}).

For ERA-I input, trajectories are subjected to diabatic heating as the vertical advection component on a vertical grid of potential temperatures (further details in Liu et al., 2010), whereas for the UM10.4 and UM-UKCA (non-hydrostatic) input vertical advection is driven by vertical velocities (kinematic) on the model hybrid height grid.

For the investigations in this thesis, trajectories are calculated for each of the climate model experiments listed in table 2.2. The sensitivity of their configuration is tested in section 2.4.2. In brief, they are all configured as back-trajectories for one year, with ten advection timesteps between six hourly snapshots of wind velocities and temperature fields. They are initialised on a horizontal surface above the tropical tropopause (ERA-I: 83 hPa, UM-UKCA: 400 K, UM10.4: 75 hPa), between 30 °N–S every 2° in latitude and longitude. Only trajectories that reach the troposphere within 12 months are considered to represent troposphere-to-stratosphere transport. The criteria for reaching the troposphere are (potential temperature) θ <340 K, and $SMR > 10^3$ ppmv.

The ERA-I 6 hourly diabatic trajectories were calculated by Dr Y S Liu as part of earlier studies (Fueglistaler et al., 2013; Liu, 2009; Liu et al., 2010). For this thesis, I have defined troposphere-to-stratosphere transport differently and separately calculated Lagrangian dry points from this set of trajectories. I carried out all other trajectory calculations. Evaluation of Lagrangian dry points in the current study are described in sections 3.2 and 4.2.

2.4.1 Formulation of saturation limit of water vapour

The calculations of saturation mixing ratio require a formulation of the Clausius-Clapeyron relation for saturation vapour pressure over ice. The theoretical form of this relation is dependent on a number of terms which are sensitive to temperature. The complexity of this

Table 2.3 Factors in equation (2.2), determined by Wagner et al. (2011).

i	a_i	b_i
1	$-0.212\,144\,006 \times 10^{2}$	$0.333\,333\,333 \times 10^{-2}$
2	$0.273\,203\,819 \times 10^{2}$	$0.120\,666\,667 \times 10^{1}$
3	$-0.610\,598\,130 \times 10^{1}$	$0.170\,333\,333 \times 10^{1}$

sensitivity has meant that approximations are required to derive the theoretical relationship (Rogers and Yau, 1989, chapter 2). Some amount of empirically-based data is required for an accurate formulation of the saturation limit.

A number of empirically-based formulations for the saturation vapour pressure over ice have been proposed in recent decades. The formulation of Marti and Mauersberger (1993), which is based on experimental measurements and has a reported accuracy of about 2 %, has been used in some studies (Liu, 2009; Liu et al., 2010). The review of Murphy and Koop (2005) clarified earlier publications and the application of experimental data to the extreme low temperatures that occur in regions of the atmosphere. Their formulation has also been used in a number of studies (Jensen et al., 2005; Schoeberl et al., 2012; Ye et al., 2018). Since then, Wagner et al. (2011) have calculated a more accurate estimate from empirical data. More recent and more accurate experimental measurements of saturation vapour pressure over (hexagonal) ice have been made by Bielska et al. (2013). Comparing with these earlier formulations, they found closest agreement from the formulations of Murphy and Koop (2005) and Wagner et al. (2011). Figure 2.1 shows the relative difference of these formulations for the saturation vapour pressure over ice.

The calculations of saturation vapour pressure over ice in the advection-condensation method in this thesis will follow the formulation of Wagner et al. (2011). It is:

$$p_{subl} = p_0 \exp\left(a_1 \left(\frac{T}{T_0}\right)^{b_1-1} + a_2 \left(\frac{T}{T_0}\right)^{b_2-1} + a_3 \left(\frac{T}{T_0}\right)^{b_3-1}\right) \tag{2.2}$$

where p_0 =611.657 Pa and T_0 =273.16 K are properties of the water triple point. The additional factors are provided in table 2.3.

The difference between the formulations of Goff-Gratch (used in the UM experiments) and Wagner (used in Lagrangian dry point calculations) can be seen in figure 2.1 is less than 0.2 % in the range 183.16–273.16 K.

The saturation mixing ratio (with units of parts per million per unit volume, ppmv) can then be determined by dividing by the local pressure:

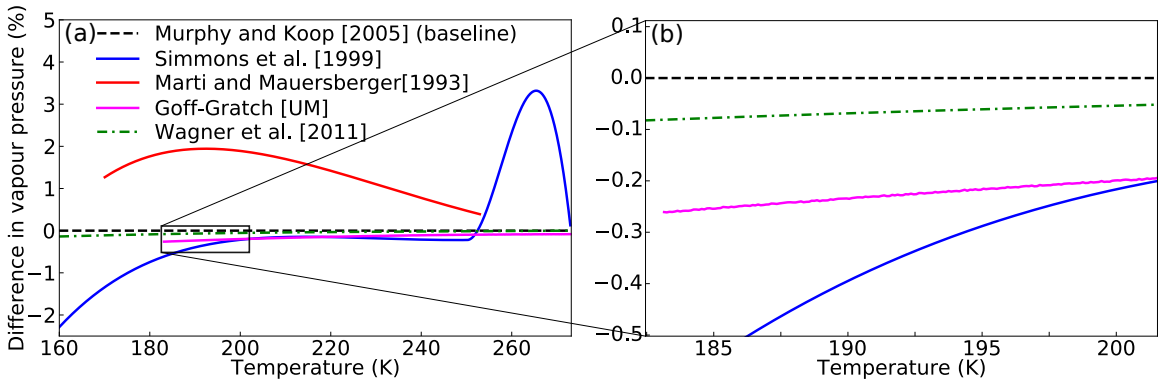

Fig. 2.1 Formulations of the saturation limit over ice. (a) Percentage difference between various formulations relative to Murphy and Koop (2005) formulation, (b) sub-region of (a) relevant to typical temperatures of the tropical tropopause layer.

$$SMR(\text{ppmv}) = \frac{p_{subl}}{p} \times 10^6 \tag{2.3}$$

Alternatively, the saturation mass mixing ratio of water vapour (with units of kilograms of water per kilogram of air $\text{kg}\,\text{kg}^{-1}$) is determined by multiplying the volume mixing ratio by the ratio of molar masses for water vapour and air:

$$SMR(\text{kg/kg}^{-1}) = \frac{p_{subl}}{p} \frac{m_{\text{H}_2\text{O}}}{m_{\text{air}}} \tag{2.4}$$

where $m_{\text{H}_2\text{O}}$ is $18.02\,\text{g}\,\text{mol}^{-1}$ and m_{air} is $28.97\,\text{g}\,\text{mol}^{-1}$ (Andrews, 2000).

2.4.2 Configuration of trajectories

The configuration of trajectories is intended to capture troposphere-to-stratosphere transport and to analyse the entry value of water vapour entering the stratosphere. Because comparisons will be made between multiple driving datasets (ERA-I, UM-UKCA, UM10.4), differences in configuration will be minimised.

ERA-I

The configuration of the provided ERA-I trajectory dataset has been shown to be suitable for analysis of annual and interannual variability in tropical tropopause temperatures and lower stratospheric water vapour by Fueglistaler et al. (2013). The dataset trajectory calculations have 1 year histories, and are initialised every month at 83 hPa every $2° \times 2°$ within 30 °N–S (5580 particles per initialisation).

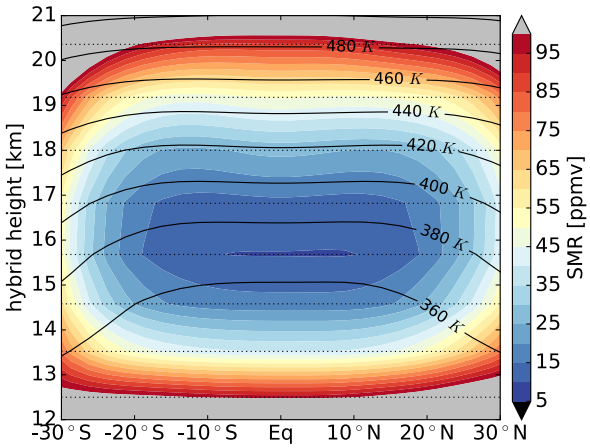

Fig. 2.2 Zonal mean 10 year mean of saturation mixing ratio (shading), potential temperatures (black contours) and model levels (dotted) lines in UM-UKCA.

UM-UKCA

The temperature distribution in a climate model will differ to reanalysis, and therefore the initialisation height must be considered for each case. Trajectories initialised too low will miss final dehydration positions, and a release too high will not be efficiently transported back to the troposphere, thereby insufficiently capturing the process of large-scale troposphere-to-stratosphere transport.

Figure 2.2 shows the variation of time mean saturation mixing ratio and potential temperature with latitude and height in UM-UKCA. The values of saturation mixing ratio are lowest between 20 °N–S and 360–390 K. Trajectories initialised at 400 K are therefore considered to be sufficiently above the vertical dry points of UM-UKCA, and will be used throughout this thesis.

Figure 2.3a shows the sensitivity of ensemble mean q_{LDP} to history length, which will depend on the impact of the wind field for each input dataset. For a longer history, more trajectories are transported to the troposphere, and more opportunities for tropopause sampling are made. Therefore, longer histories lead to drier calculations of water vapour entering the stratosphere. The amplitude (peak-to-peak) of the annual cycle (blue line), the maximum difference of the monthly calculations (grey lines), also reduces. Ensemble mean values stabilise within about 300 days. For histories longer than 300 days, the drying and damping effects are substantially less than the time-mean and amplitude of annual cycle. Trajectories will therefore be calculated for 360 days (1 modelyear), which also retains similarity to the ERA-I calculations.

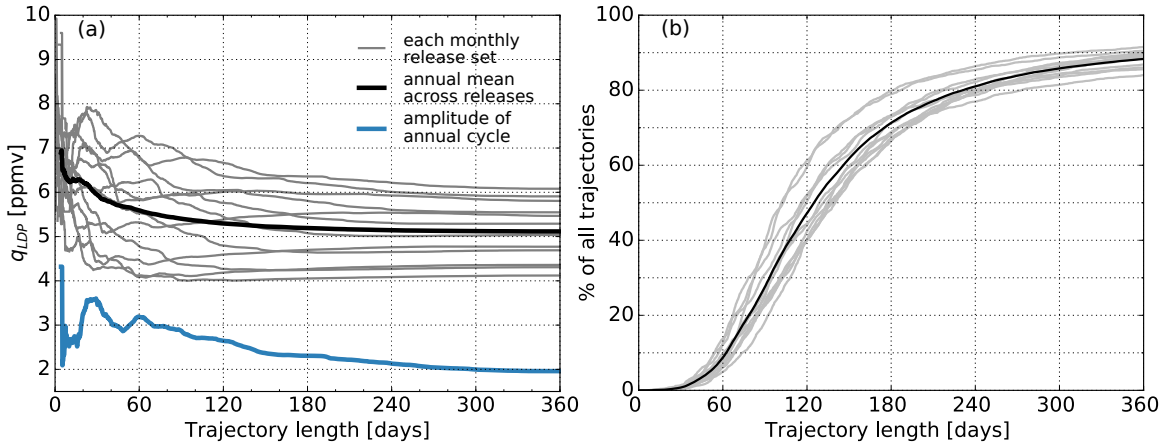

Fig. 2.3 Sensitivity of LDP calculations to history length of back-trajectories released at 400 K 30 °N–S across one year in UKCA 2000 experiment. (a) prediction of stratospheric water vapour, (b) efficiency of transport to troposphere.

Figure 2.3b also shows that, for trajectories calculated for 360 days, the fraction that reach the defined troposphere is 85–92 percent which is very close to the efficiency of troposphere-to-stratosphere transport in ERA-I calculations initialised at 400 K (94 %, figure 2, Liu et al., 2010).

UM10.4

Determining an optimal initialisation height requires more care in the UM10.4 calculations because stronger changes are expected between forcing scenarios. As chapter 6 will confirm, typical responses to higher CO_2 concentrations and sea surface temperatures is a stronger Brewer-Dobson circulation, and a tropical tropopause that is lifted and warmer.

The percentage of ensemble back-trajectories reaching the troposphere should be sufficiently high, which will deteriorate with height. Second, the level of initialisation should be high enough that the Lagrangian dry point locations are insensitive to it.

A variety of initialisation surfaces have been tested with releases across climate forcing experiments. Trajectories have been released in March and October of a particular year, to span seasonality in transport time (as suggested by Figure 2.3b and will be shown in figure 4.4). Transit times are longer in October, and dry points are generally lower, therefore efficiency is expected to be lower.

Table 2.4 shows the percentage of trajectories that reach the defined troposphere for certain configurations. As expected, efficiency decreases with higher release. Overall, the initialisation in October is less efficient and is more sensitive to release height. For

Table 2.4 Percentage of trajectories that reach the troposphere (as an indicator of transport efficiency) defined as θ =340 K and $SMR = 1000$ ppmv when released at indicated surface 30 °N–S for different months and different climate forcing experiments.

experiment		month 3			month 10		
		$CO_2\times1$	$CO_2\times2$ SST +2 K	$CO_2\times4$ SST +4 K	$CO_2\times1$	$CO_2\times2$ SST +2 K	$CO_2\times4$ SST +4 K
init height	unit						
17.35	km	77	83	85	71	80	86
18.05	km	74	80	85	64	75	83
18.76	km	65	73	84	55	68	79
19.48	km	56	67	78	47	63	74
100.0	hPa	83	85	87	78	82	86
90.0	hPa	78	84	86	74	80	84
80.0	hPa	75	80	86	67	74	82
75.0	hPa	72	76	84	62	71	79
70.0	hPa	68	74	81	58	69	76
60.0	hPa	55	64	74	49	60	70

the CONTROL experiment efficiency ranges between 47–83 %. Efficiency increases for stronger forcing scenarios, as expected from changes in the Brewer-Dobson circulation (and large-scale ascent in convection). This suggests that any initialisation surface used in the CONTROL case will be at least as efficient for the other scenarios here.

Figure 2.4 shows the normalised vertical distribution of Lagrangian dry point events for back-trajectories initialised at different heights in the strongest forcing scenario $CO_2\times4$,SST+4 K. The three lowest releases at 100 hPa, 90 hPa and 17.4 km show distributions slightly lower than the rest. This indicates that all higher releases, from 80 hPa and 18.1 km and above, experience the region of lower saturation mixing ratios to a similar extent.

The 75 hPa release level is therefore considered high enough to sample the low saturation limits of the tropical tropopause layer, without substantially reducing transport efficiency, and is therefore used for timeseries analysis in all Lagrangian calculations in UM10.4.

Additionally, a trajectory history length of 360 days remains appropriate in all three UM10.4 forcing scenarios, shown in Figure 2.5.

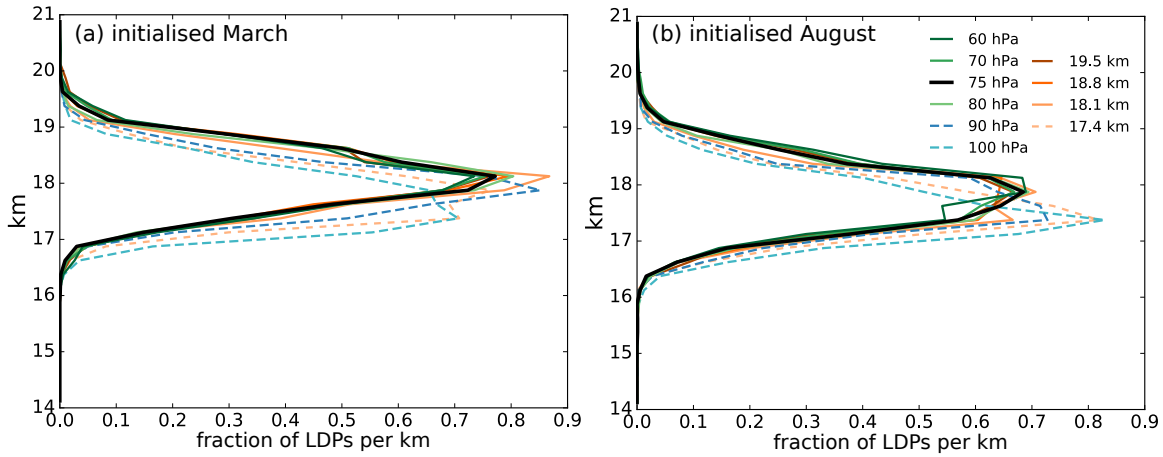

Fig. 2.4 Distribution of Lagrangian dry points for different release heights in $CO_2 \times 4$,SST+4 K case. For trajectories initialised in (a) March and (b) October.

2.5 Simple dehydration tracer advected by a global climate model

2.5.1 Method

For the particular purpose of assessing transport of water vapour entering the stratosphere, the simple water tracer, χ, undergoes advection in UM10.4 as for all other prognostic fields, including water vapour. To simulate instantaneous dehydration, the following conditions are applied at each model timestep:

$$\chi(t_{i+1}) = \begin{cases} \chi(t_i), & p < p_{lid} \text{ and } q_{sat}(t_{i+1}) > \chi(t_i) \\ q_{sat}(t_{i+1}), & p < p_{lid} \text{ and } q_{sat}(t_{i+1}) < \chi(t_i) \\ q_{sat}(t_{i+1}), & p > p_{lid} \end{cases} \tag{2.5}$$

where q_{sat} is the saturation mixing ratio, calculated using the Goff-Gratch formulation as in the rest of UM10.4, and p_{lid} represents the transition to a definitely wet troposphere. At altitudes below p_{lid}, the tracer is reset to saturation. This condition is not required to directly calculate Lagrangian dry points from back-trajectories because history older than the dry point is neglected. However, forward trajectory calculations do set an initial concentration from a starting level in the upper troposphere (for example, Dessler et al., 2016; Schoeberl and Dessler, 2011). Its purpose here is to provide a region of rehydration to tracers, without it there is only a dehydrating effect on this tracer. Its incorporation should make an equilibrium state possible. The implemented value is:

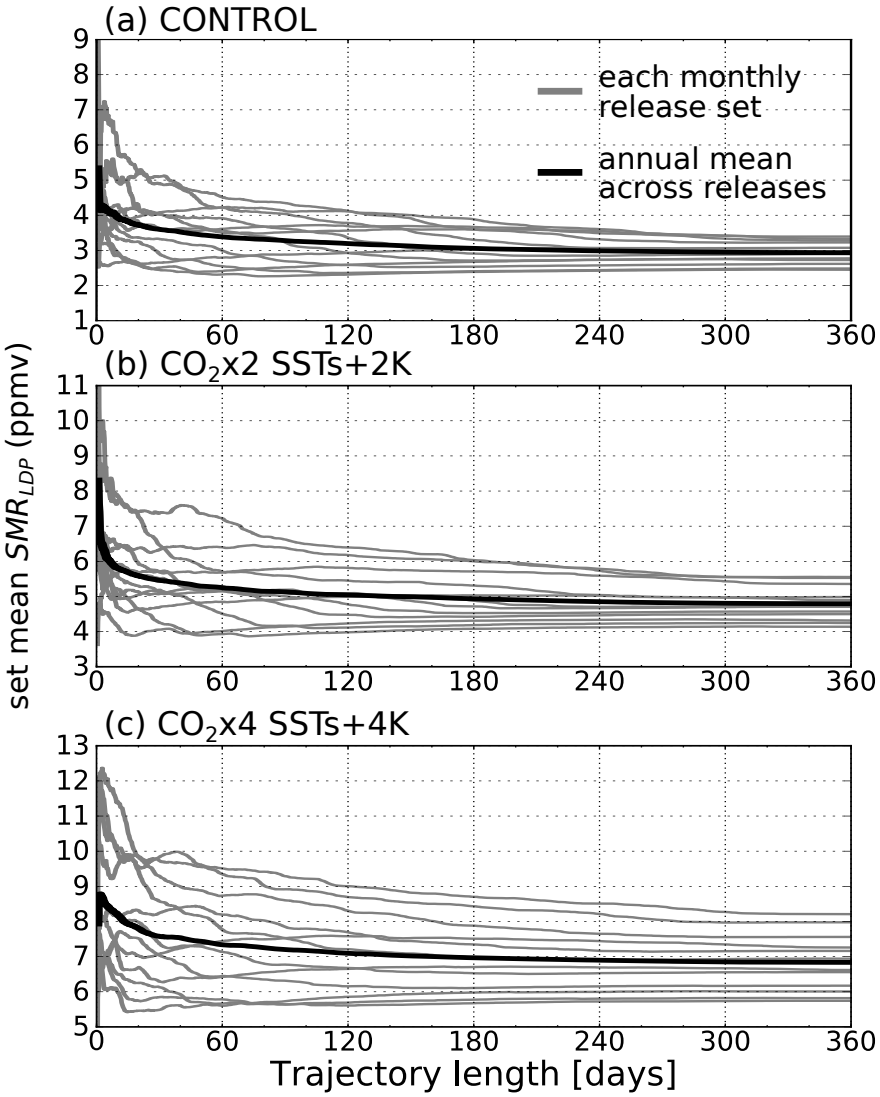

Fig. 2.5 Sensitivity of LDP prediction of stratospheric water vapour to history length of trajectories released across one year of monthly releases for each forcing scenario. (a) CONTROL, (b) $CO_2 \times 2$,SST+2 K, (c) $CO_2 \times 4$,SST+4 K. Showing monthly releases (grey lines) and their annual mean (black line).

$$p_{lid} = 300\,\text{hPa} \tag{2.6}$$

A second value of p_{lid}, 200 hPa will also be tested, and little difference is anticipated because final dehydration commonly occurs at altitudes well above 200 hPa.

This construct aims to resemble the instantaneous dehydration applied to offline Lagrangian trajectories as closely as possible. The relatively frequent timestepping of the climate model calculations — every 20 minutes in the UM10.4 whereas the Lagrangian

calculation data frequency is every 6 hours — may lead to overly strong dehydration. At the same time, the UM10.4 water vapour adjustment to saturation is relaxed according to physical conditions. Other forms of the tracer dehydration which modify the frequency of adjustment are tested in section 3.3.1.

2.5.2 Testing implementation of the new tracer

A first step with the construction of a tracer is to ensure that the calculations have no numerical artefacts. In initial experiments it was found that the advection scheme may be challenged by instantaneous dehydration which applies strong and inhomogeneous perturbations to the tracer field. It is therefore possible that the model advection scheme will be sensitive to the associated tracer gradients. This section performs some initial tests into how the model handles dehydration according to different gradient strengths.

For the tracer dehydration scheme in equation (2.5) the saturation limit is q_{sat}, defined physically as saturation mixing ratio (units of $\mathrm{kg\,kg^{-1}}$). To investigate the effect of field gradients, the artificial tracer, $\tilde{\chi}$, will now dehydrate according to a function of the saturation field. The dehydration scheme then looks like:

$$\tilde{\chi}_j(t_{i+1}) = \begin{cases} \tilde{\chi}_j(t_i), & p < p_{lid} \text{ and } f_j(q_{sat}(t_{i+1})) > \tilde{\chi}_j(t_i) \\ f_j(q_{sat}(t_{i+1})), & p < p_{lid} \text{ and } f_j(q_{sat}(t_{i+1})) < \tilde{\chi}_j(t_i) \\ f_j(q_{sat}(t_{i+1})), & p > p_{lid} \end{cases} \tag{2.7}$$

The previous case (labelled $j = 1$) is then :

$$f_1(q_{sat}) = q_{sat} \tag{2.8}$$

$$\tilde{\chi}_1 = \chi \tag{2.9}$$

And the four functions tested ($j = 2, 3, 4, 5$) provide a proportional easing of the gradients in the saturation field applied to dehydrate the tracer:

$$f_2(q_{sat}) = q_{sat}^{1/2} \quad (2.10)$$

$$f_3(q_{sat}) = q_{sat}^{1/4} \quad (2.11)$$

$$f_4(q_{sat}) = 10^3 + ln(q_{sat}) \quad (2.12)$$

$$f_5(q_{sat}) = 10^3 + log(q_{sat}) \quad (2.13)$$

These preserve gradient directions, but scale their magnitudes. The initialisation of each tracer field $\tilde{\chi}_j$ is similarly $f(10^{-8}\,\mathrm{kg\,kg^{-1}})$. The advection is then performed on $\tilde{\chi}$, and it is converted back to represent water vapour concentration as χ separately after. Any values in χ less than q_{sat} and less than the initialisation value of $10^{-8}\,\mathrm{kg\,kg^{-1}}$ are not physically expected unless introduced by the advection scheme. Values of exactly zero point to numerical artefacts.

Results

Figure 2.6 shows the count of zero mixing ratio gridpoints on each model level and each 6 hourly datapoint in the first month after initialisation. For model water vapour (a), the count is of its allowed numerical minimum, $10^{-8}\,\mathrm{kg\,kg^{-1}}$. Returned tracer fields are converted back to units of $\mathrm{kg\,kg^{-1}}$ for all except (g, h) which show the advected field $\tilde{\chi}_4$ and $\tilde{\chi}_5$. The model water vapour and some tracers return spuriously low zeros.

The model water vapour field encounters its minimum allowed value of $10^{-8}\,\mathrm{kg\,kg^{-1}}$ only within the troposphere, up to about 14 km. Without investigating further, it is not clear what causes these localised features in the water vapour field (likely it is an aspect of cloud and boundary layer turbulence processes which can be spatially irregular). Being tropospheric, they are not intended to be resolved by the dehydration tracer. It is noticeable that the minimum threshold events in modelled water vapour occur throughout the troposphere while the erroneous tracer field minima occur around the upper troposphere and lower stratosphere (10–20 km). This points to different causes in model water vapour and the dehydration tracer, affecting the tropopause differently. Furthermore, this is not a spin-up issue for the tracer as the spurious values persist 10 years after initialisation (not shown). It is therefore desirable to alter tracer calculations to prevent such erroneous values.

Additionally, f_2 and f_3 (equations 2.10 and 2.11) still allow a zero value to be experienced, whereas f_4 and f_5 (equations 2.12 and 2.13) do not by construction (unless q_{sat} drops below $10^{-1000}\,\mathrm{kg\,kg^{-1}}$).

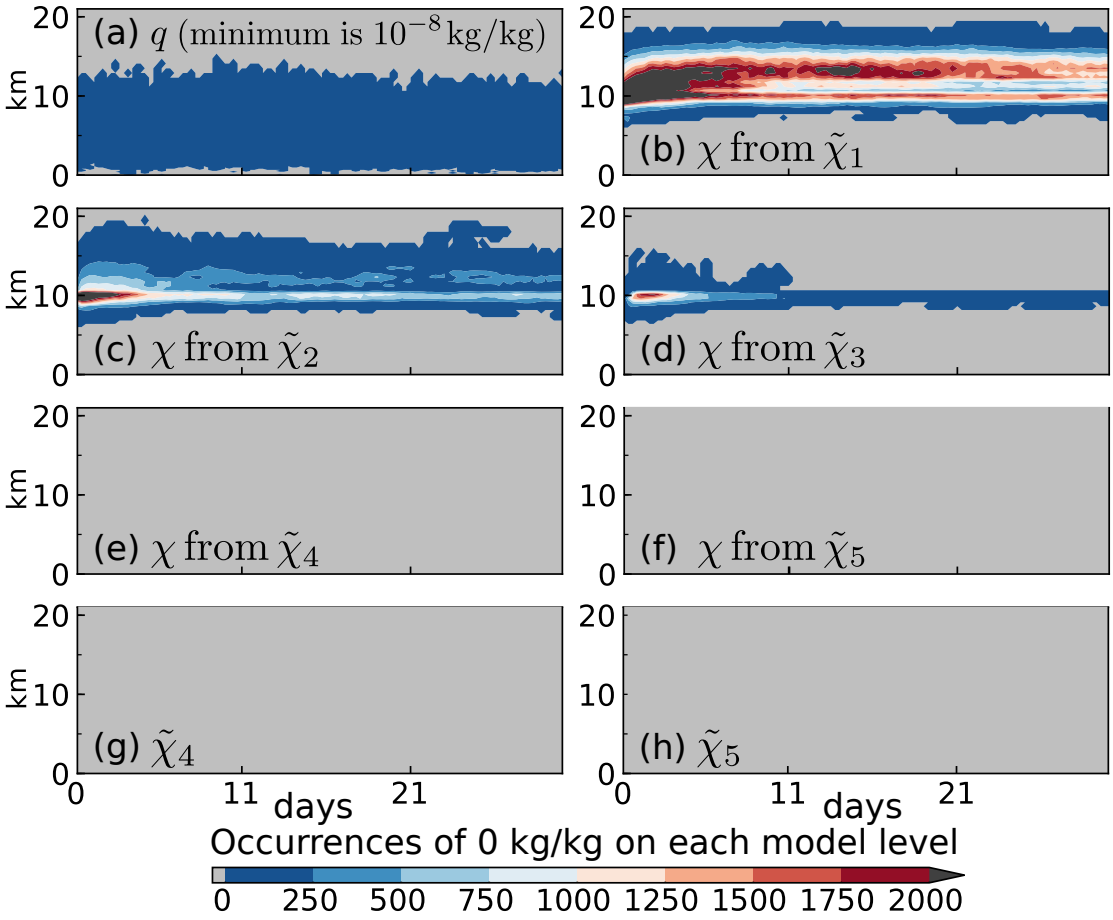

Fig. 2.6 Occurrences of minimum concentrations on model levels each 6 hours of first month after initialisation. Showing (a) water vapour (q, minimum is 10^{-8}), (b-f) formulations of tracer following equations (2.9)–(2.13) (minimum is 0), (g-h) the final two tracer formulations in the form advected by the model. No minimum values occur on model levels above 20 km.

The altitude of gridpoints showing most zero values in the tracer is close to the p_{lid} definition separating dehydration from tropospheric rehydration, raising it as the potential cause.

In figure 2.6 (e-h), the logarithmic tracers show no spurious zeros in the first month of simulation (or 10 years beyond initialisation). This is seen in both their physically scaled values (e,f) and advected values (g,h). This identifies the spurious zeros as a result of the strong gradients, which are removed in these cases.

Furthermore, choices of f with spurious zeros cause outstanding tracer concentrations in the lower stratosphere. Figure 2.7 shows the 10 °N–S zonal mean vertical profiles in month 18 (during spin-up) of mass mixing ratio for saturation mixing ratio, and tracers corresponding to f_1 and f_5 with two different values of p_{lid}. The differences between the

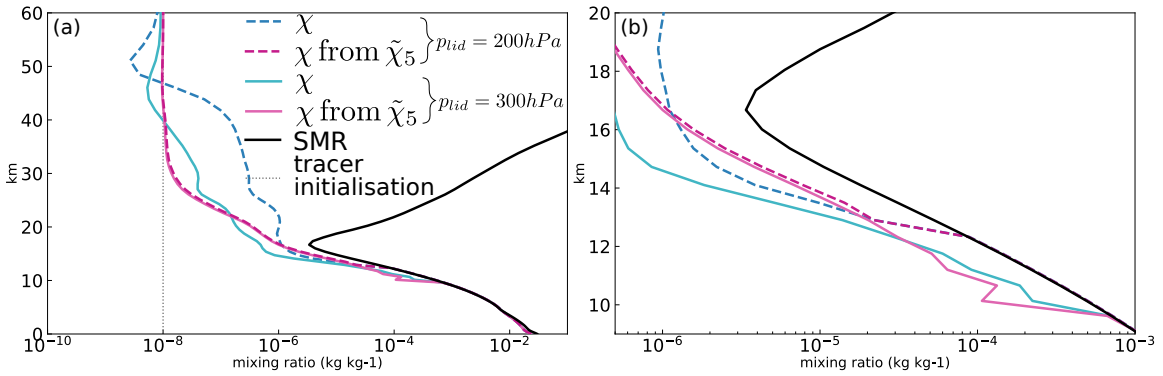

Fig. 2.7 (a,b) Vertical profiles of 10 °N–S zonal mean month 18 vertical profiles. Showing saturation mixing ratio (black) and tracers with two particular dehydration formulations equation (2.9) (blue) and equation (2.13) (pink) with different p_{lid} of 200 hPa (dashed) and 300 hPa (dotted). (b) is sub-region of (a). Note that the fields in this figure were calculated in a non-identical but comparable simulation.

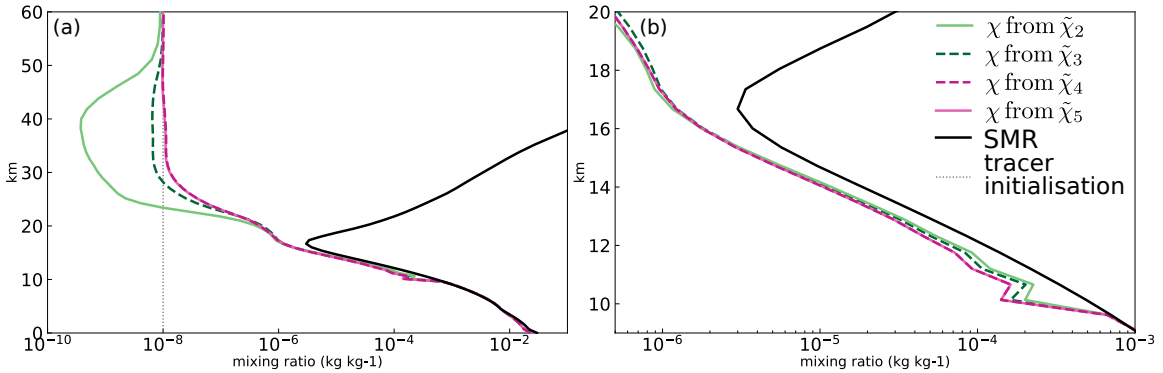

Fig. 2.8 As for figure 2.7 but showing all tracer dehydration formulations in equations (2.9)–(2.12) with p_{lid} =300 hPa.

dehydration tracers set with p_{lid} at 200 hPa and 300 hPa are expected to be small. However, implementing f_1 finds differences of several orders of magnitude vertically (blue lines) and exhibit different temporal variability (not shown). Meanwhile, the difference for the logarithmically smoothed dehydration cases (pink lines) shows only small differences near the two lid heights, and imperceptible differences above.

Further evidence for the non-physical behaviour of the non-logarithmic tracers can be seen at higher altitudes in the stratosphere. Figure 2.8 shows the tropical mean vertical profiles of cases f_2, f_3, f_4, f_5 with the same p_{lid} of 300 hPa, after 18 months. All of the non-logarithmic cases in both figures 2.7 and 2.8 (blue and green lines) show changes as high as 50 km which indicates anomalously fast signal propagation compared to the typical upwelling timescales. This indicates spurious numerical impacts.

Discussion

Spurious zeros were found when applying this instantaneous dehydration configuration to a tracer field subject to UM10.4 advection and conservation schemes. By applying various reduced-gradient forms of the same field, their incidence is removed. One suspect cause is the strong gradient reversal in the saturation limit near tropical tropopause (figure 2.7 and figure 2.8 black line), which may challenge the advection scheme. The gradual reduction of spurious zeros with eased gradients supports this as the cause. Another cause may come from the p_{lid}, which can introduce a step change in the tracer field when enforcing saturation values below and saturation minimum above.

The occurrence of spurious zeros when applying this simple limitation to a tracer field points to a loss of accuracy. Hence, this raises the question, why does this form of spuriously low values not occur for actual model water vapour, q, which is also subject to dehydration. Generally, the least physical aspect of the method above is the application of instantaneous dehydration to the saturation mixing ratio, as it will incorporate timescales for condensation. In particular, there is no p_{lid} in the microphysical scheme. Additionally, for model water vapour, the balancing effect of rehydrating processes are also accounted for as the conservation and monotonicity schemes check the resulting fields.

Loss of mass conservation in a semi-Lagrangian advection scheme is a typical problem arising from interpolating fields which are not smooth. This is the motivation for monotonicity and mass conservation schemes (for example, see Zerroukat, 2010, and references therein) which must balance computational cost and accuracy. The mass conservation calculation is undisturbed by instant dehydration of this tracer because it addresses mass changes across the advection scheme only. However, the distribution of mass adjustments and the monotonicity scheme are sensitive to inhomogeneity in the tracer field. It is clear that an irregular tracer field due to strong and inhomogeneous dehydration above p_{lid} may challenge the enforcement of monotonicity. However, the effect of conservation and monotonicity are only ever to move towards a more linear interpolation scheme, and therefore the only expected outcome is numerical diffusion. It is therefore unclear how spurious low values emerge.

Conclusion

A result of these initial tests for the tracer implementation in UM10.4 is that certain additional numerical steps are required to reliably advect a field subject to instantaneous dehydration with a semi-Lagrangian transport scheme and associated mass conservation. Two suspected causes challenging this are the step change across the p_{lid} definition for rehydration, and the

strong vertical gradiation changes in saturation mixing ratio in the tropical tropopause layer. An alternative formulation might apply a relaxed tendency towards saturation conditions in both the troposphere and stratosphere. For example, the UM10.4's deposition-sublimation balance equation throughout the troposphere and stratosphere would achieve this with similar timescales. A more stable outcome for this simple dehydration tracer was obtained by setting dehydration to be sensitive to the logarithm of the saturation mixing ratio with a large positive offset.

Unlike a Lagrangian calculation, this complication appears to have arisen from the additional steps in timestepping of a grid of values which must apply conservation to the results. Nevertheless, by resolving the discrepancy in climate model advection, a reliable estimate of a tracer concentration subject to instantaneous dehydration is available to compare with model water vapour and offline Lagrangian dry point calculations.

Chapter 3

Advection-condensation method in climate models

3.1 Introduction

Global climate model estimates of H_2O_{strat} can show systematic differences from observations. This indicates the relevant processes of transport and dehydration may be misrepresented. Consider figure 3.1 which shows the average annual cycle of water vapour above the tropical tropopause in the merged satellite observation dataset, SWOOSH (Davis et al., 2016), and in two global climate model configurations, UM-UKCA and UM10.4. While an annual cycle is prominent in all three cases, both models exhibit a high bias in H_2O_{strat} concentration. Depending on the timing and position in the annual cycle, UM-UKCA is wetter by 3.5–4.25 ppmv, roughly twice as wet as SWOOSH observations. At its seasonal minimum and maximum, UM10.4 is wetter by 0.5 ppmv and 1.75 ppmv.

The timing and latitudinal positions of the minima also differ. The models are generally earlier (April-May and February-March) compared to SWOOSH (May). So are their maxima (models are October and September compared to SWOOSH November). If a latitudinal mean is applied, the timing in SWOOSH and in model minima are unchanged, but the model maxima are closer to observations. Observations also show peaks closer to the equator (0–10 °N) whereas models are focused in the northern tropics (10–20 °N).

Their structure in the southern tropics also differ. Above the tropical tropopause, SWOOSH observations show humidity increases with latitude. Whereas UM-UKCA shows a secondary seasonal minimum at 10–30 °S, and the UM10.4 shows a relatively uniform field.

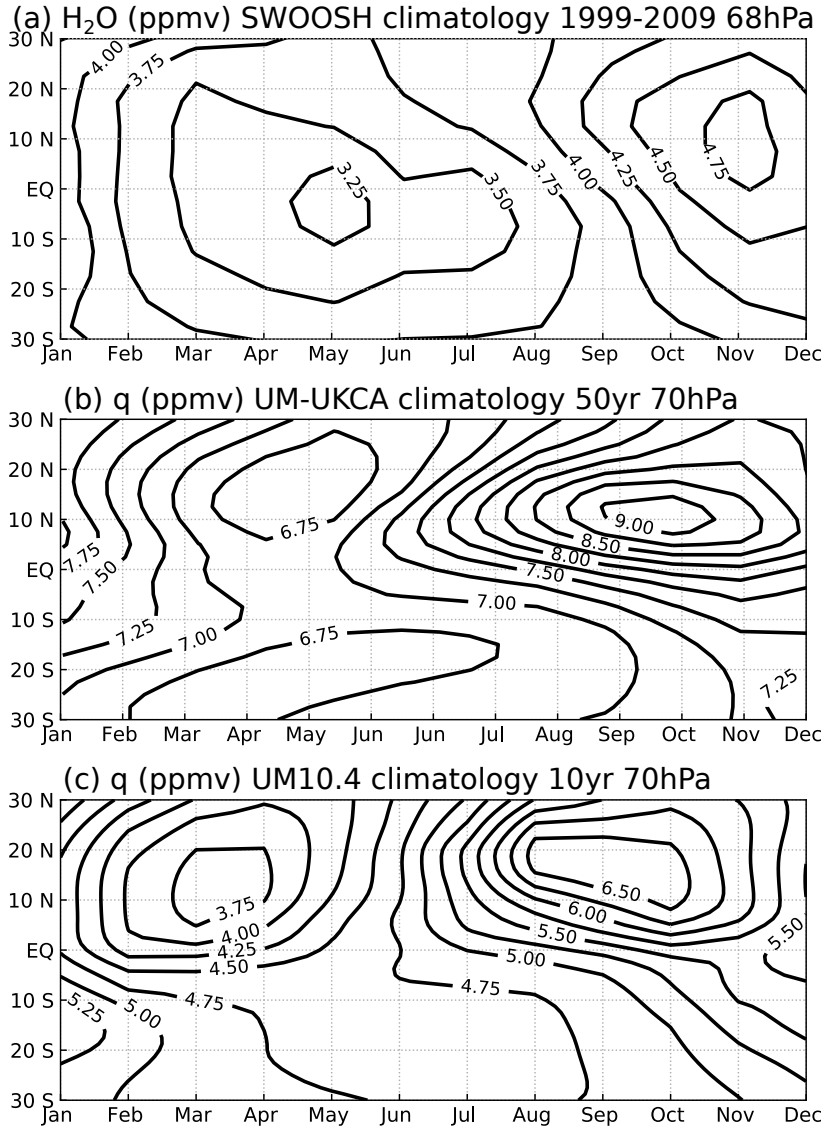

Fig. 3.1 Average annual cycles of water vapour (in units of parts per million per unit volume, ppmv) about the tropical tropopause layer.

As introduced in chapter 1, the cause of the water vapour annual cycle is a corresponding annual cycle in tropical tropopause temperatures. Its phase is also sensitive to seasonality in the height of the vertical dry point and the upwelling rate. The latitudinal distribution will be associated with the meridional shifts to tropopause cold pool with season (more equatorial near February, and in the northern tropics near August, shown later in this chapter).

Earlier studies have recognised a warm bias in the tropical tropopause layer of global climate models (Kim et al., 2013), causing the wetter stratosphere of UM-UKCA and UM10.4 (Hardiman et al., 2015). Differences from model transport have not been clarified.

Earlier studies have found the advection-condensation method represents the observed variability of H_2O_{strat}, on both annual and interannual timescales (Fueglistaler and Haynes, 2005; Fueglistaler et al., 2013; Liu, 2009), when using reanalysis temperature and wind fields. It has been applied infrequently to global climate models (for example, Dessler et al., 2016; Kremser et al., 2009). In order to examine climate model representation of water processes in the tropical tropopause, this thesis will apply Lagrangian dry point calculations.

First, it is necessary to establish the representativeness of the Lagrangian dry point method in the climate models. Specifically, in this chapter UM10.4 and UM-UKCA will be tested for whether the annual cycle features of their own calculation of water vapour is captured by the advection-condensation method. This is done in section 3.2. Differences arising from the transport schemes will be investigated in section 3.3. This will be achieved by applying the instantaneous-dehydration approximation to a tracer advected by the climate model (UM10.4 in this case), and comparing with Lagrangian dry point calculations and model water vapour. Section 3.4 will assess the impact of sub-seasonal temperature fluctuations on Lagrangian estimates of H_2O_{strat} in reanalysis and the UM-UKCA.

The suite of experiments in this chapter will provide a thorough indication of the representation of climate model water vapour by the simple advection-condensation method. Section 3.4 will discuss and summarise the results of this chapter. This will allow the deeper investigation of the advection-condensation method in chapter 4 before turning to complete the climate model water budget in Lagrangian calculations in chapter 5 and to assess trends in chapter 6.

3.2 Climatology studies

Many aspects of stratospheric water vapour are still not well captured in some climate models. Earlier work has shown the annual and interannual variability of H_2O_{strat} to be well represented by the advection-condensation method applied to reanalysis temperatures and winds. This provides a method to evaluate model processes that contribute to these differences, which has been utilised only occasionally (Dessler et al., 2016; Kremser et al., 2009). This section introduces current understanding of the advection-condensation methods from climatology studies with ERA-Interim before comparing it with the global and chemistry climate models, UM10.4 and UM-UKCA.

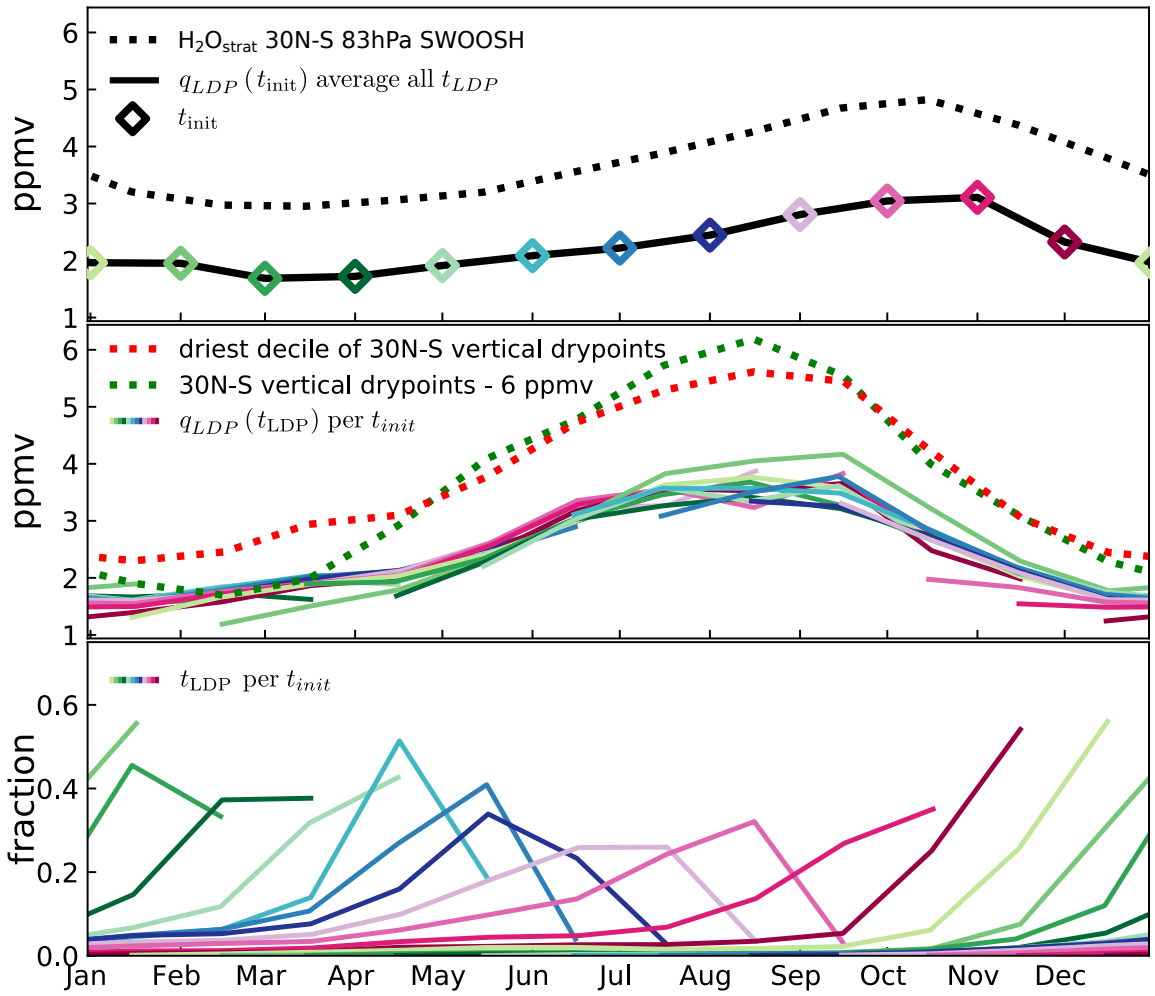

Fig. 3.2 Average annual cycle of SWOOSH observed tropical lower stratospheric water vapour, ERA-I vertical minimum of saturation mixing ratios (vertical dry points), and ERA-I diabatic Lagrangian dry point calculations. Data spans 1999-2009 and trajectories are initialised (t_{init}) monthly at 83 hPa. Results separated into mixing ratios at 83 hPa (top panel), final dehydration estimates (middle) and fraction contribution of Lagrangian dry point events each month (t_{LDP}) for each release date (t_{init}). Resembling figure 6 of Fueglistaler et al. (2013) but showing predicted concentrations — not temperatures — from trajectories released within 30 °N–S monthly, as well as observations and additional Eulerian estimates of water vapour. See text for description.

3.2.1 ERA-I reanalysis

Figure 3.2 indicates how features in temperature and transport affect H_2O_{strat} predictions. The top panel shows water vapour at 83 hPa in SWOOSH observations (black dotted line) and Lagrangian prediction for trajectories initialised at that level (solid black line with coloured diamonds). For each date marked by a diamond, a set of trajectories is released and the

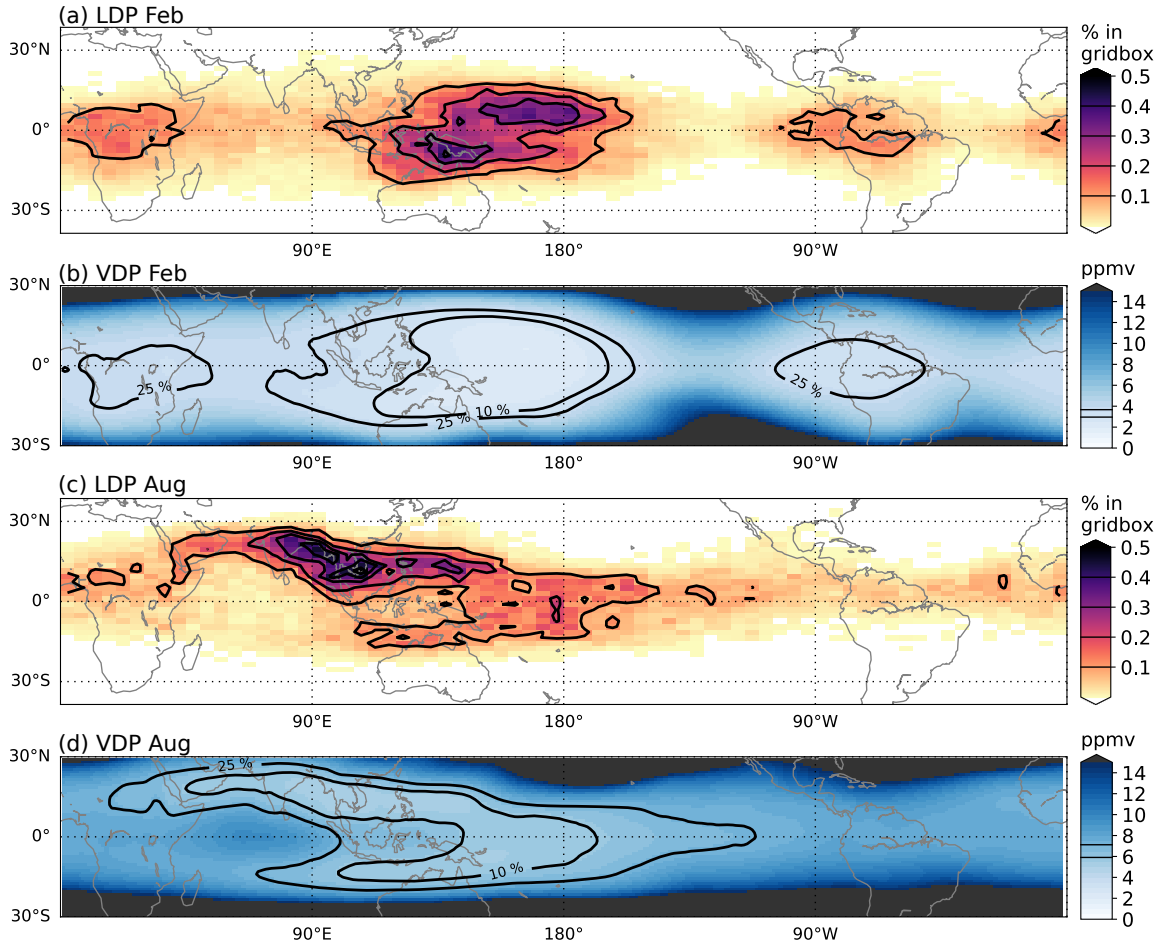

Fig. 3.3 Spatial distribution of ERA-I (a,c) Lagrangian dry points for diabatic trajectories released in February and August at 83 hPa over 1999-2009, and (b,d) Eulerian vertical dry points averaged over the same months over 1999-2009.

Lagrangian prediction is derived from the mean of all Lagrangian dry point events in that set (the Lagrangian dry point calculation was detailed in section 2.4). The roughly constant dry bias of the simple advection-condensation method, $\sim$1.5 ppmv, is apparent in the top panel.

The middle panel shows the saturation mixing ratios of Lagrangian dry point events occurring each month for each release set (coloured solid lines). Eulerian estimates of the locations of lowest saturation limits are also shown (coloured dotted lines): at each horizontal gridpoint, the vertical minimum in saturation mixing ratio defines the vertical dry point. This is practically similar to the more commonly analysed vertical cold points, but more accurate to the process of dehydration. The 30 °N–S zonal mean monthly mean of vertical dry points is shown with an offset of -6 ppmv to fit the scale of other results (green dotted line). Also, to obtain some selection of the horizontal minimum in saturation limits (cold pool) regions,

the driest decile of the horizontal distribution of these vertical dry points has been calculated (red dotted line; similar to Garfinkel et al., 2013; Oman et al., 2008). The choice of driest decile serves as a rough indicator, but an exact form needs to be assessed more accurately.

The lowest panel shows the fraction of each trajectory set's Lagrangian dry points that occur in a given month. For example, for trajectories released in August (dark blue line), no Lagrangian dry point events occurred in the first month of release. The second month saw about 25 % and the third month about 35 %. The next months in the 12 month history saw gradually less. The product of the fraction distribution (bottom panel) with LDP-per-month timeseries (middle panel) leads to the prediction-per-release-date in the top panel.

In the 83 hPa timeseries, a clear annual cycle is seen with a minimum in March of around 1.7 ppmv and a peak in November of 3.1 ppmv. The Lagrangian result shows the same phase and a similar amplitude, complementing the results in Fueglistaler et al. (2013). There is a distinct dry bias of $\sim$1.5 ppmv. Earlier studies describe this as a result of the instantaneous dehydration approximation being overly efficient (Liu et al., 2010).

At the level of final dehydration, Lagrangian dry points find a very similar phase to the Eulerian vertical dry points. The power of spatial sampling with a transport method is also made clear. The 30 °N–S zonal mean monthly mean of vertical dry points timeseries (green dotted line) has a similar phase, but is much wetter (with an offset of 6 ppmv) and has a larger amplitude. Selecting the cold pool regions statistically as the driest decile of the horizontal distribution of vertical dry points, finds a climatology of similar phase and magnitude as the Lagrangian calculations.

The phase of the Lagrangian dry points (middle panel) is also earlier than their water vapour prediction at 83 hPa. Resulting from the transit time for trajectories between these levels, transport applies a temporal weighting to the sampling of tropopause temperatures. Each month along each history is weighted differently, seen in the lower panel. In summer, the month with most Lagrangian dry point events is the second or third month after release (for example, trajectory set released in August - dark blue line - peaks in May), whereas in winter it is the first month. This points to shorter transit times from LDP locations to trajectory release height in winter (as in figure 4.4), which is consistent with stronger upwelling of the Brewer-Dobson circulation and higher altitude of cold point temperatures for this time of year (seen in GPS observations in Kim and Son, 2012; Randel et al., 2003).

Another reason for the broader transit time distribution in summer months is the seasonality of tropopause temperatures. A warm period is less likely to provide an extreme dehydration event, therefore trajectory histories are more likely to experience their lowest saturation mixing ratios away from June to September.

This also indicates why the annual cycle inferred from Lagrangian dry points at 83 hPa is distorted relative to the dry point seasonal cycle (black solid line in figure 3.2), with a longer moistening time (April-November) and faster drying time (November-March). The slow increase in spring and summer is due to broader transit time distributions which stretch out this part of the annual cycle signal. Conversely, the narrower distributions in winter give a more immediate signal and so a rapid decrease.

In figure 3.3 the horizontal distribution of dry point events also exhibits a pronounced seasonal cycle. Panels (a,c) show February mean and August mean Lagrangian dry point distributions. Panels (b,d) show vertical dry points and contours of lowest decile and lowest quartile of spatial distribution for comparison. As a result of changes in temperature and wind patterns, winter dehydration typically occurs over the equatorial west Pacific. Other dehydration events occur at the equator over South America and Africa in spring (not shown) and winter. In August when the tropopause is warmest, dry points are concentrated over south east Asia with a small contribution dispersed along the equator. These Lagrangian patterns are consistent with earlier studies (for example, Schoeberl and Dessler 2011 and references therein, and Bonazzola and Haynes 2004).

The horizontal minimum (driest decile) of vertical dry points broadly identifies the same regions as Lagrangian calculations of dehydration. The distribution of vertical dry points also agree generally with observed seasonality of the vertical cold point distribution shown in ECMWF analysis by Bonazzola and Haynes (2004) (figure 5) and GPS observations by Kim and Son (2012) (figure 3).

Figure 3.4a and figure 3.5a show seasonal mean (summer and winter respectively) observations of outgoing long-wave radiation (OLR) in the tropics from the HIRS satellite dataset, introduced in section 2.1.2. The lowest radiances in OLR identify deep convection, which radiatively cools the atmospheric layers above. The seasonality in OLR distribution indicates co-ordinated shifts of deep convection and lowest saturation mixing ratios in the tropical tropopause layer.

3.2.2 Chemistry climate model

This section compares Lagrangian dry point calculations in the chemistry climate model UM-UKCA with reanalysis results in the previous section. The model configuration was described in section 2.3.1.

The UM-UKCA model trajectories are released monthly every $2° \times 2°$ between 30 °N–S on the 400 K potential temperature surface for 49 years, with further details in section 2.4.2.

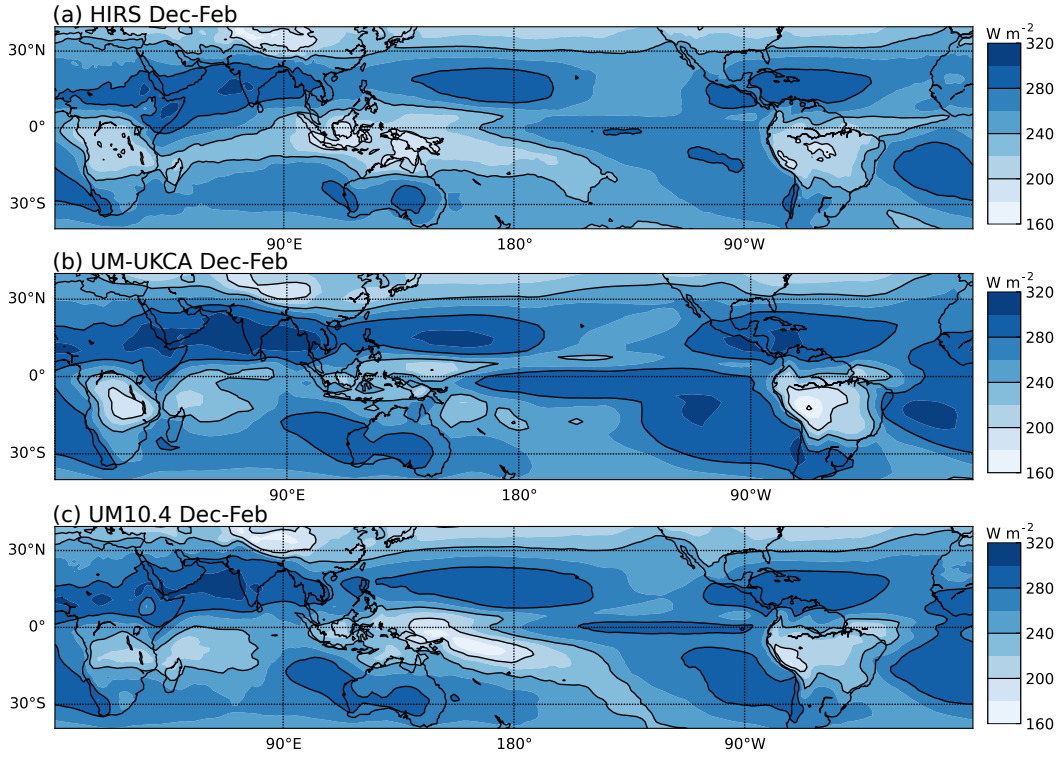

Fig. 3.4 December-February mean outgoing long-wave radiation (OLR) in (a) HIRS, (b) UM-UKCA, (c) UM10.4 averaged across 1999-2009, 50 and 11 years respectively.

The features of Lagrangian dry points over the annual cycle for comparison with ERA-I reanalysis are shown in figure 3.6. Water vapour is shown at 80 hPa because it is the first model level above 400 K and therefore reports the stratospheric signal of water vapour more clearly than the level below. While the annual variations are similar, a number of key features differ. The Lagrangian estimate of specific humidity is wetter throughout the year by about 3 ppmv, with annual cycle minimum and maximum of about 4.5 ppmv and 6.4 ppmv. The minimum is also later by about a month. The fractional contributions per month are also smaller, reaching no higher than 0.35, and peak later in the second to fourth month after release. The wetter signal results from the UM-UKCA being warmer (inferred from the higher saturation limit of vertical dry point measures). This may be expected to increase the annual cycle amplitude through the non-linearity of the Clausius-Clapeyron relation, but the annual cycle is also weaker because of the broader sampling timescale.

The trajectory transit time is longer in UM-UKCA than in ERA-I reanalysis, despite the initialisation height (of 400 K) being closer to the level of dry points. This suggests that vertical advection is weaker in the chemistry climate model than in reanalysis. This agrees with the finding of the chemistry climate model intercomparison of Gettelman et al.

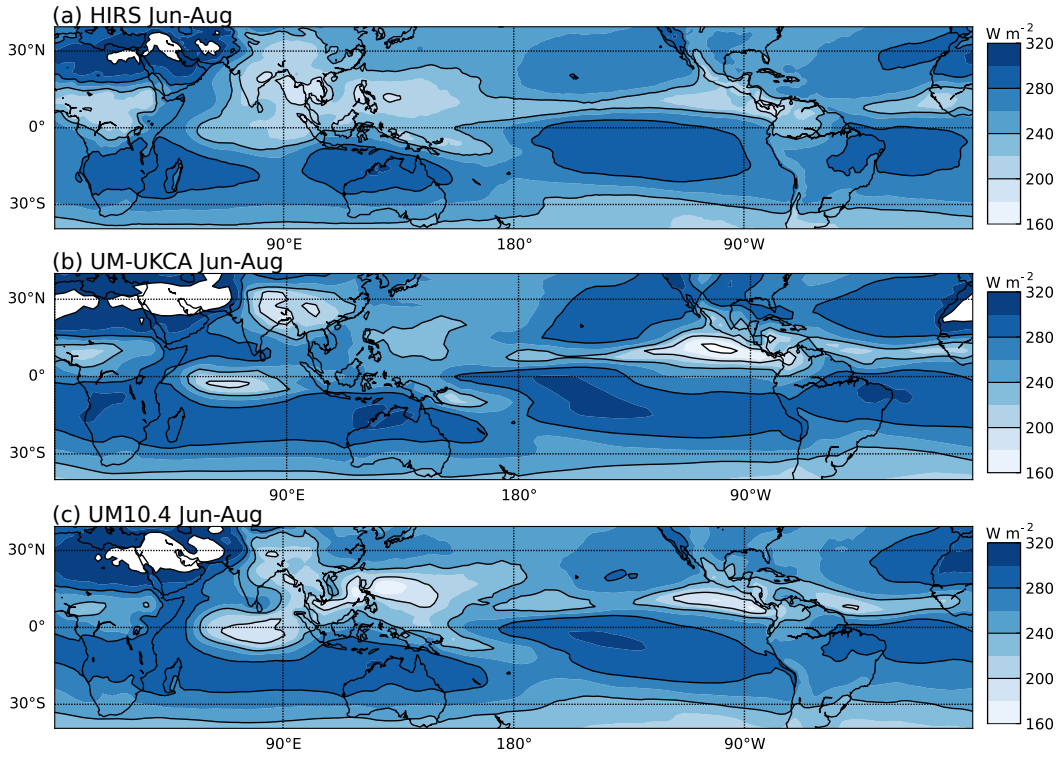

Fig. 3.5 June-August mean outgoing long-wave radiation (OLR) in (a) HIRS, (b) UM-UKCA, (c) UM10.4 averaged across 1999-2009, 50 and 11 years respectively.

(2010) who had found tropical lower stratospheric water vapour annual cycle to be delayed compared to observations.

The first month of nearly all trajectory releases contribute wetter Lagrangian dry points (the tails of coloured lines are wetter than their middles). This is a sign they are not occurring in the coldest regions of the tropical tropopause in that first month of history, probably due to their early advection to the troposphere. This would occur if there is substantial vertical advection in the wind fields. Physically this might occur in deep convective events. Alternatively it may be an introduction of noise in vertical winds represented kinematically rather than diabatically. If it is the former it highlights that diabatic tendencies must ensure that convective tendencies are included.

The difference between kinematic and diabatic Lagrangian calculations have been studied for some reanalyses including ERA-I (where the difference is smaller than earlier versions) (Liu, 2009). One contributing factor is that hydrostatic models, like ERA-I, obtain vertical wind estimates by assuming hydrostatic balance of horizontal wind fields which introduces additional noise. This chemistry climate model is non-hydrostatic so this effect is not expected to be strong. However, a diabatic view of the atmosphere also removes adiabatic

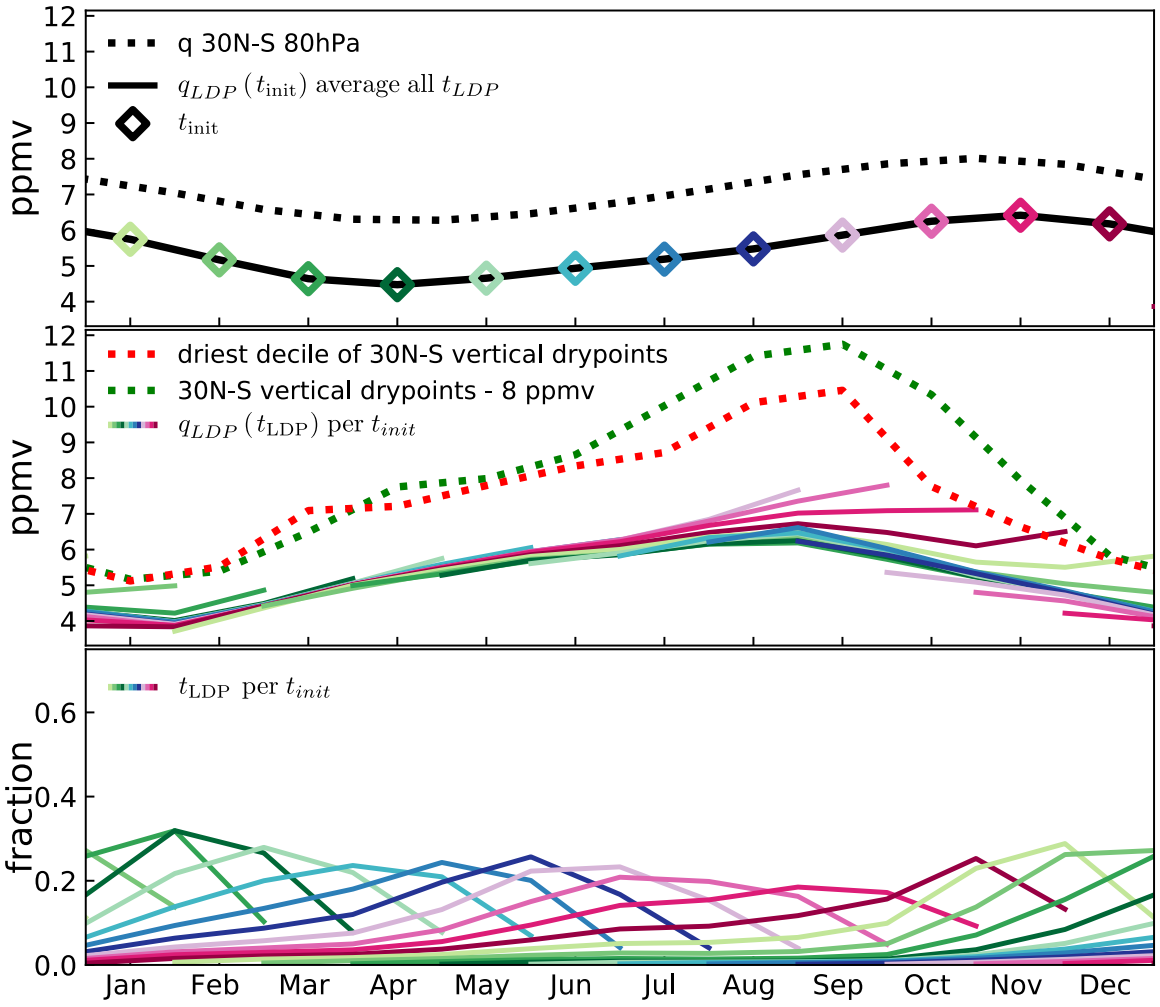

Fig. 3.6 As for figure 3.2 but for UM-UKCA water vapour and kinematic trajectories for 49 years. Note the higher concentration scale on the vertical axis than in figure 3.2.

motions. These are a strong feature of the tropopause, particularly in the sub-tropics. A kinematic view will retain this additional vertical motion which still increases errors and numerical diffusion. Therefore, the poorer resolution of temperature vertical structure by the kinematic results may add to the quick advection of some trajectories to the troposphere. In any case, this first month of trajectory history makes a relatively small contribution (bottom panel of figure 3.6) to the monthly means entering the stratosphere (top panel).

The spatial distribution of Lagrangian dehydration events is also different in the UM-UKCA, see figure 3.7. The spatial patterns are generally more confined than for reanalysis. This is likely to occur due to the larger sample of years for the chemistry climate model (50 instead of 11), as well as the lack of forced interannual variability in the repeat-year boundary conditions.

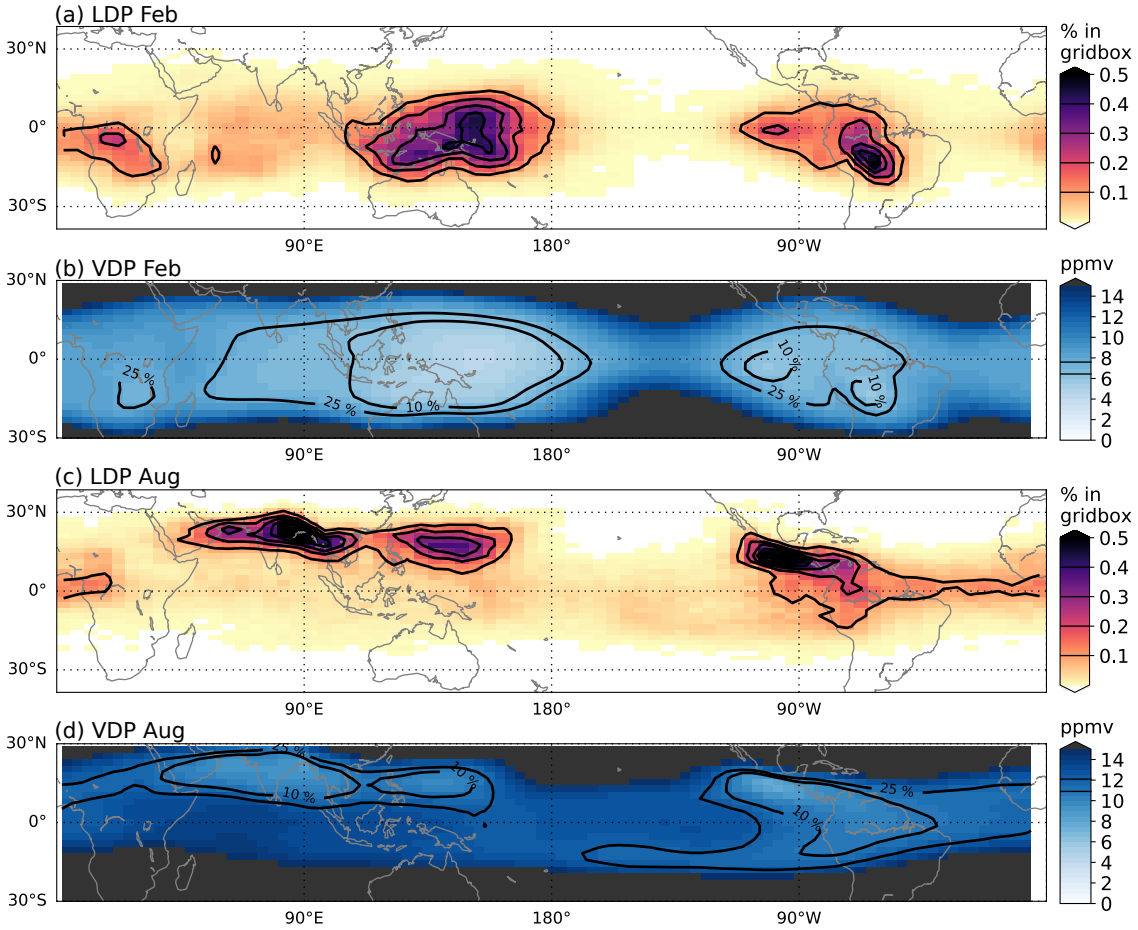

Fig. 3.7 As for figure 3.3, but for UM-UKCA with kinematic trajectories released at 400 K, and averages are over 49 years. (a,c) Lagrangian dry points in February and August, (b,d) vertical dry point events of the same months.

The tropical west Pacific is found to be a strong contributor as in reanalysis, but now so too are the Americas and south Asia. In August, the south east Asian peak is focused very closely over the northern coast of the Bay of Bengal (about 21 °N, 90 °E) and there is a similar strong contribution from the tropical Americas. Tropical south America is also a strong contributor in winter now. This is a reflection of where deep convective events occur in the chemistry climate model, shown in figure 3.4b and figure 3.5b.

3.2.3 Global climate model

This section compares Lagrangian dry point calculations in the global climate model UM10.4 with reanalysis and UM-UKCA results in the previous sections. Its configuration was described in section 2.3.1.

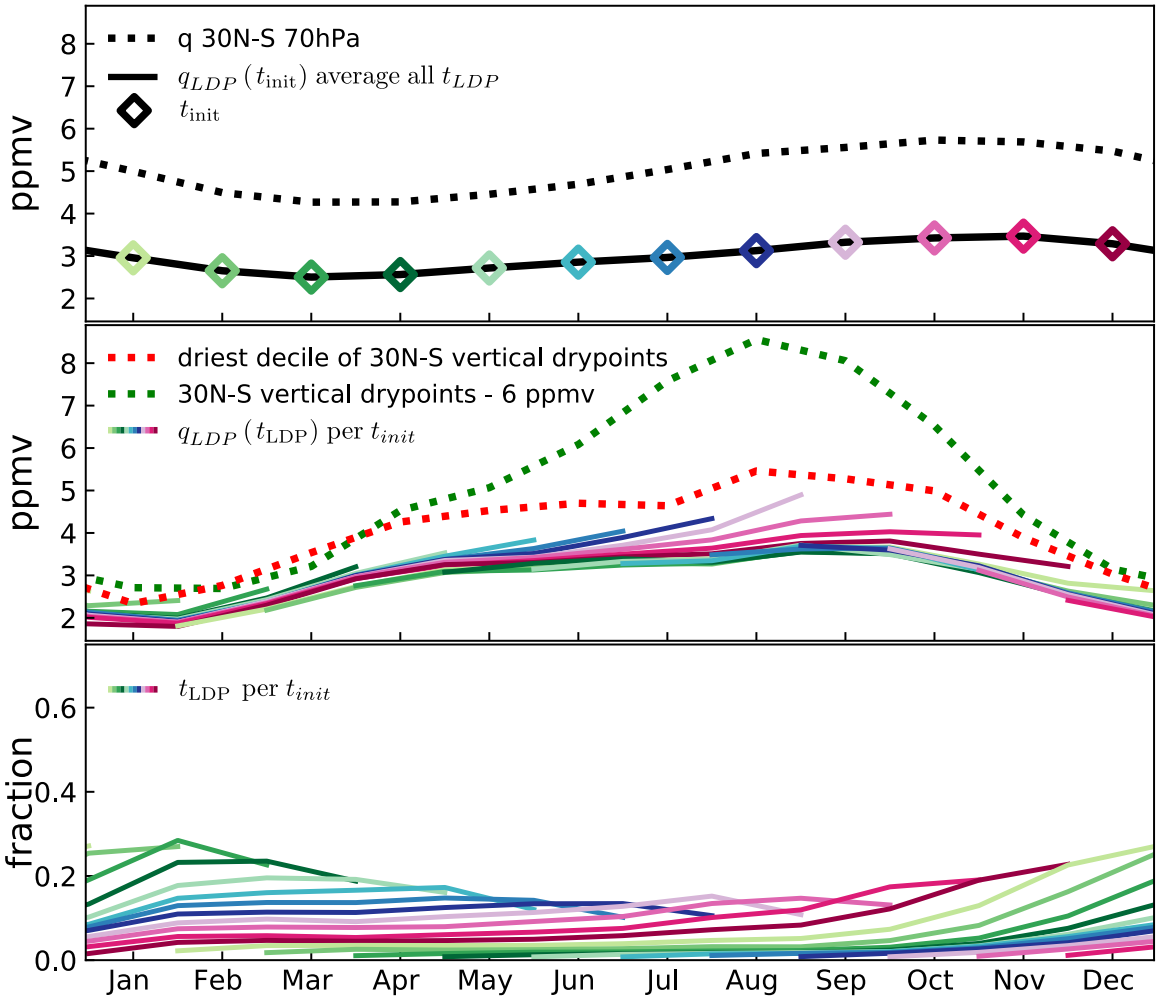

Fig. 3.8 As for figure 3.2 but for UM10.4 water vapour and kinematic trajectories released at 75 hPa for 10 years. Note the wetter mixing ratio scale.

The top panel of figure 3.8 shows the annual cycle of UM10.4 water vapour is more similar to observed magnitude and phase. The global climate model time mean (q) in the lower stratosphere is 5.0 ppmv (standard deviation of deseasonalised timeseries is 0.2), which is a smaller wet bias from SWOOSH (3.7 ppmv, 0.3) than UM-UKCA (7.0 ppmv, 0.2. The reported values are presented later in table 4.1). The middle panel shows the vertical dry point climatology is very similar to ERA-I reanalysis, suggesting a similar seasonality in tropical tropopause temperatures. Peak transit times are also in closer agreement (peaks within first to third month after release), however there is still a broad timescale contributing to each release set in the bottom panel, leading to a slight delay in q_{LDP} compared to q.

Figure 3.9 shows the spatial distributions for Lagrangian dry point events in February and August for UM10.4. The patterns are similar to the UM-UKCA result, but the key difference

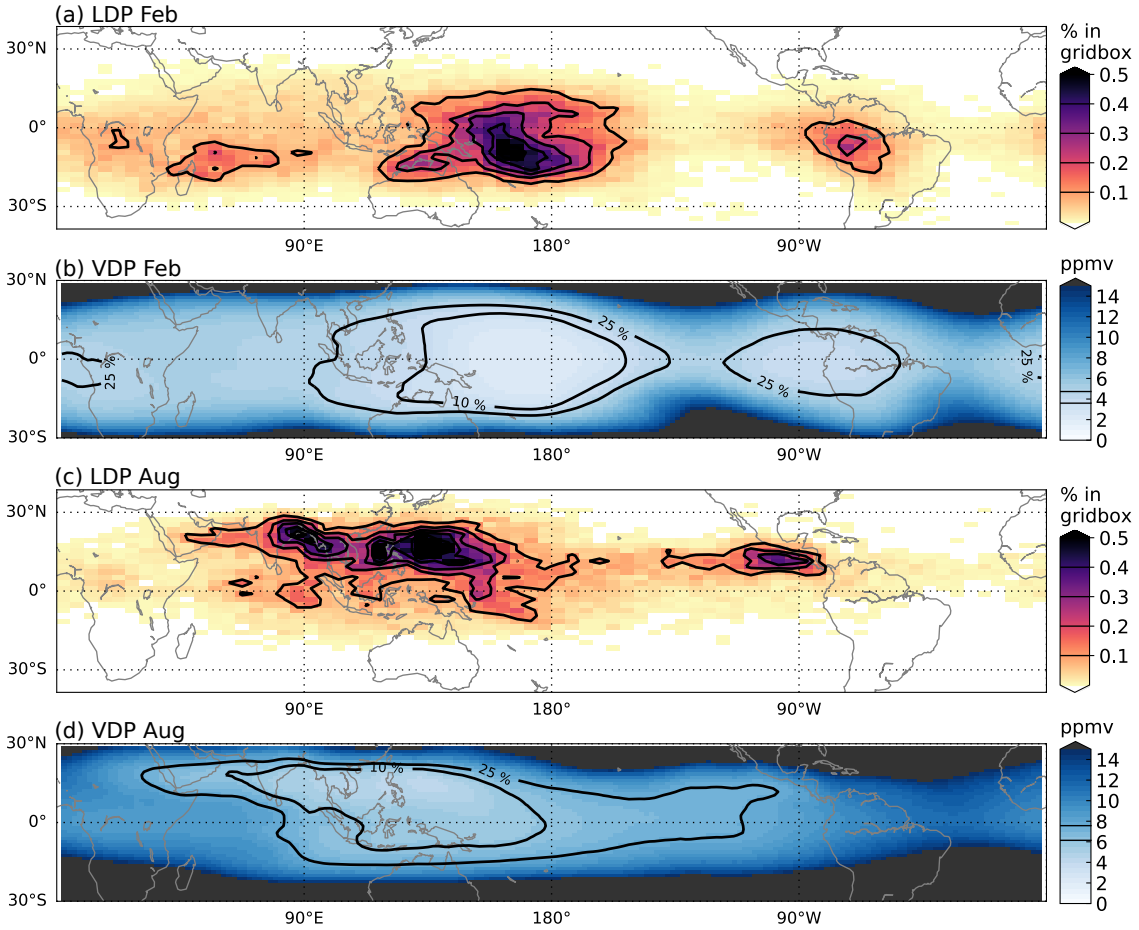

Fig. 3.9 As for figure 3.3, but for UM10.4 with kinematic trajectories released at 75 hPa, and averages are over 11 years. (a,c) Lagrangian dry points in February and August, (b,d) vertical dry point events of the same months.

is that the tropical west Pacific dominates contributions from elsewhere in the tropics. The August peak is also shifted eastward towards the tropical west Pacific.

The OLR maps in winter and summer in figure 3.4c and figure 3.5c indicate deep convection locations, which again agree with the shifts in Lagrangian dry point and vertical dry point locations. One exception is the apparent strong convection in the Indian Ocean which is not highlighted by locations of Lagrangian or vertical dry points.

As introduced in section 2.3.1, there are several reasons for the differences between the UM-UKCA and UM10.4 results. Firstly, chemistry is interactive in UM-UKCA whereas for UM10.4 it is prescribed. This allows additional interannual variability in the tropical tropopause layer through radiative-dynamical feedback processes such as from ozone (Fueglistaler et al., 2011; Ming et al., 2017). Secondly, while they employ the same schemes

for the most part, the UM10.4 has developed these toward the aim of reducing the H_2O_{strat} wet bias (Hardiman et al., 2015). The numerical schemes for interpolation and mass conservation are chosen to improve accuracy of the tropical tropopause's sharp and fluctuating gradients. The physical schemes relating to clouds and microphysics have also been modified to better represent the latest understanding of high cloud properties. Thirdly, the resolution is higher but its direct impact on predicted H_2O_{strat} is unclear (Walters et al. 2019 point out that even higher resolution models reverse the benefit from the developments of Hardiman et al. 2015). As a result of these last two points, convection impacts will be different.

This section has presented Lagrangian calculations of instantaneous dehydration in reanalysis, UM-UKCA and UM10.4. These two model configurations give an idea of the sensitivity in their H_2O_{strat} predictions. Temperatures continue to control q in different models, with a similar seasonality emerging. The horizontal distribution is somewhat dependent on model-specific processes. In particular are the structure of deep convective activity in the tropics, and the model advection scheme. The UM versions use a semi-Lagrangian advection scheme which behaves differently to the offline Lagrangian calculations. The next section will therefore develop a new tracer diagnostic that is calculated in UM10.4. This tracer will implement the instantaneous dehydration criterion in the model advection scheme. The influence of sub-seasonal temperature variations will then be investigated.

3.3 Simple dehydration tracer advected by a global climate model

The previous section found offline Lagrangian dry point calculations in ERA-I, UM-UKCA and UM10.4 to capture the average annual cycle in tropical lower stratospheric water vapour (observations for ERA-I, and climate model's own water vapour). Their individual differences are due to tropical tropopause temperatures. Additional differences may arise from model transport and convection.

The climate model cases advect with a semi-implicit semi-Lagrangian method, which is not the same as the offline trajectory Lagrangian method. Climate model advection provides some amount of small-scale mixing, as well as separate conservation and monotonicity calculations. Additional transport differences will relate to the timescale of wind evolution, and interpolation schemes. The Lagrangian method uses 6 hourly data and the semi-Lagrangian method experiences 20 minute data. For interpolation, Lagrangian calculations are cubic polynomial in the vertical and linear in horizontal while the UM is configured differently. The UM10.4 interpolates as cubic Hermite (spline) in the vertical and cubic polynomial in the horizontal (see Hardiman et al., 2015, for analysis of impact on tropical tropopause layer). Furthermore, the UM also corrects fields for mass conservation and monotonicity (short wavelength oscillations) across the advection scheme.

To investigate the impact of choice of transport scheme, I have designed a passive tracer that is subject to instantaneous dehydration. The aim is also to bridge the gap between the offline Lagrangian dry point calculations and the model's full representation of water vapour. The method was outlined in section 2.5. To increase the likeness of the Lagrangian dry point method and tracer dehydration, a test of the sampling rates will be made in section 3.3.1. Section 3.3.2 will then compare the tracer with modelled water vapour.

3.3.1 Sensitivity to dehydration sampling rate

As raised earlier, the timescale of winds and temperatures driving offline Lagrangian calculations is 6 hourly, whereas for advection in UM10.4 it is 20 minutes. To align the dehydration sampling rate of the UM10.4 tracer with the Lagrangian method, it is tested with various sampling rates between 20 minutes and 24 hours. This may also test the simple assumption of instantaneous dehydration becoming unrepresentative at short timescales due to the finite timescale of microphysical processes associated with actual phase change of water vapour in

the model. This experiment aims to determine the impact of dehydration sampling rate on the simple water vapour tracer at various sub-daily timescales.

Method

As determined in section 2.5, dehydration is set according to $f_5 = 10^3 + log_{10}(q_{sat})$ with initial field of $f_5(10^{-8}\,\mathrm{kg\,kg^{-1}})$.

Here, tracer sensitivity experiments are performed which differ only in the sampling rate of the dehydration conditions. The sampling rate is varied from every model timestep (once-in-20 minute) to every seventy second timestep (once-in-24 hours). In this way, the 6 hourly frequency of offline Lagrangian calculations lie within the range of model tracer results.

These tracers are initialised and run for 269 months ($\sim$22 years) each (except for the once-in-20 minute case which was calculated for 42 years). Typically, 10 years is sufficient for a UM10.4 simulation to propagate a passive tracer throughout the middle atmosphere, thereby reaching a steady state (see, for example, the setup of Hardiman et al., 2015). This section therefore compares both the tracer behaviour during spin-up and near steady state.

Results

Figure 3.10 shows the evolution of equatorial tracer concentration in units of $\mathrm{kg\,kg^{-1}}$. It is clear from figure 3.10c and d that at 17.4 km the concentrations roughly achieve steady state within only a couple of years for all sampling rates. A slight positive trend in the final simulated years in all tracers should be noted, suggesting they have not quite reached a steady state.

Above the tropical tropopause layer however, the tracers with lower sampling rates unexpectedly experience stronger vertical gradients and faster signal propagation into the stratosphere, and hence a shorter time to equilibration. At 20 km, the lowest sampling rates reach a steady state within 120 months, but the once-in-20 min and once-in-1 h cases only approach an approximate equilibrium after the full simulation time of 269 months. Figure 3.10a shows this difference propagates through the stratosphere. Because this behaviour is not reflected by the tracer evolution at 10 °N–S 17 km (figure 3.10c and d), it suggests an influence from outside of the equatorial tropopause layer.

Importantly, tracers reach steady state with different concentrations in the lower stratosphere as expected, shown in figure 3.10b. Once at steady state, stratospheric concentrations at 30 km are roughly equivalent to those at 20 km (figure 3.10a). Figure 3.11 shows the

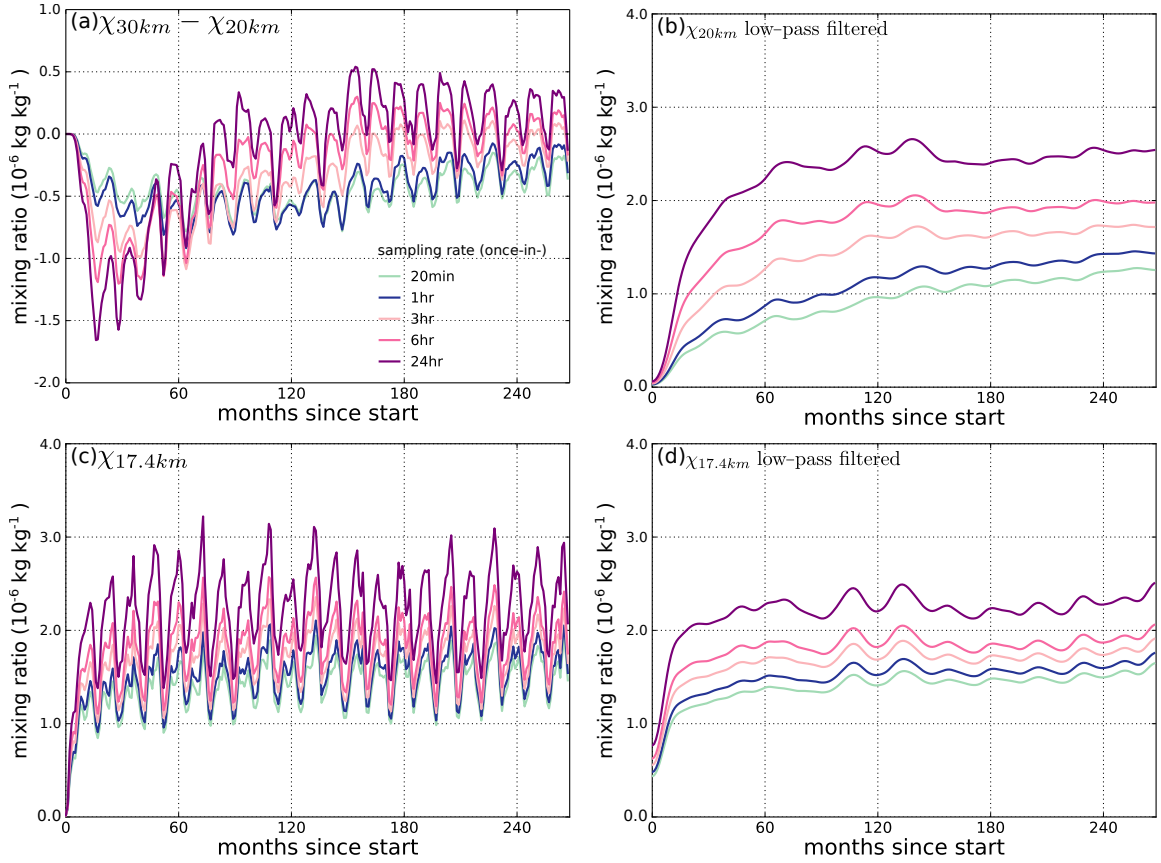

Fig. 3.10 Zonal 10 °N–S monthly mean evolution of tracer concentrations across the dehydration sampling rate sensitivity experiments. (a) Difference between 30 km and 20 km, (b) 20 km with 24 month low-pass cosine-squared filter applied, (c) 17.4 km without filtering, (d) 17.4 km with the same low-pass filter.

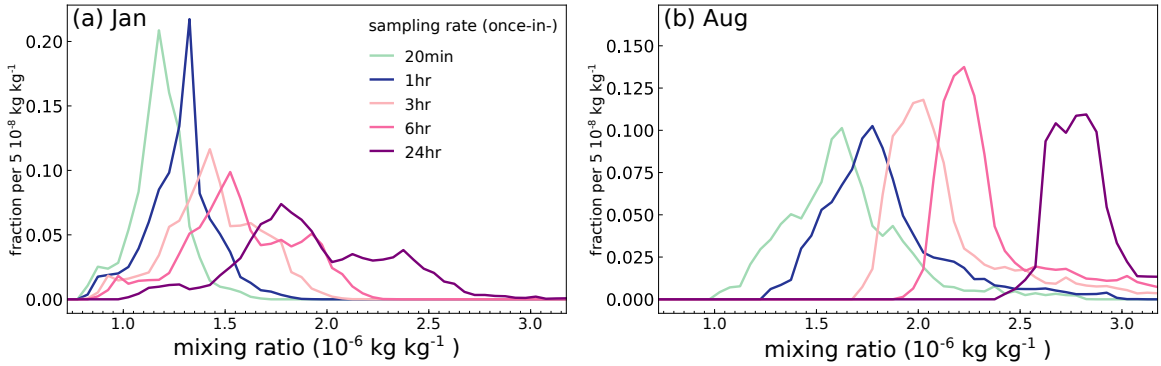

Fig. 3.11 Probability density function of tracer concentrations, for different dehydration sampling rates, monthly mean gridpoints between 30 °N–S and at 17.4 km after ∼13 years in (a) January and (b) August.

tropical tropopause (30 °N–S 17.4 km) tracer distributions are within 1.2–1.7 $\times 10^{-6}$ kg kg^{-1} in winter and 1.6–2.8 $\times 10^{-6}$ kg kg^{-1} in summer. The summer values follow closely the range of tracer mean values at 20 km. While there is some skew in the distributions (possibly as a result of including less influential regions beyond the tropics), mean values in the tropical tropopause layer will be similar.

Why the seasonal variations of tracer distributions with different dehydration sampling rates have different amplitude also appears to be clear. The variety of tracer distributions in summer and winter contrast in figure 3.11. In winter, they exhibit similar saturation minima but tracers with lower sampling rates show a broader distribution, whereas in summer their distributions shift entirely to higher concentrations. These suggest that in winter sensitivity experiments sample the same underlying distribution with different efficiency. In summer, they may sample different distributions. Part of this is an amplification of the Clausius-Clapeyron non-linearity; even if the relative temperature sampling efficiency is the same in summer, because it is warmer it will lead to larger changes in saturation mixing ratio. Whether the underlying temperature distributions are different remain to be seen.

The differences in timescales of vertical gradient evolution are harder to explain. Possible explanations might include advection from the sub-tropics, dehydration unexpectedly applying above 20 km, and an altered response from the advection and conservation schemes mixing vertically the wetter tropospheric air and the dry $\sim 10^{-8}$ kg kg^{-1} stratospheric air. These are considered in turn below.

At 17.4 km, steady state values at 30 °N–S zonal mean are higher than for 10 °N–S zonal mean, and similar to 10 °N–S zonal mean 20 km concentrations (comparing figure 3.11a and figure 3.10b). This is a sign that, in a zonal mean perspective, dehydration is strongest over the equator. Sub-tropical dehydration appears to impact the equatorial lower stratosphere, in agreement with the Lagrangian transport experiments with latitudinal mixing barriers of Poshyvailo et al. (2018). However, this will not explain the continuing gradients above 20 km.

One possible explanation of the sensitivity of dehydration tracer gradient between 20 km and 30 km to dehydration sampling rate is if the dehydration scheme is acting above 20 km. Some experiments with an age-of-air tracer sensitive to the instant-dehydration scheme indicates no dehydration is occurring at these levels for any of the sampling rate cases (not shown). This is therefore not an explanation of gradient differences in the stratosphere.

The discrepancy in horizontal dehydration distributions (in figure 3.11) provides some evidence that not all stratospheric air will have sampled the same low temperature of the tropical tropopause in the summer months. Some studies have identified such a seasonal

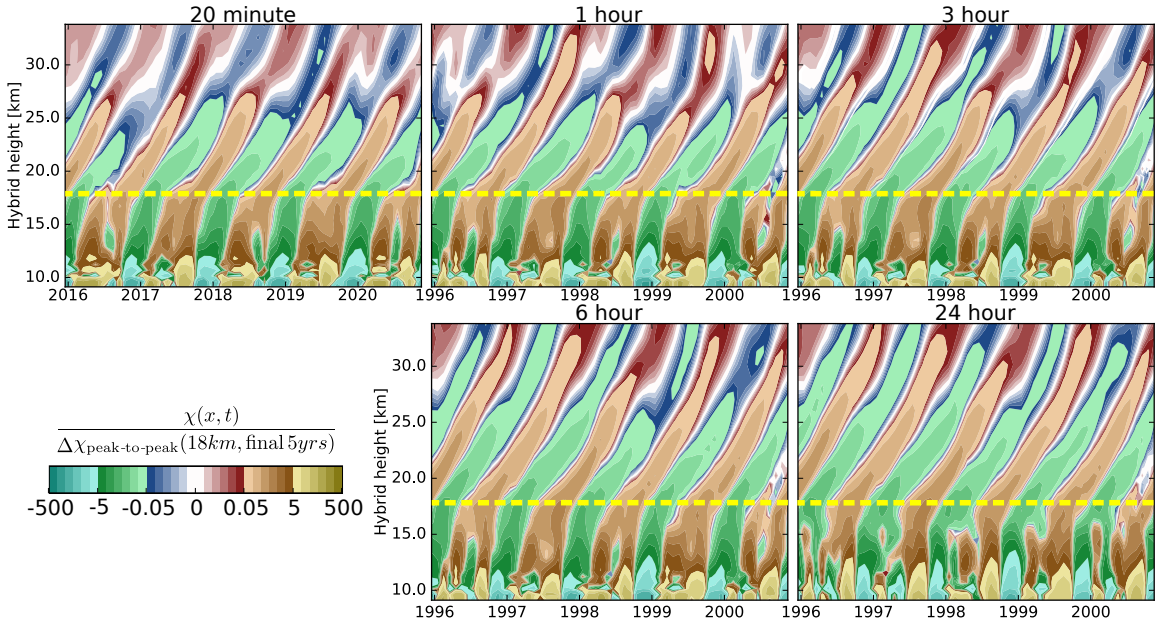

Fig. 3.12 For the different tracer sampling rate experiments, showing final 5 years of high-pass filtered timeseries divided by climatological peak-to-peak at 18 km of final 5 years (yellow dashed line). Note that 20 min case's final 5 years is 2016-2020 because it has reached steady state then, whereas others are for 1996-2000. Also note for the colour scale, the contours within -0.05–0.05 are linear, and outside of this range they are logarithmic.

dependence of pathways (Bannister et al., 2004; Bonazzola and Haynes, 2004; James et al., 2008; Kremser et al., 2009; Tissier and Legras, 2016; Wright et al., 2011). This requires further clarification, as the Clausius-Clapeyron relation obscures the conclusion from the semi-Lagrangian instant-dehydration tracer.

Results – vertical signal propagation

Water vapour is known for a prominent annual cycle propagating upwards through the tropical lower stratosphere, the tape recorder effect (Mote et al., 1996). The vertical propagation speed and vertical attenuation rate is studied for different tracer dehydration sampling rates in figures 3.12 and 3.13. These figures show the zonal mean 10 °N–S monthly mean concentrations of tracer in the first and last five years respectively. To remove timescales longer than a year, a high-pass filter (cosine square with full width of 26 months) is applied. A normalisation factor is also applied by dividing by the amplitude of the average annual cycle at 18 km in their latest 5 years of simulation (yellow dashed line), taken to be in final state. By filtering and normalising in such a way, the remaining variations represent annual

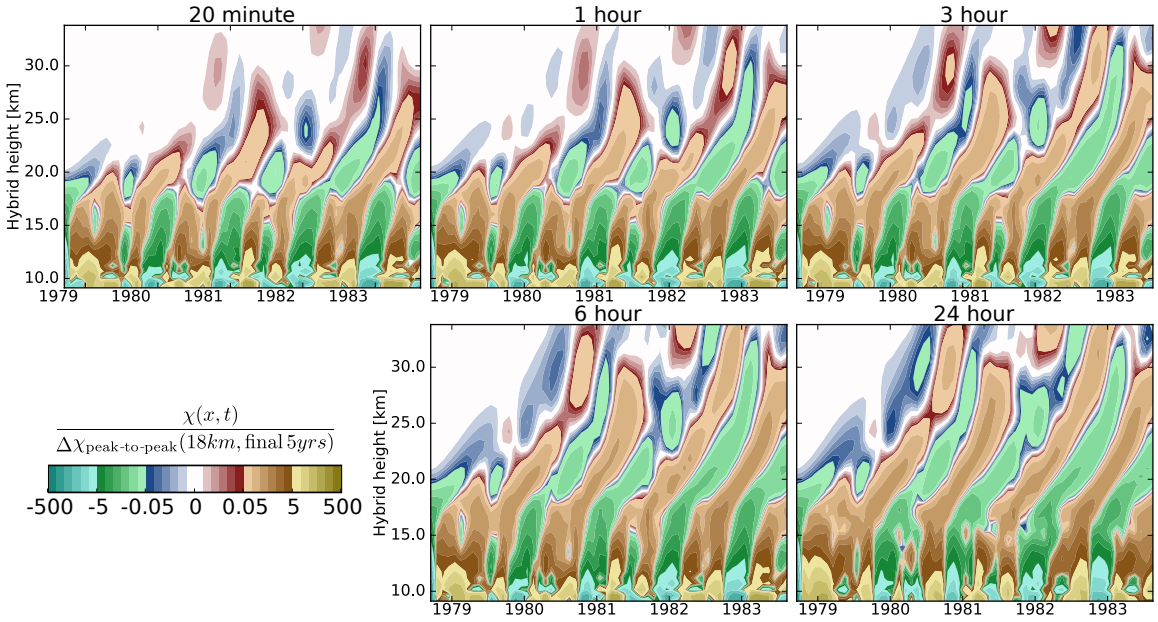

Fig. 3.13 Showing first five years of the timeseries calculated in figure 3.12.

cycle variability of the equatorial stratosphere that is comparable across tracers with different dehydration sampling rate.

A slightly different method has been used in literature to quantify propagation speed, based on vertical time-lagged correlations (see Niwano et al., 2003). That method was tested here (not shown), the same results are found and the displayed method is more practical because it shows the spin-up stage clearly where quick variations prevent a clear correlation analysis.

The results for the final 5 years of the simulation are shown in figure 3.12. It appears that the vertical propagation speed is the same in each sampling rate experiment, as seen from the timing of the maxima, minima and zero-values occurring at altitudes in the lower stratosphere. There is no lag in variations advected upward as the sampling rate frequency is changed. However, the attenuation rate differs slightly. The once-in-20 minute case appears to attenuate more quickly, for example the ± 0.05 contour extends to around 25 km, but the once-in-24 hour case reaches around 35 km. This specifies the impact of more frequent dehydration sampling is increased attenuation in the vertical.

There may be some impact on the normalisation calculation from high sample rate cases not yet being in steady state. However, the once-in-20 minute case has been simulated for an additional 20 years and the same conclusions are seen.

Figure 3.13 shows the first five years of the same high-pass filtered normalised timeseries. This shows how similar the tracer variability is above and below the tropical tropopause at

early times, and that the once-in-24 h sampling rate case arrives at its steady state values within a couple of years. Again, because the timing in variability is so similar across tracers with different dehydration sampling rates, it suggests that the vertical propagation speed is the same for each of the tracers, but the higher sampling rate still causes tracer concentrations to attenuate in the vertical more strongly. This may account for much of the slow spin-up seen in higher sampling rate configurations.

The upper troposphere signal also appears to be different across sampling rate cases. Being above p_{lid}, this region is also influenced by the simple dehydration calculation of equation (2.5). Vertical signal propagation for the 10–15 km tropical region is nearly immediate in the lower sampling rate cases. This leads to reduced vertical gradients in lower sampling rate case in the upper troposphere, which may associate numerically with reduced vertical gradients throughout the stratosphere.

Summary

To summarise the investigation of this section, dehydration sampling rate affects not only concentration of the tracer in the stratosphere, but also, surprisingly, the vertical attenuation rate of concentrations. This may also impact model water vapour, q, as the timescales of ice microphysics to dehydrate may be interpreted similarly by the advection and conservation schemes.

3.3.2 Comparison with model water vapour and Lagrangian calculations

The earlier parts of this section developed a tracer that is advected by the UM10.4 transport scheme to be instantly dehydrated at various rates. The rest of this section will compare its behaviour with the model water vapour (q) and with Lagrangian dry point calculations (q_{LDP})

Figure 3.14 shows the average annual cycle of monthly mean q, q_{LDP} and the tracer subjected to different sampling rates of instant dehydration (q_{trac}). q_{LDP} (grey line) and q (black line) are consistent with figure 3.8 (the only difference is q is shown here at 18 km), with the characteristic dry bias of the q_{LDP} method. The Lagrangian average annual cycle is also delayed by 1–2 months.

The concentration of q_{trac} is sensitive to sampling rate of dehydration, as seen in the last section. The concentrations of the q_{LDP} throughout the annual cycle are in close agreement with the tracer when dehydrated once every 6 hours. This is the same frequency of

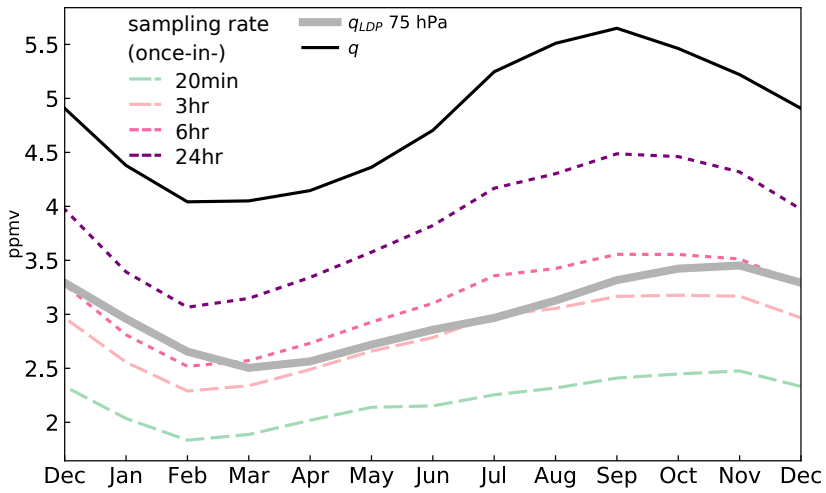

Fig. 3.14 Climatological annual cycles of tracers with different dehydration sampling rates (q_{trac}), Lagrangian dry point calculations (q_{LDP}) and model water vapour (q). Climatological average is over 10 years 30 °N–S at 18 km for q_{trac} and q and at 75 hPa for q_{LDP}.

dehydration as the applied in Lagrangian calculations. The similarity in monthly mean concentrations is a sign that the difference in transport scheme makes little difference to the predicted concentrations of H_2O_{strat}.

At the same time, the annual cycle phase of tracers subject to instant dehydration are all in close agreement with q. This suggests that the transport scheme affects the annual variation of water vapour in the tropical lower stratosphere. This conclusion might be inferred from earlier studies of ECMWF reanalyses, where the Lagrangian calculations are based upon reanalysis winds and temperatures find better agreement with observed water vapour than the reanalysis calculation of H_2O_{strat} (for example, Glanville and Birner (2017) had attempted to diagnose the mixing required for ERA-I reanalysis transport to obtain a realistic tape recorder, while Liu et al. (2010) section 5.3.2 had found that Lagrangian transport calculations achieve this). However, the tracer calculation removes all other model processes, thereby obtaining a clearer result that transport affects the temporal variation.

To further compare the spatial and temporal estimates of H_2O_{strat}, figure 3.15 shows for the same cases the distribution of concentrations in the tropical tropopause layer for the months of February, May, August and November. q_{trac} cases are similar to those shown in figure 3.11, but here they are shown at 18 km for consistency with q and q_{LDP}. A number of features can be distinguished between these calculations of H_2O_{strat}.

The distributions of Lagrangian values are consistent with previous studies (Liu, 2009) but are very broad compared to both q and q_{trac}. It should be pointed out that analysis of Lagrangian dry points generally compares only the mean of this horizontal distribution with

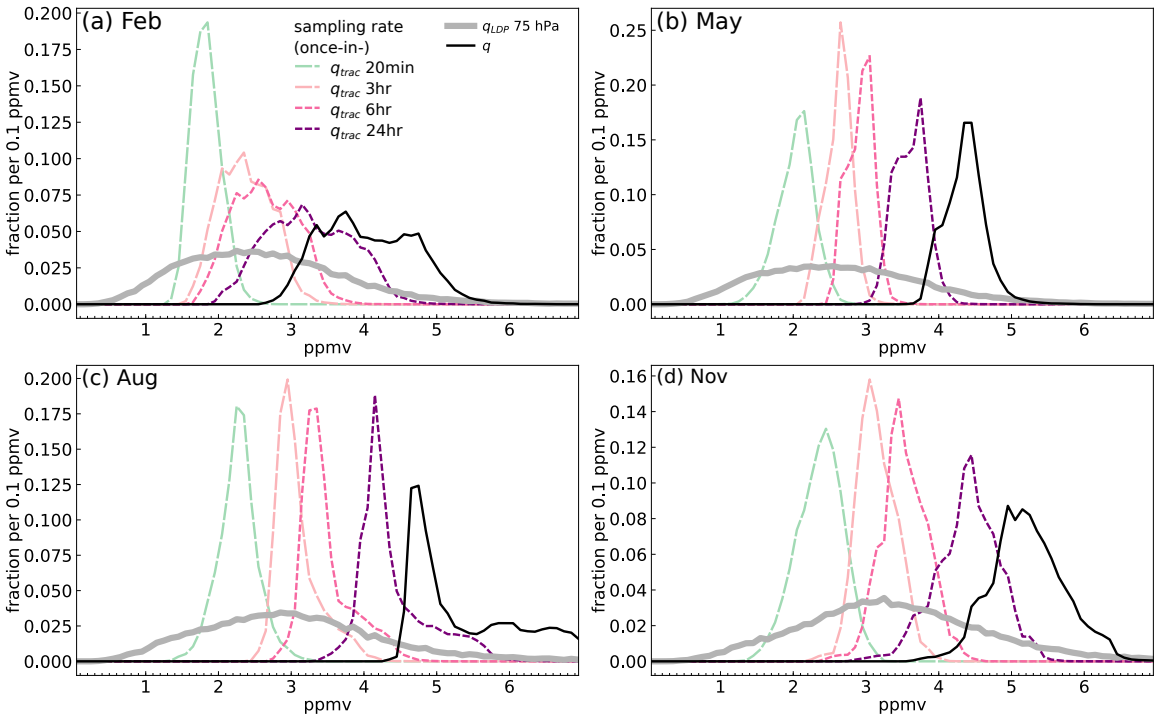

Fig. 3.15 Probability density function of tracer concentrations, for tracers with different dehydration sampling rates (q_{trac}), model water vapour (q), and Lagrangian dry points (q_{LDP}) monthly mean gridpoints between 30 °N–S and at 18.0 km (q_{LDP} are at 75 hPa) after ∼13 years in (a) February, (b) May, (c) August, (d) November.

H_2O_{strat}. In this case of estimating model water vapour in the tropical tropopause layer, the seasonality in mean concentrations is followed, however it is clear that the Lagrangian method does not resolve the horizontal distribution in concentration. The broad distribution may be partly due to the kinematic approach to advection.

Using the climate model advection scheme, every case of q_{trac} shows a much sharper distribution of concentrations in the tropical tropopause layer, and resembles that of q, including seasonal changes. This further identifies that the spatial variations of q in the tropical tropopause layer are determined by both instantaneous dehydration and large-scale transport.

Tracers with high sampling rates of dehydration find a simpler distribution than q, for example in August (figure 3.15c) there is a wet tail to the distribution of q which also appears in q_{trac} but diminishes for sampling rates more frequent than once-in-12 hours. The model-advected tracer may obtain the concentrations and horizontal distribution of q in all seasons if it is dehydrated at a rate less frequent than once-in-24 hours. The dependence on sampling rate is a sign of the dehydration timescale in the climate model.

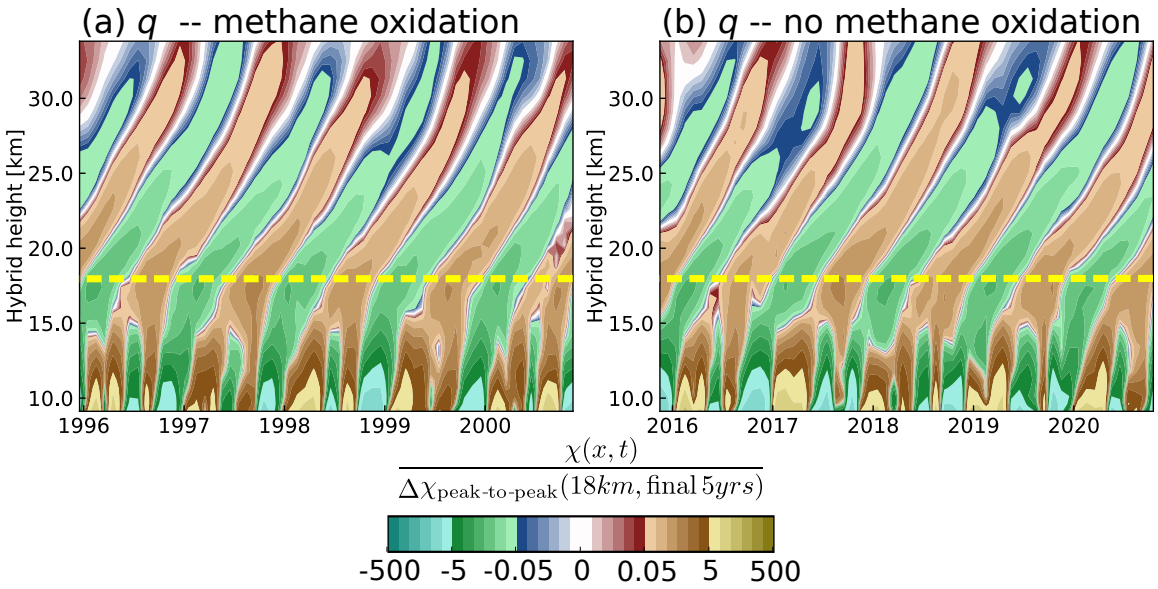

Fig. 3.16 As for figure 3.12, but for model water vapour. Showing 9–34 km for two experiments, (a) the same simulation as figure 3.12 where q includes methane oxidation, (b) different simulation with the same forcing (but different variability) and no methane oxidation.

The consistent result across seasons is interesting because of the contrasts in transport and temperature patterns. This dehydration tracer captures the horizontal structure in q throughout the annual variation. Summer months present relatively confined horizontal transport (due to the Asian summer monsoon) in a warmer tropical tropopause, and winter months present stronger vertical advection through very low temperatures. Furthermore, the timescale of dehydration has a crucial influence.

Vertical and horizontal distribution in lower stratosphere

The distribution of tracer concentrations agrees well with q in the tropical tropopause layer, where it is designed to resemble the key processes of transport and dehydration. It may yet describe water vapour throughout the stratosphere.

The tracer evolution in the tropical pipe that was shown in figure 3.12 can be compared with model water vapour shown in figure 3.16. The model dynamics of the tracer experiments included methane oxidation, causing a steady hydration in the stratosphere. However, because the tracer is not subject to methane oxidation, its vertical profile will differ.

Model water vapour from the same experiment but with methane oxidation inactive is shown in figure 3.16b. The vertical attenuation rate of model water vapour resembles the dehydration tracer with dehydration sampling rates around once-in-3–24 hours. This tests

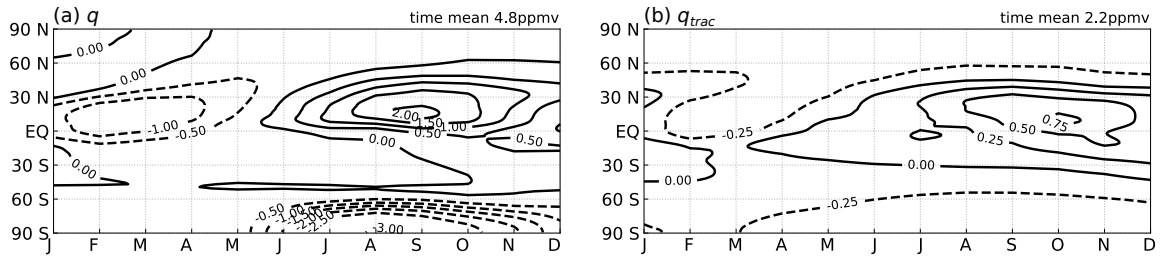

Fig. 3.17 Zonal mean average annual cycle of (a) water vapour and (b) semi-Lagrangian tracer in 20 min case, at 18 km over years 32–41. Note that the contour levels are 0.5 (left) and 0.25 (right).

a more extensive range of timescales than has been possible with the Lagrangian dry point method which is usually limited to 6 hourly frequencies. The results here suggest that a sub-daily timescale applying instantaneous dehydration captures the vertical variations of model water vapour in the tropical stratosphere.

Conversely, when H_2O_{strat} is modified by methane oxidation, shown in figure 3.16a, the annual variations agree but the signal in q is lost above about 35 km.

The above findings suggest that the tracer resembles water vapour variation in the tropics. The tracer is now compared across all latitudes at 18 km. At mid-latitudes and the poles, this level is in the lower stratosphere where air also originates from the tropical tropopause but also more local events of exchange with the troposphere. Figure 3.17 shows the average annual cycle across all latitudes for model water vapour and q_{trac} with 20 minute sampling rate. Despite the average concentration difference, the tracer's meridional and seasonal variation resemble model water vapour in the lower stratosphere quite closely. The poleward propagation of tropical anomalies is clear in both q and the tracer, as in observations (for example, Randel and Jensen, 2013). The tracer does not exhibit strong dehydration over the Antarctic due to already having low concentrations. There is some delay near the tracer's peak (September-November) compared to q (August-October). This may be related to the over-strong signal dissipation in this tracer, or because of possibly hydrating processes not described by the tracer, for example, convective ice injection.

3.3.3 Conclusions

To compare the effects of transport on Lagrangian calculations of climate model water vapour, in this section instantaneous dehydration was applied to a tracer transported by the UM10.4 semi-implicit semi-Lagrangian advection scheme. To provide a region of rehydration in the troposphere, a discrete boundary was introduced which caused numerical difficulties which

were overcome. The sensitivity to numerical aspects of advection and conservation motivate applications of dehydration in a non-instantaneous form.

A climate model advection scheme works on much shorter timesteps than an offline Lagrangian calculation (20 minutes and 6 hourly, respectively, for the configurations in this thesis). Investigating sampling rates of instant dehydration for these model-advected tracers provides information on the timescales between them. As expected, more frequent dehydration sampling resulted in a drier estimate of the stratosphere. When the tracer tested for dehydration at a rate of once-in-6 hours, its annual cycle concentrations in the tropical lower stratosphere were very similar to the results of the Lagrangian dry point method.

However, the stronger vertical gradients in the tropical tropopause region caused by more frequent dehydration also led to stronger vertical attenuation of tracer concentrations into the tropical stratosphere. This has yet to be fully understood and, because it may be a side-effect of ice-microphysics deposition timescales parameterised in the UM, it motivates further study of the effects of climate model transport on estimates of stratospheric water vapour.

At the same time, the tracer subjected to sub-daily timescales of dehydration could resemble the vertical attenuation rate of model water vapour in the stratosphere. The vertical tape recorder signal in model water vapour, and its average annual cycle of the lower stratosphere, were fairly well represented by the model-advected tracer. This indicates most of the spatial and temporal variability of model water vapour is dictated by transport and dehydration. Further work will extend this analysis to interannual variability in section 4.2, and compare climate forcing trends in section 6.4.1.

3.4 Impact of resolved sub-seasonal temperature variability

Section 3.2 found the advection-condensation method captured the average annual cycle of water vapour in the tropical lower stratosphere in reanalysis. Inter-model differences were retained by the Lagrangian calculation. The previous section found that applying the instantaneous dehydration method to different transport schemes yields similar representations of model H_2O_{strat}, further suggesting that differences between climate model results are not dominated by differences in transport.

The remaining aspect of advection-condensation that might cause differences between estimates of climate model water vapour are short-timescale temperatures, which are studied in this section. Other possible influences include rehydration of any ice present in the tropical

tropopause, originating from earlier dehydration or deep convection, which are investigated in chapter 5.

Kim and Alexander (2015) show the impact of observed temperature fluctuations on seasonal mean estimates of the tropical cold point tropopause at particular sites in the west Pacific Ocean. Without sub-seasonal variations, temperatures were found to be 1.6 K warmer overall. These variations result from a broad spectrum of waves. When neglecting sub-seasonal temperature variations in ERA-I reanalysis at the same locations and over the same period (1990–2014), they found a similar but reduced warm bias of 0.56 K. Typical scaling to water vapour ($\sim$0.5 ppmv/K, for example, Hardiman et al. (2015)) would lead to a $\sim$0.3 ppmv wet bias in the tropical lower stratosphere.

Kim et al. (2019) go further in comparing the representation of wave activity in the tropical stratosphere of reanalyses. They report relative contributions, spatial distributions, and a positive trend in variance of tropical tropopause temperatures across all reanalyses. Scherllin-Pirscher et al. (2017) study the composition of the Kelvin wave impacts on UTLS temperature variability. They point to a large contribution from sub-seasonal waves with periods less than 30 days. They also find some coincidence with strong convective events, but not as a conclusive driver of Kelvin wave variability in the upper troposphere and lower stratosphere.

The impact of ERA-I sub-monthly temperature fluctuations on Lagrangian dry points is indicated by Fueglistaler et al. (2013), without it the Lagrangian mean is warmer by 3.2 K. Their method keeps dry point locations fixed when removing short-timescale fluctuations, neglecting any changes to the timing of saturation minima along trajectory histories, thereby fixing transit times. Bonazzola and Haynes (2004, section 4.3) have calculated the full impact of removing sub-daily and $<$90 day temperature variability from Lagrangian dry point positions and estimates of H_2O_{strat}, in ERA-40 (previous generation of ERA-I) reanalysis across three seasons. They quantify the moistening effect, but do not report on the structure of impact across timescales, nor compare the representation of temperature variability to observations.

It is therefore anticipated that under-represented sub-seasonal temperature fluctuations lead to a wetter prediction of water vapour entering the stratosphere. However, it is not clear what the average impact is from reanalysis, nor to what extent this occurs in UM-UKCA.

This section will examine the importance of sub-seasonal temporal variability in temperatures for Lagrangian calculations of H_2O_{strat} in ERA-I reanalysis and in UM-UKCA. Specifically, it will identify the relative impact of various sub-seasonal timescales, and relate this to the findings of Kim and Alexander (2015). It will also demonstrate the impact of

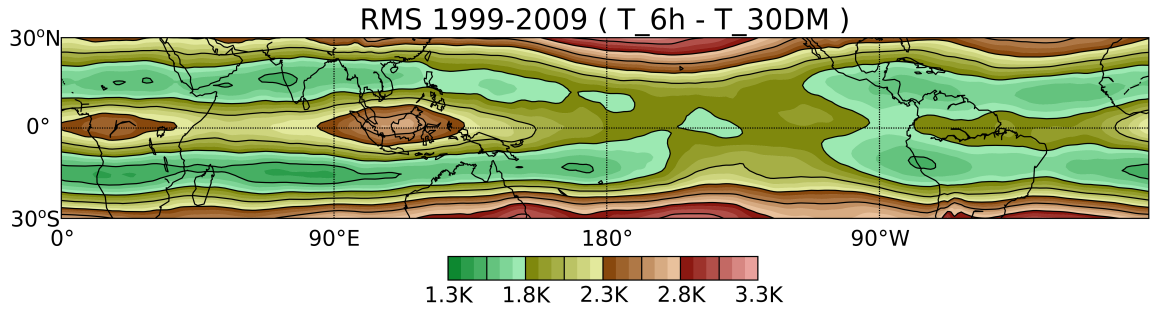

Fig. 3.18 Root-mean-square difference in 1999-2009 ERA-I temperatures timeseries at each 96 hPa gridpoint between 6 hourly and 30 day mean.

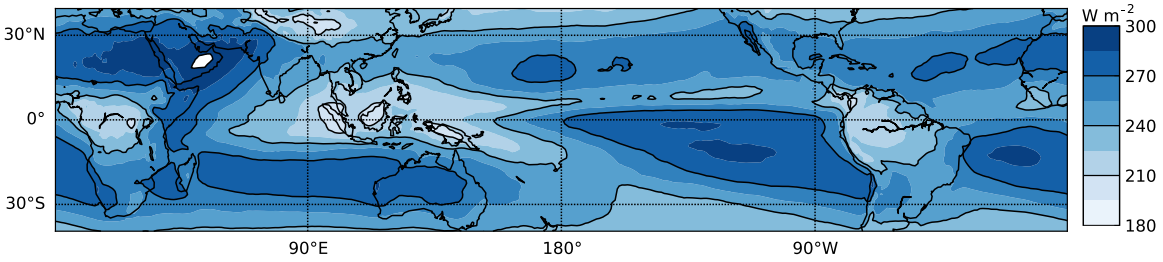

Fig. 3.19 Map of 1999-2009 mean of daily OLR radiances from HIRS satellite dataset.

neglecting transit time changes for Lagrangian dry points calculated with a smoothed temperature field, quantifying the error in values reported by Fueglistaler et al. (2013). Finally, the difference between representation in UM-UKCA and ERA-I will be highlighted, quantifying whether there is a mis-representation of sub-seasonal temperature variation in UM-UKCA and to what extent it impacts estimates of H_2O_{strat}.

3.4.1 Method

To test the sensitivity of q_{LDP} to different timescales in temperature variability, trajectory pathways are repeated with smoothed temperature fields. The trajectory sets are ERA-I diabatic back-trajectories introduced in section 2.4. These are compared with equivalent results from the UM-UKCA yr2000 kinematic back-trajectories.

The smoothed temperature fields are calculated as moving-window averages of the original 6 hourly Eulerian field. The moving window averages are applied to each gridpoint and span 1–120 days for ERA-I, and 1–30 days in UM-UKCA. Additionally, to test the impact of longitudinal variations, zonal mean temperature fields are sampled in the 6 hourly and 30 day mean fields in ERA-I. From 10 years of monthly releases, an average annual cycle of Lagrangian dry point estimates for H_2O_{strat} are calculated.

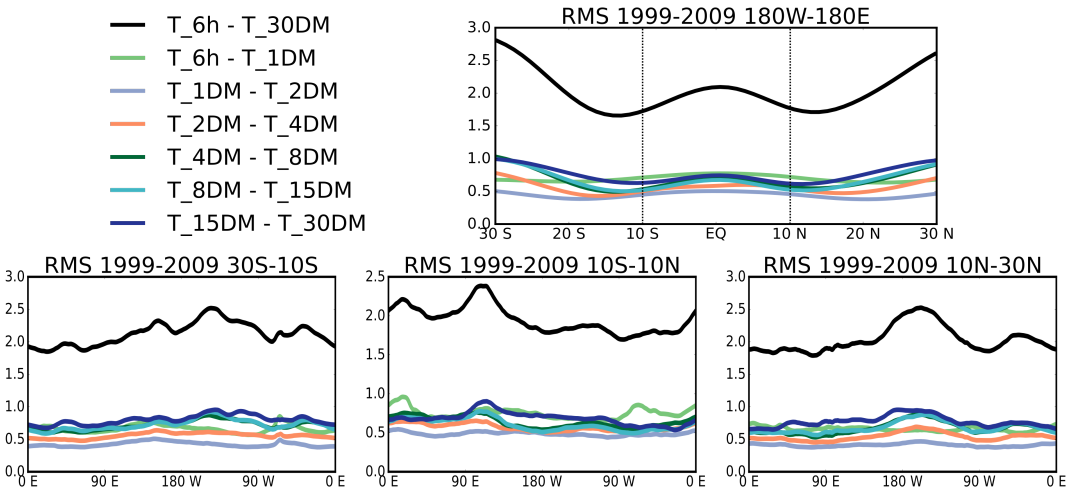

Fig. 3.20 As for figure 3.18 but for successive smoothed temperature fields and calculated across 1999-2009 and (a) longitudes, (b) 30 °S-10 °S, (c) 10 °N–S, (d) 10 °N-30 °N.

3.4.2 Results – reanalysis

Structure of fluctuations

Figure 3.18 shows the time variability of ERA-I temperatures in the tropical tropopause layer. Sub-monthly temperature fluctuations in the tropics peak along the equator over Africa, the Indian Ocean and the Maritime Continent. This points to the action of different waves such as equatorial Kelvin waves and mixed Rossby-Gravity waves. Respectively, these modes peak over east Africa and east Pacific according to analysis of 2–20 day filtered variances of Kim et al. (2019). One difference is the maritime continent region. Figure 3.19 shows the time average of daily OLR across this time of interest from the HIRS satellite (Schreck et al., 2018). Low OLR radiance indicates high convective cloud tops — approaching the tropopause. Lowest OLR radiances appear above the maritime continent, and similarly over equatorial Africa and South America. This indicates deep convection which will introduce short-timescale (daily) temperature fluctuations to the tropical tropopause layer above.

The contribution between each of the applied temporal filters to the total sub-monthly variability is shown in figure 3.20. Values range between 0.4–0.8 K for different timescales of averaging. As for standard deviations, the total is reached by adding the individual contributions in quadrature. Some structures can be seen, for example sub-daily (T_6h-T_1DM) timescales make the strongest contribution over Africa and South America along the equator, pointing to the influence of insolation (with a stronger daily cycle over land) and convection. Also, daily to two-daily (T_1DM-T_2DM) timescales have the lowest RMS

Table 3.1 Changes to Lagrangian dry point temperatures and predictions of H_2O_{strat} due to removal of sub-monthly timescales in the temperature field (6h - 30DM). See text for further details.

		re-evaluating LDP location		fixed LDP location	
		ERA-I	UM-UKCA	ERA-I	UM-UKCA
ΔT_{LDP}	(K)	2.52	1.7	4.35	2.6
ΔSMR_{LDP}	(ppmv)	1.04	1.7	1.7	2.8

at most places in the tropics, pointing to strongest influences from sub-daily and many-day events.

Lagrangian dry point response

The average response of Lagrangian dry point temperatures to removing different timescales of temperatures is shown in table 3.1. The change to average Lagrangian dry point temperatures, by neglecting sub-monthly temperature variability, is a warming of 2.52 K.

Figure 3.21 shows the distribution of Lagrangian dry point locations calculated in the 6 hourly and the 30 day mean temperature fields. The colour field refers to percent of all dry point events within $4.5° \times 2°$ gridboxes, with black contours of 0.1 % gradation. The large dashed boxes provide broad regions for distribution comparison. It is clear that when experiencing 6 hourly temperature variability the Lagrangian dry point locations are more diffuse. Gridboxes in the west Pacific and south east Asia show smaller percentages of events, and more broadly a loss of $\sim$7 % of events from this region (grey dashed box). There is $\sim$2 % increase over Africa (purple dashed box), and little change near the tropical Americas (orange dashed box), inferring the other events now occur over the Indian, Pacific and Atlantic oceans.

Because the sub-monthly temperature fluctuations are quite extensive, it is not a surprise that the general response is less focused dry point locations. But, most dry points occur in regions where sub-monthly temperature variability is very low (figure 3.18). This suggests its introduction would move dry point events little. Regions with stronger temperature variability would be most disruptive, such as along the equator between Africa and the maritime continent. Indeed, this region appears to have gained the most Lagrangian dry points (figure 3.21).

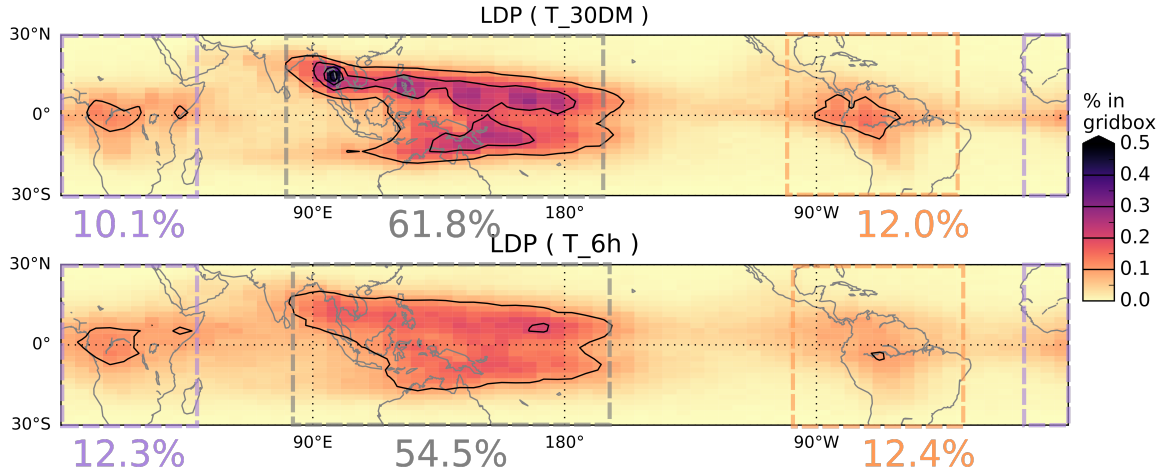

Fig. 3.21 Spatial distribution of Lagrangian dry point events for trajectories subject to (a) 30 day mean temperature field and (b) 6 hourly temperatures. The colour field refers to percent of all dry point events within 4.5°×2° gridboxes, with black contours of 0.1 % gradation. The large dashed boxes provide broad regions for distribution comparison.

Water vapour response

Figure 3.22 shows the Lagrangian dry point predictions of water vapour resulting from sampling the different smoothed temperature fields in ERA-I and UM-UKCA. The figure shows the time mean and the average range of the annual cycle (as points and lines respectively), with the timescales of temperature averaging scaled along the horizontal axis. The grey datapoints re-evaluate Lagrangian dry point locations for each smoothed temperature field. This allows dry point locations to move as presented in figure 3.21 and for transit times from Lagrangian dry point to tropical lower stratosphere to change.

Without sub-monthly temperature fluctuations, Lagrangian estimates of stratospheric water vapour in ERA-I are higher by 1.04 ppmv. Remarkably, varying the timescale of temperature averaging between 1–30 days follows a roughly logarithmic relationship to H_2O_{strat} predictions. No particular timescale is found to have a stronger impact. This may be a surprise compared to the varying magnitude of temperature fluctuations at different timescales (0.4–0.8 K) in figure 3.20.

The effect of averaging the temperature field zonally can also be seen (light grey points), the predicted H_2O_{strat} annual cycle is wetter. It is also delayed (not shown). Dehydrating according to zonal mean temperature fields removes most of the influence of sub-monthly temperature variability. Because this timescale is associated with synoptic scale variability, it is not organised zonally and therefore a longitudinal average has a similar effect to averaging

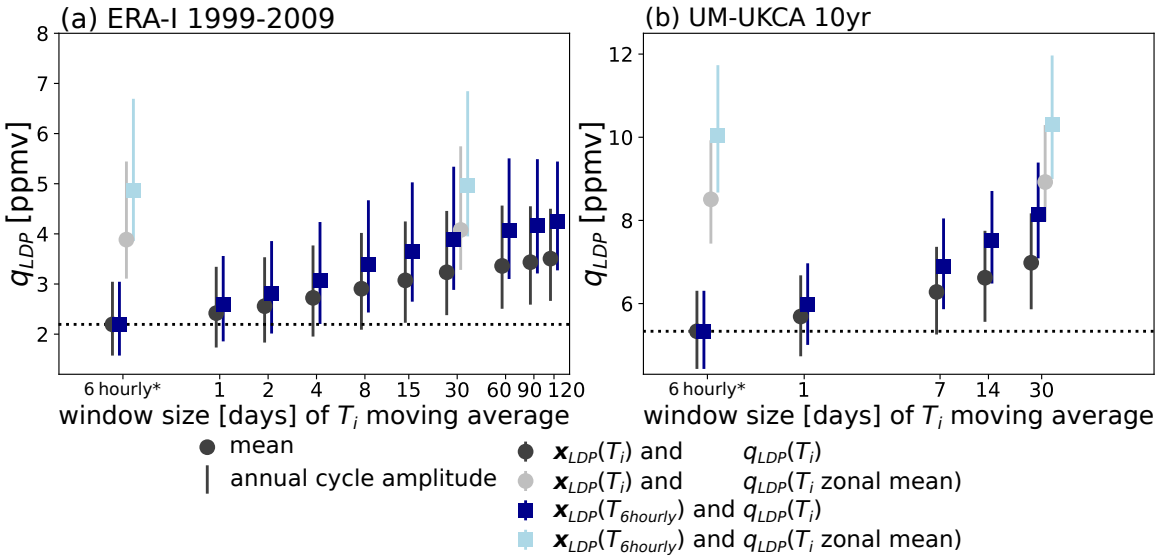

Fig. 3.22 Predictions for stratospheric water vapour time mean (points) and annual cycle amplitude (whiskers) from Lagrangian dry point calculations (q_{LDP}) experiencing different moving-window time averages in (a) ERA-I across 11 years and (b) UM-UKCA across 10 years. Timescales averaged over include 1-day (1DM), 2-day (2DM) and zonal mean (light colour points). (*) Note that 6-hourly temperature field is instantaneous, not averages. Calculations are divided into those which re-evaluate dry point locations according to averaged temperature field (grey datapoints) and those which fix dry point locations from 6 hourly calculation (blue datapoints).

over sub-monthly timescales. Diurnal convection impacts are azonal and these will also be lost in a zonal mean view.

Water vapour response – sensitivity of Lagrangian dry point timing

A second calculation is shown in figure 3.22 with dark blue and light blue datapoints which also calculates dry points in averaged temperature fields. However, dry point locations remain fixed from the original 6 hourly temperature calculation. This therefore loses additional pathway information from the trajectory results.

The impact of not re-evaluating dry point locations in ERA-I sub-monthly temperature fields is a further 0.66 ppmv (63 %) increase in H_2O_{strat} predictions. In total, this is approximately equivalent with the 3.2 K temperature bias reported by Fueglistaler et al. (2013). The positive response makes sense from the view of calculating that saturation minimum, less freedom for trajectories to locate that minimum leads to a wetter result. The difference is quite substantial, even if the pathways are the same and the overall spatial distribution of dry points has not changed greatly. It is therefore encouraged that timing of saturation

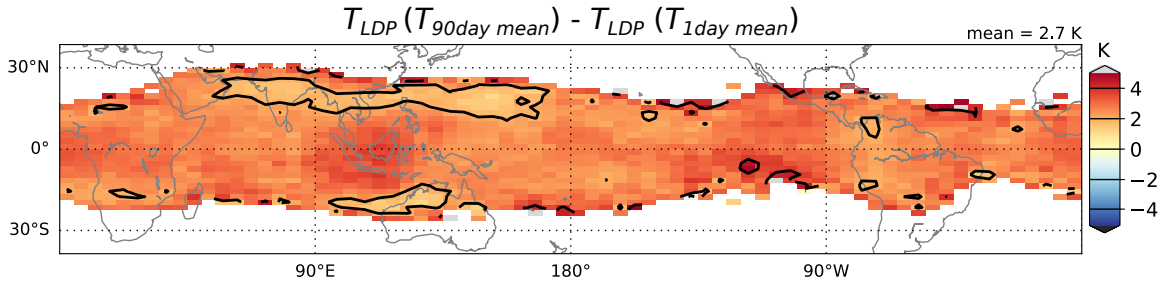

Fig. 3.23 Map of differences in temperatures of Lagrangian dry points between 90 day mean and 1 day mean, calculated over 11 years of ERA-I reanalysis.

minima along Lagrangian pathways should be re-evaluated when an alternative temperature (or saturation mixing ratio) field is provided.

Temperature and water vapour response – sub-seasonal variability

Figure 3.22a shows a further moistening when filtering out temperature variability on monthly to seasonal timescales. The horizontal distribution of this impact is shown in figure 3.23. Specifically, the spatial distribution of difference in Lagrangian dry point temperature between 90 day mean and 1 day mean temperatures is shown. The smallest and largest impacts are near the maritime continent, in the subtropics and at the equator respectively. The horizontal distribution is otherwise quite uniform.

3.4.3 Results – chemistry climate model

Water vapour response

Figure 3.22b shows comparable calculations using UM-UKCA. Note that not all of the temporal filter window sizes match those applied in the ERA-I case (so the positions on the horizontal axis are not the same), but the horizontal axis is also to scale. As raised earlier in sections 3.2.1 and 3.2.2, UM-UKCA exhibits a wet bias compared to reanalysis. This is also visible in figure 3.22 as the offset in predicted H_2O_{strat} concentrations.

Without sub-monthly temperature fluctuations, Lagrangian dry point temperatures are warmer on average by 1.7 K, and Lagrangian estimates of stratospheric water vapour are higher by 1.7 ppmv. With re-evaluation of dry point locations in sub-monthly temperature fluctuations, the result moistens by another 1.16 ppmv (70 %). Compared to ERA-I, the annual cycle in UM-UKCA is less sensitive to the removal of sub-monthly temperature variability.

The log-linear relationship across temperatures scales seen in reanalysis does not hold in UM-UKCA. The H_2O_{strat} prediction from 1 day mean temperatures does not follow from the scaling shown across 7–30 day mean results. This suggests that sub-weekly temperature fluctuations are under-represented compared to those in the week-to-month timescale.

3.4.4 Discussion

Predictions of H_2O_{strat} from Lagrangian dry point analysis are sensitive to the timescales of temperatures observed. Keeping advection data at 6 hourly frequency as commonly available from reanalyses, the effect of averaging temperatures to a 30 day moving-window is a moistening. This is seen in both reanalysis and a chemistry climate model where the effect is weaker. This points to a crucial role of sub-monthly temperature variability in accurate estimates of H_2O_{strat}, and its under-representation in UM-UKCA.

The relative impact of intermediate timescales in reanalysis are proportional (that is, halving the window size always leads to a drying of similar magnitude). The same scaling applies for reanalysis from 30 day mean to 6 hourly. The results may be applicable to other climate models where the structure of sub-seasonal temperature variability is quantified and compared.

The results also raise the question of convergence at small timescales in ERA-I and in UM-UKCA. It appears that if timescales shorter than 6 hours were captured, the Lagrangian dry point calculations would predict a drier stratosphere. As in section 3.3, this emphasises that the instant dehydration approximation loses validity for fluctuations shorter than the process it represents. It can be argued that this does not apply at the 6 hourly timescale due to good correlation of resulting calculations with observed water vapour (discussed further in chapter 4). However, it contributes to the cold bias – the over-efficient sampling – of the instantaneous dehydration method. This also has implications for Lagrangian studies that parameterise sub-gridscale temperature fluctuations (Schoeberl and Dessler, 2011, and subsequent experiments).

Of course, for the UM-UKCA case, in a chemistry climate model there is a distinct threshold for resolved timescales at the model timestep. In combination with possible sub-model-timestep schemes (such as ice microphysics), experiments can determine behaviour at the model timestep. This is investigated with the dehydration tracer advected in UM10.4 sections 3.3, 4.2 and 6.4.1. The drying effect of shorter timescale variability occurs for that application of instantaneous dehydration as well (section 3.3.1).

Kim and Alexander (2015) found that temperature fluctuations between 1–90 days in observations cool the tropical cold point by 1.56 K, but in ERA-I the effect is 0.56 K. Here, the impact of daily to 90 day temperature variability on Lagrangian dry points is 2.34 K and 1.02 ppmv (or, without re-evaluating dry point locations, 2.89 K and 1.18 ppmv). While this is over a shorter period of 1999-2009 and full tropical extent, the impact of temperature fluctuations is around four times larger for the locations that contribute to final dehydration locations. This raises the question of how strong the impact is on observed stratospheric water vapour. It also adds weight to the under-representation of sub-seasonal temperature fluctuations in ERA-I.

One factor contributing to the different impacts on LDP temperatures is that they are not confined to the equatorial West Pacific (∼7 °N, 134–171 °E) where the vertical coldpoint impact is reported by Kim and Alexander (2015). Looking at how LDP temperature impacts are spatially distributed in figure 3.23, it is clear that there is some zonal structure which resembles that of temperature fluctuations in figure 3.18. One peak is over the maritime continent, and minima are ∼20 °N, 70–160 °E and ∼20 °S 100–130 °E. As such, the equatorial West Pacific is not fully representative of the spatial structure.

Comparing ERA-I and UM-UKCA shows further impact from loss of temperature fluctuation on Lagrangian predictions of H_2O_{strat}.

When the timescale of 6 hour to 30 day fluctuations are included, ERA-I estimates of LDP are 2.52 K cooler and 1.04 ppmv drier, whereas UM-UKCA is 1.7 K cooler and drier by 1.7 ppmv (without re-evaluating dry point locations: ERA-I 4.35 K and 1.70 ppmv, UM-UKCA: 2.6 K and 2.8 ppmv).

The scaling of temperature and saturation mixing ratio may be explained by the non-linearity of the Clausius-Clapeyron equation, as the saturation mixing ratio becomes more sensitive at higher temperatures.

Temperature variability will also impact trajectory transport, as diabatic heating changes drive vertical motion in the tropical tropopause. Tissier and Legras (2016) test sensitivity of diabatic trajectory source regions from convective-tops to a 30 day cosine window smoothing of diabatic heating to remove diurnal (and other short-timescale) diabatic heating. Little difference is seen in relative contributions and heights from different source regions in winter and summer. Therefore, the method applied here can focus on impact of temperature history.

While Kim and Alexander (2015) find the sub-seasonal temperature fluctuations at the tropical tropopause are under-represented in ERA-I, these results show that the impact is amplified at Lagrangian dry points and that there is further under-representation in UM-UKCA.

Conclusion

In summary, the results show the impact of not resolving sub-monthly temperature variability in ERA-I results in the Lagrangian prediction of H_2O_{strat} to be too high by 1.04 ppmv (47 %). Sub-monthly temperature variability is under-represented in UM-UKCA and its loss leads to the Lagrangian prediction of model water vapour to be too high by 1.7 ppmv (32 %). This result is sensitive to re-evaluating dry point timing along trajectory pathways. Sampling the averaged temperature field without doing so increases the wet bias by 63–70 %. The majority of this change occurs to Lagrangian dry points between the Indian and west Pacific oceans.

These results also question the validity of the instantaneous dehydration approximation at short timescales. $<$6 hourly frequency data used in Lagrangian studies of instantaneous dehydration will need to justify the representativeness at this timescale.

3.5 Discussion and conclusions

The results of this chapter confirmed that the Lagrangian dry point method is representative of the H_2O_{strat} average annual cycle in the chemistry and global climate models, UM10.4 and UM-UKCA, as it is in ERA-I reanalysis. The Lagrangian result continues to exhibit the dry bias attributed to the over-efficiency of the instantaneous dehydration approximation. Therefore, differences in resolution and underlying schemes (such as interactive ozone, convection, and numerical conservation) do not fundamentally alter the underlying control of temperature and large-scale transport on time mean stratospheric water vapour and its annual cycle. The spatial distributions of final dehydration events are also similar, with changes reflecting model convection schemes.

Applying the advection-condensation method in UM10.4 using a semi-implicit semi-Lagrangian advection scheme resulted in some numerical complications that were overcome. These related to the strong gradients, and possibly to the step-change resulting from instant dehydration at the altitude cut-off (p_{lid} in equation (2.5)). The first issue was resolved by instead dehydrating according to a logarithmic function of the saturation mixing ratio, $f_5(q_{sat}) = 10^3 + log(q_{sat})$ (equation (2.13)), which preserves shape but reduces gradients, with transformation back to appropriate units in model output. The second issue might be overcome by applying a gradual modifier to tracer concentrations, relaxing linearly to local saturation in the troposphere, and towards drier saturation encountered above. This was not tested as the formulation would be less like the Lagrangian dry point method of interest, but it introduces the ability to investigate dehydration timescales.

Previous studies have recognised a contribution of sub-monthly temperatures to temperature variability that is under-represented in ERA-I reanalysis. Results here confirmed this impact on Lagrangian predictions, as in Fueglistaler et al. (2013) but with a more accurate method that also accounts for changes to Lagrangian dry point locations in the smoothed temperature fields. Short timescales modify both ensemble mean temperatures and locations of final dehydration. An idealised injection of sub-monthly temperature fluctuations was carried out by Liu et al. (2010), showing a linear response of ensemble mean Lagrangian dry point temperatures to increases in standard deviation of temperature fluctuations. Results here confirmed this relationship across wider timescales for reanalysis, and quantified it in the historical timeseries of reanalysis, and the UM-UKCA year 2000 conditions. The timescales of temperature variability were found to be different in reanalysis and the chemistry climate model.

Throughout this chapter, various limitations of approximating dehydration as an instantaneous process have cropped up. In this framework, a saturation minimum is just as likely to be induced by the fastest resolved temperature oscillations as slower ones. Therefore, advection-condensation predictions are wetter if dehydration is tested less frequently or on a filtered temperature timeseries. The adjustment of Lagrangian dry point calculations to match observed entry values of H_2O_{strat} entry by a temperature adjustment of 3 K (Fueglistaler et al., 2013; Liu et al., 2010) is left without clear physical explanation. Because less frequent dehydration leads to a wetter result, it raises the question of an optimal timescale for temperature data when applying the assumption of instantaneous dehydration. The discrepancy may also be overcome in other ways, such as defining dehydration to a level above 100 % saturation, which some modelling studies consider (for example, Dessler et al., 2016; Ye et al., 2018) but is not tested here. However, overall, Lagrangian method with 6 hourly instantaneous dehydration results show a good representation of seasonal changes to H_2O_{strat} in ERA-I and two contrasting UM model configurations, but dehydration timescales are worthy of further study.

Additionally, seasonality in that short-timescale variability (as demonstrated in observations and reanalyses Kim and Alexander, 2015; Kim et al., 2019) affects estimates of the seasonal cycle and this could be investigated further.

The two versions of the UM considered here differ in interactive chemistry, and the advancement of many schemes to represent the tropical tropopause layer specifically (Hardiman et al., 2015). While they share many aspects, being different generations of the same global climate model, their differences lend some confidence that the results apply to other climate models. It is clear that Lagrangian predictions of model H_2O_{strat} are closely controlled by

model temperature as much as in reanalysis, and is therefore sensitive to the short-timescale variability present. However, the limitations of applying instantaneous dehydration with a sharp tropopause boundary will depend on the details of climate model advection and conservation scheme.

A number of implications are made for the development of global climate models. As well as tropopause time mean temperatures, sub-monthly variability of temperatures influences average water vapour concentrations in the stratosphere. It has also been seen that water vapour is quite sensitive to numerical aspects of the advection scheme (see also Hardiman et al., 2015), which may cause unintended changes, for example when adjusting water vapour deposition rates. There are other ways to test q for this. For example, modifying a climate model grid to reduce potential numerical diffusion, by using a diabatic grid close to the tropopause so that quasi-isentropic mixing involves only two-dimensional interpolation.

One possible avenue of further work is to utilise the results of section 3.4 to approximate the impact of sub-seasonal temperature variations on stratospheric water vapour concentrations in other climate models, by comparing with the tropical tropopause temperatures structures presented in figures 3.18 and 3.20 (however a better comparison might be a power spectrum).

In conclusion, temperatures and large-scale transport exert a strong control on chemistry and global climate model calculations of the annual cycle of stratospheric water vapour as in reanalysis studies. However, characteristics of temperature variability can differ, and unresolved sub-monthly variability will lead to an overall wet bias. This is the case for ERA-I. For the UM-UKCA experiment, under-represented sub-monthly temperature variability compared to ERA-I will contribute to its wet bias in lower tropical H_2O_{strat}.

The UM10.4 climate model advection scheme transports water vapour into the stratosphere in a similar way to Lagrangian calculations. However, transport differences may exist between climate models due to the advection scheme. Therefore, Lagrangian analysis can also yield clues where numerical aspects of modelled water vapour are awry. In the cases of UM-UKCA and UM10.4, the advection-condensation method represents the seasonal variations of model water vapour in the lower stratosphere.

The effect of convective injection of ice in climate models has not been investigated, but may modify model water vapour. This raises the question of whether differences are seen in other aspects of climate model predictions of H_2O_{strat}.

Chapter 4

Isolating temperature and transport influence on interannual variability

4.1 Introduction

The previous chapter studied the average annual cycle of water vapour entering the stratosphere. It confirmed that observed H_2O_{strat} was reasonably well represented by the Lagrangian calculations using temperature and wind fields from ERA-I. Then, Lagrangian calculations were found to represent stratospheric water vapour in two climate models, UM-UKCA and UM10.4. Differences from using a different transport scheme were small. Furthermore, the impact of sub-seasonal temperature variability was quantified.

Interannual variations in tropical tropopause temperatures are considerable and therefore obscure long-term trends in observed H_2O_{strat} (Hegglin et al., 2014). A number of physical processes contribute to this, as introduced in chapter 1. The Fourier decomposition of the timeseries for ERA-I vertical dry point saturation mixing ratio in figure 4.1 clearly points to a number of periodic contributions. These include the Quasi-Biennial Oscillation (Baldwin et al., 2001; Kawatani et al., 2014) with a roughly two-year period, an annual cycle related to the seasonality of the Brewer-Dobson circulation (see Fueglistaler et al., 2009; Randel and Jensen, 2013, for further explanation) and the ozone radiative feedback (Fueglistaler et al., 2011; Ming et al., 2017), a semi-annual component that is related to solar annual cycle in the atmosphere above and below the tropical tropopause, and daily fluctuations primarily associated with convective activity. Other, less regular sub-seasonal ($<$90 day) fluctuations have been studied in relation to the MJO (for example, Virts and Wallace, 2014) and wave activity. Other longer timescale or non-periodic influences not resolved in the figure include

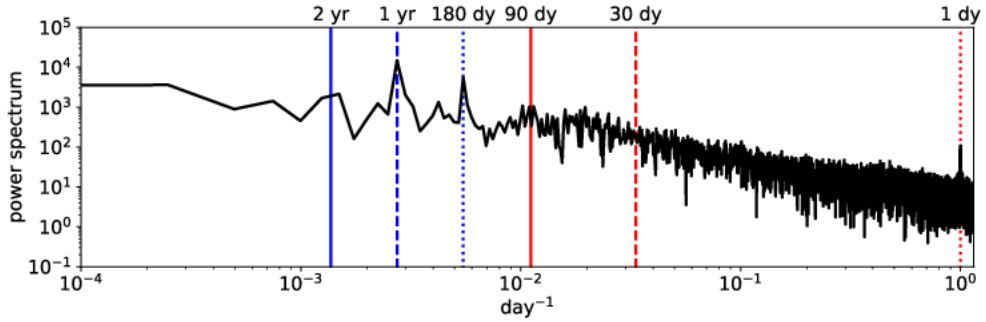

Fig. 4.1 Fourier decomposition of vertical dry point timeseries in ERA-I reanalysis across 1999-2009. Some particular timescales are highlighted with vertical lines.

major sudden stratospheric warmings (occurring in winter roughly every other year), the solar cycle (∼11 years), El-Niño Southern Oscillation (∼2–7 years) and large volcanic eruptions.

While these process are influential through their effect on tropical tropopause temperature fluctuations, many also present changes to stratospheric dynamics, which in combination explain most of the changes in H_2O_{strat}. Because of the thermodynamic balance of radiation and upwelling of the Brewer-Dobson circulation in the tropical tropopause, changes to temperatures (affecting radiation flux) and vertical velocities are connected (for instance, see Dhomse et al., 2008).

The effect of wind fields on Lagrangian calculations is to determine how air parcels move through the tropical tropopause, and will therefore be referred to as transport pathways. The temperature field (in combination with the pressure field) determines the saturation mixing ratios encountered along trajectory paths. The transport pathways and the temperature field experienced by trajectories describe the two key components of the Lagrangian dry point calculation.

The interannual variations of transport timescales and upwelling in the tropical tropopause have been been found to be substantial (Abalos et al., 2012; Ploeger and Birner, 2016). This raises the question as to how influential the interannual variability of winds is in Lagrangian calculations of the variability of H_2O_{strat}.

Hasebe and Noguchi (2016) have proposed the influence of transport pathways in a case study of the observed water vapour timeseries. They have provided evidence that the observed step-wise drop in lower stratospheric water vapour concentrations in the years after 2000 is caused by both tropopause cooling, as determined in other studies (Randel et al., 2006), but also from a weaker constraint of pathways surrounding the Asian summer monsoon. These two explanations are offered to explain the single result of changes in dehydration patterns. However, the impacts of changes in temperatures and transport may be separated further by

investigating how dehydration patterns respond to separately evolving the timeseries of wind and temperature.

This chapter first evaluates the relevance of Lagrangian dry points for analysing interannual variability of H_2O_{strat}. A technique will then be introduced to isolate and quantify the influence of each of the key processes in the Lagrangian dehydration method: transport pathways and temperatures.

4.2 Comparing measures of interannual variability

Knowing H_2O_{strat} is largely controlled by temperatures at the tropical tropopause, as demonstrated in section 3.2, has led to the use of several basic proxies in the literature. These are commonly utilised to compare model representation of processes, and to infer subsequent influences on H_2O_{strat}. The proxies include temperatures at specific levels, such as fixed pressure levels (100 hPa) and vertical cold points (see, for example, Randel, 2010).

Horizontal definitions in the tropical latitudes commonly apply a uniform horizontal weighting (such as a 10 °N–S average). Qualitative discussions often point to contours of specific temperature thresholds to locate the cold pool and changes in certain circumstances (such as an eastward shift during El Niño events, Garfinkel et al., 2018; Konopka et al., 2016). Quantitatively, Zhou et al. (2004) have studied volumes contained within a specified isotherm. An alternative method which applies across trends and model variability is applied by Oman et al. (2008) who calculate a cold pool timeseries from monthly averages from gridboxes surrounding lowest tropical temperatures. They find this can describe both the magnitude and variability of water vapour entering the stratosphere. A statistical definition is similarly possible, selecting the coldest decile of vertical cold (or dry) points of horizontal distribution, as applied by Garfinkel et al. (2013).

In the examples raised, minimum temperatures (cold points) are usually analysed. A more accurate control of dehydration is minimum saturation mixing ratios (dry points), however the difference between them is often unremarkable.

In the literature some other measures have been tested to represent relevant processes, such as a multi-variable regression (for example, Dessler et al., 2013; Smalley et al., 2017; Ye et al., 2018) with components representing the QBO, Brewer-Dobson circulation, and mid-tropospheric temperatures. These regressions appear to produce high correlations with annually averaged timeseries in observations and climate models, enabling a quantification of the relative roles of their regression terms.

Table 4.1 provides calculations of average concentration and interannual variability of stratospheric water vapour and estimates from observations, reanalysis and climate models UM-UKCA and UM10.4. The table reports time mean concentration, and standard deviation of deseasonalised monthly mean timeseries, and correlations with tropical lower stratospheric water vapour of either observations or global climate model. The correlations are defined as the coefficient of determination (von Storch and Zwiers, 1999, section 8.3.3), the measure of variance in the correlatand explained by the correlator, R^2, which is equivalent to the square of the Pearson r correlation coefficient.

The water vapour timeseries are 30 °N–S zonal mean. The observation timeseries of H_2O_{strat} is from the SWOOSH dataset at 83 hPa. The UM-UKCA timeseries of q is also at 83 hPa 30 °N–S, whereas for UM10.4 it is at 18 km. SMR_{100} is the 10 °N–S zonal mean monthly mean 100 hPa saturation mixing ratio, SMR_{VDP} is the 10 °N–S zonal mean monthly mean of vertical dry point saturation mixing ratio. $SMR_{VDP10\,\%}$ is the monthly mean of driest decile of vertical dry point saturation mixing ratio within 30 °N–S. Respectively, these three variables exhibit smaller time-mean values and reduced interannual variability (as measured by the standard deviation of their deseasonalised timeseries). Their R^2 correlations are reported with one month lag, representing the time for the dehydration signal to transit from dry points to the 83 hPa surface. The correlations are fairly similar for the same source of temperatures and winds; for ERA-I: ∼20–30 %, UM-UKCA: ∼50–55 %, and UM10.4: 35–42 %). The cases of higher correlation may suggest a stronger sign of the dehydrating regions. This may be expected due to the warmer models inducing higher sensitivity on saturation mixing ratios through the Clausius-Clapeyron relation.

The more sophisticated measure of Lagrangian dry points is also shown. As introduced earlier, this samples temperatures according to estimated transport of air parcels entering the stratosphere. Higher correlation with H_2O_{strat} indicates more realistic representation of processes. Transport pathways are therefore clearly relevant to variability of H_2O_{strat}.

The ERA-I correlations are not as high as reported elsewhere (Fueglistaler and Haynes, 2005; Fueglistaler et al., 2013; Randel, 2010), which is due to the observation timeseries and the method of combining them. These published methods merge HALOE and MLS satellite timeseries with a method focused on a consistent H_2O_{strat} timeseries. Results here use the SWOOSH homogenised dataset of HALOE, MLS and several other satellite products, weighted according to the number of records per month. Additionally, monthly gridboxes with insufficient records are filled with a 1979-2017 climatology. Using a method resembling the published methods, the only presented variable which correlates differently is q_{LDP} which increases to $R^2 = 0.42$.

Table 4.1 Characteristics of climatology and interannual variability of H_2O_{strat} and various methods of estimation. († correlation is calculated in a non-identical simulation of the same configuration (model state, including q, is not identical to other simulation but is subject to the same forcing and so reaches a statistically similar state). See text for further details.

dataset	variable	time-mean (ppmv)	standard deviation	R^2 with q deseasonalised (month offset)
SWOOSH	$H_2O_{strat}(83hPa)$	3.7	0.3	-
ERA-I	SMR_{100}	5.3	0.9	0.19 (+1)
	SMR_{VDP}	5.0	0.6	0.29 (+1)
	$SMR_{VDP10\%}$	2.91	0.3	0.23 (+1)
	q_{LDP}	2.2	0.2	0.32 (0)
UM-UKCA	q_{83hPa}	7.0	0.2	-
	SMR_{100}	11.6	1.2	0.55 (+1)
	SMR_{VDP}	9.4	0.7	0.51 (+1)
	$SMR_{VDP10\%}$	6.04	0.5	0.52 (+1)
	q_{LDP}	5.4	0.3	0.84 (-1)
UM10.4	q_{18km}	5.0	0.2	-
	SMR_{100}	7.0	0.5	0.35 (+1)
	SMR_{VDP}	6.0	0.4	0.39 (+1)
	$SMR_{VDP10\%}$	3.4	0.31	0.42 (+1)
	q_{LDP}	3.0	0.1	0.60 (0)
	q_{trac}	2.4	0.1	0.70 (0) †

The tracer subjected to climate model transport, as introduced in section 3.3, with dehydration sampling rate of once-in-20 minutes is also provided for UM10.4 as 10 °N–S zonal mean at 83 hPa (q_{trac}). It reports a very dry time mean, as discussed in section 3.3.2. It also reports a high value for explained variance of model water vapour at the same level, which suggests a good representation of the dehydration and transport of water vapour entering the stratosphere.

Seasonal aspects of controls on transport pathways have been studied extensively (Bannister et al., 2004; Bonazzola and Haynes, 2004; James et al., 2008; Kremser et al., 2009; Tissier and Legras, 2016; Wright et al., 2011). In particular, persistent strong convection over south east Asia forces a seasonal monsoon anticyclone which constrains pathways into the stratosphere, potentially providing air that has not experienced the lowest saturation limits and is therefore less dehydrated. For this region during northern hemisphere summer, the relative importance of constrained pathways and deep convection has been debated, as well

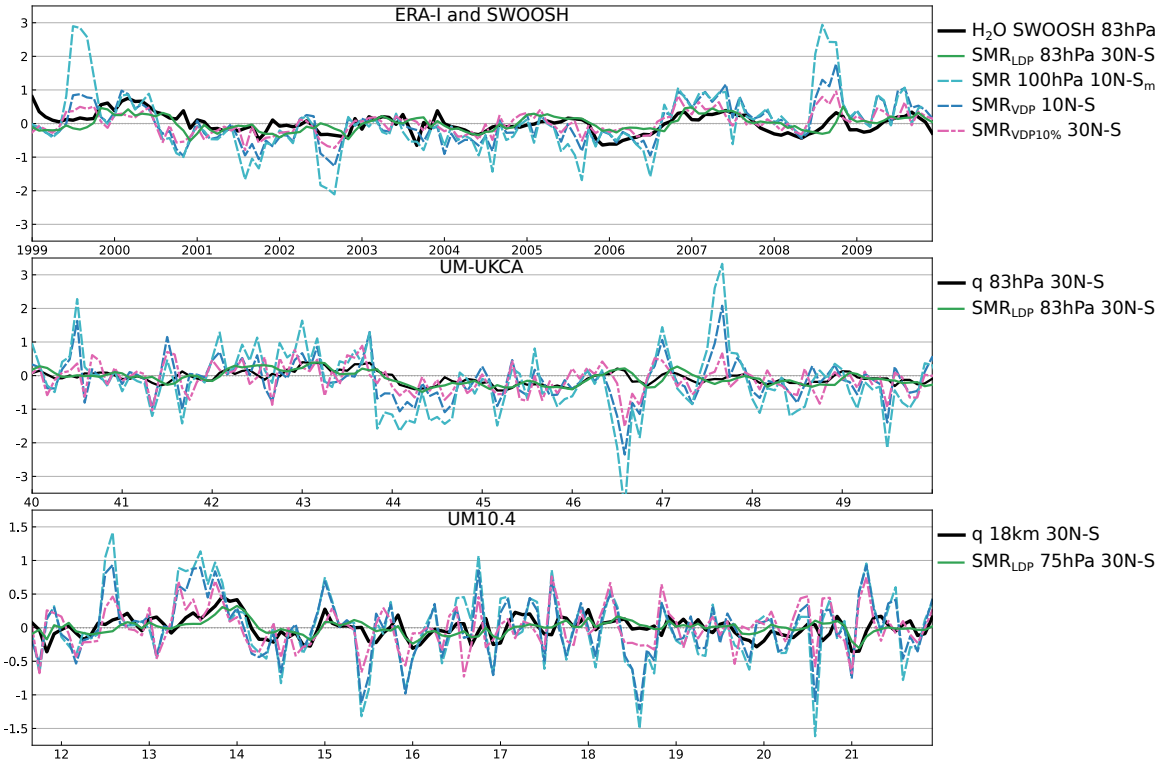

Fig. 4.2 Deseasonalised monthly mean timeseries of variables (ppmv) shown in table 4.1.

as their overall contribution to tropical stratospheric water vapour. In the specific case of the year 2000 water vapour drop, Hasebe and Noguchi (2016) indicate that rerouting this transport away from the east Indian ocean towards the west Pacific ocean contributed to the onset of the unusually dry stratosphere.

Interannual aspects of dynamical features including major sudden warmings, QBO and ENSO, have been studied in relation to temperature and vertical velocity changes (for example Konopka et al., 2016; Tao et al., 2015, 2019). However, the impact of pathways on interannual variability remains unclear.

4.2.1 Lagrangian calculation comparison

The comparison with observations above provides some further validation of the Lagrangian dry point method beyond section 3.2. This section, as additional validation and to demonstrate likeness with the method of Hasebe and Noguchi (2016), the Lagrangian dry point timeseries will be compared with their published calculations.

Hasebe and Noguchi (2016) calculate a Lagrangian prediction of H_2O_{strat} using the same reanalysis dataset (ERA-I) to drive temperatures and winds, and their back-trajectories

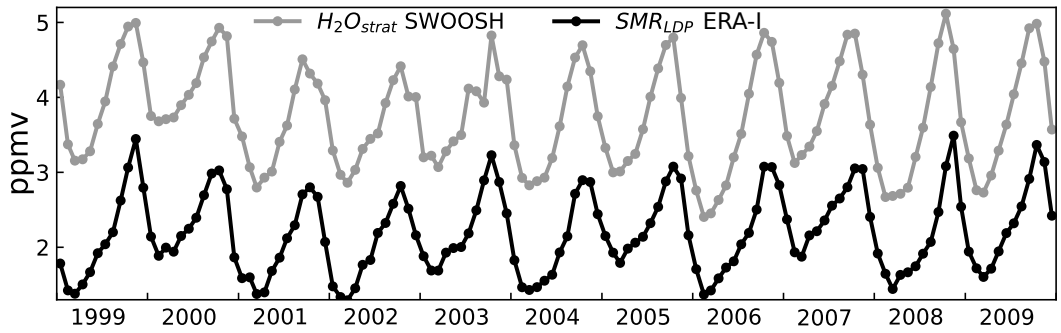

Fig. 4.3 Timeseries of monthly mean H_2O_{strat} from SWOOSH dataset and monthly Lagrangian dry point estimates, both for 83 hPa 30 °N–S.

are released similarly at 400 K every 5°×1.5° within 30 °N–S every month. Therefore, the 1999-2003 timeseries in their figure 3a is comparable to ERA-I driven results presented in the previous section, and whose timeseries is shown as the black line in figure 4.3.

Features in the timeseries are very similar (such as a wetter minimum in 2000, and consistently drier peaks in 1999, 2000, and 2001) and the minimum mixing ratios are also very similar ∼1.5–2.0 ppmv. The timing of the minima is in good agreement too.

One difference is the annual maxima in figure 4.3 are drier by ∼0.7–1.0 ppmv. In the figure of Hasebe and Noguchi (2016), the annual maxima are 3.5–4.5 ppmv, and in this study ∼2.8–3.5 ppmv. Because the seasonal peaks refer to a warm period, each trajectory's coldest event is more likely to be further back in its history. That Hasebe and Noguchi (2016) follow trajectories only for 90 days indicates that they may miss these older and colder events. Figure 4.4 shows the transit time from release height to LDP for trajectories recorded for 360 days being longer in the peak months near October. Indeed, the mean of the distribution exceeds 90 days at this time of year.

These peaks are sensitive to the persistence of trajectories in the tropical tropopause layer. Other differences in configuration may encourage longer transit times through this region in the configuration presented in this chapter. Hasebe and Noguchi (2016) interpolate wind and temperature fields onto 91 pressure levels, whereas this chapter's results use the ERA-I model (η) grid with 60 levels. The form of this interpolation may produce different winds in the TTL and affect the lifetime of trajectories in the TTL. There are other differences which may also contribute but appear to be minor (vertical level choice may affect phase of annual cycle, but phase is similar; kinematic instead of diabatic advection of trajectories has only a small impact, Liu et al. 2010).

In summary, the qualitative timeseries behaviour is very well captured, and many of the mixing ratios also agree. This provides confidence that the configuration of Lagrangian

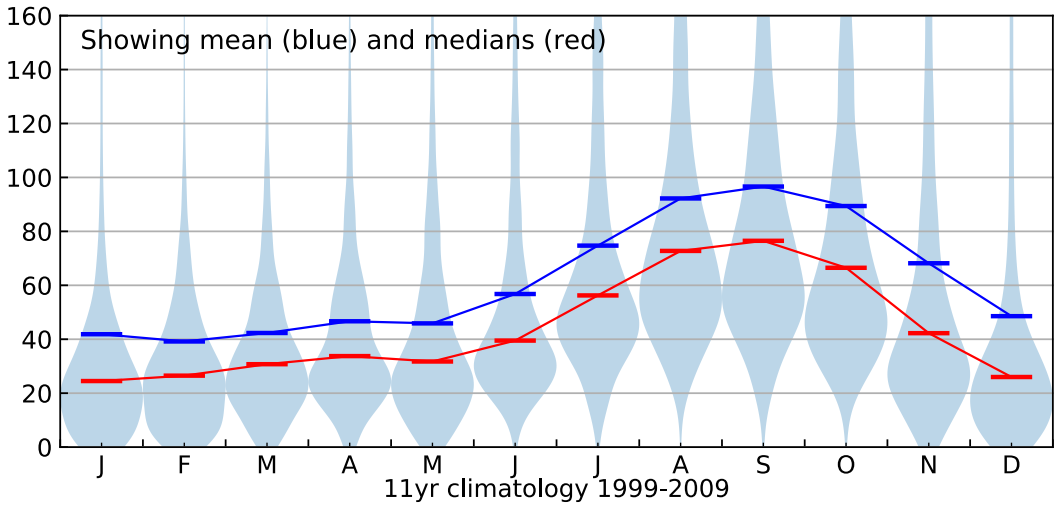

Fig. 4.4 Transit time from trajectory release (30 °N–S 83 hPa) to Lagrangian dry points for ERA-I diabatic back-trajectories, averaged across 1999-2009. This extends the results in the bottom panel of figure 3.2.

calculations in this thesis will provide results comparable to the study of Hasebe and Noguchi (2016).

4.3 Isolating temperature and transport influences

As introduced at the beginning of this chapter, certain case studies have suggested that pathways are influential in the final water abundance, such as the stratospheric water drop around year 2000 where Hasebe and Noguchi (2016) have indicated that the overall response is in part caused by a shift in transport pathways. The challenge for this particular case study is that there are changes in both transport pathways and temperature fields, and the relative importance of each has not been disentangled.

In this section, an experiment is presented to isolate the two effects of transport pathways and temperatures on Lagrangian calculations of H_2O_{strat} interannual variability. The method aims to resolve whether a feature of the water vapour timeseries would have occurred if the pathways encountered temperatures corresponding to a different year or a different month.

The first section will describe the experimental setup. Next, the year 2000 drop will be presented as a case study, thereby expanding on the conclusions of Hasebe and Noguchi (2016). Conclusions will then be made about the role of interannual variability of transport pathways in explaining variations in H_2O_{strat}.

4.3.1 Method

The basis of calculations in this chapter is the Lagrangian dry point method with back-trajectories as described in section 2.4. The usual approach with this method is for temperature and wind fields to vary concurrently. This experiment releases trajectories in the wind field and records time-offset temperature fields.

Winds and temperatures that are not concurrent will not be in thermal wind balance, and therefore do not provide a fully physical result. The interest here is on the impacts of experiencing a different temperature field on final dehydration locations and saturation mixing ratios for a given set of transport pathways. Some of the impacts may be seen as due to mis-matching physical fields, but the conclusions will be shown to be robust overall.

For the purposes of estimating stratospheric water vapour, the key calculation of saturation mixing ratio depends on pressure and temperature (equation (2.2)), which are each a function of position and time. Along one trajectory, assuming pressure is primarily a function of position, its record of saturation mixing ratio depends on position and temperature generally as:

$$SMR_{traj}(t_x, t_T) = f\left(\mathbf{x}_{traj}(t_x), T\left(\mathbf{x}_{traj}(t_x), t_T\right)\right) \tag{4.1}$$

where t_x is the time in the wind field (equivalently, the time of pathway initialisation) and t_T is the time in the temperature field. In this study the time period of 1999-2009 is applied to t_x and t_T.

The calculation of Lagrangian dry point is then a function of trajectory pathway and temperatures experienced. For all trajectories initialised at a given date, the ensemble mean of their Lagrangian dry points obtains $SMR_{LDP}(t_x, t_T)$.

This field with two time dimensions can be thought of as three separate experimental configurations. Simplified examples are shown in figure 4.5, and figure 4.6 shows corresponding initialisation times in a particular year for each of the three configurations:

1. Co-varying winds and temperature initialisation dates. Here, a trajectory set is initialised each month of the eleven year period. The winds and temperature fields are concurrent throughout (left-most case in figure 4.5, black points in figure 4.6). In this standard configuration, $t_x = t_T$.

2. Vary pathway initialisation dates, temperature initialisation dates from single year. Trajectories are initialised every month across the eleven years and the temperature

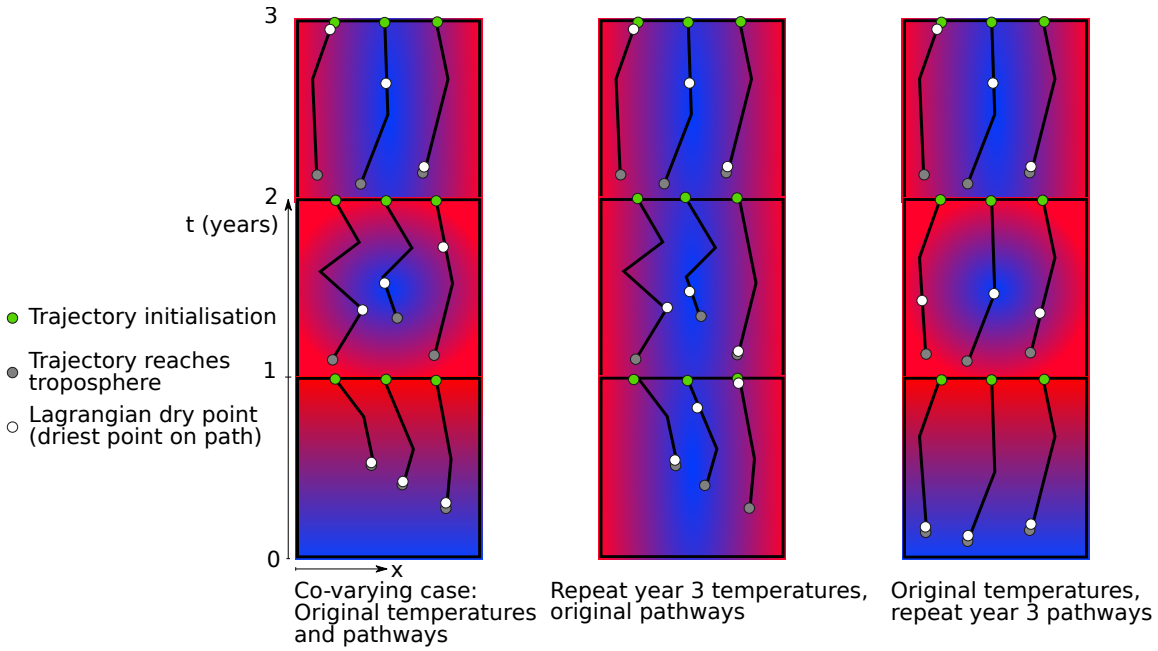

Fig. 4.5 Schematic of the three experiments carried out. In this schematic, there is one spatial dimension, and one initialisation date for three trajectories per year with maximum history record of one year. The black lines refer to pathways (calculated from winds) and the colour field refers to temperature distribution.

field they experience is always initialised within a single year (middle case, and light coloured points). Here, have $t_x = t_{T+N}$ where N is a multiple of months.

3. Pathway initialisation dates from single year, vary temperature initialisation dates. Here, trajectory sets are initialised each month of a single year. Each initialised set records their locations in multiple temperature fields which are offset by whole years (right-most case, and dark coloured points). Here, have $t_T = t_{x+N}$ where N is an integer in units of months.

This provides a way to study fixed pathways in a varying temperature field and then separately study varying pathways in a fixed temperature field. It should be made clear that in these experiments trajectories are always advected backwards in both wind and temperature fields for up to one year. The fields encountered by trajectories remain continuous as they always span the year prior to release date.

For these three configurations, N changes by integer years. In this way, the months of the year remain concurrent which keeps the strongest fluctuations in balance, from the annual cycle (as figure 4.1 shows). The results of these configurations therefore relate to interannual variability.

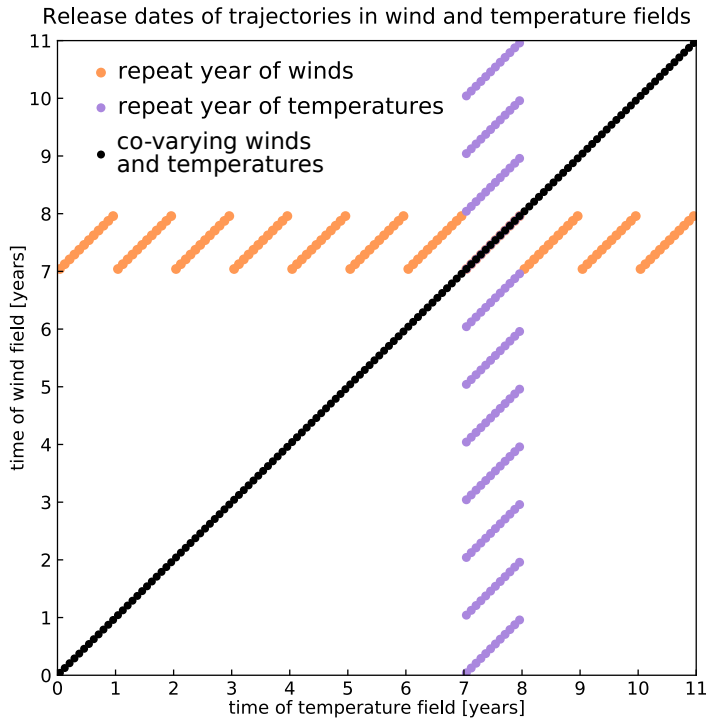

Fig. 4.6 Example dates in each of temperature and wind fields where the three timeseries configurations initialise trajectory sets. Note that for every initialisation, trajectories are advected backwards in both fields for one year.

The second formulation will vary N by integer months, so that the fixed field always initialises at the same date. This allows identification of the separate impacts of transport and temperatures over the annual cycle.

4.3.2 Results – reanalysis

The changes to variability of ERA-I Lagrangian dry points across the three sensitivity experiments are now analysed. First, the control of winds and temperatures around the year 2000 are presented. Second, the overall influences of variability across 1999-2009 are analysed. After this, variations in the overall results are discussed, first interannually and then seasonally.

Isolating variability around year 2000

Specific timeseries of Lagrangian dry point predictions of H_2O_{strat} are shown in figure 4.7, including the co-varying case (black line) and repeat winds and temperatures in years 1999, 2000 and 2001. The sudden drop reported in literature (Randel et al., 2006) is more clearly

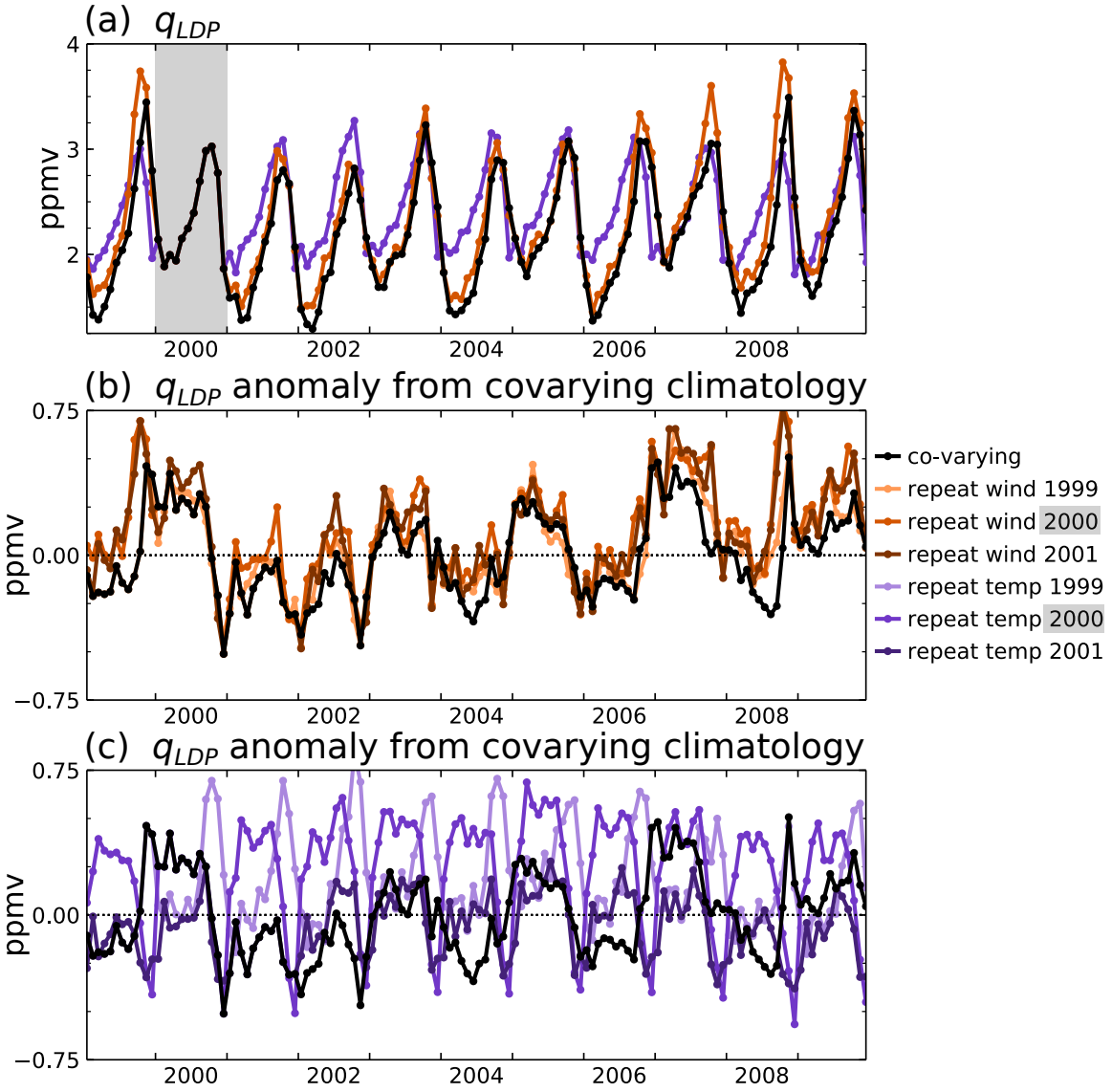

Fig. 4.7 Timeseries of ERA-I Lagrangian predictions of H_2O_{strat} for different cases as introduced in figure 4.6. (a) Ensemble mean Lagrangian dry point prediction for monthly releases of co-varying winds and temperatures (black), repeat wind (orange) and repeat temperatures (purple) of year 2000. (b,c) Anomaly from climatological annual cycle of co-varying case for the same cases and for 1999 and 2001.

seen in figure 4.7b and c where the average annual cycle of the co-varying timeseries is removed. For any year of pathways experiencing year 2000 temperatures (orange lines in figure 4.7), the drying event is seen. Conversely, repeating any year of temperatures other than 2000 (purple lines) generally lacks this event along with the rest of the interannual variability.

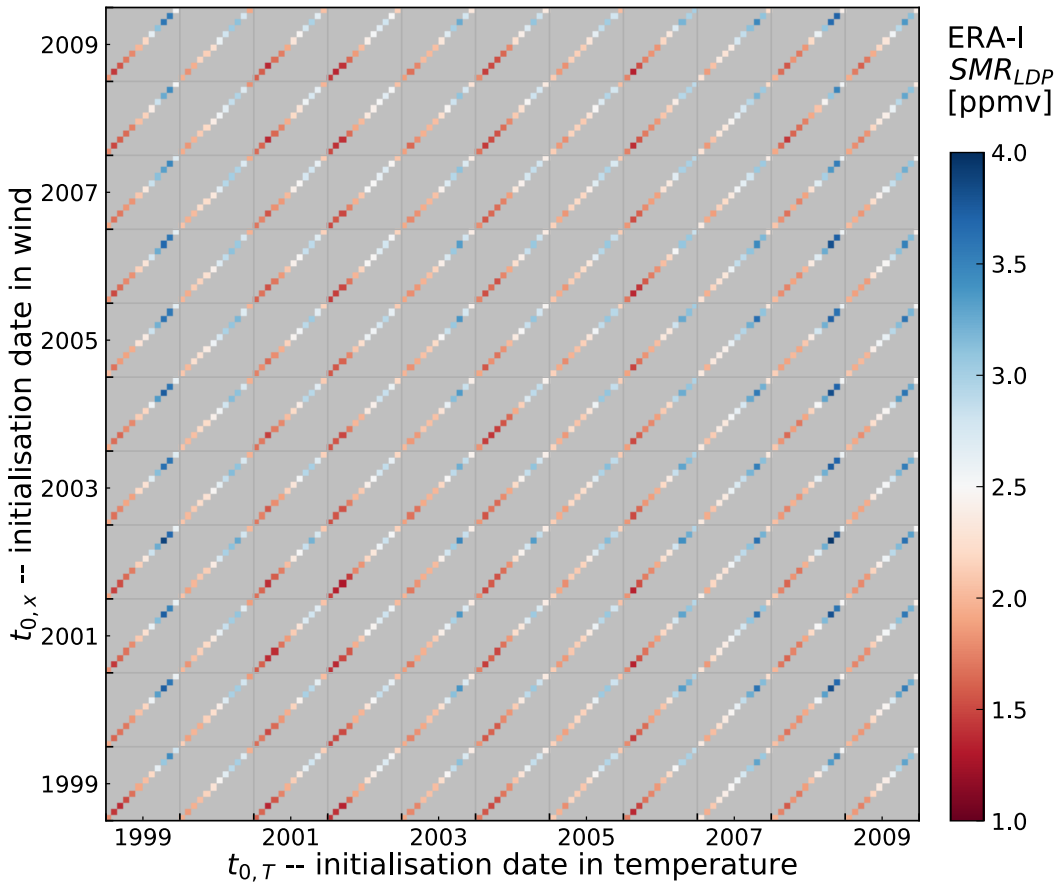

Fig. 4.8 All ERA-I Lagrangian dry point predictions of H_2O_{strat} for different combinations of initialisation date in wind and temperature fields, including those shown in figure 4.7a, illustrated by figure 4.6.

These results explicitly show that the temperatures encountered in 2000 cause the drop in H_2O_{strat}. The pathways associated with the event are not unusual compared to the same season in other years.

While the interannual variability is lost in experiments that repeat temperature and allow winds to vary (note that figure 4.7c is a difference from climatology), they exhibit a new seasonality, resembling the year of temperatures being repeated.

Interannual variability

The above results are now extended to every monthly release date combination between 1999 and 2009, the results are shown in figure 4.8. Results from figure 4.7a are contained in this figure, as described by figure 4.6. As was seen for the year 2000 case in figure 4.7, commonalities are more apparent for a given release date in temperature, indicating that

Table 4.2 Correlations of diabatic ERA-I cases in the period 1999-2009, and two cases of UM-UKCA repeat year 2000. They are calculated with each monthly mean timeseries with its climatological annual cycle removed.

	R^2		
correlatand correlator Repeat releases in	repeat u co-varying T	repeat T co-varying u	repeat u repeat T
1999	88%	6%	0%
2000	71%	1%	1%
2001	75%	13%	1%
2002	72%	13%	2%
2003	71%	0%	5%
2004	74%	12%	1%
2005	67%	1%	3%
2006	70%	4%	1%
2007	74%	2%	9%
2008	88%	4%	0%
2009	75%	1%	1%
UM-UKCA yr3	81%	1%	0%
UM-UKCA yr8	85%	3%	7%

temperature is consistently the key driver of H_2O_{strat} interannual variability. Regardless of which year is chosen, the repeat temperature case does not correlate with the co-varying case and has relatively little interannual variability. However, the cases with repeat winds correlate well with the co-varying case, capturing most of the characteristic variations.

Table 4.2 shows correlation values between the three cases confirming the general indifference of stratospheric water vapour variability to interannual variations in transport pathways. This is despite substantial interannual variation in the upwelling of the Brewer-Dobson circulation, and age of air spectrum, in the tropical tropopause (Abalos et al., 2012; Ploeger and Birner, 2016).

The overall findings can be simplified by averaging along one particular timeseries, resulting in figure 4.9a. Indeed, averaging over wind dates (that is, retaining temperature variability, purple line) leaves a similar pattern of interannual variability to the co-varying case and it has very little standard deviation between different years. Meanwhile, averaging over temperature release dates (orange line) has little interannual variability remaining and a larger standard deviation, which probably resembles the average annual cycle of the co-varying case.

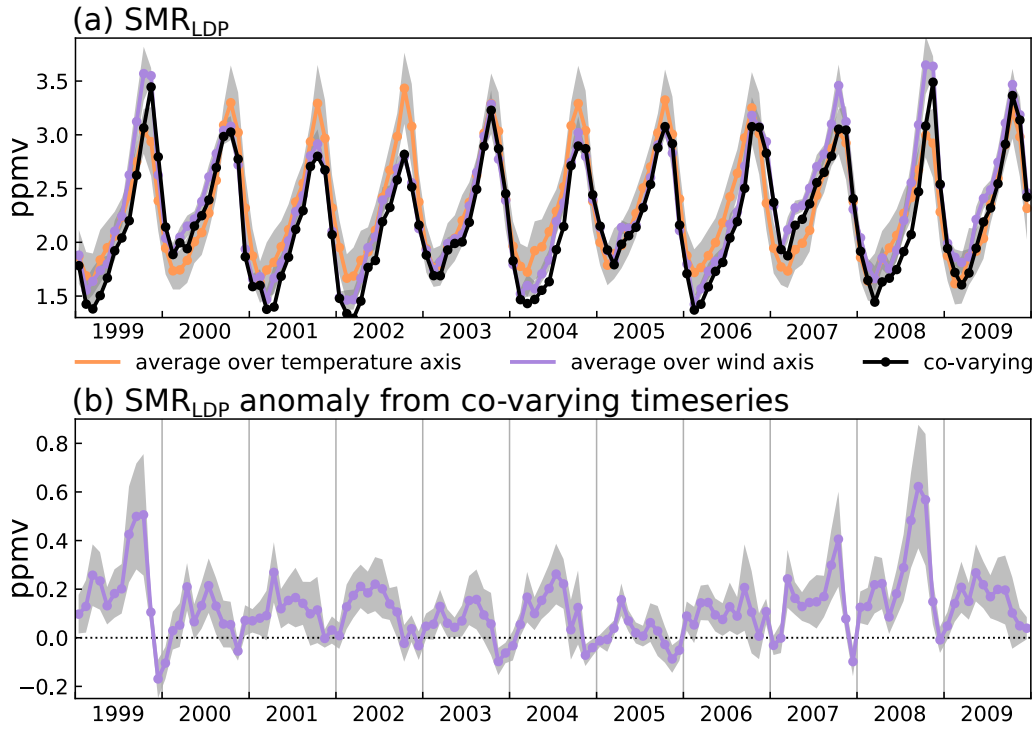

Fig. 4.9 (a) Timeseries of all trajectory releases, co-varying case (black) and repeat-wind cases averaged according to temperature time axis (orange line) and repeat-temperature cases averaged along wind time axis (purple), and their standard deviations (grey shading). Equivalent to averaging across one of the time axes in figure 4.8. In that sense, they are essentially the climatological annual cycle for each repeat year case. (b) Anomaly from co-varying case. Equivalently, this is average over wind timeseries in figure 4.10. This identifies a measure of efficiency across repeat-temperature cases.

General inefficiency and interannual variations in temperature control

If temperatures are the sole control of interannual variability, the particular choice of wind pattern would be expected to be inconsequential. If so, in figure 4.9 the purple and black lines would match exactly. However, there are discrepancies and they are nearly always positive (wetter). For clarity, the differences between the co-varying and repeat temperature cases averaged over t_x are shown in figure 4.9b. Any differences are due to the winds being more or less capable of sampling the lowest temperatures encountered. A wetter result means fewer encounters of cold events, and is therefore considered less efficient. It can be seen from figure 4.9b that the two least efficient time periods are August-October months of 1999 and 2008 (anomaly of $\sim$0.5–0.6($\pm$0.2)ppmv).

For the same conclusion of temperatures being the only control, choice of a single year of wind pathways across the temperature timeseries would be expected to also obtain the

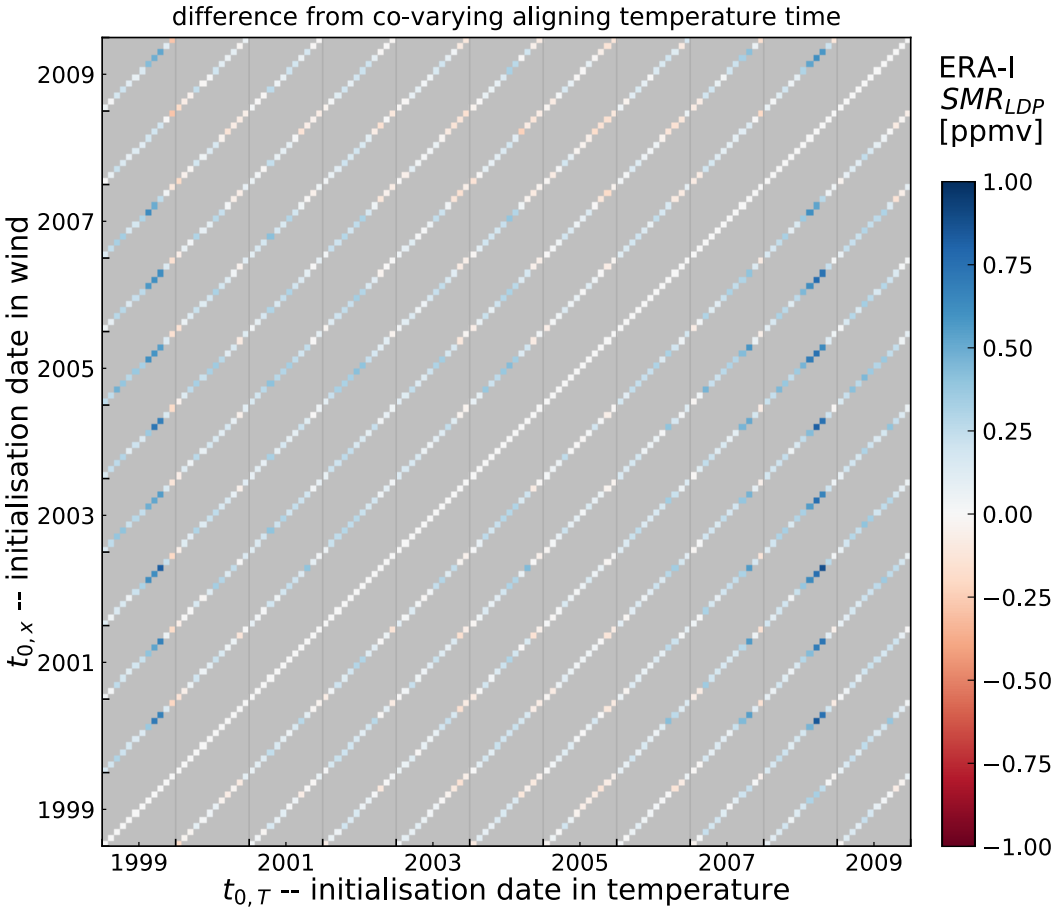

Fig. 4.10 All ERA-I Lagrangian dry point predictions for different combinations of initialisation date in wind and temperature fields, subtracting co-varying value aligned with temperature time axis. This identifies a measure of efficiency across all repeat wind timeseries.

original pattern of variability. However, as the orange line in figure 4.7a shows, this is not exactly so. The differences between orange and black lines in figure 4.7b for each choice of repeating wind field is shown in figure 4.10. Again, there are discrepancies and they are nearly always positive (wetter). Two exceptions appear to be for wind fields of summer-autumn 1999 and 2008, which show more efficient dehydration than the respective co-varying cases. The summer-autumn period of 1999 and 2008 also experienced relatively warmer temperatures than the climatological annual cycle peak in tropopause temperatures. Paired with the inefficient repeat-temperatures timeseries discussed above, this points to relatively efficient pathways occurring at these times. Particularly because in the co-varying timeseries they are anomalously wet and warm years, sampling efficiency is more important

in these years. It appears that, if experiencing the temperatures of other years, these pathways remain relatively efficient.

Both of these years are straddled by La Niña winters (based on winter El-Niño indices reported by Domeisen et al., 2019) which displace the tropopause cold pool eastwards (Konopka et al., 2016). However, horizontal sampling is usually not a limiting factor in the tropical tropopause (Holton and Gettelman, 2001). Furthermore, as the clearest constraint on horizontal advection, and given the timing of these discrepancies in autumn where transit time from final dehydration has been ∼2–3 months figure 4.4, the Asian summer monsoon is most likely involved. Hasebe and Noguchi (2016) identify an anomalously strong monsoon anticyclone in 1998 and 1999. Therefore there may be some involvement of monsoon strength and pathway variability on interannual timescales. A temporal or spatial shift in the monsoon anticyclone could also be a factor. Further work might clarify this over a longer timeseries with more examples of outstanding years of pathway control.

There also appears to be an ongoing inefficiency in both cases (2000-2007) which point to the impact of mis-matching winds and temperatures, considered to be a residual effect from loss of thermal wind balance (∼0.25 ppmv in figure 4.9b) in the H_2O_{strat} estimates.

This section has identified the general control of temperatures on interannual variability of Lagrangian dry point predictions of H_2O_{strat}. By investigating the discrepancies, there are some events of opposing efficiency (1999 and 2008) which hint at some interannual variability to the relative roles of wind and temperature. Additionally, an underlying inefficiency is seen which indicates the impact of mis-matching winds and temperatures.

Seasonal variability

The annual cycle variability can also be removed by repeating releases from a single month. The seasonal cycle comprises a variation in temperatures at the tropical tropopause, as seen in earlier results (for example, figure 3.2 middle panel). There is also some variation in the strength of vertical upwelling which is weakest around June-August (figures 4 and 6 of Seviour et al., 2012). Variation in the height of the tropopause cold point, which is lowest in July-September (figure 5b of Kim and Son, 2012, showing pressure variation), will be captured in the seasonality of temperature in this experiment.

To test the corresponding impact through transport and temperatures on H_2O_{strat}, trajectories are initialised every month across 1999-2009 (inclusive) in the temperature field, and in the wind field the release date is fixed to one of four values: t_x = 1st Feb 2004, 1st May 2004, 1st Aug 2004, 1st Nov 2004. The same fixed release dates are then applied to the temperature field, t_T. The estimates from each combination of release dates in wind and

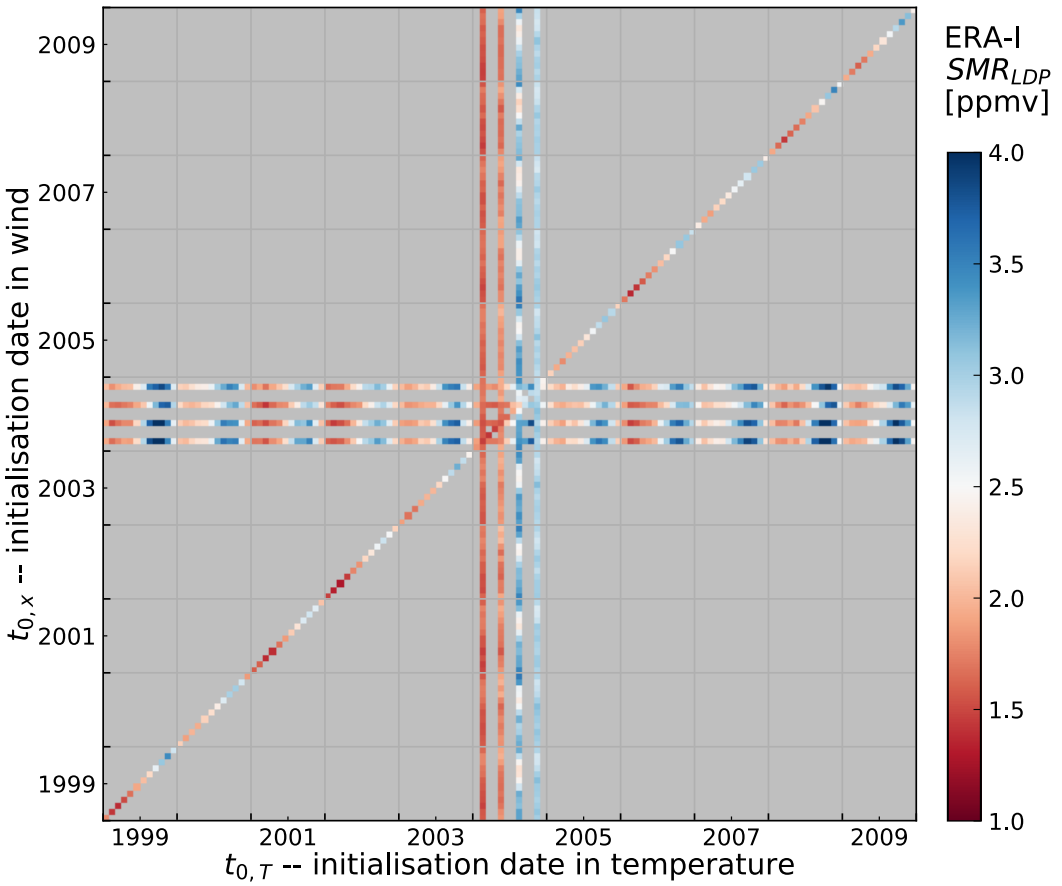

Fig. 4.11 Calculated ERA-I 1999-2009 cases with repeat-month releases of February, May, August and November 2004.

temperature fields are shown in figure 4.11, along with the co-varying case (one-to-one line) as shown earlier.

Very distinct patterns result when fixing the seasonality of transport and temperatures. For the case of fixed wind patterns, all of the conclusions of interannual variability remain. In addition, an annual cycle is still observed, as is expected because of the dominance of temperatures. Also, the results are generally wetter because of the lower efficiency of mis-matched wind and temperature fields.

For initialisation dates of the wind field fixed to August, the timing of the annual maximum is somewhat delayed compared to the co-varying case. This can be explained by slower vertical transport in this month. A similar delay may be lacking at the annual minimum (February) because temperatures are generally colder and higher in altitude, and therefore vertical transport rates do not exert as much influence.

For the case of temperature field initialisation fixed to the months of February, May and November, the annual cycle is lost. This points to the sole control of temperature at these times of the year.

For trajectories whose temperature field is always initialised in August, however, a different seasonality emerges. With a minimum across summer months, and maximum in winter, this must be caused by differences in transport. Particularly, because the first months following August are warmest and therefore favouring drier predictions from longer-residing trajectories, the drier H_2O_{strat} at this time of year with slowest upwelling must be due to spatial sampling differences. This lack of control of tropical cold point temperatures in the summer has been noted in observations. For example, Randel and Jensen (2013) focus on interannual variability, but point out the seasonal differences in their figure 5, where 1992-2012 seasonal means from HALOE, MLS and GPS radio occultation records are used with a lag of one season. The findings here identify the same conclusion in the Lagrangian dry point method, attributing the difference to seasonal influence of transport pathways.

Changes to Lagrangian dry point distribution

Since the Lagrangian dry point prediction of H_2O_{strat} has changed as a consequence of the different sampling of wind and temperature fields, it raises the question of what other ways they differ.

First, do predictions that are wetter than the co-varying case correspond to longer or shorter transit times? Figure 4.4 gives an indication of the transit time distribution and its seasonality. Figure 4.12 shows the distribution of changes to transit times of each trajectory in the repeat year 2000 cases relative to the co-varying case (excluding the year 2000 where results are identical). First of all, the shapes of the distributions are very different. The repeat year 2000 winds trajectories (a) show a broad distribution of transit time changes, only 1.2 % are unchanged, whereas the repeat year 2000 temperatures (b) shows a narrower and stronger peak at zero, indicating most Lagrangian dry points move very little. In fact, 5.0 % of them are unchanged. These contrasting distributions might be expected because pathways are modified by repeat winds and not by repeat temperatures. By repeating temperatures, only the timing of the saturation minimum along the pathway might be modified.

Still, the high percentage of unchanged repeat-temperature Lagrangian dry point times is surprising. Figure 4.12c shows the timing of the Lagrangian dry point events that are unchanged from the co-varying case. For repeat winds, it is the earliest timesteps that are unchanged, before pathways diverge substantially. For repeat temperatures, it is throughout the transit time spectrum because the pathways are the same and therefore the timing of

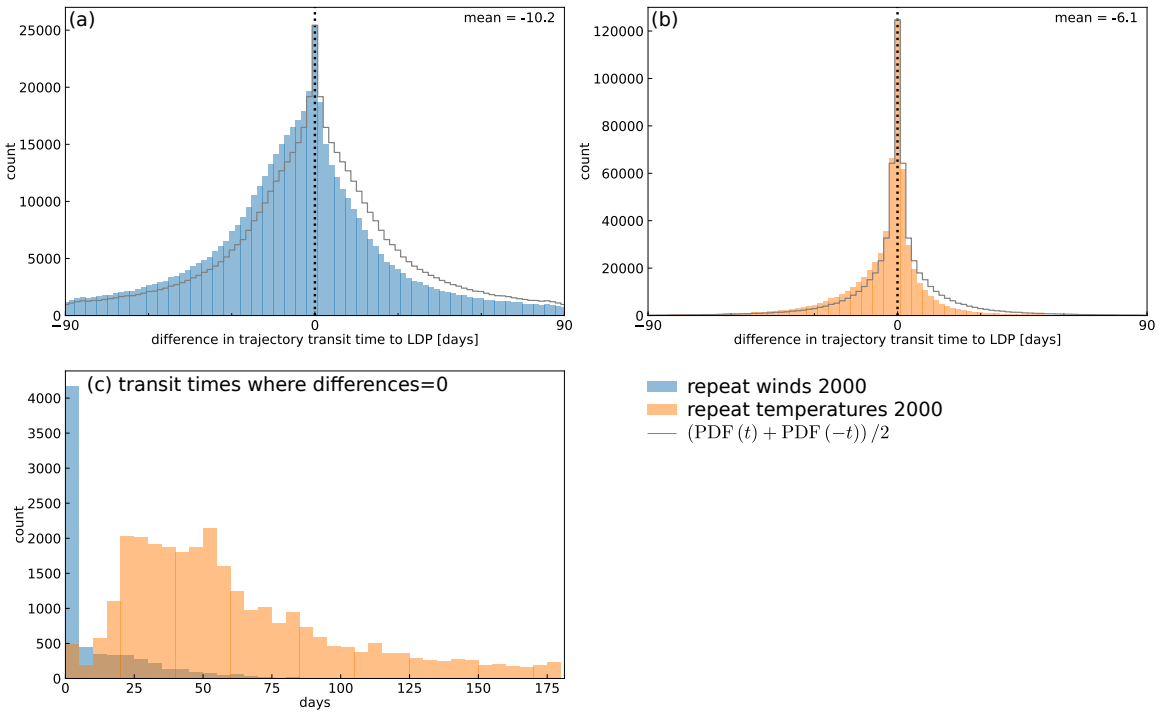

Fig. 4.12 Distribution of trajectory transit times to Lagrangian dry points. (a) Repeat winds 2000 difference from co-varying case. (b) Repeat temperatures 2000 difference from co-varying case. Year 2000 trajectories are identical and are therefore excluded from the comparison across 1999–2009. The grey line shows the distribution's modulus for a symmetric representation. Note the different vertical scales. Both mean differences of -10.2 and -6.4 days are significant at the 0.1 % level (using a two-sample t-test, von Storch and Zwiers, 1999, Section 6.6.5). (c) Distribution of transit times to Lagrangian dry points for the repeat year 2000 trajectories which are unchanged from their co-varying case (difference $= 0$ in a, b). Showing first 180 days only.

encounters with particular spatial regions (for example, the west Pacific cold pool) are unaffected.

Both distributions show a general shift to earlier times in figure 4.12. The timeseries repeating year 2000 winds (a) shows an average change of -10.2 day across the 10 years, while the timeseries repeating year 2000 temperatures (b) shows a change of -6.1 days. The generally shorter transit times may be associated with the general inefficiency of dehydration for both cases compared to the original timeseries.

Compositing spatial distributions for the anomalously inefficient dates in 1999 and 2008 temperatures highlights any differences from the distribution of co-varying trajectories, see figure 4.13b. Generally, there is a reduction over the Indian ocean and maritime continent combined with an increase near the subtropical regions of Australia and south east Asia.

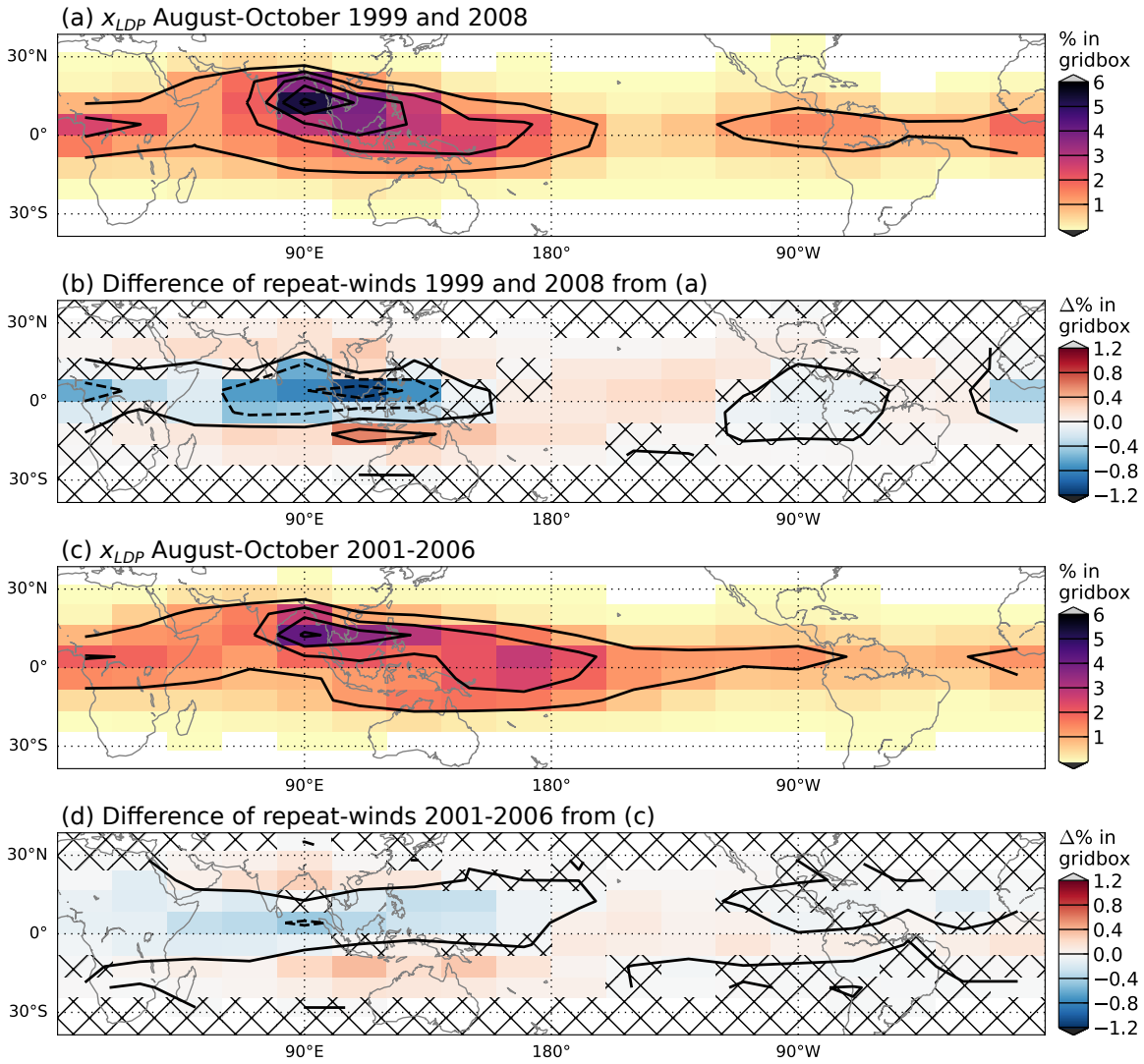

Fig. 4.13 Distribution of Lagrangian dry point locations (a,c) and their differences (b,d) from co-varying case for (a,b) anomalously inefficient months in 1999 and 2008, and (c,d) background inefficient months in 2001-2006. The same months August, September and October across the 11 year are used. Units are percentage of total LDP events. Hatching indicates either no events occurred or that difference is not statistically significant at 1 % level according to a binomial approximation of the two-sample t-test, as described in Hasebe and Noguchi (2016).

The maritime continent is a region of strong fluctuations at short timescale (see figure 3.19 and figure 3.20) associated with convective activity. The mis-match of temperatures and velocities may prevent trajectories from correctly resolving the lowest temperatures in this quickly fluctuating region. At the same time, the coldest temperatures (and most frequent Lagrangian dry points) are located at these subtropical locations. Therefore, this change

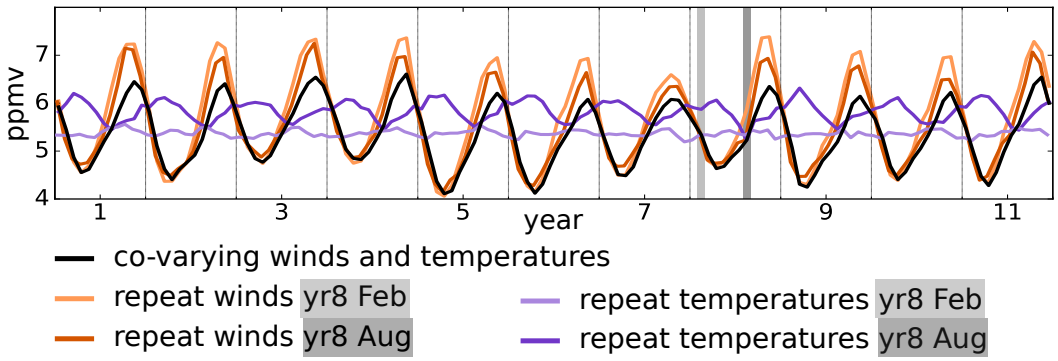

Fig. 4.14 UM-UKCA cases removing seasonal variability.

equates to a redistribution of Lagrangian dry points away from a region of strong variability at short timescales to regions of consistently low temperatures.

Figure 4.13d is constructed in the same way as figure 4.13b, but for the years 2001-2006. The figure shows there are similar but weaker patterns associated with background inefficiency. The poor strength of the pattern may be caused by the larger time period being averaged over, but requires further investigation.

4.3.3 Results – chemistry climate model

The experiment has also been conducted briefly in UM-UKCA. This provides insight to model representation of influences on q. Table 4.2 shows some of the relevant correlations. There is a similar relationship, the interannual variability of the wind field is not required to explain the variability of the Lagrangian prediction for H_2O_{strat}.

In figure 4.14 the seasonal variability is also removed by repeating releases from a single month for a couple of cases in the chemistry climate model. As for reanalysis in figure 4.11, repeat pathways shows similar interannual variability while the repeat temperatures case loses it, except for repeat temperatures starting in August which show an out of phase annual cycle.

This confirms that temperatures dominate both the seasonal and interannual variability of H_2O_{strat} in UM-UKCA, as found for ERA-I.

4.3.4 Discussion

The results show that the interannual variability of tropical lower stratospheric water vapour can be accurately predicted by Lagrangian calculations with winds fixed to any single year. However, it is clear that decoupling temperatures and winds will lead to thermodynamic

imbalance. This makes the conclusion all the more interesting, that the balance along trajectories is not needed to explain most of the interannual variability in H_2O_{strat} on the large-scale.

This conclusion is unlikely to apply for small-scale differences. The effect of imbalanced winds and temperatures should be more obvious when distinguishing fine-scale features. For example, where strong eddy heat flux enhances upward transport and adiabatic cooling concurrently. Stronger vertical advection will also cause shorter residence times in the TTL and therefore less efficient sampling (Fueglistaler et al., 2014). This is an essential aspect of the Brewer-Dobson circulation in the tropical tropopause region. Replacing the winds or temperatures at this time would distort the effect, either vertical transport strength or encountered temperatures would be inconsistent. Further investigation might compare eddy heat flux variability with departures of the repeat-temperature and repeat-wind trajectories.

Interestingly, in figure 4.9a, averaging along the time axis for temperature (thereby retaining only wind variability, orange line) does leave some years looking wetter than others, seemingly opposite to when averaging over the time axis for wind (purple line). Perhaps this is a sign of the opposition of temperature and vertical advection on the large-scale. Confirmation may be sought with a longer timeseries.

The impact of mis-matching winds and temperatures is seen more generally in repeat-month figures (figure 4.11) as a relative inefficiency in dehydration. Across the 1999-2009 timeseries, the repeat-wind experiments produce Lagrangian dry point water vapour concentrations that are generally higher than in the co-varying case. The repeat-month case also demonstrates that the loss of efficiency is sufficiently small that the conclusion is unaffected.

There is seasonality in the transit time from Lagrangian dry point events to 83 hPa release level. It is neatly described by figure 4.4 where in summer average transit times are longer. Earlier studies (for example Bergman et al., 2012) associate this with longer residence time due to slower Brewer-Dobson circulation. The aspect of changes to seasonality of transit time has not been investigated here. However, the seasonal importance of wind patterns reflects on this seasonality. There are two competing reasons for longer transit times: a warm season enables relatively cooler temperatures to be experienced further along a trajectory history, and secondly longer residence time in the tropical tropopause layer. The findings here support the involvement of the second explanation, which will be retained in repeat-wind timeseries. Acting together, these also reduce the amplitude (peak) of the annual cycle of H_2O_{strat}.

Normally, 10 years are insufficient for studying interannual variability in the tropical tropopause layer due to the large variability in underlying processes. Indeed, a detailed investigation of low frequency phenomena like ENSO and QBO cannot be made here. However, the conclusions described above, supported by strong and contrasting correlations, appear to be well resolved in this timeseries.

This analysis has considered only one reanalysis dataset. Tao et al. (2019) have used multi-variable regression of Fourier components of H_2O_{strat} timeseries from a domain-filling Lagrangian full chemistry transport model (CLaMS). They have compared findings from the reanalysis products ERA-I, MERRA-2 and JRA. They have considered the representation of annual cycle and QBO to be close between the reanalyses, and responses to volcanic aerosol and ENSO to be consistent but of different magnitudes. They have advised the study of multiple reanalyses for longer-term variability and trends. Their results provide some confidence of the finding in this chapter for the separated roles of temperature and large-scale transport on seasonal and interannual timescales, as well as the similar result seen in UM-UKCA. However, the results of this chapter may need to be tested in other reanalysis datasets before confirming the general effect..

Implications for model development can also be drawn from this work. There is general agreement in findings between the reanalysis and chemistry climate model tested. This again reassures that variability in temperatures and winds determine H_2O_{strat} for both cases. It also points to the variability of temperatures as the priority for improved representation of interannual variability. For seasonal variability the influence of the Asian monsoon, and seasonal convection patterns are important.

Year 2000 water vapour drop

It is interesting to test specific events against the above conclusion that interannual variability of pathways is not needed to capture stratospheric water vapour variability. Can the contribution of the pathways and temperatures of a specific event be separately identified in the predicted response of stratospheric water vapour?

The method discussed above may isolate the influences on individual events in time, for example a sudden rise or drop in the water vapour field. Some events have been studied in the literature. In one instance, Hasebe and Noguchi (2016) show differences in spatial and H_2O distributions of LDP events from before and after the year 2000 water vapour drop, which is visible in the co-varying timeseries in figure 4.7a and figure 4.7b. Studies have associated this event with a coincidence of QBO phase change to easterly, ENSO index change to La Niña, and stronger Brewer-Dobson circulation all acting to cool the tropical

tropopause (Brinkop et al., 2016; Dhomse et al., 2008; Randel et al., 2006). Hasebe and Noguchi (2016) suggest the connection to water vapour is through changes to the circulation and temperature field, affecting both transport pathways and Lagrangian temperatures. The experiments performed here have clarified their explanations by separating the sensitivity to pathway and temperature fields at this time.

The deseasonalised timeseries of figure 4.7 show that when winds are repeated from any year of 1999, 2000, 2001, the drop in the year 2000 is still captured. However, when temperatures are repeated the timeseries no longer shows the step-wise drop. This extends across the 1999-2009 years in figure 4.8. Therefore, any changes in pathways occurring at that time of year are not particular to the resulting drying. Findings here suggest they represent a seasonal shift and contribute to the resulting sampled temperatures, but not unusually so.

Of course changes to the wind field may have played a driving role in the changes to temperature. This coupling is not accounted for in the experiments here, where the reanalysis temperature field is externally prescribed.

4.4 Conclusions

A novel method was applied in this chapter to isolate variability of temperatures and transport on Lagrangian predictions of H_2O_{strat}. The method was applied to ERA-I and to UM-UKCA. When retaining only the annual variability of the wind field (from any one year), the interannual variability of temperature explains 67–88 % of the interannual variability of the Lagrangian estimate for H_2O_{strat}. Conversely, retaining only the annual variability of temperatures, interannual variability in transport pathways explains 0–13 % of the interannual variability of the Lagrangian estimate for H_2O_{strat}. The strong control of temperatures in both ERA-I reanalysis and in UM-UKCA chemistry climate model agrees with earlier studies (Fueglistaler and Haynes, 2005). For interannual variability of H_2O_{strat}, wind variations are found not to be important generally. The same conclusion is reached for individual events like the year 2000 drop in water vapour, in contrast to the results of Hasebe and Noguchi (2016). In the studied timeseries of 1999-2009, two periods indicated significant differences in transport. The trajectory pathways corresponding to the summers of 1999 and 2008 exhibited transport pathways that were more efficient than in the same months of other years.

There is a clear seasonal influence of winds which is strongest in summer months, in agreement with studies that have focused on the Asian summer monsoon.

The physical imbalance between temperature and winds is a limitation of these conclusions, but it is not needed to describe H_2O_{strat} interannual variability on the large scale. Its impact at other scales has yet to be investigated.

The results suggest Lagrangian studies of interannual variability of H_2O_{strat} may decouple winds and temperatures: provided a typical year of Lagrangian pathways is calculated, only temperature variability is needed to describe the majority of H_2O_{strat} variations.

It is also apparent that advection and condensation alone do not describe all physical processes modifying water vapour in an air parcel. This chapter explored the fundamental roles of temperature and transport on H_2O_{strat} variability. With this clearer, the role of modifying processes such as ice and convection on H_2O_{strat} climatology, interannual variability and trends will be questioned next.

Chapter 5

The role of ice

5.1 Introduction

Chapters 3 and 4 showed that variability of stratospheric water vapour in global climate models on seasonal to interannual timescales is well described by the advection-condensation method. However, its instantaneous dehydration approximation only represents deposition and assumes ice sediments immediately. Therefore, it lacks any representation of rehydration from ice sublimation which may come from two sources. One is in-situ ice that has arrived by advection or earlier deposition, the other is lifting in convective updraughts from the humid troposphere (hereafter convective injection).

The interaction of ice with water vapour in the lower stratosphere is a crucial uncertainty for accurately predicting future trends. A general consensus has been reached that the vertical dry point is occasionally surpassed by convection (Fueglistaler et al., 2009, and references therein). These events alter the radiative balance and transport ice into the tropical tropopause layer.

However the fate of this ice in the tropical lower stratosphere is unclear, with a wealth of observation campaigns not yet providing an agreed overall view (Corti et al., 2008; Danielsen, 1993; Kim et al., 2018; Rolf et al., 2018; Rollins et al., 2016; Sherwood and Dessler, 2000; Thornberry et al., 2017). Ice nuclei may be a sink or source of water vapour, depending on local saturation level (Jensen et al., 2007). At the same time, the radiative and thermodynamic effects of deep convection are to cause local cooling which lower the saturation (for example, Kim et al., 2018). Modelling studies have also not found consensus on the overall effect from convectively injected ice (Avery et al., 2017; Dessler et al., 2007; Dion et al., 2019; Jensen and Pfister, 2004; Jensen et al., 2018; Khaykin et al., 2009; Schoeberl and Dessler, 2011; Schoeberl et al., 2019; Ueyama et al., 2018, 2015). Therefore, a key challenge is to

uncover the conversion rate of lofted ice to vapour, thereby determining how convective injection impacts water vapour abundance above the tropopause. In particular, without this understanding, future projections of H_2O_{strat} remain uncertain.

While global observations are limited to large-scale measurements of water phase quantities, global climate models provide full moisture budgets based on their physical schemes. This provides a precise testing ground to understand how the presence of ice modifies predictors of H_2O_{strat}.

In this chapter, the full model water budget will be assessed in the tropical tropopause region (section 5.3). Upon confirming the presence of ice and sublimation above the tropical tropopause in section 5.4, Lagrangian methods incorporating rehydration will be compared in section 5.5. How the incorporation of ice modifies Lagrangian estimates of H_2O_{strat} climatology and interannual variability from earlier chapters will also be clarified. Spatial analysis of the relevant fields will yield clues about what makes a suitable indicator of ice modification for the advection-condensation method.

This will provide a more complete water budget in Lagrangian calculations of model H_2O_{strat}, which will be used to analyse climate models trends in chapter 6.

5.2 Water budget calculations in a global climate model

The next sections of this chapter will introduce and analyse the individual contributions from different schemes within the UM10.4 global climate model to changes in water. First, it is necessary to clarify some details of the computation of the water vapour budget before analysing the outcome in simulation.

Analysing full water budgets of a global climate model requires knowledge of how physical processes are represented by the model schemes. These are described in this section. Water vapour, being a field whose evolution depends on its value at the last model timestep, is referred to as a prognostic variable. Other prognostic variables include winds, temperature, ice concentration, and ice cloud fraction per gridbox.

As in most global climate models, water in UM10.4 is partitioned into vapour, liquid water and ice (strictly, the types of water suspended in air are vapour, cloud liquid condensate and cloud ice condensate). In the tropical tropopause layer, vapour and ice form the complete water budget. It is too cold for liquid water to exist, and therefore liquid water is not considered further. The key processes are then the net change of phase from ice to vapour (sublimation), its opposite (deposition), convective injection of ice and sedimentation (fallout) of ice. Advection is also important, and this brings with it a correction parameter in its

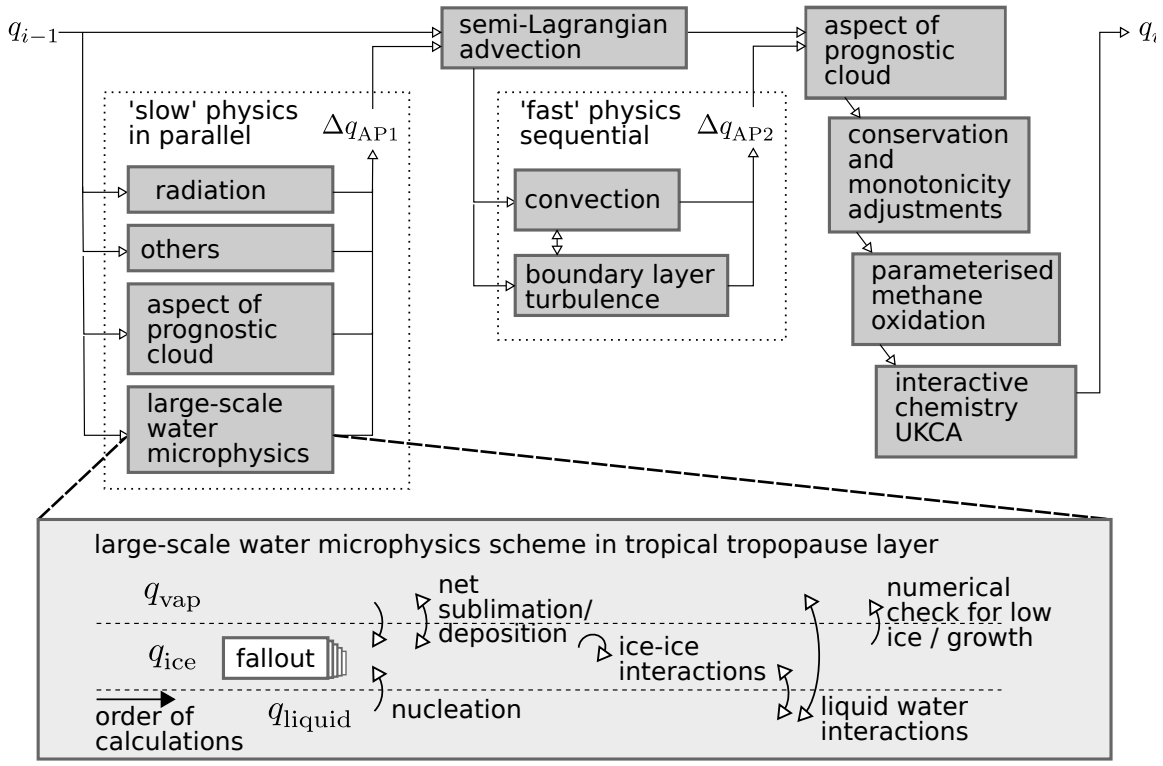

Fig. 5.1 Schematic of processes and their order in the UM10.4 timestep. Adapted from Wilson et al. (2008).

interpolation scheme. The correction tests for monotonicity (to reduce oscillations of field gradients near the grid scale), and mass conservation. Any losses of mass or monotonicity are minimised by choosing lower order interpolation. The other UM10.4 schemes are found to make little or no contribution in the region of interest (17–18 km in the tropics).

5.2.1 Order of schemes in timestep

The order of scheme calculations, and details of contained processes that affect ice and water vapour above the troposphere, are shown in figure 5.1. The UM10.4 equation to calculate a prognostic field at timestep *i* can be written as:

$$q_i = D\left[q_{i-1} + \Delta q_{\mathrm{AP1},i-1}\right] + \Delta q_{\mathrm{AP2},i-1} + \Delta q_{\mathrm{AP3},i-1} \tag{5.1}$$

Where D refers to the semi-Lagrangian advection of quantities on the model grid, AP1 refers to slow atmospheric physics schemes that are summed from independent (parallel) calculations, and AP2 refers to fast physics schemes (where the rate of change is very

large compared to the model's resolved grid and timestep) which are calculated together (sequentially) along the advection timestep. AP1 schemes include radiation, gravity wave drag, water microphysics and entrainment of ambient air into the prognostic cloud fractions. AP2 includes boundary layer turbulence and convection. Applied at the end of the timestep are mass conservation and monotonicity corrections, aspects of the prognostic cloud fractions, any parameterised methane oxidation or gas-phase chemistry (UKCA) calculations. These schemes are collectively described by AP3.

It should be noted that AP2 and each constituent of AP3 are performed sequentially, and therefore depend on the output of preceding schemes.

Schemes with a large influence on water in the tropical tropopause layer are detailed in the rest of this section. Note that not all model schemes modify every prognostic field of the model. Schemes not described impose little or no direct effect on H_2O_{strat}.

The model water budgets have been demonstrated to be closed (P. Earnshaw, personal communication, 2018). However, for the model version used here (v10.4) not every scheme contribution to the water budgets is available; methane oxidation and advection-conservation corrections are unavailable. The first is insignificant in the tropopause region and can otherwise be estimated where necessary. Because the budgets are closed, the second increment can therefore be identified as the residual of all other increments.

5.2.2 Water microphysics scheme

Amongst the parallel schemes is the model's water microphysics scheme, which determines phase changes of water and precipitation processes, including deposition and sublimation. It interacts with the cloud fractions, however the evolution of convection and cloud fractions are handled by other schemes (UMDP30, 2015). The scheme works through levels from model lid to the Earth's surface. Increments from specific processes within this scheme are also obtained and analysed in this chapter.

Sedimentation

This is the first calculation by the scheme, which moves ice (and liquid water) down in model levels with gravity as a function of the ice particle size distribution. The UM10.4 configuration uses a generic particle size distribution for ice calculations, as is typical for UM simulations.

Nucleation

Both homogeneous and heterogeneous forms of ice nucleation act in the presence of supersaturated liquid water. For the cold tropical tropopause layer, where liquid water is absent, nucleation is not anticipated to occur. Therefore the only significant terms converting water between ice and vapour are deposition and sublimation.

Deposition and sublimation

The UM function for rate of exchange between vapour, q ($\mathrm{kg\,kg^{-1}}$), and ice, q_{cf} ($\mathrm{kg\,kg^{-1}}$), is applied when $T < 0\,^{\circ}\mathrm{C}$, and (presumably) when ice is already present. It is given in UMDP26 (2017) as:

$$\frac{dq}{dt} = -\frac{dq_{cf}}{dt} \tag{5.2}$$

$$\frac{dq_{cf}}{dt} = \left(\frac{q}{e_{isat}} - 1\right)\frac{\mathcal{V}_i}{\rho A_{\mathrm{ice}}} \tag{5.3}$$

where e_{isat} is the saturation mixing ratio over ice ($\mathrm{kg\,m^{-1}\,s^{-2}}$), $\mathcal{V}_i$ represents the ice surface availability to the ambient air ($\mathrm{m^{-2}}$) integrated across the particle size distribution, ρ is the density of moist air in the gridbox ($\mathrm{kg\,m^{-3}}$), and A_{ice} represents the thermodynamic timescale of the process ($\mathrm{m\,s\,kg^{-1}}$):

$$A_{\mathrm{ice}} = \left(\frac{L_S}{R_v T} - 1\right)\frac{L_S}{K_a(T)\,T} + \frac{R_v T}{e_{isat}\,\psi(T,p)} \tag{5.4}$$

where L_S is the latent heat of sublimation ($\mathrm{m^2\,s^{-2}}$), R_v is the gas constant of water vapour ($\mathrm{m^2\,s^{-2}\,K^{-1}}$), K_a is the thermal conductivity of air ($\mathrm{kg\,m\,s^{-3}\,K^{-1}}$), and ψ is the diffusivity of water vapour in air ($\mathrm{m^2\,s^{-1}}$). This approximate form of ice mass change is based on Rogers and Yau (1989) equation (9.4) and the values and functions of these parameters in the UM are described further in UMDP26 (2017).

The representation of ice as clouds also responds to deposition and sublimation. The model scheme assumes deposition increases in-cloud ice concentration without adjusting ice cloud fraction (with overall increase in gridbox ice concentration), whereas sublimation reduces ice cloud fraction without changing in-cloud concentration (and overall reduction of gridbox ice concnetration). Physically, this makes sense as deposition is growing ice particles which are already present, whereas sublimation may remove them entirely. The overall effect

of this scheme on ice clouds near the tropical tropopause layer (without liquid water present) is that they are able to shrink in area, increase concentration, and fall.

Concentrations of ice and vapour form a balance according to Equation (5.3), with water vapour tending towards the saturation limit. Because deposition and sublimation provide a latent heat change which modifies saturation, there is a correction for the available moisture. The process is not instantaneous due to $\mathcal{V}_i$ and A_{ice}. Importantly, sedimentation is determined before the calculation of sublimation and deposition.

Because it is the same calculation that results in either deposition or sublimation, the microphysics scheme reports the net contribution of deposition and sublimation as one diagnostic.

It should be noted that there are a number of approximations in the model configurations. One example is the particle size distribution is estimated from empirical data for hexagonal ice, whereas there are other forms of ice that can be created at the low temperatures of the tropical tropopause layer. Further details are in UMDP26 (2017).

5.2.3 Methane oxidation

Being the second direct source of water vapour in the stratosphere (le Texier et al., 1988), the parameterisation implemented in the UM is detailed here. It is the same as introduced by Untch et al. (1998), which has approximated a vertical rate of water vapour increase from methane oxidation, and of loss from photolysis at the highest model levels. The scheme nudges (i.e. applies a fractional increase of) H_2O_{strat} towards $3.75 \times 10^{-6}\,\text{kg}\,\text{kg}^{-1}$ ($\sim$6.2 ppmv) (detailed in Untch et al., 1998), by a vertically dependent rate. The rate is zero at 100 hPa and increases roughly exponentially throughout the stratosphere.

This is designed to parameterise the effects of photochemical reactions that convert methane to water and is constrained by historical observations of total hydrogen (Brasseur and Solomon, 2006). For this reason, it would be somewhat insensitive to any prescribed methane changes.

5.2.4 Summary

This section has presented the schemes contributing to the UM10.4 water budget in the tropical tropopause layer. The microphysics scheme details the phase change and sedimentation aspects of ice and water vapour relevant to the tropical tropopause layer. Nucleation is not anticipated to occur. Therefore, net deposition and net sublimation will be the main focus of this chapter. Additional modifications to ice and water vapour in the tropical tropopause

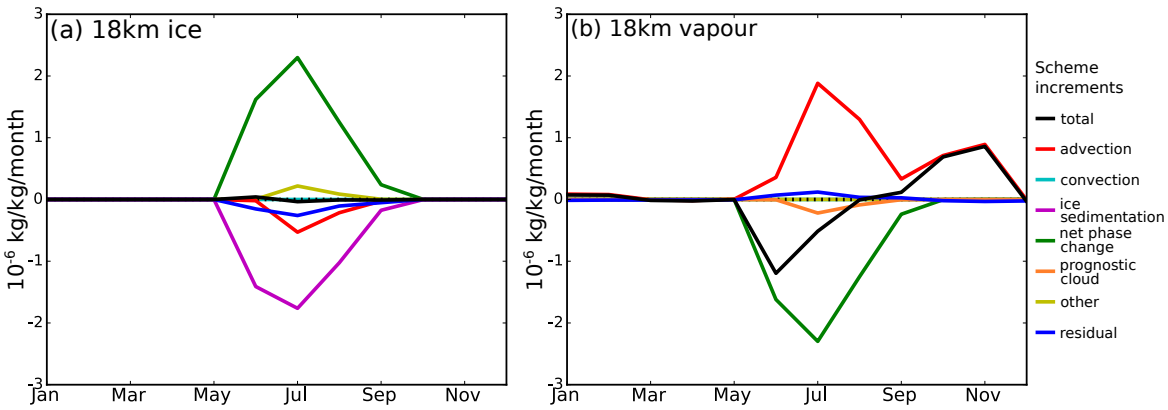

Fig. 5.2 Monthly mean 90–70 °S zonal mean of UM10.4 6 hr instant increments for budgets of (a) ice and (b) water vapour at 18 km across one year of the UM10.4 CONTROL experiment. 'net phase change' is the combination of deposition and sublimation, 'other' is composed of all other available scheme increments, 'residual' applies to the unavailable scheme increment from advection conservation corrections.

layer may occur from the convection scheme which redistributes heat, momentum and water vertically. With this knowledge, the next sections can analyse their relative role in different regions of the atmosphere.

5.3 Water budget analysis in a global climate model

This section will introduce and analyse the individual contributions from different schemes within the UM10.4 global climate model to changes in water. The model forcing scenario is the CONTROL case (repeat year 2002 conditions) as introduced in table 2.2 and studied in chapter 3 and section 4.2.

5.3.1 Large-scale deposition alone – Antarctic polar vortex

Based on Lagrangian calculations of advection-condensation, the water budget in the tropics is expected to be composed of processes describing large-scale deposition, and potentially convective injection. To gain clarity on the full effect of large-scale deposition separately to any convective influence, this section analyses large-scale deposition where it acts alone.

A clear example of large-scale deposition acting alone is in the Antarctic polar vortex. Figure 5.2 shows monthly mean contributions to ice and vapour from different scheme components at 18 km and south of 70 °S. In this region, stratospheric air is devoid of convective activity. Therefore, radiation and polar dynamics control the perturbations of

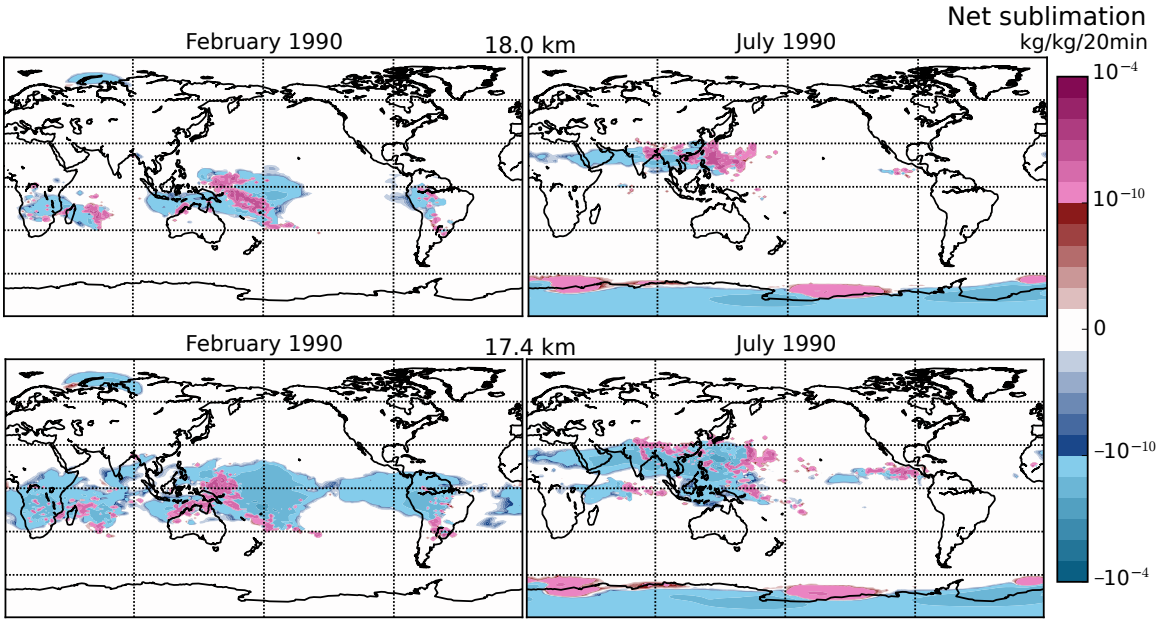

Fig. 5.3 Monthly mean of 6 hourly increments for water vapour from ice in UM10.4 CONTROL at 17.4 km (bottom) and 18.0 km (top) in February (left) and July (right). Positive indicates net sublimation, negative indicates net deposition.

H_2O_{strat} through large-scale deposition. Typically, it presents as a phase change of vapour into ice and subsequent sedimentation.

In the months-long Antarctic polar night (May-July), the lack of solar radiation allows extreme low temperatures to be reached. The low temperatures cause ice deposition (green lines in figure 5.2) with subsequent fallout (purple line in figure 5.2a). The loss terms are dominated by fallout ($1.5–2.0 \times 10^{-6}$ kg/kg/month), advection and its correction terms are three times smaller ($\sim 5.0 \times 10^{-7}$ kg/kg/month).

Furthermore, the strong south polar vortex isolates the air in this region preventing wetter sub-polar air from mixing into the region horizontally (see Joseph and Legras, 2002, and references therein for more detail). As such, in combination with the Brewer-Dobson circulation, only downward advection of water is anticipated. But, towards the bottom of the polar vortex, where the water contained in the air from above has already been deposited, water cannot be resupplied by advection, leading to a net loss of water vapour during this period (May-July black line in figure 5.2b) (Nedoluha et al., 2000; Vömel et al., 1995). As the polar night ends, incoming solar radiation raises temperatures thereby decreasing ice formation and deposition rates. The vortex eventually breaks up and enables strong mixing of wetter sub-polar air (red line in figure 5.2b) and a net gain of water vapour (black line).

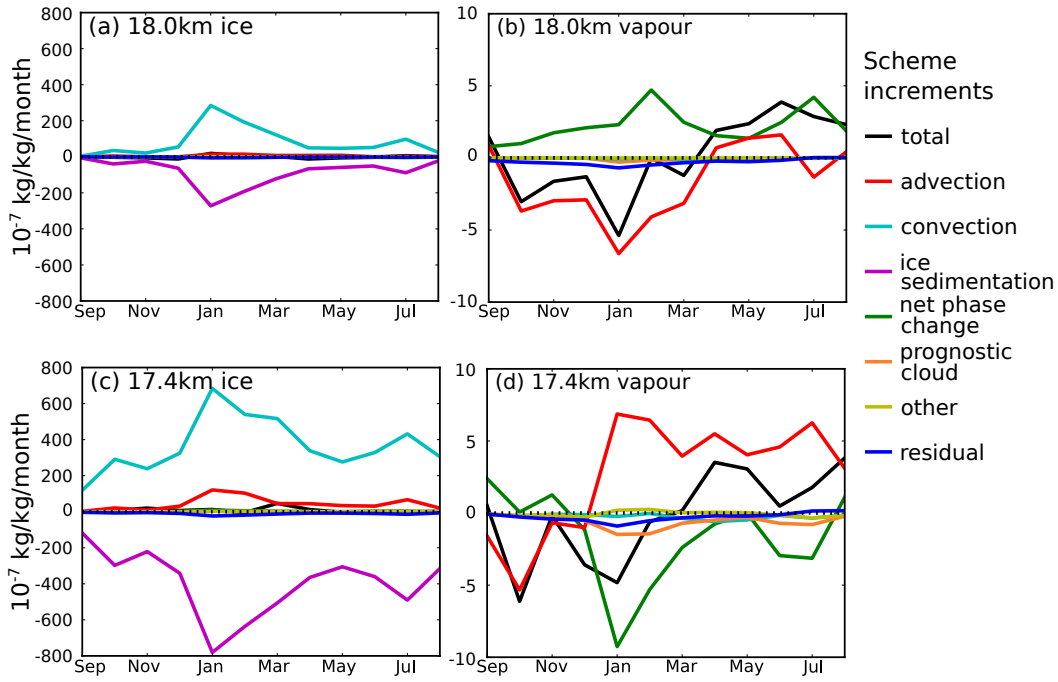

Fig. 5.4 As for figure 5.2 but for 30 °N–S at 17 km (bottom) and 18 km (top) for ice (left) and water vapour (right). Note the different vertical axis scales, and that the net phase change increment reverses sign between vapour and ice.

Throughout this time, at the polar vortex edge, water vapour increases. Saturation mixing ratios are higher thereby lowering relative humidity. Therefore, some ice is advected to sub-saturated gridpoints where it sublimates figure 5.3 .

This provides a standalone view of the model processes involved in large-scale deposition, in the context of scheme increments, to provide context for teasing apart the more complicated tropical tropopause layer.

5.3.2 Deposition and sublimation – tropical tropopause layer

After large-scale deposition, additional modification of the water budget may come from sublimation of ice. Figure 5.4 shows all instantaneous increments in the water vapour and ice budgets of the tropical tropopause layer over one year as monthly means, where contributions seen to be relatively insignificant (by plotting all contributions individually, not shown) have been combined and described as ‘other’. The advection conservation correction (residual) term is reassuringly small.

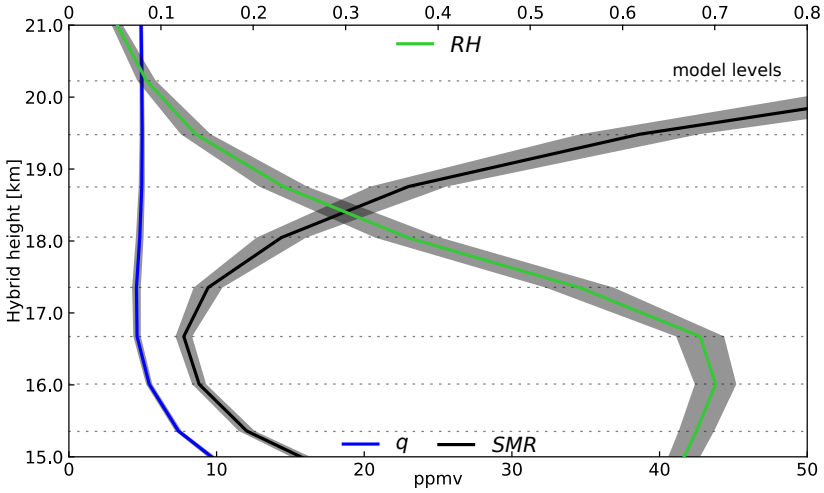

Fig. 5.5 Vertical profile of UM10.4 water vapour, saturation mixing ratio and relative humidity, as 20 °N–S zonal mean 10 year mean. Shaded regions span two standard deviations of the deseasonalised timeseries for each variable. The heights of model levels are indicated by horizontal lines.

At 17.4 km, the ice budget shows a total change of $<10^{-5}\,\mathrm{kg\,kg^{-1}}$ in any given month, yet this is the residual of two very large opposing increments $\sim 7\times10^{-5}\,\mathrm{kg\,kg^{-1}}$ from convective injection and sedimentation.

The exchange with water vapour through deposition and sublimation is insignificant on the ice budget ($<10^{-6}\,\mathrm{kg\,kg^{-1}}$). This suggests that it is inaccurate to assume all ice is lost in sublimation events unless the saturation mixing ratio is very high.

At the same time, the deposition and sublimation is a key balancing factor for vapour (note the different vertical axis scale than for the ice budget). In these monthly mean figures, deposition dominates at 17.4 km and sublimation dominates at the level above (18 km). This is a strong reversal in simulated phase change across neighbouring model levels, visible on the monthly mean timescale.

The explanation for the reversal relates to local saturation. When the air is saturated ($RH \geq 1$) ice deposition dominates, whereas sub-saturated air allows ice to sublimate into water vapour. The saturation mixing ratio increases sharply in the lower stratosphere, which reduces relative humidity away from saturation across a small vertical distance, shown in figure 5.5 . This grid-scale change in microphysical processes points to a likely strong sensitivity to vertical resolution and level placement, applicable to both modelling and analysis.

On the neighbouring model levels (16.7 km and 18.8 km) contributions to the ice budget from convective injection and sedimentation, which remain balanced, weaken with altitude.

For the water vapour budget, the effect of deposition and sublimation also decays with altitude. At 18.8 km there is still some rehydration from sublimation, but advection is now the single dominant term in the timeseries.

The monthly means of these 6 hourly snapshots of model evolution provide a seasonal variation of dq_{total} that resembles model water vapour. This provides confidence that overall evolution of the water budget is sufficiently described by the 6 hourly dataseries.

There is also seasonality to the relative roles of the processes as shown in figure 5.4. January and February show largest increment values in convective ice injection, sedimentation and net phase change in the tropical tropopause layer. The horizontal distribution around this time (February mean shown in figure 5.3) show phase change focusing over the equatorial west Pacific (deposition more broad and sublimation events are sharp). There is also a secondary peak near June and July, where events focus towards the Asian Pacific coast.

These broad regions of deposition at 17.4 km in figure 5.3 align with Lagrangian dry point and vertical dry point spatial distributions infigure 3.9. The horizontal distributions at 18 km are weaker and less extensive, in agreement with figure 5.4. The sharp regions of sublimation vary on the gridpoint scale. They show some relationship to the deposition regions, they occur around them at 17.4 km and above them at 18.0 km. This may indicate the top-of-convective activity.

The total vapour increment's seasonality is consistent with the overall water vapour annual cycle at 18 km. Besides the effect of phase change with ice, it is otherwise dominated by advection, indicating in-mixing of wetter air. Being a local minimum, this does not clearly identify upward transport of wetter tropospheric air, as it can also point to mixing of air from the extratropical tropopause and the lower stratosphere which are also generally wetter.

To summarise the results of analysing the climate model's water budget, the convection scheme provides large quantities of ice to the tropical tropopause region. Almost all of this is removed by sedimentation. A small conversion to vapour at higher altitudes suggests an increase of H_2O_{strat} from convectively lofted ice. This ratio of sublimation to sedimentation near 18 km may be identifiable in the results of individual measurement campaigns.

Such a view of the deposition in the tropical tropopause may help to constrain large-scale ice deposition. For example, the spatial and seasonal distribution of ice deposition in the model may be compared against Lagrangian dry point distributions (which will be done in section 5.5.1) or against observations of relative humidity. Alternatively, as was the case here, the Antarctic polar vortex may provide a simpler region to observe ice deposition and sedimentation.

Importantly, this points to an additional process introducing water vapour into the tropical lower stratosphere which is not usually accounted for in the advection-condensation method in chapters 3 and 4. The challenges of the UM10.4 wet bias in the tropical lower stratosphere may not be entirely caused by the warm bias in the tropical tropopause layer. The warm bias may not translate directly to water vapour through the Clausius-Clapeyron relation. This will be discussed further in the next section.

This influence of ice sublimation is inhomogeneous (figure 5.3) and intermittent (seen in the total ice increment averaging to zero, despite large contributions, in figure 5.4). This makes it hard to quantify the impact on H_2O_{strat} with large-scale averages. The challenge of analysing inhomogeneous and intermittent events, such as from ice sublimation, may be overcome by compiling a set of events considered representative. This will be overcome in the next section by analysing grid point values.

As raised earlier, this makes it a challenge to observe globally too. However, these results of a relationship between ice and water vapour budgets include observable quantities. For example, with a vertical profile of convective injection, tropospheric observations may be able to infer quantities of ice reaching the tropopause. Alternatively, vertically resolved observations of relative humidity and water vapour may be able to estimate the height convection needs to reach in order to rehydrate.

5.4 Ice sublimation events at and above the tropopause

The properties of individual ice sublimation events in the tropical tropopause are investigated in this section. This provides a clearer description of sublimation than from large-scale averages. This will also guide the representation of vapour rehydration in Lagrangian calculations that follow.

A set of events is identified where net phase change is from ice to vapour, occurring at or above the tropopause. This set is drawn from two years of 6 hourly instantaneous model output on the model grid. To define the tropopause boundary, this set is restricted to events occurring at or above the local vertical dry point. Furthermore, the set is restricted to within 40 °N–S since tropical trajectories may also sample the sub-tropical tropopause.

Ice sublimation above the vertical dry point appears to be fairly regular but not widespread. Across the two year period, an average of 481 gridpoints (with standard deviation of 108) exhibited sublimation above the vertical dry point at each point in time. This is about 1.0 % of potential gridpoints. To calculate this, figure 5.6 shows the vertical distribution of these events. Roughly 80 % occur within 16–18 km and all within 14–19 km. Relative to the

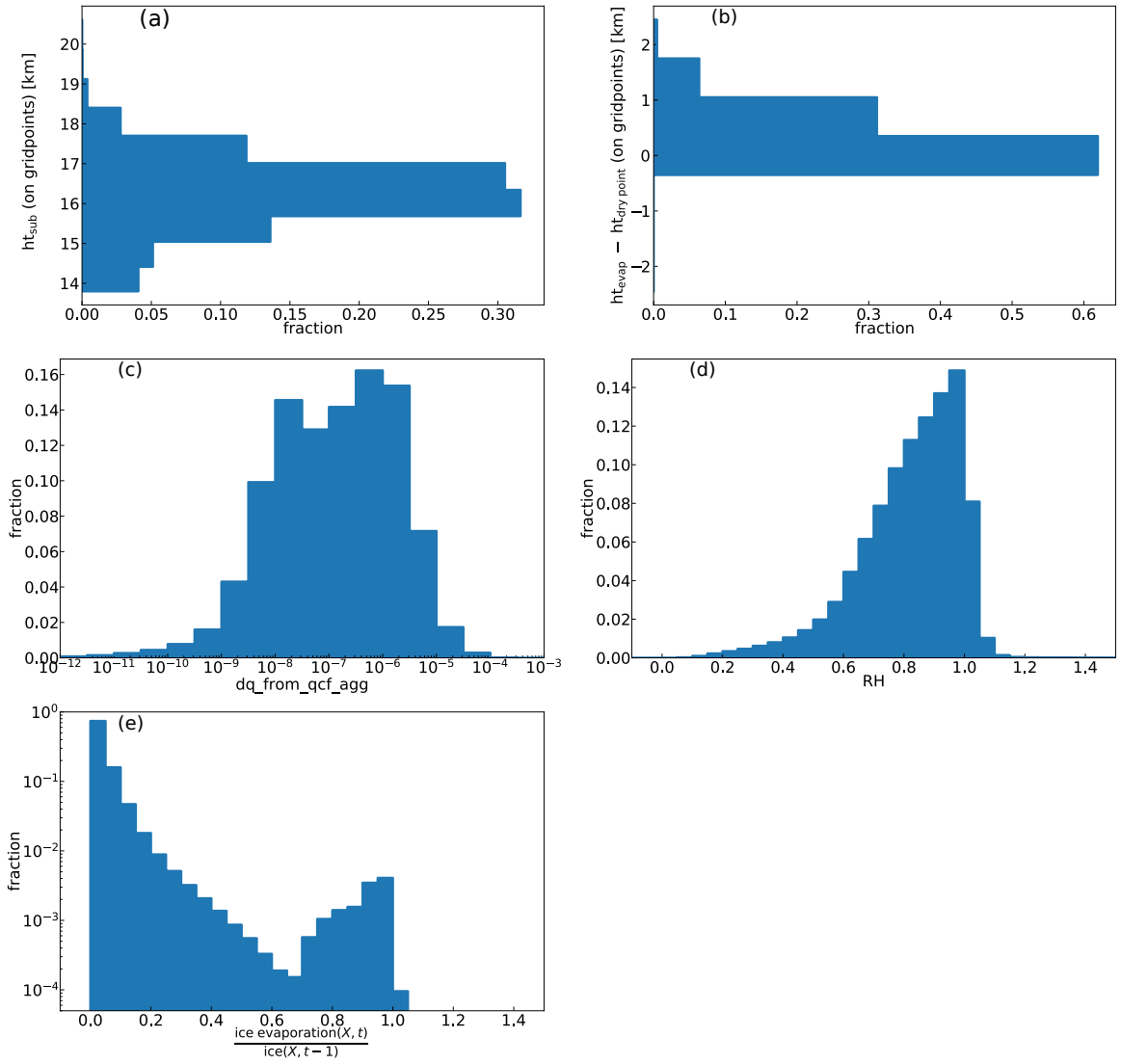

Fig. 5.6 Distributions of 2 years of sublimation events above vertical dry point within 40 °N–S. (a) Altitude, (b) vertical offset from vertical dry point, (c) amount of ice sublimated (kg/kg/6hr), (d) relative humidity, (e) fraction of ice sublimated.

vertical dry point, two thirds occur at the same level and the rest occur on the three model levels above (within ∼2 km). On these four levels, each with 12 288 horizontal gridpoints between 40 °N–S, are the gridpoints considered to potentially experience convective injection.

Figure 5.6 also shows distributions of other quantities associated with this set of events. The distribution of quantities sublimated above the vertical dry point peak between 10^{-8}–10^{-6} kg/kg/6hrs, with contributions spanning 10^{-11}–10^{-4} kg/kg/6hrs (the 6 hrly timespan is chosen for comparison with the Lagrangian dehydration method following this section). The end-of-timestep gridpoints have a high relative humidity and are rarely supersaturated

(according figure 5.6d). This is complicated by showing the result of advection and all model schemes, not just sublimation. However it demonstrates that, at individual gridpoints where water vapour is increasing because it was sub-saturated, the model does not supersaturate often.

The fraction of ice sublimated to vapour is quantified in figure 5.6e. Less than 5 % of available ice is converted to vapour in 74 % of events and less than 10 % sublimates in 90 % of events.

This model observes some events of near 100 % conversion of ice but they are a very minor contributor. This suggests that sublimation is generally not limited by the amount of ice available. The alternative limiting factor is expected to be saturation. If this is the general limiting factor, then sublimation rates would match the remaining capacity for water vapour. This can be expressed as a fraction, for a given gridpoint where sublimation occurs ($\Delta q_{sub,i} > 0$), as:

$$F = \frac{\Delta q_{sub}}{q_{pot}} \tag{5.5}$$

where q_{pot} is the potential capacity for water vapour (saturation minus absolute humidity):

$$q_{pot} = SMR - q \tag{5.6}$$

When saturation is a limiting factor, $F = 1$. (It should be noted that q_{pot} should be determined from the quantities preceding the increment calculation). The data are not available to calculate q_{pot} accurately for these events. Alternatively, applying a method similar to Dessler et al. (2016) and setting this fraction to 1 will test this limiting factor. This is tested and discussed later in this chapter and in chapter 6.

Figure 5.7 shows the horizontal distribution of sublimation events. There is a focus over the Indian Ocean and West Pacific with some contributions over equatorial continents and the South Pacific. Weighting by the amount of ice sublimated reduces the spread for all but one location. The exception is the West Pacific which makes a smaller contribution, suggesting the region provides relatively little water vapour from ice despite the presence of overshooting convection. The American continents at 30–40 °N and S also show strong contributions, probably due to the lower altitude of vertical dry points qualifying more convective events as overshooting. Compared to figure 5.3 — which shows only two of the months contributing to the two years of event-based study — the equatorial distributions agree well. The July contributions over South East Asia at 17.4 km and 18.0 km do not

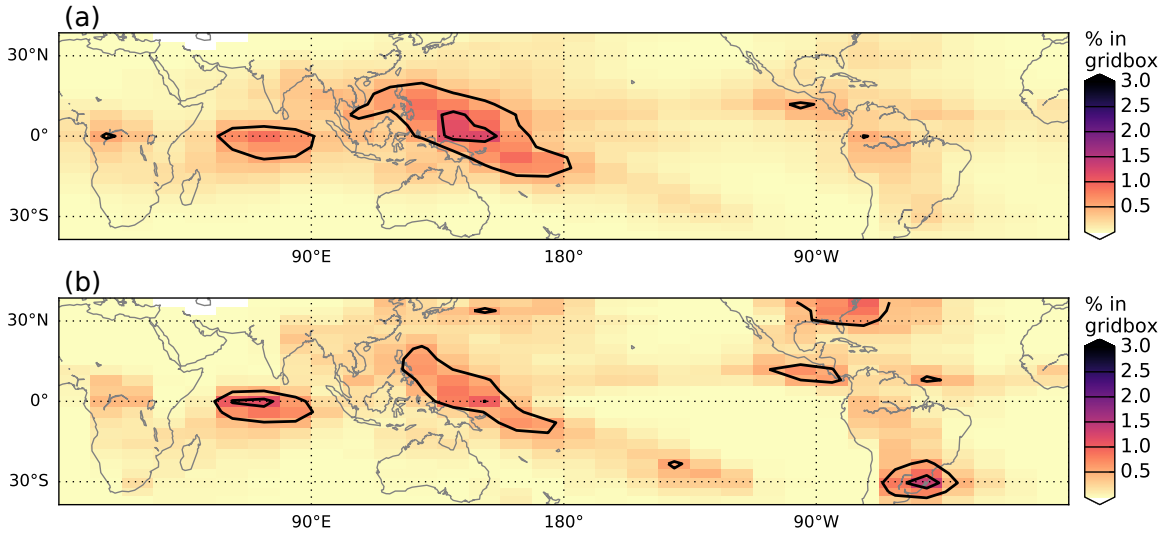

Fig. 5.7 Horizontal distribution of 2 years of sublimation events above vertical dry point. (a) Unweighted and (b) weighted by the gridbox contribution to total ice sublimated above vertical dry point.

appear in the time mean event-based study, suggesting a relatively small contribution, or a high vertical dry point in this region.

To summarise the Eulerian results, it is clear that ice sublimates above the vertical dry point in this global climate model. This is possible because of the presence of ice, in part due to convection, and increasing saturation mixing ratios with altitude — so that relative humidity falls below 100 % — above the vertical dry point. Because these regions coincide with air that has passed its final dehydration location, this process may impact H_2O_{strat} abundance. The efficacy of ice to rehydrate to local saturation is yet to be confirmed.

5.5 Impact of ice on Lagrangian dry point calculations

Lagrangian dry point analysis offers a quantitative view of changes to H_2O_{strat}. However, it so far assumes instantaneous dehydration to saturation mixing ratios along trajectory pathways. In chapters 3 and 4, it has been shown to represent interannual and seasonal variability of model H_2O_{strat} reasonably well. However, by not considering ice along trajectories, it represents only a portion of the full water budget.

The spatial representation of large-scale Lagrangian dehydration can be evaluated against model ice deposition in figures 3.9 and 5.3. The patterns broadly agree but ice deposition is more widespread and inhomogeneous. This motivates a more detailed comparison in the first part of this section.

Secondly, section 5.3 showed that ice deposition is interspersed with net sublimation throughout the domain, particularly at 18 km altitude. Section 5.4 demonstrated explicitly that deposition occurs above the vertical dry point, implying some effect of increasing q in the lower stratosphere. It is therefore useful to incorporate rehydration into the Lagrangian dry point method as it allows the impact of such an intermittent process to be quantified.

Section 5.3 also identified that, of the large increments in the ice budget in the tropical tropopause, only a small fraction corresponds to the process of sublimation. Whether saturation mixing ratios are the limiting effect can be clarified by testing this condition. In this way also, the methods of Dessler et al. (2016) may be clarified.

The rest of this chapter will assess the impact of incorporating the precise model description of ice rehydration into Lagrangian calculations.

5.5.1 Comparing deposition

To better compare the representation of deposition in the climate model with the Lagrangian dry point calculations, figure 5.8 analyses the timing and quantity of the closest model deposition increments along Lagrangian pathways.

Figure 5.8a shows, as a distribution for all trajectories released across 10 years, the times along trajectories from Lagrangian dry point to nearest deposition event. About half are concurrent, and in total $\sim$90 % experience deposition within $\pm$4.25 days of their Lagrangian dry point. However, the deposited quantities disagree. As shown in figure 5.8b, the quantity of water deposited at these events are smaller than the amount inferred by instantaneous dehydration by at least a factor of 10. One aspect of this disagreement stems from the trajectory calculation's linear interpolation of the small and inhomogeneous field of ice increment.

A drawback of this method is the poor representation of all dehydration by the instantaneous method. Dehydration often occurs over several trajectory history timesteps (as saturation mixing ratio reduces over time). More deposition is expected from the Lagrangian dehydration method and therefore the differences will be larger. Comparing a more extensive region would yield more accurate results.

Overall, the model's ice deposition is in reasonable agreement with spatial patterns of Lagrangian dry points. Deposition events also appear to coincide within a couple of days, however the considered quantities deposited differ by at least an order of magnitude. Lagrangian dry points define a specific deposition event along trajectories. Therefore, a more accurate comparison with deposition in the climate model may be possible by compiling all

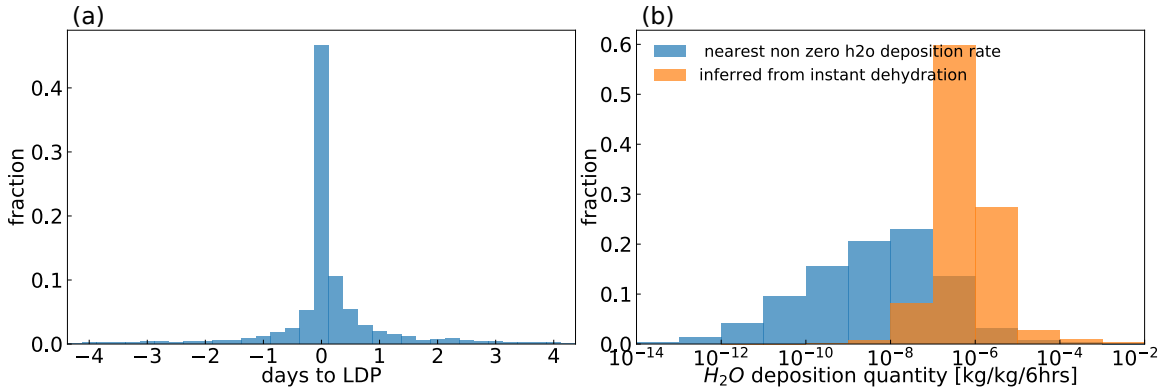

Fig. 5.8 Distributions for Lagrangian dry points from 10 years of Lagrangian calculations. (a) Proximity of nearest ice deposition events, only showing nearest ±4.25 days (90 % of all Lagrangian dry points). (b) Magnitude of increments of nearest ice deposition field events (blue) in (a) as well as the deposition inferred from instantaneous dehydration in the timestep before the Lagrangian dry point.

trajectory timesteps recording dehydration within a region of the tropical tropopause layer, not just using the Lagrangian dry points.

5.5.2 Incorporating sublimation

The analysis in earlier sections of this chapter indicates that ice in the lower stratosphere of the UM10.4 climate model increases H_2O_{strat} to some extent. To quantify this impact further, the advection-condensation method is modified here to incorporate the model ice increments. Two alternative calculations are performed which are described next. Figure 5.9 provides the calculated histories of one trajectory to demonstrate some of the different methods.

Method

As introduced in section 1.2, a number of Lagrangian studies have tested various parameterisations for the interaction of water vapour and ice. However, global observations of the precise conversion processes cannot be made directly. The novel aspect of the method applied in this section is to make use of model increments as indicators for the presence of ice. These provide precise, process-based, ice descriptions otherwise unavailable from observations, thus providing clearer conclusions of the involved processes. The Lagrangian calculations of ice sublimation are detailed below, along with the indicators of ice sublimation used from the model. Each calculation is summarised in table 5.1.

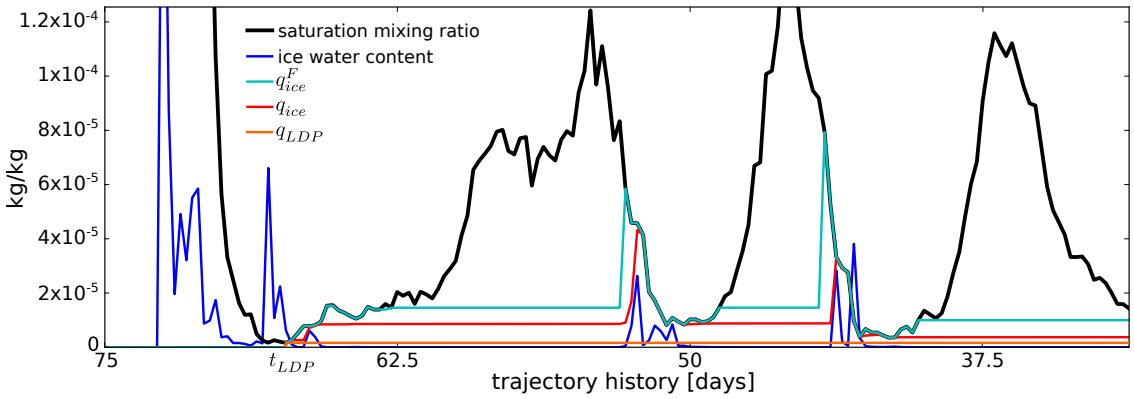

Fig. 5.9 Water fields and ice rehydration calculations along a single trajectory. Showing days 40–76 only. Trajectory released September 1989, 30 °N, 136 °E, 75 hPa.

For a trajectory with history timesteps $i = 0, \ldots, N$ every 6 hours from troposphere to stratosphere, the final estimate for H_2O_{strat} is $q_{LDP,N}$ ($\text{kg}\,\text{kg}^{-1}$). The calculation of the Lagrangian dry point method may be written as:

$$q_{LDP,N} = \min\Big(SMR_0\,, SMR_1\,, \ldots\, SMR_N\Big) \tag{5.7}$$

Equivalently, if the method were to assess each timestep separately, at timestep i:

$$q_{LDP,i} = \min\Big(q_{LDP,i-1},\; SMR_i\Big) \tag{5.8}$$

and

$$q_{LDP,0} = SMR_0 \tag{5.9}$$

This says that whatever the saturation mixing ratio at the start of the trajectory history, the final estimate can only get drier.

Incorporating an ability to rehydrate, the calculation becomes:

$$q_{ice,0} = SMR_0 \tag{5.10}$$

$$q_{ice,i} = \min\Big(q_{ice,i-1} + \Delta q_{ice,i},\; SMR_i\Big) \tag{5.11}$$

where $\Delta q_{ice,i}$ is the modification due to an indicator of ice along the pathway. That is, the trajectory estimate of water vapour carried into the stratosphere is unchanged unless it encounters a non-zero indicator of sublimation, $\Delta q_{ice,i}$, or it is forced to dehydrate by a SMR_i smaller than its concentration of water vapour, $q_{LDP,i-1}$. This introduces a dependence on the order of events in the trajectory history. $q_{LDP,N}$ will be unaffected by large values of sublimation if small *SMR* values are encountered afterwards.

Several indicators of sublimation will be tested. The first indicator is net sublimation (the modified Lagrangian dry point estimate of H_2O_{strat} will be referred to as $q_{\Delta sub}$), the exact model value for the process of interest. The second is net ice increment from the convection scheme (H_2O_{strat} estimate referred to as $q_{\Delta conv}$). They are both ice tendencies with units of kg/kg/timestep. As explained in section 5.3.2, the 6 hourly snapshots are considered representative of the overall model evolution. Therefore, their units are scaled up to kg/kg/6hours.

The third indicator that will be tested is ice concentration (H_2O_{strat} estimate referred to as q_{ice}) with units of $\mathrm{kg\,kg^{-1}}$. This requires the additional assumption that all ice sublimates in that 6 hour period. Note that this differs from the method of Dessler et al. (2016) who assess the water vapour evolution with ice at every trajectory integration timestep, thereby allowing the potential for a single 6 hourly instant value of ice to be entirely sublimated multiple times, whereas this method only checks the local ice (and saturation) fields once at each 6 hourly datapoint. The difference in ice available to sublimate will be a factor of $\sim$10.

One possible justification for allowing over-counting of ice sublimation is that the process might be assumed to be saturation limited. No over-counting would occur if even a small initial value is already capped by SMR_i in equation (5.11). Using the annotation of equation (5.5), the assumption is that $F = 1$. To test for this effect, a simpler, qualitative form is calculated that allows any non-zero ice increment to rehydrate the water vapour record to local saturation mixing ratio. For these fixed $F = 1$ cases, the ice indicator is modified to be:

$$\Delta q_{ice,i} = \begin{cases} SMR_i - q_i, & \text{if } q_{ice,i} > 0 \\ 0, & \text{otherwise} \end{cases} \tag{5.12}$$

Equation (5.11) then becomes:

Table 5.1 Description of method to calculate each prediction of stratospheric water vapour, q.

	calculated by	semi-/ Lagrangian advection?	all UM10.4 schemes?	instant dehydration?	rehydrate according to?	$F = 1$?
q	UM10.4	SL	Y	-	-	-
q_{trac}	UM10.4	SL	-	Y	-	-
q_{LDP}	offline	L	-	Y	-	-
q_{ice}	offline	L	-	Y	ice concentration	-
q^F_{ice}	offline	L	-	Y	ice concentration	Y
$q_{\Delta sub}$	offline	L	-	Y	net sublimation increment	-
$q^F_{\Delta sub}$	offline	L	-	Y	net sublimation increment	Y
$q_{\Delta conv}$	offline	L	-	Y	net convective injection increment	-
$q^F_{\Delta conv}$	offline	L	-	Y	net convective injection increment	Y

$$q^F_{ice,i} = \begin{cases} SMR_i, & \text{if } \Delta q_{ice,i} > 0 \\ \min\left(q^F_{ice,i-1},\, SMR_i\right), & \text{if } \Delta q_{ice,i} = 0 \end{cases} \tag{5.13}$$

with a superscript F to denote the $F = 1$ case for each of the three fields tested for sublimation.

The Lagrangian trajectories forming the basis of this analysis are the same as used in section 3.2.3. 11 years of monthly releases at 75 hPa distribution between 30 °N–S every 2°×2° record the UM10.4 repeat year 2002 experiment conditions of 6 hourly kinematic wind, temperature, pressure, and water budget terms along 360 day backward histories.

As introduced in chapter 2, the offline Lagrangian calculations interpolate vertically with a cubic polynomial scheme between datapoints of winds, temperature and pressure. For the weak, intermittent and inhomogeneous ice fields, to prevent spurious negative values, the code has been modified to interpolate linearly.

Only back-trajectories that reach the defined troposphere, potential temperature $\theta < 340$ K and saturation mixing ratio $SMR > 1000$ ppmv, in this time form the set of troposphere-to-stratosphere transport pathways. For these, Lagrangian dry points are defined as the minimum saturation mixing ratio experienced by each trajectory (orange line in figure 5.9, with timing marked by t_{LDP}). Then, moving forwards in time, the ice records are assessed and may rehydrate the concentration carried from the Lagrangian dry point by following one of the described methods. The resulting value at time of trajectory initialisation contributes to the predicted (ensemble mean) water vapour concentration.

First, an indicative method following equation (5.13) is used, where some identifier of sublimation events is used to reset a trajectory's water vapour content back to saturation. For the example trajectory in figure 5.9, the example indicator is ice water content (dark blue line), resulting q^F_{ice} (light blue line). Note that this method resets parcel water vapour content, thereby eliminating any memory of its earlier history. In that way, it resembles the cloud-intercepting trajectory calculations of Tissier and Legras (2016). The flexibility of this approach may be applicable for the limited global observations that may indicate the influence of ice in the tropical lower stratosphere.

Second, the specific quantity of modelled ice may be added to a trajectory's water content, with an upper limit set to the saturation mixing ratio. This applies the model's natural distribution of F. q_{ice} in figure 5.9 (red line) shows this for the example trajectory. This does

not assume water content is close to saturation and the impact of this assumption can be tested.

Comparing these two methods tests the assumption of whether saturation is a robust limiting factor of sublimation. This will clarify the impact of over-frequent ice sampling.

These two approaches are further motivated by studies emanating from Dessler et al. (2007); Schoeberl and Dessler (2011), which typically apply stochastic along-trajectory rehydration calculations based on proxies of observations. The approach here is more precise, as it records directly the Eulerian process-based calculations of the climate model water budget. The two methods described above, without the over-frequent ice sampling, test F sensitivity and clarify whether saturation is a robust limiting factor.

To summarise, the method employed here compares ice fields after each trajectory's Lagrangian dry point along the trajectory history. For simplicity, a test for sublimation is made at every 6 hrly instant ice record. Fields considered include total ice water content, and ice increments from convection and net sublimation. Because increment records are in units of kg/kg/20min, they are scaled up to the trajectory sampling timescale kg/kg/6hr. Also for quantitative calculations, ice water content (units of $\mathrm{kg\,kg^{-1}}$) is assumed to entirely sublimate in $\sim$6 hours (treated as kg/kg/6hr). Because the total monthly means compare well to the water vapour annual cycle, they appear to be representative of overall increments.

Results

The impact of the different methods for incorporating ice sublimation on $\mathrm{H_2O_{strat}}$ predictions are shown in table 5.2, and compared with both the instantaneous dehydration approximation (q_{LDP}) and the model water vapour concentration (q). The results vary depending on the approach used. The wettest time mean is reached when rehydrating the ice field q_{ice}. Rehydration indicators based on increments of net sublimation $q_{\Delta sub}$ and convective ice injection $q_{\Delta conv}$ also moisten the time mean estimate by 30–50 %.

Ice indicators with fixed $F = 1$ (q^F_{ice}, $q^F_{\Delta conv}$ and $q^F_{\Delta sub}$) are wetter than their non-fixed counterparts (q_{ice}, $q_{\Delta conv}$ and $q_{\Delta sub}$ respectively). This may be a sign that ice increments are usually smaller than the available water capacity of the air (therefore insufficient to rehydrate to local saturation). However, this would be at odds with earlier results showing large ice increments, and with the idea that ice is present where the air is already saturated. A plausible explanation is offered by figure 5.10a, which shows the vertical distribution of each ice field encounter after trajectories' Lagrangian dry points. The tails suggest small ice quantities have a high reach, where saturation values are higher.

Table 5.2 Characteristics of time mean and deseasonalised monthly mean variability of model water vapour, q, and various methods of estimation introduced in table 5.1. Trajectories are reported for 30 °N–S zonal mean at 75 hPa, q and online tracer are at 15 °N–S zonal mean. Reported correlations with q have no time lag.

	μ	σ	R^2
q (70 hPa)	5.0	0.13	-
q (18 km)	5.0	0.16	-
q_{LDP}	3.0	0.10	0.60
q_{ice}	4.6	0.17	0.85
q^F_{ice}	10.0	0.55	0.50
$q_{\Delta sub}$	4.0	0.21	0.29
$q^F_{\Delta sub}$	5.6	0.39	0.15
$q_{\Delta conv}$	4.4	0.23	0.33
$q^F_{\Delta conv}$	7.6	0.54	0.32

One systematic cause relating to this high reach is the linear interpolation applied by the Lagrangian calculations causing non-zero values to be found throughout the gridboxes above and below a gridpoint. The extended reach of small ice concentrations becomes a substantial modifier to the rehydration indicator when $F = 1$ is fixed, as it can reset to larger values of saturation mixing ratio. This is a spurious effect in the calculation which may be minimised (for example, by setting a minimum threshold value to allow rehydration in the $F = 1$ cases).

This results in different altitudes for final ice modification events. Figure 5.10b shows the unweighted distributions from each indicator at the time of their final modification. This final modification may be either dehydration or rehydration depending on the ice increment and saturation mixing ratio at that time. In particular, the distributions with ice sublimation as indicator are broad and peak within a kilometre of the Lagrangian dry point distribution, whereas ice water content indicators peak sharply around 1 km higher again at 18 km. This has two implications. For one, this exposes the qualitative calculations to higher saturation mixing ratios thereby hydrating H_2O_{strat} predictions further, which explains the difference in table 5.2 between time mean of q_{ice} and $q^F_{\Delta ice}$. Second, it highlights the importance of Lagrangian calculations sufficiently sampling regions above the tropopause that experience ice.

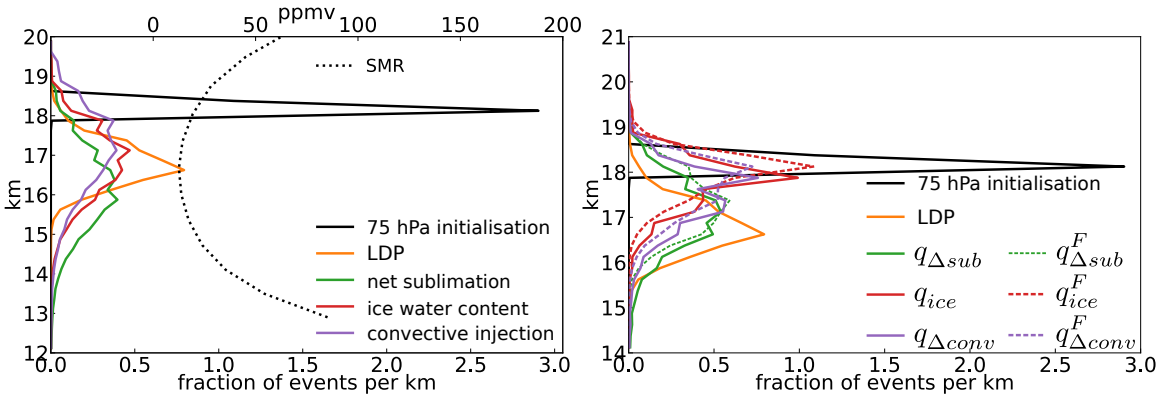

Fig. 5.10 Vertical distribution of ice events encountered by trajectories after their Lagrangian dry points. For 10 years of trajectory calculations. (a) All ice encounters along trajectories, (b) final modification by advection condensation and corresponding ice fields. Time mean tropical mean saturation mixing ratio (ppmv) is also shown for comparison.

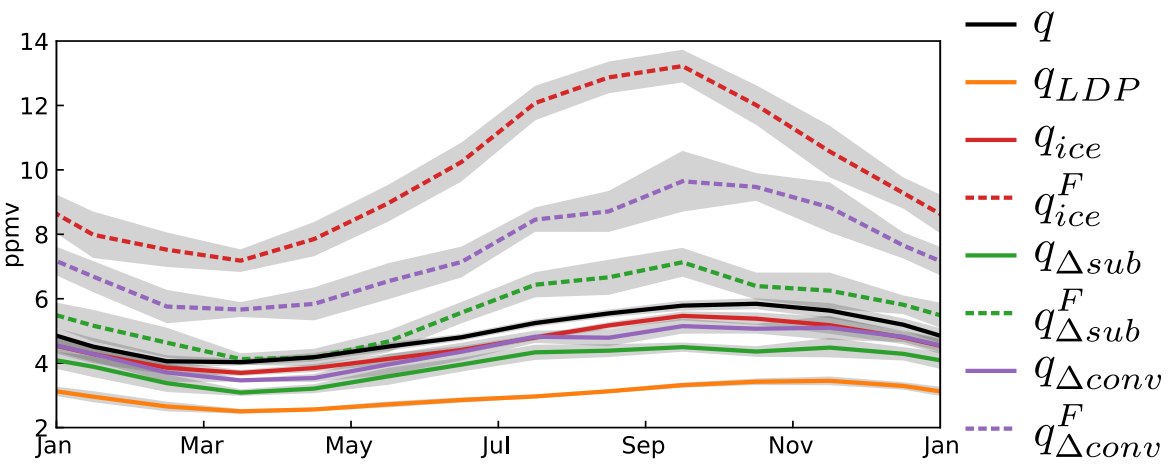

Fig. 5.11 Average year concentrations of H_2O_{strat} predicted with Lagrangian dry point methods and different ice rehydration calculations. Grey shading marks one standard deviation above and below each average value.

Occurrences of the ice fields reach above the levels of trajectory initialisation. This indicates that trajectories will experience further ice rehydration if initialised at higher altitudes. Predictions of H_2O_{strat} therefore remain height dependent at this release level.

To describe how much month-to-month variability agrees between q and each rehydrated Lagrangian calculation, table 5.2 also reports the correlation coefficient of determination, R^2. Most of the assessed calculations struggle to improve the amount of explained variability as represented by the advection-condensation method (q_{LDP}). Only q_{ice} reports a higher correlation with model water vapour. Its similarity is also apparent in its time mean and annual cycle, shown in figure 5.11.

To investigate this correlation, and because both of the applied methods depend strongly on the final encounters, the spatial distributions of final modification events are clarified. Figure 5.12 shows the horizontal distribution of final modification events (twinned with Figure 5.10b) which are very similar. In all cases, the same specific regions appear to be responsible for rehydrating trajectories. This suggests that the different correlative strengths do not refer to large-scale horizontal sampling differences. Therefore, it is the differences in vertical profiles that distinguish the effect of these ice sublimation formulations.

5.6 Discussion

This chapter has identified a critical role for ice in the tropopause water vapour budget of the UM10.4 global climate model. This implies a considerable influence from deep convection in the model. Event-based analysis overcomes the large variability, and demonstrates the presence of ice sublimation above vertical dry points. Lagrangian analysis quantified the impact on H_2O_{strat} predictions from several alternative methods of ice sublimation based upon explicit model process increments.

Like Dessler et al. (2016), the Lagrangian analysis in this chapter differs from earlier studies of climate models by determining ice evolution as an external field to be advected through, rather than a development of the microphysical calculations along trajectory pathways. This work goes further than Dessler et al. (2016) by testing the extent of control by the saturation limit as well as different measures of ice encountered by trajectories,

While climate model deposition coincided with Lagrangian dry points quite well in section 5.5.1, suggesting some resemblance of model phase change processes, Lagrangian calculations incorporating net sublimation ($q_{\Delta sub}$) show only a small moistening and a poorer agreement with q in terms of interannual variability (μ and R^2 in table 5.2). One reason for this poor direct comparison is that the climate model's microphysical scheme implicitly involves timescales. The rate of relaxation of water vapour concentrations towards saturation in the presence of ice (equation 5.3) depends on temperature and a number of parameterised water distribution properties. Its non-instant nature means that instantaneous dehydration of the advection-condensation method may coincide with only portions of overall phase transitions.

Other methods to rehydrate trajectories had a stronger impact on time mean concentration entering the stratosphere. Using convective events as an indicator for air parcel rehydration ($q_{\Delta conv}$, proposing a direct relationship between convective lofting and increases in q) found wetter predictions, but again an overall loss of likeness in variability. However, allowing

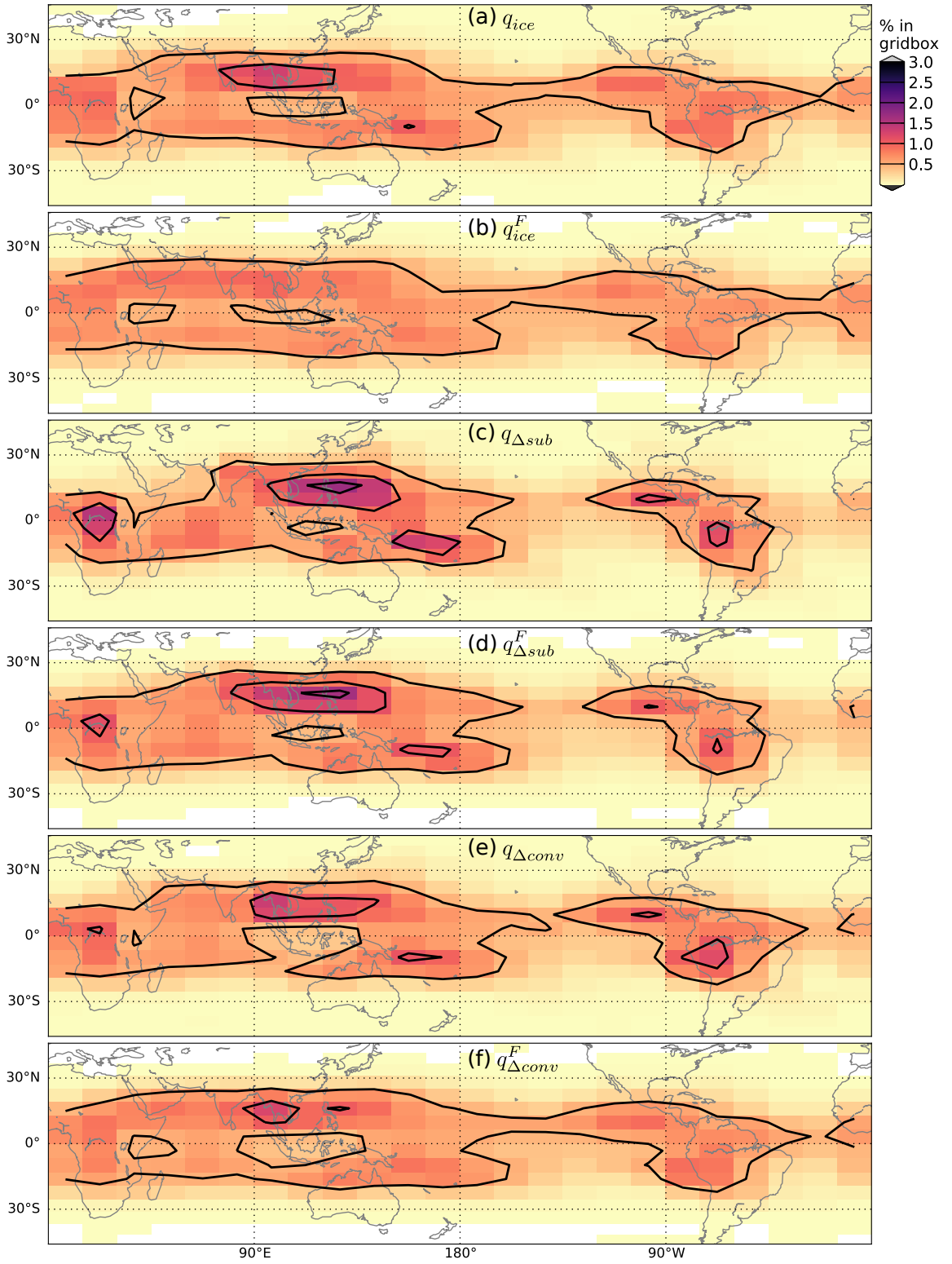

Fig. 5.12 Horizontal distribution of final ice modification events encountered after the Lagrangian dry points of 10 years of UM10.4 CONTROL trajectories for each of the six rehydration calculations described in table 5.1.

complete sublimation of all ice experienced along trajectories (q_{ice}) predicted water vapour in the lower stratosphere about as wet as model water vapour and, perhaps surprisingly, very high agreement in variability which increased R^2 to 85 %.

Such a close similarity prompts the question of how physical it is to assume all encountered ice sublimates immediately. In one sense, this follows very similar assumptions to the instantaneous-dehydration approximation of the advection-condensation method, and therefore seems entirely appropriate. However, figures 5.4 and 5.6d point out that only a small fraction of total ice sublimates into water vapour at any instant. Therefore, these results could be a sign of two cancelling errors. Over-efficient dehydration of the LDP method (Liu et al. 2010 and chapter 3) is counteracted by over-efficient rehydration of sublimating all encountered ice.

To test the hypothesis that ice sublimation in the tropical tropopause layer is saturation limited, the same methods to rehydrate Lagrangian trajectories were modified to set an air parcel to local saturation regardless whenever rehydration was called for ($q^F_{\Delta sub}$, $q^F_{\Delta conv}$, q^F_{ice} in table 5.1 and table 5.2). For these cases, what matters is only the saturation mixing ratios sampled by each model process. The impact on variability from all of these is either negligible or a detriment. This indicates that the ice sublimation methods tested here are not always limited by local saturation. Instead, it is both the vertical distribution of the ice field as well as its local concentrations that provide its close relationship with q.

Dessler et al. (2016) apply a method similar to q_{ice} to study long-term trends of H_2O_{strat} in two chemistry climate models, but they tested the 6 hourly ice field more frequently than 6 hours. The presumed justification for this is that saturation would prevent over-counting. However, the difference between q^F_{ice} and q_{ice} here suggests that the ice field does not rehydrate to saturation mixing ratios very readily, implying over-counting of the impact of ice sublimation is occurring in the calculations of Dessler et al. (2016), potentially by a factor of 10.

Dessler et al. (2016) have also suggested interannual variability is not affected by assuming total sublimation of ice present. For this global climate model however, interannual variability is quantified to be more similar as a consequence of including ice sublimation, the explained variance has increased from 60 % to 85 %. This may be an aspect specific to each global climate model, as it will be strongly tied to their convection and microphysical schemes.

It should also be noted that, in this global climate model, sedimentation of ice is calculated before sublimation in the large scale precipitation scheme. This allows the large sedimentation response to convection (figure 5.4) before sublimation is calculated. Poten-

tially, this redistribution of ice also lowers the levels of sublimation. This may explain why, in figure 5.10, the effect of convective injection is higher than the fields of ice and sublimation.

This points out a strong dependency on the construct of the model microphysics scheme. Because sedimentation is always calculated first, the height of potential sublimation above the tropopause is lowered systematically, shifting the bulk of ice to regions of lower saturation mixing ratio and therefore reducing its ability to hydrate. Alternative constructs may not introduce this systematic lowering and may therefore lead to increased sublimation above the tropical tropopause. This aspect is informative for model development.

Lagrangian calculations have assumed water vapour and ice water content are homogeneous within each gridbox. Instead, they are partitioned into ice cloud and clear sky areas. So, the probability of a particle encountering ice should be as likely as the cloud fraction for that gridbox. This could be incorporated into calculations.

There is one contributing factor to the difference between $F = 1$ and non-fixed F ice rehydration methods in these Lagrangian calculations, raised earlier. Because ice and increment fields are very inhomogeneous, they are interpolated linearly in all dimensions to the trajectory positions. This is a numerically diffusive form of interpolation, thereby broadening concentrations encountered between gridpoints. This may be particularly obvious in the vertical for a qualitative calculation (as in figure 5.10a) which would effectively extend the reach of non-zero gridpoints to the top of the gridbox above, even when the next gridpoint is zero. With vertical levels every $\sim$700 m in the tropical tropopause of this model, ice signals can therefore reach over $\sim$1.4 km. This provides a very large net for slowly rising trajectories, which will be sensitive to the positioning of the model vertical grid. Tests with less diffusive sampling of the ice field might result in smaller differences between, for example, $q^F_{\Delta sub}$ and $q_{\Delta sub}$.

Furthermore, ice sublimation increments appear to reach the trajectory initialisation height of 75 hPa ($\sim$18 km). Considering the model's ice field extends higher again, further rehydration of H_2O_{strat} may be possible above this level. This can be investigated further.

The investigations in this chapter found ice content to be a better proxy for ice rehydration in the tropical tropopause than seemingly more accurate increment fields available in the global climate model. Fortunately, unlike model increment fields, total ice is observable on the global scale (for example, from the MLS data record, Livesey et al., 2011). Such a study with satellite records of ice would test this method further, providing a fuller understanding of processes controlling stratospheric water vapour abundance and variability.

Ultimately, the improved estimates of q variability from the Lagrangian dry point method by incorporating rehydration of all encountered ice is a sign that the variability of the ice field in the tropical lower stratosphere is influential on H_2O_{strat}.

5.7 Conclusions

This chapter analysed the presence and impact of ice above the tropical tropopause in a global climate model (UM10.4). With the added detail of complete water budgets, the role of ice in tropopause water vapour processes are shown, originating from both deposition and convective injection. Most convectively lofted ice sediments very quickly, but a small proportion sublimates to water vapour. Where the model explicitly sublimates ice above the vertical dry point was then described, demonstrating a contribution to the lower stratosphere. Different methods of incorporating ice rehydration into the Lagrangian calculations were then tested to represent sublimation to varying degrees.

The rehydration method which brings Lagrangian estimates of H_2O_{strat} into closest agreement with the mean and interannual variability of model water vapour is the instantaneous sublimation of the ice field (q_{ice} in table 5.2). Incorporating it hydrated the Lagrangian dry point prediction by 1.61 ppmv ($\pm$0.27), and increased the explained variance in model water vapour by 25 % to a total of 85 %. This is understood to be due to its effect at altitudes above Lagrangian dry points — which is partly due to the order of microphysical processes in the climate model timestep — and its concentrations. A crucial aspect of this result is that increases due to ice are insufficient to return an air parcel immediately to its saturation mixing ratio limit in all cases. Therefore, the overall effect on modelled water vapour in the tropical stratosphere is sensitive to both the order of microphysics processes in the climate model timestep, the vertical profile of temperatures above the vertical dry point, and the vertical reach of convective injection.

With a more complete understanding of the water budget acting in a global climate configured to represent the current climate, the next chapter considers how the control of H_2O_{strat} by large-scale transport, temperature-based dehydration and subsequent sublimation responds in future forcing scenarios.

Chapter 6

Impact of future forcing scenarios

6.1 Introduction

Earlier chapters have established the representativeness of Lagrangian calculations in predicting lower stratospheric water vapour in two global climate models. Chapter 3 found that the annual cycle of climate model water vapour, q, is captured by the processes of temperature and large-scale transport captured in the advection-condensation method. It also determined that the effect of transporting instead by the climate model advection scheme is relatively slight, and that the representation of sub-seasonal temperature variability affects the prediction of water vapour entering the lower stratosphere. Chapter 4 quantified the relative roles of temperature and large-scale transport in the Lagrangian method. Chapter 5 assessed the complete water budget of the UM10.4 climate model and incorporated model budget increments into the Lagrangian calculation, and found the total sublimation of ice encountered every 6 hours explained most of the remaining difference in time mean and interannual variability of model water vapour. In this chapter, analysis methods of large-scale deposition and additional processes developed in earlier chapters will be applied to climate forcing scenarios to characterise the response of H_2O_{strat}.

Climate models consistently show that higher CO_2 concentrations and warmer sea surface temperatures cause a strengthening of the Brewer-Dobson circulation (Butchart, 2014). The tropopause is also projected to warm and lift under climate change (Kim et al., 2013; Lin et al., 2017). Alongside these changes, models predict a wetter stratosphere under climate change (Gettelman et al., 2010; Oman et al., 2008). However, the predictions of H_2O_{strat} are in poor agreement between climate models. With the incomplete understanding of H_2O_{strat} control in the present climate, the relative role of different processes for future trends may be inaccurately represented in climate models. Particularly, how the multitude

of processes affecting tropical tropopause temperatures will change is uncertain. Therefore, future predictions of H_2O_{strat} remain uncertain.

One previous study had suggested that projections of H_2O_{strat} cannot be explained by large-scale condensation alone (Dessler et al., 2016). This implicates an important role for convective injection of ice above the tropopause to explain model trends. They had applied a similar technique to one of those presented in chapter 5. This hypothesis will therefore be tested in UM10.4 as well as its representation of trends in convective injection and ice microphysics.

First, the climate forcing experiments which were described in section 2.3.1 are re-introduced. Then, section 6.2 examines the forced response of the governing features of the tropical tropopause layer. Similarly to section 5.4, convective injection and ice sublimation gridpoint values will be assessed in section 6.3 to understand changes in the interaction of water vapour and ice. A more detailed view with Lagrangian dry points, and the impact of ice sublimation along trajectories, will then be reported in section 6.4. Implications and limitations are discussed further in section 6.5 and chapter 7.

6.1.1 Method and data

This chapter studies climate forcing scenarios in the atmosphere-only Met Office Unified Model version 10.4 (GA7) (referred to as UM10.4), details of the model configuration and forcing scenarios were introduced in section 2.3.1. As raised there, Butchart et al. (2018) have designed the forcing scenarios as part of the QBOi project, for which Dr A. Bushell conducted the simulations in UM10.4. I have re-run the scenarios to obtain diagnostics to provide complementary analysis of Lagrangian dry point calculations, model water budget, and development of the model-advected instant-dehydration tracer.

Briefly, the repeat year 2002 experiment studied in sections 3.2 and 4.2 and chapter 5 forms the baseline scenario (hereafter referred to as the CONTROL experiment). Major drivers of atmospheric conditions that are predicted to increase with anthropogenic climate change include carbon dioxide concentrations and sea surface temperatures (Intergovernmental Panel on Climate Change, 2013a, chapter 12). The model forcing scenarios applied here increase carbon dioxide concentration and sea surface temperatures. Specifically, CO_2 is doubled and sea surface temperatures are increased uniformly by 2 K in the first case (referred to as $CO_2\times2$,SST+2 K). In the other, CO_2 is quadrupled and 4 K is added to sea surface temperatures everywhere (referred to as $CO_2\times4$,SST+4 K). No other changes are made to chemical drivers of the atmosphere (for example, ozone climatology) or sea ice.

In these experiments, CO_2 concentrations are 373 ppmv, 745 ppmv and 1489 ppmv, respectively. Besides the year 2002 concentration, these approximately span representative concentration pathways (RCP) scenarios RCP4.5 ($\sim$650 ppmv) and RCP 8.5 ($\sim$1370 ppmv) (Moss et al., 2010) as adopted by CMIP5 and the Intergovernmental Panel on Climate Change (Intergovernmental Panel on Climate Change, 2013a; Taylor et al., 2012). Similarly, 2–4 K represents the medium and extreme estimate of ocean warming change associated with that CO_2 concentration change in the 21st century (Intergovernmental Panel on Climate Change, 2013a, Table 12.2).

The thermodynamic impacts in the tropical tropopause layer of increasing carbon dioxide and sea surface temperatures have been investigated separately by Lin et al. (2017), which will be referred to throughout this chapter. The authors find that both effects cause net radiative warming at the tropical tropopause. They describe sea surface temperature increases as the cause of the tropopause lift and stratospheric moistening; by driving higher convection, a stronger Brewer-Dobson circulation, lower static stability occurs at the tropical tropopause layer and results in a dipolar temperature change over the region. Cloud fraction reduces near the tropopause when increasing CO_2 concentrations. Any warming of the tropical tropopause layer induces a wetter tropical stratosphere which ultimately leads to a negative radiative feedback in the tropical tropopause layer.

The setup of Lin et al. (2017) allows for interactive ozone. Because there is no interactive chemistry in the model configuration tested here, there will be no ozone response in the tropical tropopause. Ozone is not a leading order effect, but can provide a positive feedback on temperatures in this region (Ming et al., 2017). Therefore, changes in the tropical tropopause may be stronger in a configuration with interactive ozone.

6.2 Differences in governing processes

6.2.1 Stratospheric water vapour

The vertical profile of q is shown in figure 6.1a (as 20 °N–S zonal mean) for each of the climate forcing experiments. The time mean concentration of $\sim$5 ppmv in the CONTROL case at 18 km resembles the value reported in table 4.1. It is clear that future forcing scenarios are wetter throughout 15–30 km column displayed in the figure. The altitude of smallest concentrations in the lower stratosphere has risen from 17.4 km to 18.0 km.

The effect of methane oxidation appears at the top of the CONTROL profile in figure 6.1a as a slight positive gradient. No effect occurs in the stratosphere of $CO_2 \times 2$,SST+2 K and

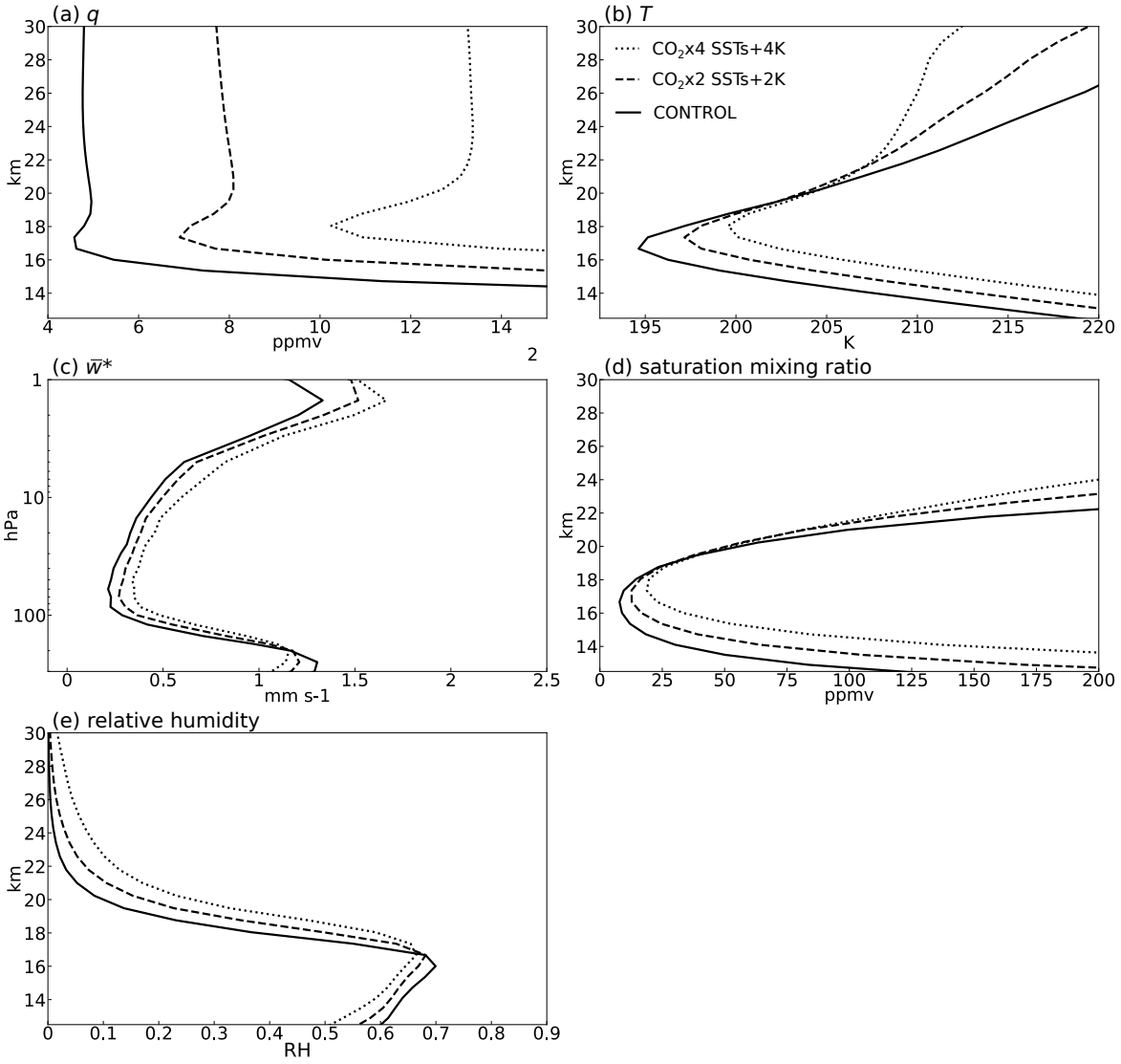

Fig. 6.1 Vertical profile of standard diagnostics in the climate forcing experiments. Calculated from 20 °N–S zonal mean monthly mean values across the same 12 years timeseries as for Lagrangian calculations in chapter 5 and section 6.4. (a) model water vapour, (b) temperatures, (c) upwelling strength of the Brewer-Dobson circulation (transformed Eulerian-mean residual vertical velocity (Andrews et al., 1987), note the different vertical scale and extent), (d) saturation mixing ratio, and (e) relative humidity.

$CO_2 \times 4$,SST+4 K cases because water vapour concentrations are so high that the parameterised hydrogen budget is unable to supply water vapour.

The climatological annual cycle of q in each climate forcing experiment is shown in figure 6.2 at 18 km 30 °N–S zonal mean. The average concentrations are similar to results discussed above. With increased climate forcing, the amplitude of the annual cycle also increases. The peak around September does not change timing on average, but the minimum

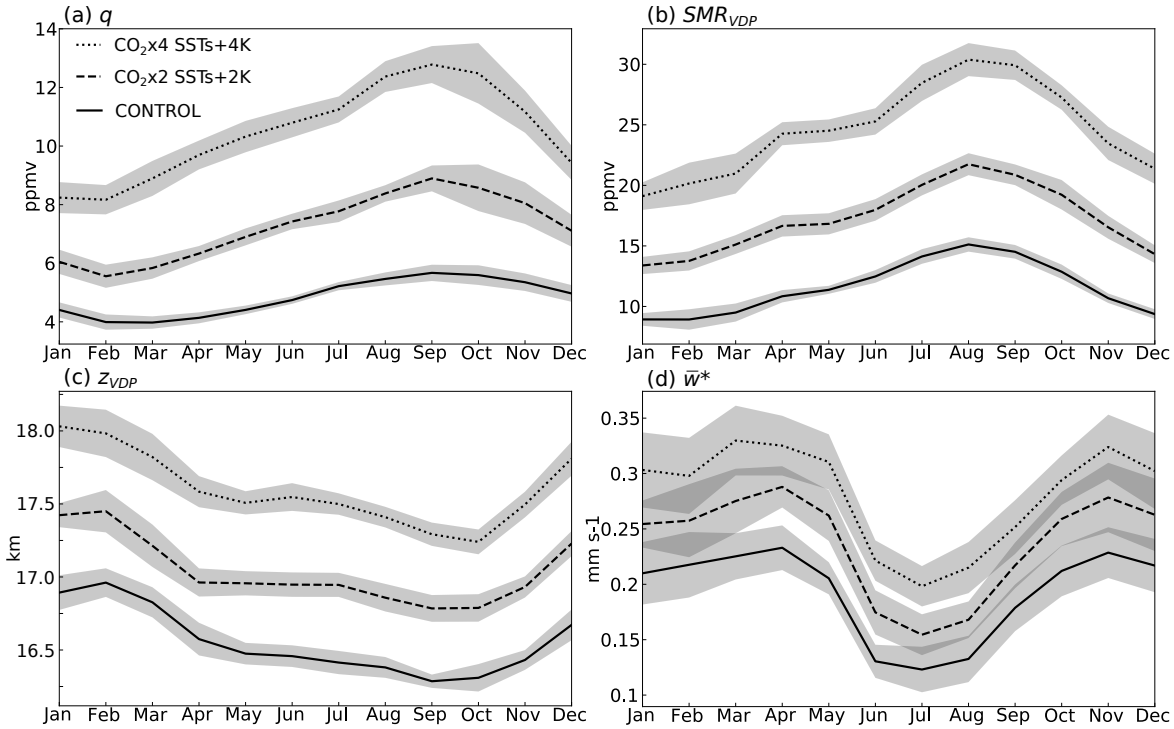

Fig. 6.2 Climatological annual cycle of diagnostics from each of the climate forcing experiments. Showing 30 °N–S zonal mean monthly mean over timeseries of 6 hourly datapoints of (a) model water vapour at 18 km, (b) saturation mixing ratio of vertical dry point, (c) altitude of vertical dry point, (d), residual vertical velocity at 85 hPa. Shaded region indicates one standard deviation for each monthly mean. The 12 year timeseries used for (b,c) is the same as for Lagrangian calculations in chapter 5 and section 6.4, while timeseries is 32 years for (a,d).

is slightly earlier. This appears as a stronger drying phase in October-January and a slower moistening phase in February-September.

Table 6.1 presents tropical timeseries statistics of q in its top two rows. The other rows are described in subsequent sections of this chapter. The same columns are reported as in table 4.1. The table reports for each climate forcing scenario, the time mean (μ), the deseasonalised monthly mean standard deviation (σ), the correlation of this timeseries with q at 18 km (R^2 as described in section 4.2), and the percentage increases of mean and standard deviation from CONTROL ($(\mu/\mu_0 - 1)$ and $(\sigma/\sigma_0 - 1)$ respectively). The CONTROL results are repeated from table 5.2, and the climate forcing impact from the different methods of incorporating sublimation in Lagrangian calculations are discussed later in section 6.4.4. Significant changes occur for each measure.

Model water vapour is shown at 18.0 km and 70 hPa to show the similarity between the different vertical level coordinates in the lower stratosphere. In the CONTROL case,

they have a similar time mean (μ_0) and standard deviation of deseasonalised monthly mean timeseries (σ_0). In the $CO_2 \times 2$,SST+2 K case, their average concentrations (μ) are 56 % and 47 % higher respectively. The standard deviation in their deseasonalised timeseries is also increased. In the $CO_2 \times 4$,SST+4 K case, they are 110–129 % higher than in the CONTROL case. These average concentrations of q in the lower stratosphere are in agreement with figure 6.1a and figure 6.2a.

The dominant causes of these changes will be investigated in the next section.

6.2.2 Temperatures and circulation

Stratospheric water vapour concentrations are predominantly influenced by temperature in the tropical tropopause. More precisely, it is the saturation mixing ratio which determines minimum concentrations of water vapour. Impacts on temperatures and saturation mixing ratios in the tropical tropopause are the focus of this section.

A robust prediction in global climate models that resolve the stratosphere is a stronger Brewer-Dobson circulation, in response to increased wave driving from the troposphere beneath (Butchart, 2014). Figure 6.1c shows the vertical profile of tropical time mean upwelling strength of the Brewer-Dobson circulation ($\overline{w}^*$), confirming its increase in these UM10.4 experiments. Figure 6.2d shows the average annual cycle of tropical mean Brewer-Dobson upwelling strength at 85 hPa in the forced experiments. These show a pronounced seasonal cycle with weakest upwelling in boreal summer months and strongest upwelling in winter and spring.

Increased Brewer-Dobson circulation upwelling tends to raise the altitude of the coldest temperatures in the tropical tropopause. Indeed, Figure 6.1b shows the tropical time mean profile of temperatures and the coldest level of the CONTROL case is 16.7 km, whereas in the $CO_2 \times 4$,SST+4 K case it occurs at 18.8 km. The overall result in $CO_2 \times 2$,SST+2 K and $CO_2 \times 4$,SST+4 K is a warming and lifting of the coldest level in the tropics, caused by both increased CO_2 concentration and increased sea surface temperatures (Lin et al., 2017). This has been seen in other global climate models (for example, CMIP5 temperature profiles are compared in Figure 1a and 9 of Kim et al., 2013).

The climate forcing response of temperatures is different in the troposphere and the stratosphere. Tropospheric warming results primarily from sea surface temperature changes (Lin et al., 2017), which act in combination with convective mixing to warm the entire troposphere. The stratosphere cools due to the radiative impact of increase CO_2, which

Table 6.1 Water vapour trends (ppmv) reported by various calculations, and vertical cold point temperatures (T_{VCP}, K). Using ten years of monthly mean data for time mean (μ), and standard deviations (σ) and correlations (R^2) are from the deseasonalised timeseries, as defined in section 4.2. Correlations have zero lag, except where starred (*) with offset of +1 month. Trajectories are 30 °N–S at 75 hPa. Online tracer, q_{trac} is configured with 300 hPa lid, and statistics are taken from 18.0 km, 20 °N–S, in years 32–41 from initialisation. Note that q_{trac} calculations are in a non-identical experiment of the same configuration (model state, including q, is not identical with other experiments at any instant, but is subject to the same forcing and reaches statistically similar trends.)

		CONTROL			$CO_2\times2$,SST+2 K					$CO_2\times4$,SST+4 K				
	section	μ_0	σ_0	R^2	μ	$\frac{\mu}{\mu_0}-1$	σ	$\frac{\sigma}{\sigma_0}-1$	R^2	μ	$\frac{\mu}{\mu_0}-1$	σ	$\frac{\sigma}{\sigma_0}-1$	R^2
q (70 hPa)	6.2.1	5.0	0.13	-	7.8	56 %	0.34	161 %	-	11.4	129 %	0.57	338 %	-
q (18 km)	6.2.1	5.0	0.16	-	7.3	47 %	0.41	156 %	-	10.4	110 %	0.53	228 %	-
T_{VCP}	6.2.2	192.9	0.52	0.50*	195.1	1.2 %	0.83	59 %	0.35*	197.5	2.4 %	0.60	16 %	0.62
SMR_{VDP}	6.2.2	5.9	0.42	0.39*	9.0	53 %	0.69	65 %	0.50*	13.9	135 %	1.07	158 %	0.50
$SMR_{VDP10\%}$	6.2.2	3.4	0.31	0.42*	5.1	50 %	0.49	60 %	0.63*	7.7	126 %	0.64	109 %	0.59
q_{trac}	6.4.1	2.4	0.12	0.70	3.9	65 %	0.19	57 %	0.84	6.4	171 %	0.39	219 %	0.84
q_{LDP}	6.4.3	3.0	0.10	0.60	4.6	54 %	0.24	137 %	0.62	6.9	132 %	0.35	250 %	0.71
q_{ice}	6.4.4	4.6	0.17	0.85	6.9	49 %	0.37	117 %	0.92	9.9	115 %	0.55	226 %	0.83
q^F_{ice}	6.4.4	10.0	0.55	0.50	14.4	44 %	1.05	91 %	0.76	20.1	101 %	1.56	183 %	0.71
$q_{\Delta sub}$	6.4.4	4.0	0.21	0.29	6.1	54 %	0.40	87 %	0.52	9.1	128 %	0.54	153 %	0.58
$q^F_{\Delta sub}$	6.4.4	5.6	0.39	0.15	8.6	53 %	0.70	79 %	0.41	12.7	126 %	0.97	146 %	0.38
$q_{\Delta conv}$	6.4.4	4.4	0.23	0.33	6.8	53 %	0.43	92 %	0.59	10.1	128 %	0.64	179 %	0.55
$q^F_{\Delta conv}$	6.4.4	7.6	0.54	0.32	11.3	49 %	0.90	67 %	0.45	16.2	114 %	1.34	149 %	0.53

makes the atmosphere optically thicker to long-wave radiation, reducing the amount incident on the stratosphere from below, and therefore reduces radiative heating.

Figure 6.1d shows the tropical time mean profile of saturation mixing ratio, whose minimum level is also at higher altitude and higher concentration in $CO_2 \times 2$,SST+2 K and $CO_2 \times 4$,SST+4 K. Importantly, this shows a lift in the vertical dry point. There is an annual cycle in both concentrations and heights of monthly mean of 6 hourly vertical dry points within 30 °N–S which is shown in figure 6.2b and c respectively. The concentrations are highest in August and lowest in January, following the same pattern as temperature. The average altitude of vertical dry points is lowest in September-October and highest in January-February, in agreement with present day observations (for example, Kim and Son, 2012, Fig 5b).

Kim et al. (2013) perform an intercomparison of atmosphere-only global climate models across scenarios of climate change, focusing on temperatures in the tropical tropopause. In the strongest forcing scenario, RCP8.5, models warm at 100 hPa and levels beneath, while at 70 hPa and above they cool. This results in a lifting of the vertical cold point levels, which despite variety in model results is statistically significant. Importantly, the warming beneath and cooling above coincide at the vertical cold point. Therefore, small changes in the thermodynamic balance of the tropical tropopause layer can alter the projected trends in temperatures in the tropical tropopause layer.

Also in this region, the results of Kim et al. (2013) show the temperature seasonal cycle on pressure levels weakens, but is unchanged at the level of the zero-lapse-rate tropopause. The cause is suggested to be coincident changes in seasonal altitude of zero-lapse-rate temperatures. They suggest trends in Brewer-Dobson circulation and prescribed ozone are the drivers of seasonal changes.

Alongside model water vapour in table 6.1 are timeseries statistics in each climate forcing experiment for Eulerian estimates (as 10 °N–S zonal mean monthly mean) including: temperatures at tropical vertical cold points (T_{VCP}), saturation mixing ratios at tropical vertical dry points (SMR_{VDP}), and the saturation mixing ratios of the driest decile of tropical vertical dry points within 30 °N–S ($SMR_{VDP10\%}$). All three variables show an increase in climate forcing scenarios. SMR_{VDP} and $SMR_{VDP10\%}$ average concentrations increase roughly proportionally to the change in q. SMR_{VDP} and $SMR_{VDP10\%}$ also show increases in standard deviation of their timeseries in stronger forcing scenarios much like q, associated with the increased concentrations.

The correlations of deseasonalised timeseries with lower stratospheric model water vapour at 18 km have a lag of one month in CONTROL and $CO_2 \times 2$,SST+2 K experiments

Table 6.2 Number of gridpoint values exhibiting convective injection of ice (left) and net sublimation (right) above the vertical dry point in climate forcing scenarios. The table reports monthly mean (N) and standard deviation of monthly mean (σ_N) across the two year sample.

	convective injection		net sublimation	
	N	σ_N	N	σ_N
CONTROL	6560	1871	57627	8931
$CO_2\times2$,SST+2 K	8160	1431	75970	7514
$CO_2\times4$,SST+4 K	9575	1196	90859	5078

(indicated by *), but the highest correlations in the $CO_2\times4$,SST+4 K case are with zero lag, suggesting a shorter transit time for dehydration signals to propagate from the dry points to 18 km. This is due in combination to the higher tropopause, and stronger Brewer-Dobson circulation. Changes to correlations in the climate forcing scenarios are not consistent, probably due to the one month change in lag of the highest correlation and the monthly resolution of this timeseries.

In summary, the warmer and higher tropical tropopause layer is anticipated to moisten the stratosphere. The stronger Brewer-Dobson circulation appears to reduce transit times into the tropical lower stratosphere.

6.3 Differences in ice above the tropopause

As investigated in chapter 5, ice above the vertical dry point has the potential to rehydrate the tropical lower stratosphere. Because of the inhomogeneous and intermittent nature of ice events in this region, they are not well resolved by large-scale average views. Instead, to identify trends in ice above the tropical tropopause, an alternative method is applied.

Two sets of gridpoint events are identified. The first set are where ice is injected by convection (defined as a positive increment to ice from the model's convection scheme, as applied to $q_{\Delta conv}$ in table 5.1) at or above the local vertical dry point. This is expected to be the strongest source of ice in the region. The second set are gridpoints undergoing net sublimation (an extension of the study in section 5.4) at or above the vertical dry point. This set will directly indicate changes to the rehydration of the tropical lower stratosphere.

For each of the three climate forcing experiments (CONTROL, $CO_2\times2$,SST+2 K and $CO_2\times4$,SST+4 K), the events are gathered from a two year sample of 6 hourly instant

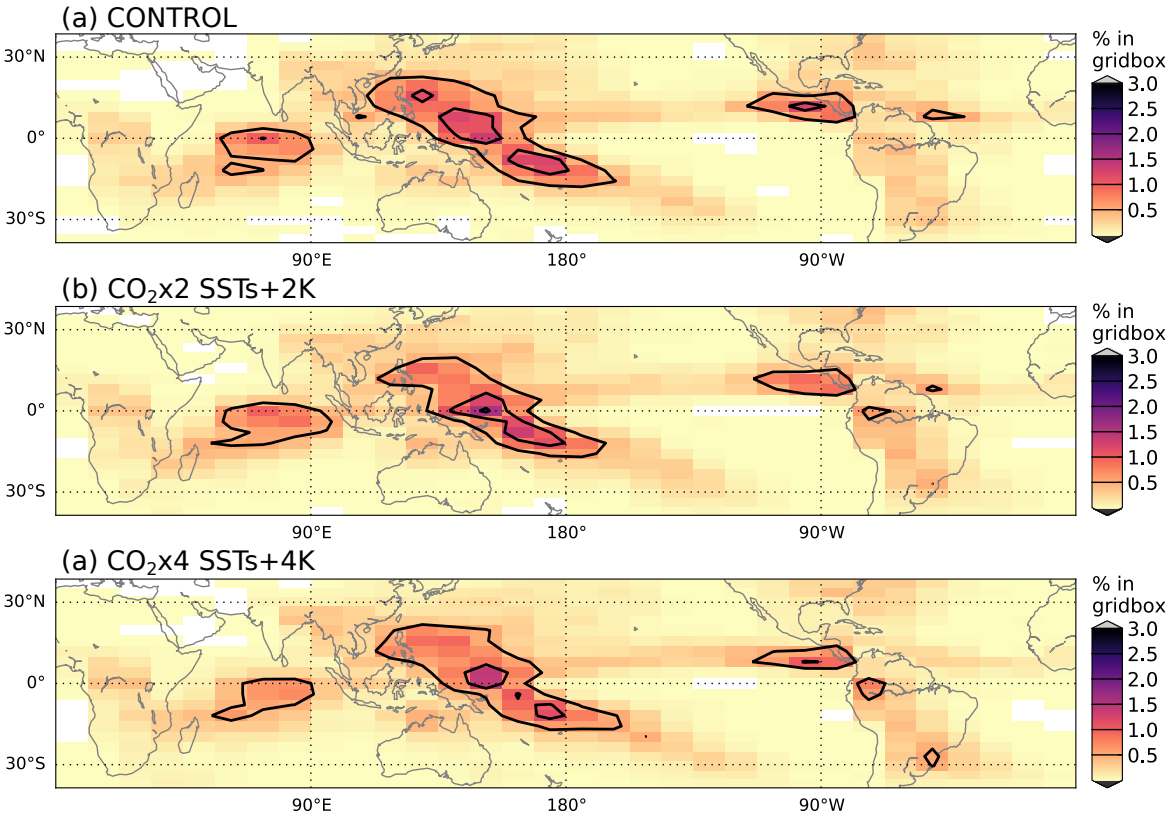

Fig. 6.3 Horizontal distribution of convective ice injection events over 10 years [kg/kg/gridbox], (a) CONTROL, (b) $CO_2 \times 2$,SST+2 K, (c) $CO_2 \times 4$,SST+4 K.

values. Both sets of convective injection events and above-tropopause sublimation events are analysed for trends in frequency, intensity and spatial distribution.

Table 6.2 reports the mean (and standard deviation) number of gridpoints exhibiting particular ice increments above the vertical dry point each month. There are increases to the number of convective injection events with climate forcing, but it is not larger than the spread from standard deviations. However, sublimation event frequency increases more significantly.

This raises the question of how ice sublimation increases frequency without a corresponding change in frequency of deep convection. One remaining possibility for the effect to be due to convective injection is if the quantity of ice lofted increases. Additionally, whether there is also a change in quantity of ice sublimated above the vertical dry point remains to be seen. The causes of this distribution, and potential changes in intensity of convection and sublimation, will now be investigated further to understand these differences.

6.3.1 Convective injection

Figure 6.3 shows the horizontal distributions of convective injection events. Compared to the CONTROL case, there is no change in distribution. This is expected because both the spatial and temporal variability of sea surface temperatures remain the same in each experiment and convection surpassing the tropopause is associated with only the most intense events. With a uniform increase in sea surface temperatures, some regions that were previously not warm enough may now show convection. At the same time, the intensity of all locations that were warm enough in CONTROL will now be stronger. The spatial pattern corresponds to the highest reach of convective events, and therefore with a uniform increase in forcing their relative strength is unchanged.

At the same time, there is a change in the vertical extent. Figure 6.4a shows the vertical distribution of convective events injecting ice above the vertical dry point. CONTROL experiment peaks at the model level at 16.0 km, and the stronger experiments peak at 16.7 km and 17.4 km. However, there appears to be no change relative to the height of the local vertical dry point. Figure 6.4b shows this offset for all scenarios is very similar. This points to a lifting of the tropical tropopause, in agreement with Lin et al. (2017).

The change in altitude comes with a change in saturation mixing ratio distribution. Figure 6.4c shows saturation mixing ratio at each event increases with climate forcing. This is expected from the warming of the tropical tropopause (figure 6.1d). Without a response in water vapour, this reduces relative humidity and will encourage sublimation of lofted ice. This is discussed further in the next section.

Figure 6.4d offsets this distribution from saturation of vertical dry points. The same relationship is seen in forcing scenarios, but weighted towards larger differences, suggesting a stronger vertical gradient in saturation mixing ratio above the vertical dry point.

Overall, this sees convective events lift, corresponding exactly to the lifting of the vertical dry point. Additionally, the saturation mixing ratio at events of convective injection is higher.

6.3.2 Sublimation

Section 5.4 demonstrated that in UM10.4 ice sublimates above the vertical dry point in present-day conditions. Typically, sublimation occurs near 16–17 km, at relative humidities that do not exceed saturation, and only a very small fraction of ice is lost through sublimation at each timestep (figure 5.6). The rest of chapter 5 demonstrated that this has an impact on H_2O_{strat}, partly due to the different vertical levels of final modification by dehydration and ice rehydration. Section 6.3.1 indicated that, with climate forcing, ice lofted above the

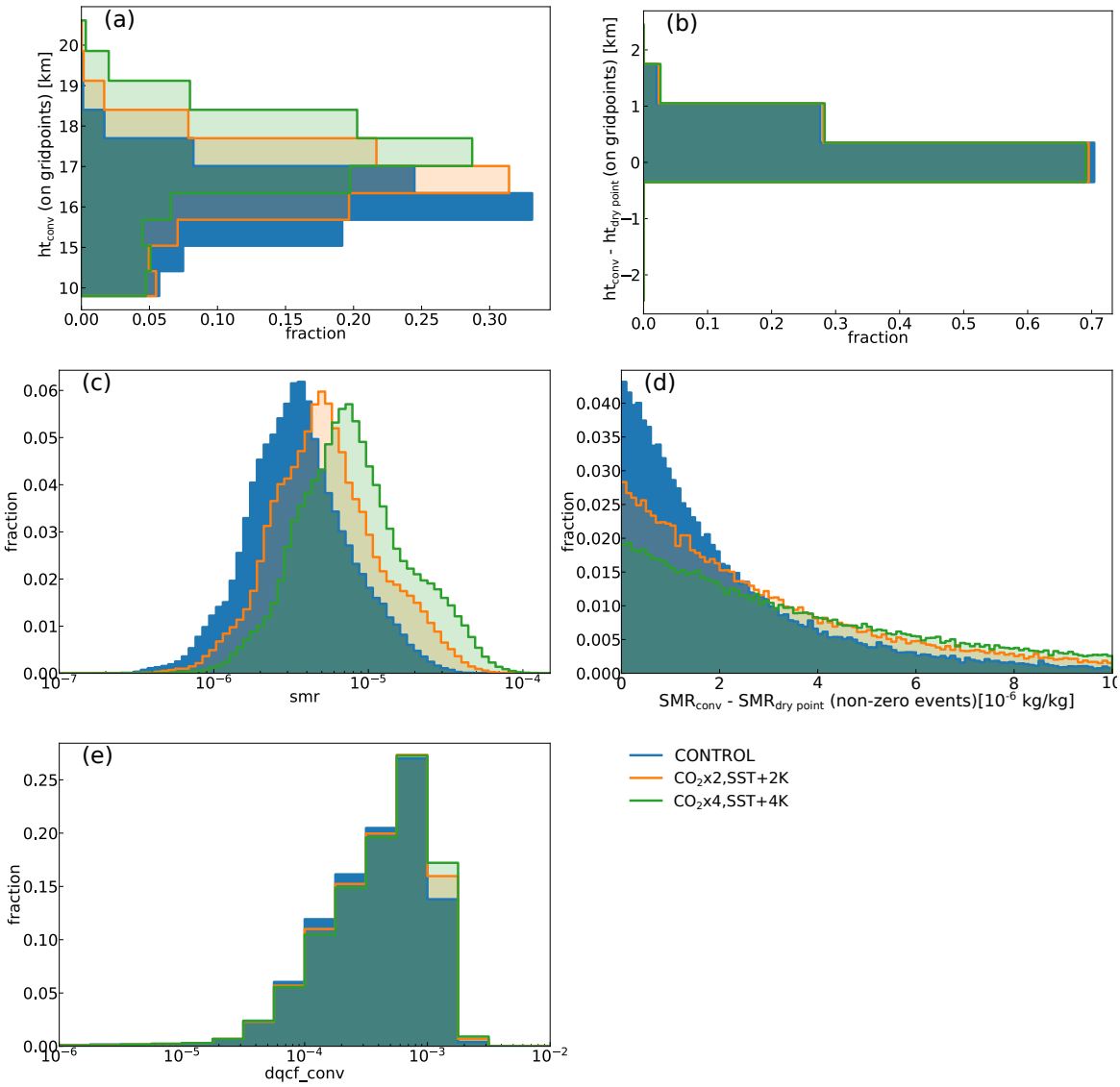

Fig. 6.4 Distributions of gridpoint values above the vertical dry point exhibiting convective ice injection within 40 °N–S. Showing (a) vertical distribution, (b) vertical offset from vertical dry point, (c) saturation mixing ratio at convection events, (d) difference between saturation mixing ratio at convection events and at vertical dry point, (e) quantity of ice lofted (kg/kg/6hr).

vertical dry point changes altitude but not quantity. This section investigates whether ice sublimation above the vertical dry point responds to the imposed forcing at all, as this could provide more evidence for a role in influencing H_2O_{strat} trends.

As for convection above the tropopause, the horizontal distribution of sublimation events changes little, as shown in figure 6.5. Also like overshooting convection, the vertical extent of ice sublimation has changed. Figure 6.6a shows the vertical distribution of sublimation

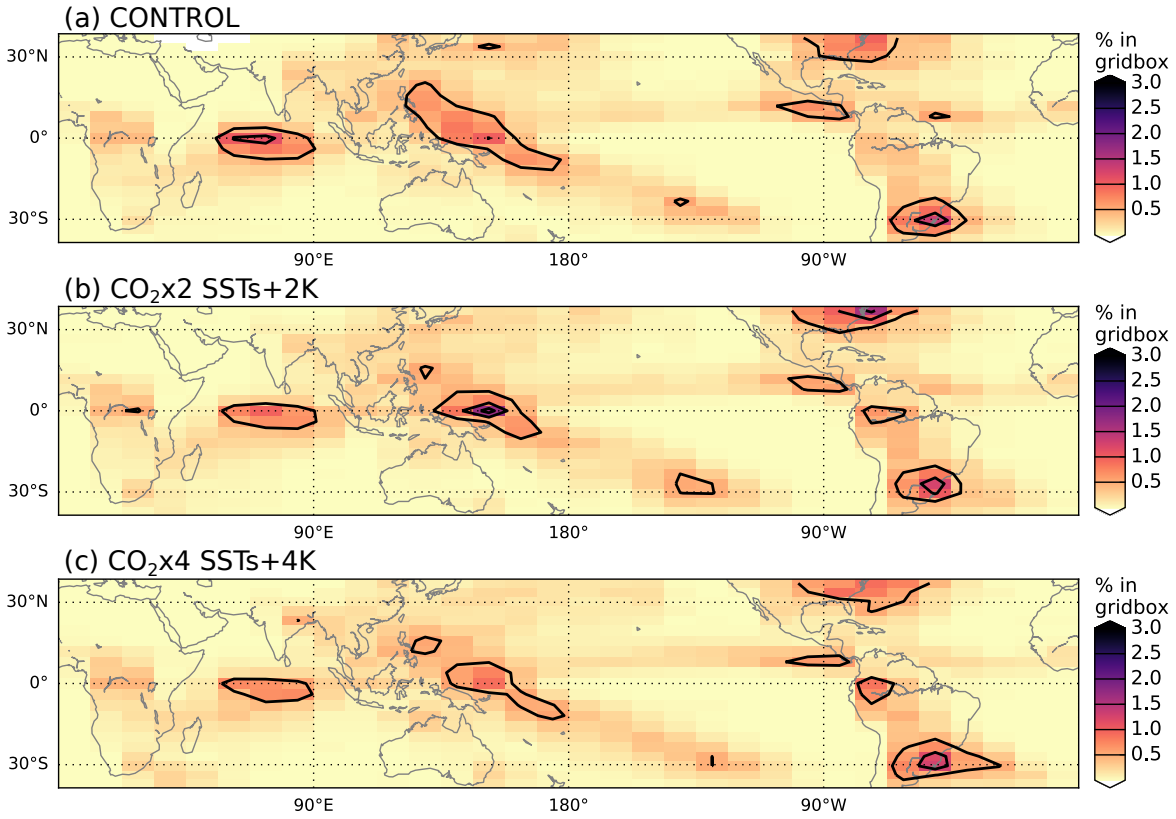

Fig. 6.5 Horizontal distribution of ice sublimation events [kg/kg/gridbox] over 10 years for (a) CONTROL, (b) $CO_2 \times 2$,SST+2 K, (c) $CO_2 \times 4$,SST+4 K.

events occurring above the vertical dry point. For each experiment in order of increasing forcing strength, the peak is at 16.0 km, 16.7 km and 17.4 km. These are slightly broader and higher than distributions of convective injection. Again, there appears to be no change relative to the height of the local vertical dry point, in figure 6.6b. The ice that sublimates can arrive from convective injection and large-scale deposition (the effect of sedimentation and advection is only to redistribute ice within the tropical tropopause layer). Because the distribution of sublimation events and convective events are very similar — with sublimation more spread out — it appears that sources of sublimation are primarily from convection.

Table 6.2 shows an increase in frequency of sublimation events. The full distribution of sublimation increments is broad as shown in figure 6.6c, indicating a large spectrum of physical activity across the two years. This makes sense as the sublimation process is dependent on a number of highly variable conditions: ice availability, q concentration, temperatures and pressures. Seeing these overall changes with two years of data from each experiment may not remove interannual variations (for example, QBO phase). However, this

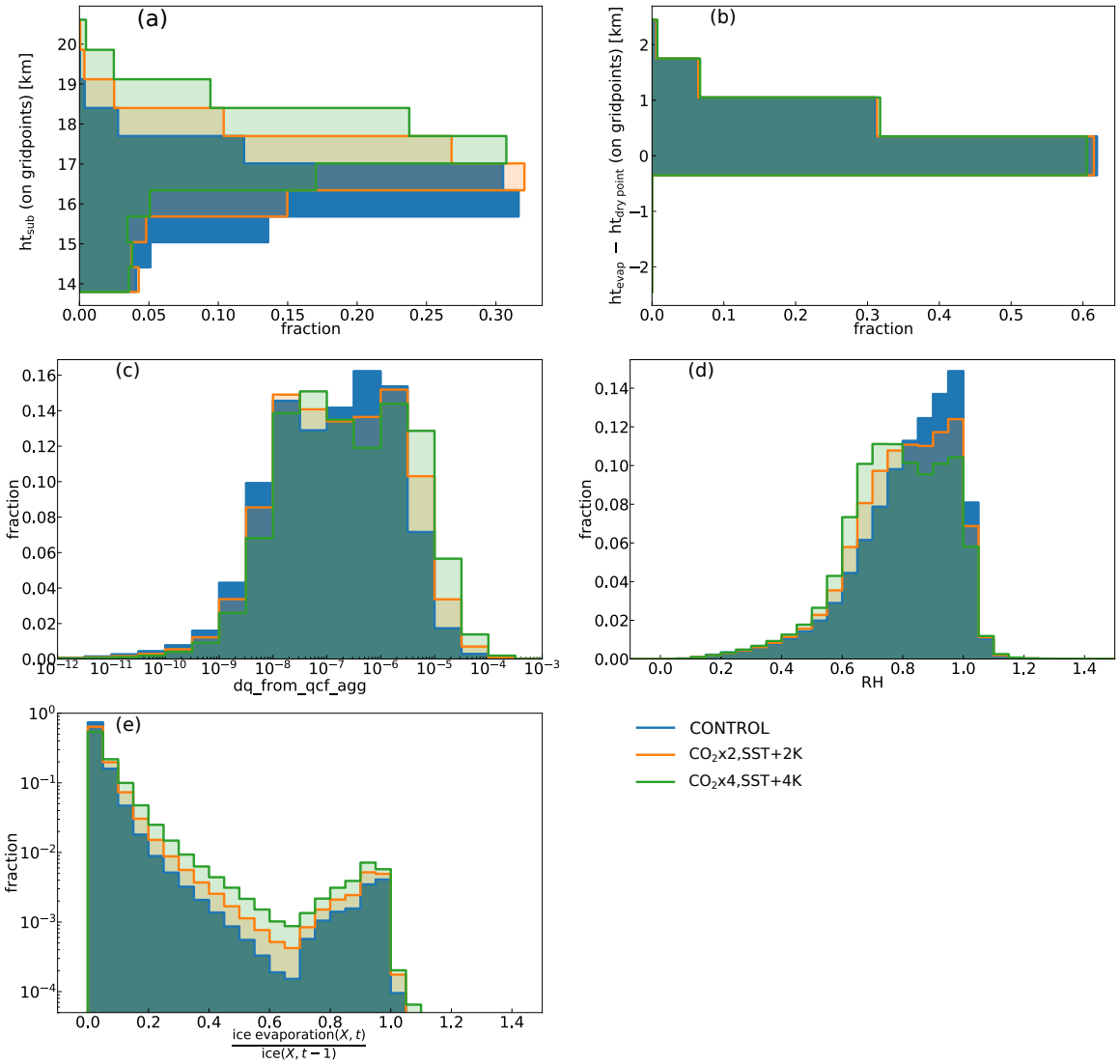

Fig. 6.6 Distributions of gridpoint values above the vertical dry point exhibiting net sublimation of ice, within 40 °N–S. (a) Altitude, (b) vertical offset from vertical dry point, (c) amount of ice sublimated (kg/kg/6hr), (d) relative humidity, (e) fraction of ice sublimated. No sublimation events occurred between 19–25 km and most events occurred between 10 °S-25 °N.

evidence motivates the Lagrangian calculation which will be carried out over a longer time period later in this chapter.

Figure 6.6d shows the local relative humidity at each sublimation event; a broader set of relative humidities are seen, the peak at 80–100 % in CONTROL has broadened to 65–100 % for the $CO_2 \times 4$,SST+4 K scenario. Additionally, figure 6.6e shows the fraction of total ice that sublimates, which has also broadened. These results also suggest an increased influence of sublimation as well as higher intensity and frequency.

This may appear at odds with the results for overshooting convection events, which are the principal source of lower stratospheric ice, since its frequency and intensity have not changed. But, it is not necessary for total convectively injected ice to increase in order to have an effect. Because it reaches higher where it is warmer, the local saturation limit is also increased, therefore broadening event RH distribution, and therefore enabling sublimation of larger quantities more often.

The implication for H_2O_{strat} is that while the displacement of both ice injection and sublimation from the tropopause may be no different, there may be more extensive moistening from ice sublimation in the future scenarios.

The gridpoint value analysis here clarifies the response of ice above the tropopause in UM10.4 climate forcing scenarios. The tropopause and overshooting convection extend higher in altitude. However, convection appears to be neither intensified nor extended further above the tropopause. Instead it is the higher saturation mixing ratios (causing lower relative humidity) at this elevated level that may allow a greater moistening from the ice clouds that are present.

However, whether this has any overall impact on H_2O_{strat} remains to be seen. Most rehydration processes occur in the troposphere, well before the low saturation mixing ratios of the tropical tropopause. Similarly for overshooting convection, subsequent dehydration can occur again and may lead to very little hydration of the stratosphere. For that, a Lagrangian analysis will be clearer.

6.4 Differences in Lagrangian calculations

The previous sections determined changes in various driving processes of q in the climate model forcing experiments in the previous section. To quantify their impact, the following analysis will consider the impact on calculations of Lagrangian dry points, and of the model-advected instant-dehydration tracer.

6.4.1 Tracer advected by global climate model

Section 3.3 introduced a tracer subjected to the UM10.4 advection scheme and instantaneous dehydration. This assessed the difference in H_2O_{strat} estimate from the advection-condensation method due to choice of transport scheme.

It found the predicted concentrations to be sensitive to the frequency of dehydration in two ways. More frequent sampling of dehydration resulted in a lower concentration in

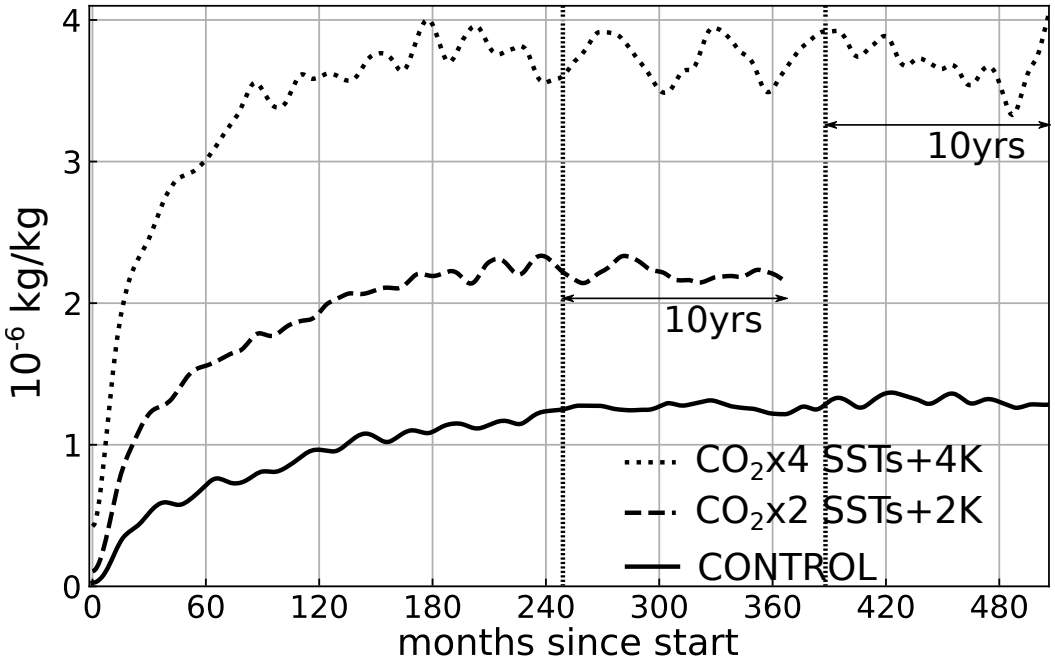

Fig. 6.7 Showing low-pass filtered timeseries of equatorial tracer concentrations at 20 km altitude across climate forcing experiments. Vertical dotted lines mark ten years before records end, the time period used for analysis.

the stratosphere as expected, but also a stronger vertical attenuation of concentrations. The once-in-6 hourly dehydration case found similar concentration to the Lagrangian dry point method (which uses a 6 hourly data series to advect and dehydrate trajectories) above the tropical tropopause layer. The tracer's concentrations found closer similarity in seasonality and distribution to q than the Lagrangian dry point method, suggesting a small but noticeable improvement in representation of q from applying a more similar transport scheme.

This section presents results of how the tracer behaves in the climate forcing scenarios. The tracer configuration applies the once-in-20 minute sampling frequency case. The CONTROL experiment here is an extension of what was reported in section 3.3.1.

Spin-up differences

To reach an equilibrium state, the tracer evolution is followed for 42 years for the cases of CONTROL and $CO_2 \times 4$,SST+4 K. Owing to computational limitations, $CO_2 \times 2$,SST+2 K is recorded for only 31 years. Figure 6.7 shows the tracer concentration spin up in the tropical lower stratosphere in each of the climate forcing experiments. In all cases, concentrations have equilibrated before the last ten years of each record (months 145–369 for $CO_2 \times 2$,SST+2 K, otherwise months 384–508).

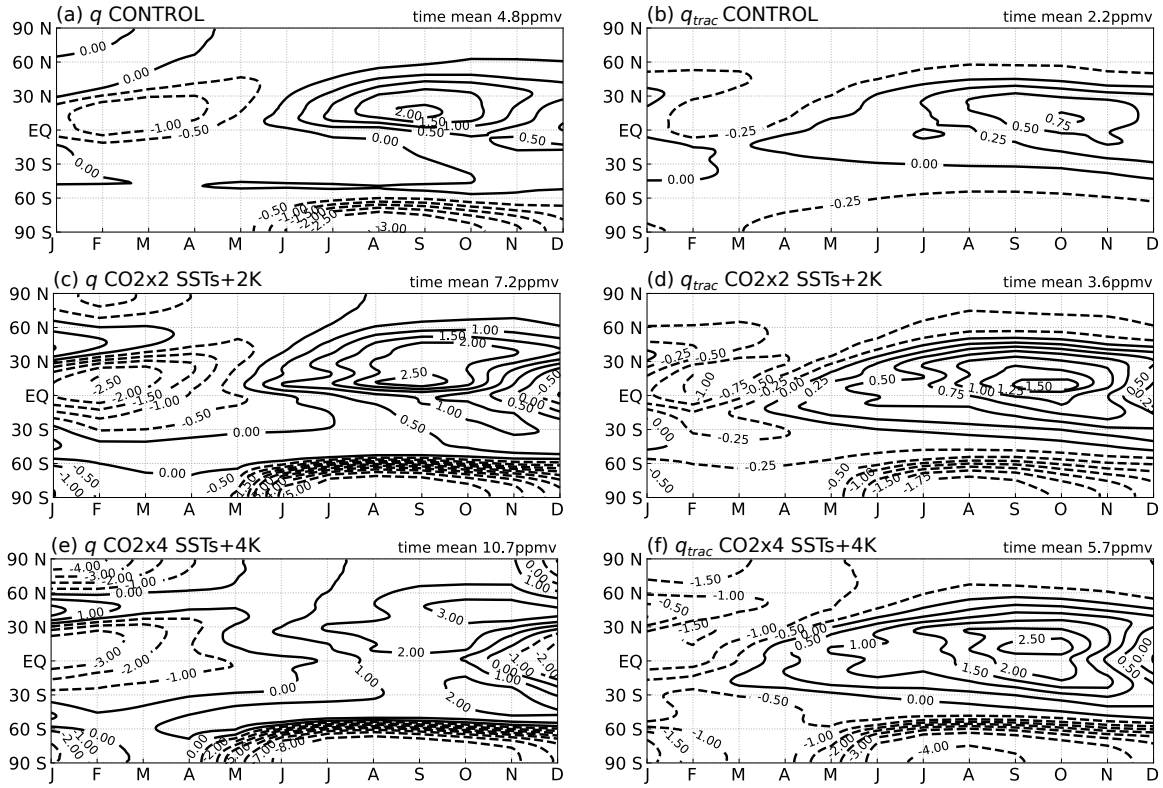

Fig. 6.8 Average annual cycle of zonal mean anomaly from zonal mean time mean (a,c,e) model water vapour and (b,d,f) model-advected instant-dehydration tracer in climate forcing experiments, (a,b) CONTROL, (c,d) $CO_2\times2$,SST+2 K, (e,f) $CO_2\times4$,SST+4 K, at 18 km over years 32–41. (a,b) are repeated from figure 3.17. Note that the contour levels are (b,d) 0.25, (a,c,f) 0.5, (e) 1.0.

Concentration in stratosphere

The statistics for the tracer in the climate forcing scenarios are shown in Table 6.1. Like q, the tracer moistens when CO_2 concentrations and sea surface temperatures are increased. As was shown in chapter 3, it is dry biased, predicting about half the concentration of the modelled water vapour. Proportional to CONTROL values, the tracer trends are stronger than for q.

Furthermore, comparing correlation (R^2) of q_{trac} and q_{LDP} with q in the forcing scenarios, the model-advected tracer continues to explain more of the variance of the model water vapour. This suggests the effect of transport scheme continues to be relevant in future forcing scenarios, despite a stronger Brewer-Dobson circulation and therefore reduced transit times which cause less time for the influence of transport differences.

Figure 6.8 shows the average annual cycle across all latitudes for model water vapour and the dehydration tracer in the forcing experiments. As in the CONTROL case reported in

section 3.3, the tracer's structure and timing resemble model water vapour to some extent. The poleward propagation of tropical anomalies is clear in both q and the tracer across forcing scenarios. The tracer is clearly dehydrated in the Antarctic polar night in forcing scenarios where concentrations are higher.

In the stronger forcing scenarios, the maximum anomalies in q shift to the mid-latitudes (particularly August-December, 30–60° N and S). The locations suggest it is related to monsoon processes. Because it is not seen in the tracer response, it may be due to rehydration processes. Looking at figure 6.5 as an indicator for mid-latitude rehydration processes (as far as possible), the large contributions may originate over North and South America. Further investigation is needed to confirm.

These results show the tracer transport by the climate model is a useful tool to inspect model water vapour processes. This is even when taking into account its over-efficient dehydration and overly-strong vertical dissipation with once-in-20 minute dehydration sampling. To improve the robustness of these results, further analysis of dehydration locations and potentially providing a rehydration process to the tracer, could be considered.

6.4.2 Lagrangian dry point configuration sensitivity

With the applied climate forcing scenarios, there are corresponding changes in the tropical tropopause layer which is typically warmer and higher. This demands a reconsideration of the vertical levels at which to initialise back-trajectories. This section will test and justify the key parameters of trajectory initialisation across climate forcing experiments.

Section 2.4.2 tests the sensitivity of the configuration of Lagrangian dry points in climate forcing scenarios, finding 75 hPa initialisaiton level suitable for all forcing scenarios studied here.

6.4.3 Lagrangian dry point without sublimation

Table 6.1 reports the results of the climate forcing experiments for Lagrangian estimates of water vapour calculations. As introduced in section 5.5.2 and described in table 5.1, q refers to climate model water vapour concentration in the tropical lower stratosphere and subscripts and superscripts describe alternative calculations, including the Lagrangian dry point (LDP).

In agreement with Dessler et al. (2016), total changes of the Lagrangian dry point method are insufficient to explain the change in modelled water vapour. However, table 6.1 shows the Lagrangian prediction is a relatively dry value in CONTROL. Considered proportionally to values in CONTROL, increases are $\sim$50 % for $CO_2\times2$,SST+2 K and $\sim$110–130 % for

$CO_2 \times 4$,SST+4 K. These are roughly the same proportional increases in q. This suggests that the Lagrangian dry point method does not describe the total increase to model water vapour but it is effective at describing the proportional change. The over-efficiency inherent in the Lagrangian dry point method appears to also respond to the climate forcing scenarios. This is further discussed later.

Figures 6.9 and 6.10 show for $CO_2 \times 2$,SST+2 K and $CO_2 \times 4$,SST+4 K scenarios the average annual cycle of Lagrangian dry points, their predictions for H_2O_{strat}, model water vapour and other proxies, in the same way as figure 3.8 showed for CONTROL. The consistent dry bias is apparent. As was seen in chapter 3, the phase of the annual cycle is well represented by the Lagrangian method. The lower panel of each figure peaks for the first month which indicates shorter transit time than the CONTROL case, consistent with a stronger Brewer-Dobson circulation and lifted tropical tropopause. This leads to an earlier signal in H_2O_{strat} prediction (solid black line) with reduced time lag from tropopause temperatures (minimum shifts to February from March, and maximum moves to October from November). The tropopause temperatures represented by vertical dry points (coloured dashed lines) agrees with figure 6.2b.

The horizontal distributions of Lagrangian dry points and vertical dry points for February and August are shown in figures 6.11 and 6.12 for $CO_2 \times 2$,SST+2 K and $CO_2 \times 4$,SST+4 K respectively. The higher concentrations corresponding to the 10 % and 25 % contours for the distribution of vertical dry point signify the higher temperatures in the tropical tropopause layer. Otherwise, the spatial distributions change little for both vertical and Lagrangian dry points, which suggests no movement of governing processes, namely tropical convection. The sea surface temperature modification amplifies what spatial pattern is already present, thereby strengthening convective activity over oceans.

The Asian summer monsoon is also a governing process over the spatial pattern, which appears to be unmoved. It is associated with both land-sea temperature contrast and moisture content of air originating from the Bay of Bengal. Therefore, it also strengthens with warmer sea surface temperatures (raising specific humidity), as well as land surface warming from higher CO_2 concentrations (Turner and Annamalai, 2012). Extensive multi-model comparisons suggest some ability of global climate models to represent the Asian summer monsoons (Sperber et al., 2013) and project the East Asian monsoon to strengthen slightly across the 21st century (Jiang and Tian, 2013).

Across the climate forcing experiments, the correlation of deseasonalised timeseries between model water vapour and Lagrangian dry point predictions remains high (R^2 >60 %).

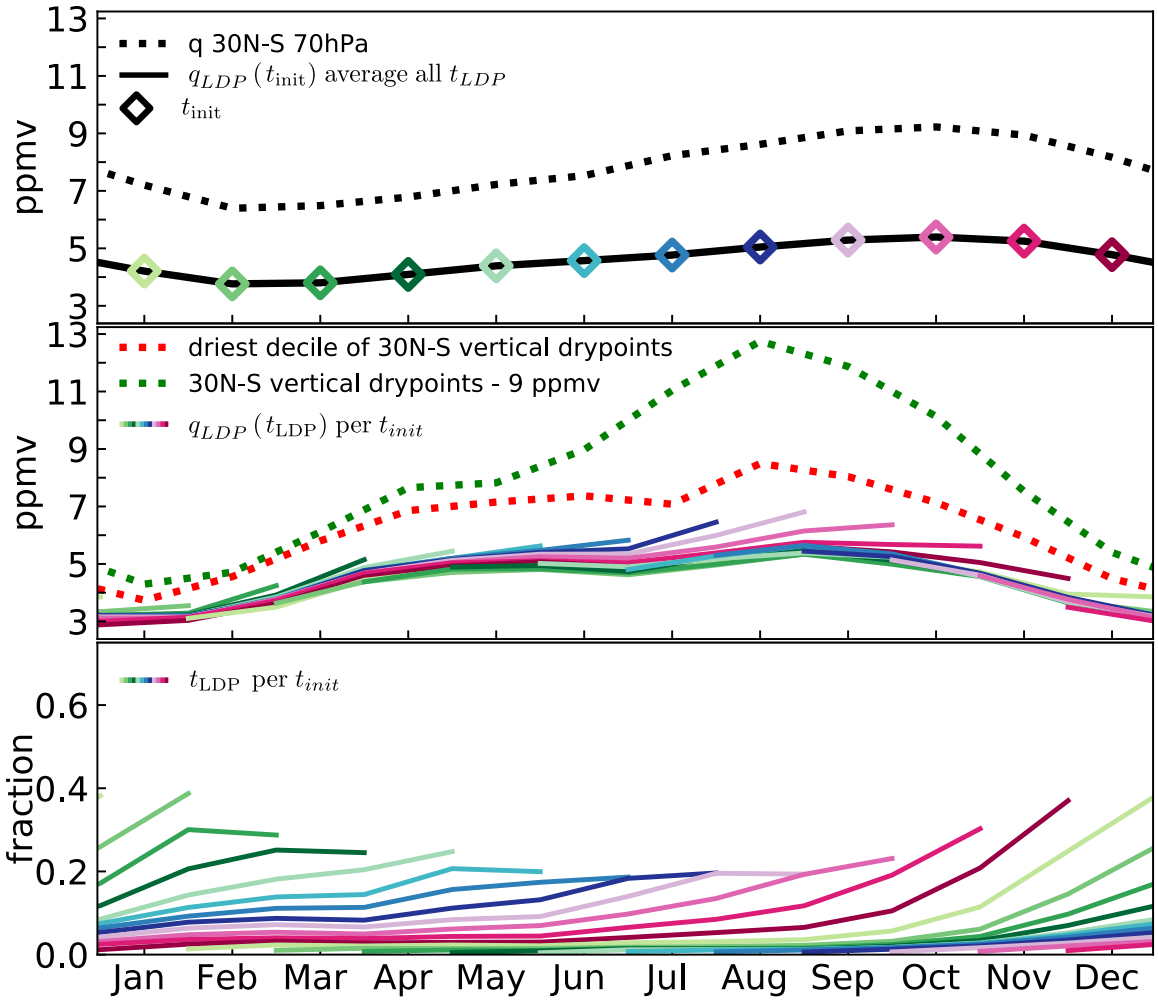

Fig. 6.9 As for figure 3.8, average annual cycle of UM10.4 $CO_2 \times 2$,SST+2 K tropical lower stratospheric water vapour, vertical minimum of saturation mixing ratios (vertical dry points), and kinematic Lagrangian dry point calculations. Data spans 10 years and trajectories are released within 30 °N–S and initialised (t_{init}) monthly at 75 hPa. Results separated into (top panel) mixing ratios of model water vapour (q) at 70 hPa and Lagrangian predictions at 75 hPa, (middle) fraction contribution of Lagrangian dry point events each month (t_{LDP}) for each release date (t_{init}).

Therefore, pathways and temperatures in the tropopause retain control, despite stronger vertical advection and being warmer.

6.4.4 Lagrangian dry point with sublimation

Table 6.1 shows the climate forcing response of Lagrangian calculations with different methods of rehydration. These include Lagrangian dry point with subsequent rehydration by

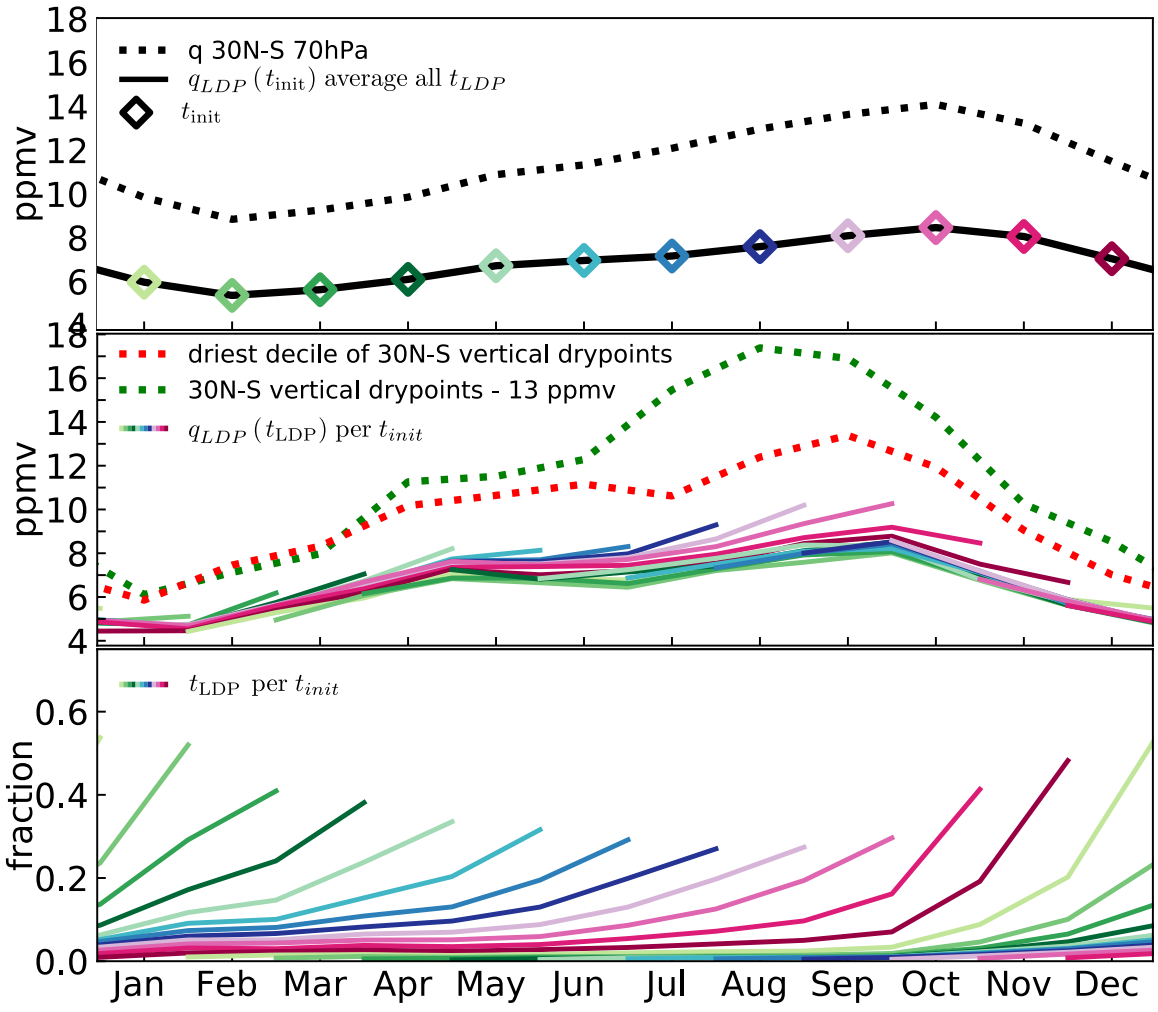

Fig. 6.10 As for figures 3.8 and 6.9, but for UM10.4 $CO_2\times4$,SST+4 K experiment.

ice indicators of ice water content (*ice*), net sublimation increment (Δsub) or net convective ice injection increment ($\Delta conv$). A superscript of F is for rehydration calculations where the quantity being rehydrated is fixed to $F = 1$, forcing the parcel to local saturation, as introduced in equation (5.5). Here too, all Lagrangian based estimates of $H_2O_{\rm strat}$ show significant and similar proportional change. Time mean estimates of $H_2O_{\rm strat}$ are 44–54 % wetter in $CO_2\times2$,SST+2 K scenario, and 101–132 % wetter for the $CO_2\times4$,SST+4 K case. As a result, the similar concentration of q_{ice} to model water vapour in the CONTROL case continues in the future forcing scenarios.

In the CONTROL case, it was shown earlier (section 5.5.2) that the height of final modification was sensitive to the method adopted to incorporate ice sublimation in Lagrangian calculations (figure 5.10). For the climate forcing scenarios, the comparable results are shown in figure 6.13. First, it is clear that the vertical distribution of Lagrangian dry points without

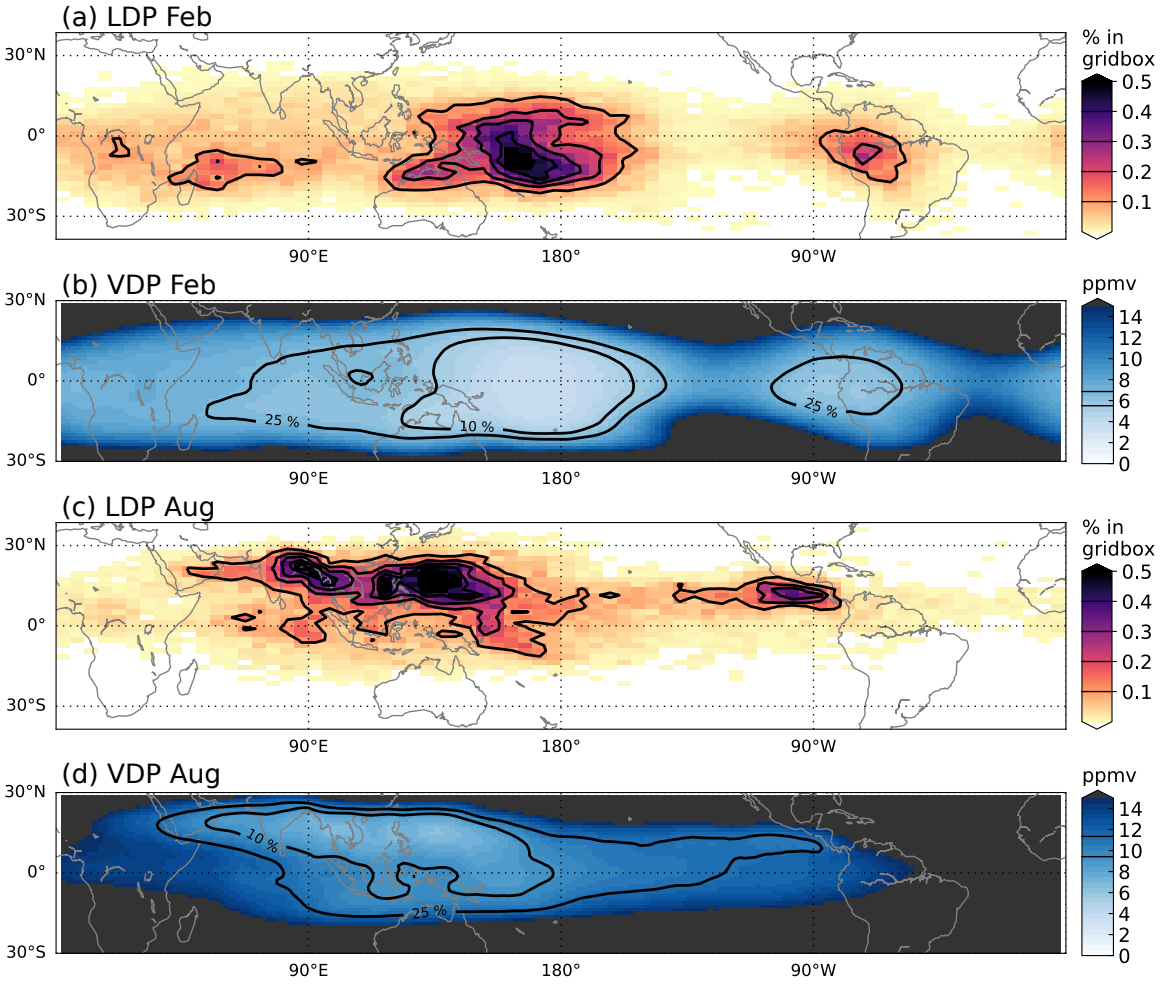

Fig. 6.11 As for figure 3.9, but for UM10.4 $CO_2 \times 2$,SST+2 K experiment, averages are over 11 years. (a,c) Lagrangian dry points in February and August, (b,d) vertical dry point events of the same months.

rehydration has shifted upwards with climate forcing, as expected from results earlier in this chapter (figure 6.1). Consistent with this, and gridpoint analysis in section 6.3, the distributions of final ice modification events also lift. The differences in height distribution between methods of rehydrating trajectories remain the same in $CO_2 \times 2$,SST+2 K and $CO_2 \times 4$,SST+4 K, albeit with less contrast. As raised in section 5.5.2, there appears to be further modification from ice indicators to H_2O_{strat} predictions at altitudes above the 75 hPa level.

Correlations of deseasonalised monthly mean variability with q generally improve, some more than others. As in CONTROL, the only ice rehydration measure explaining more variance of H_2O_{strat} than the dehydration-only calculation is q_{ice}. This suggests that the same

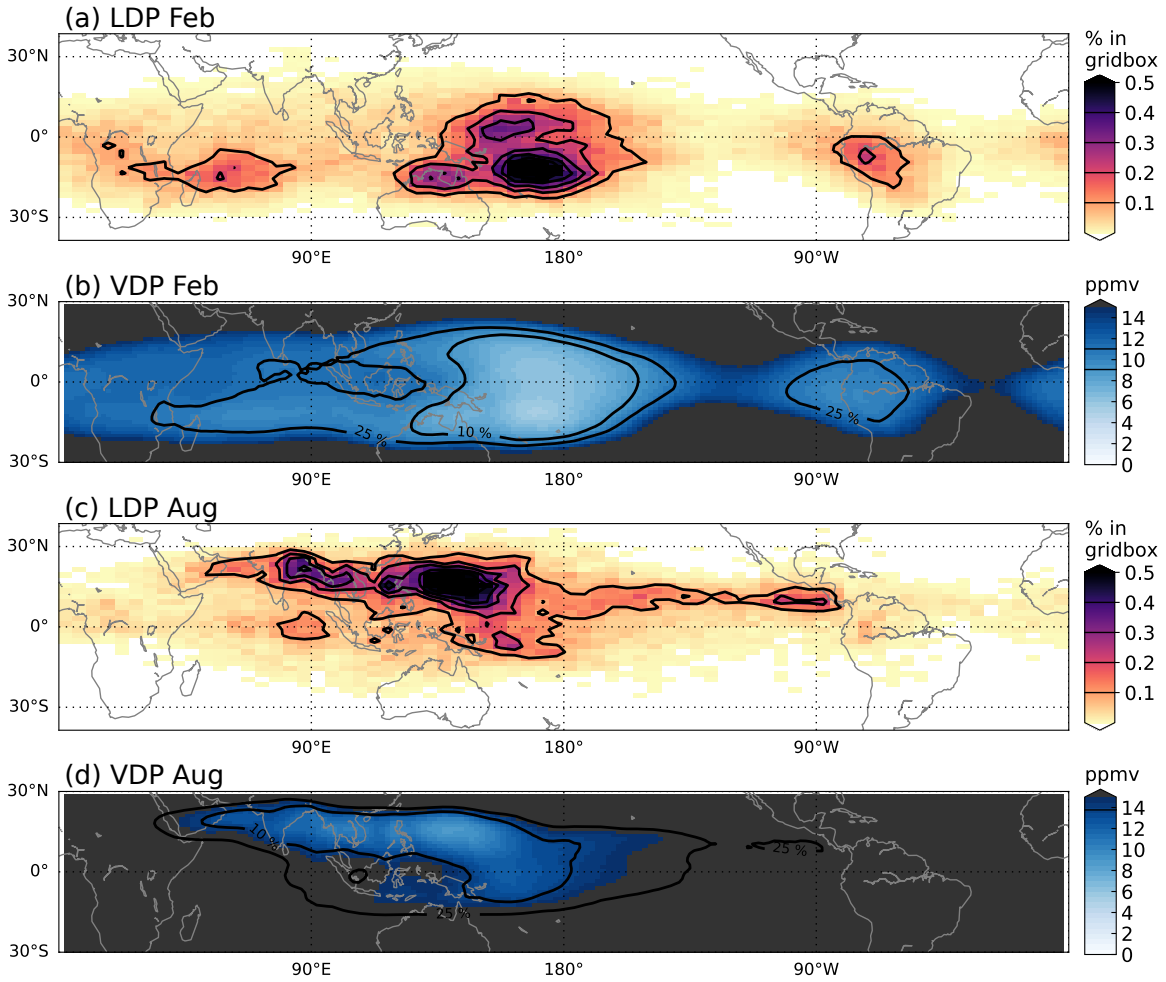

Fig. 6.12 As for figures 3.9 and 6.11, but for UM10.4 $CO_2 \times 4$,SST+4 K experiment, averages are over 11 years. (a,c) Lagrangian dry points in February and August, (b,d) vertical dry point events of the same months.

processes apply in future scenarios. As suggested earlier, the higher correlation may mean a stronger control of the same processes.

6.5 Discussion

The design of the experiments performed in this chapter allows a direct attribution of response to changing CO_2 and sea surface temperatures through atmospheric thermodynamic (dynamical, radiative and convective) interactions. However, the experiments neglect other changes that might be expected (for example, ozone in the tropical tropopause layer due to

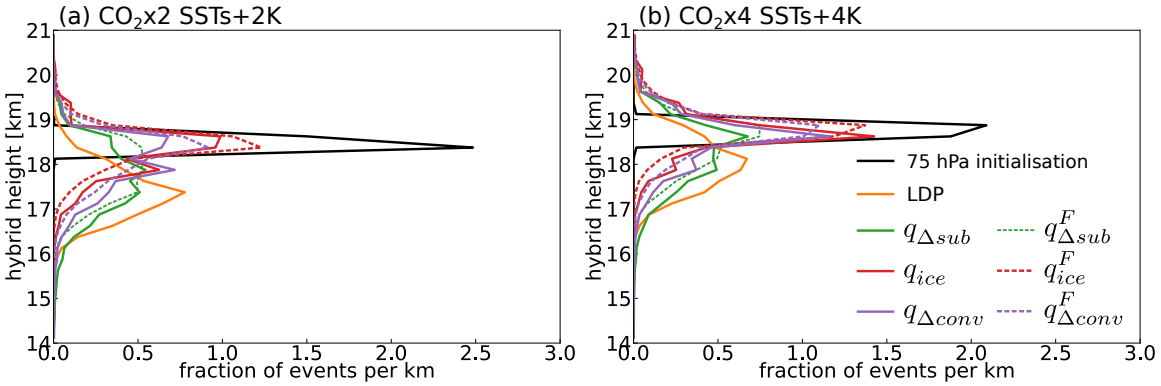

Fig. 6.13 Distribution of final modification events of encountered by trajectories after their Lagrangian dry points, as well as the trajectory initialisation height and the Lagrangian dry point heights, in (a) $CO_2 \times 2$,SST+2 K and (b) $CO_2 \times 4$,SST+4 K experiments, using 10 years of trajectory calculations.

circulation response, and other feedbacks through coupling to an interactive ocean) which would require a global climate model with more complexity.

A separate issue remains over assumed stationarity in model processes. Many aspects of model microphysics are parameterised based on present-day conditions. One relevant aspect for stratospheric water vapour is methane oxidation. As introduced in section 5.2.3, the scheme used in UM10.4 assumes q increases towards $3.75 \times 10^{-6}\,\mathrm{kg\,kg^{-1}}$ (see section 5.2.2 for details), a value determined with observed quantities of methane and a fixed total hydrogen budget in the stratosphere. While methane trends are subject to changes in human activities, Revell et al. (2016) have studied the range of IPCC projections in a chemistry climate model and found that methane has a relatively small impact on H_2O_{strat} compared to temperatures in the tropical tropopause layer. Furthermore, the results of this chapter focus on water vapour trends in the tropical lower stratosphere, therefore modification — or lack thereof — from methane oxidation may be kept separate.

The climate forcing scenarios used here, being similar to other studies, find consistency with a number of publications. Indeed, the setup by Butchart et al. (2018) will be comparable across many global climate models (Bushell et al., 2019; Holt et al., 2019; Richter et al., 2019).

The gridpoint value analyses provide an explicit view of intermittent and inhomogeneous processes otherwise lost in large-scale average views. They highlight the point that, even with convection above the tropopause not intensifying in the climate perturbation experiments, a tropopause that is warmer and higher allows more frequent ice sublimation. This appears to be due to higher temperatures surrounding the tropopause (figure 6.1b) which in turn provide

higher saturation mixing ratios (figure 6.1d), and therefore weaker dehydration. This means that even if convection is the predominant source of ice above the tropopause, its effect on water vapour on the lower stratosphere is dictated by the temperatures of the tropical tropopause layer, just like dehydration.

It is worth noting that all Lagrangian calculations improve R^2 correlation with H_2O_{strat} and with increasing climate forcing (q_{LDP}, q^F_{ice}, $q_{\Delta sub}$, $q^F_{\Delta sub}$, $q_{\Delta conv}$, $q^F_{\Delta conv}$) except for one while the exception (q_{ice}) retains the highest R^2 correlation of all calculations at 83 %. Additionally, the standard deviation of their deseasonalised monthly mean timeseries generally increases. Therefore, it appears that with higher sea surface temperatures and higher CO_2 concentration, the control of temperature and pathways increases and is more variable. This might be due to a number of factors.

Firstly, missing variability in other influences (for example, interannual variability in sea surface temperatures, or ocean circulation) may play a role in this configuration. Comparing climate model simulations with and without, for example, ocean variability will provide indication of their influence on tropopause variability. As raised above, this increases the complexity of the climate model experiment, and is therefore left for further study.

Second, there may be increased variability in tropopause temperatures which dominates the signal of H_2O_{strat} variability. However, the standard deviation of deseasonalised timeseries of vertical cold point temperatures (T_{VCP}) in table 6.1 does not indicate this is the case.

Third, through the non-linear Clausius-Clapeyron equation, the action of a warmer tropopause is to increase water vapour sensitivity to temperature. In this way, the same temperature variability leads to stronger H_2O_{strat} changes (similarly, pressure differences in dry point height become less influential).

These possibilities raise many questions for the involvement of ice in the water budget of the tropical lower stratosphere and in climate models, and are worthy of further study to better constrain trends in H_2O_{strat}.

The different Lagrangian predictions of H_2O_{strat} in table 6.1 consider primary and secondary controls, namely temperature, pathways and potential ice rehydration. The similar responses of all Lagrangian calculations across climate forcing scenarios suggests that obtaining accurate concentrations of H_2O_{strat} from the Lagrangian method is a distinct problem from identifying accurate trends. If so, analysis of anomalies and time mean are separate issues. This is an element of Lagrangian analysis by Fueglistaler et al. (2013) and Liu et al. (2010), particularly where the dehydration over-efficiency of the Lagrangian method follows a temperature offset, suggesting a Clausius-Clapeyron control on the missing process.

To further this idea, trend analysis should be based on proportional, rather than absolute, differences.

This also questions what is the correct prediction of time mean H_2O_{strat}. There is, however, one additional result supporting the processes captured by q_{ice} specifically: the improved correlation. This was discussed in section 5.7, suggesting the idea that, while less accurate than sublimating according to the model's increment for sublimation, the total and instant sublimation of all encountered ice complements the assumptions of the instantaneous dehydration method.

As raised in section 6.1, a similar method of ice rehydration has been applied to two chemistry climate models by Dessler et al. (2016). They identify increasing ice concentrations at fixed levels across climate forcing scenarios. However, ice increases at fixed levels near the present day tropopause are anticipated due to the vertical cold point lifting with increased sea surface temperatures. The results of this chapter find that both the intensity and extent of convective injection of ice is unchanged relative to the vertical dry point. Therefore, there are no changes in convection to directly explain any aspects of trends in H_2O_{strat}. But, the results in this chapter find increases in the amount of ice sublimating, which is due to Clausius-Clapeyron effects in the warming tropical tropopause layer instead of changes in convection.

Dessler et al. (2016) highlight absolute differences between Lagrangian dehydration calculations and model water vapour across the 21st century and invoke trends in convectively injected ice to explain. They do not report the time average concentrations from their Lagrangian dehydration calculations. In most publications, the Lagrangian dry point method is over-efficient and predictions of observed H_2O_{strat} are too dry, when using winds and temperatures from reanalyses (Fueglistaler et al., 2013; Liu et al., 2010; Schoeberl and Dessler, 2011; Schoeberl et al., 2012) and from many climate models (as in figures 3.2, 3.6 and 3.8 and table 5.2). The results in this chapter agree with Dessler et al. (2016) that absolute trends from Lagrangian dry point calculations differ from absolute changes in model water vapour. However, results here also find that proportional trends between the Lagrangian dry point calculation and model water vapour agree closely.

6.6 Conclusions

This chapter analysed the lower stratospheric water response of climate forcing scenarios in the UM10.4 global climate model. Specifically, the impact of increased CO_2 concentrations and sea surface temperatures were considered. Established changes occur: the Brewer-

Dobson circulation strengthens and the tropical tropopause lifts and warms. Correspondingly, the stratosphere is wetter, and in the lower stratosphere humidity is more variable.

Particular efforts were made to characterise the nature of water vapour changes. Results from assessing gridpoint values of convectively injected ice, and ice sublimation, above the vertical dry point indicated that deep convection intensity is unchanged and events remain as close to the tropopause — which itself is lifted — however, the higher local saturation mixing ratios above the tropical tropopause cause an increase to frequency and intensity of sublimation events. This contributed to the moistening of the lower stratosphere in the simulations.

To quantify the impact of temperature, large-scale transport and rehydration, Lagrangian calculations incorporating various indicators of ice rehydration were tested. They all provided the same percentage increases across forcing scenarios as the Lagrangian dry point method and model water vapour. This suggests relative trends are well described even when absolute concentrations are not. In particular, proportional changes to large-scale condensation alone (no ice rehydration modification) are sufficient to explain proportional changes in H_2O_{strat} concentrations in these experiments.

Furthermore this suggests the ability of convective injection to hydrate the stratosphere also follows a Clausius-Clapeyron-like relationship tied to temperatures in the tropical lower stratosphere.

Absolute trends in model water vapour in the lower stratosphere are well described by the Lagrangian calculation rehydrating ice at each timestep in the data timeseries (q_{ice} in table 6.1). Chapter 5 concluded that this calculation showed very high correlation with model water vapour on monthly to interannual scales (85 % of variance explained) in the present day scenario. Table 6.1 found this higher correlation remains in the future forcing scenarios. This motivates further the testing of this parameterisation to a case with observations where possible.

The Clausius-Clapeyron relation may also be the cause of stronger control of temperatures in the future. The same temperature variability in a warmer climate causes larger swings in saturation mixing ratio. Further work may be required to understand trends in temperature fluctuations, and the impact of Clausius-Clapeyron at these different timescales.

Chapter 7

Discussion and conclusions

7.1 Conclusions

The investigations in this thesis clarified the influence of dominant processes affecting water vapour entry to the stratosphere. These processes include large-scale transport, deposition and sublimation, and have been studied on sub-monthly, annual, interannual and century-wide timescales. Primarily using Lagrangian analysis, several novel methods were tested to disentangle their relative roles. Conclusions generally apply to global climate model configurations of the Met Office Unified Model, and some aspects refer to reanalysis and observations.

First, this thesis tested aspects of the advection-condensation method on annual timescales (chapter 3) in ERA-I reanalysis and two global climate model configurations, UM-UKCA and UM10.4. It showed the Lagrangian advection-condensation method — control by temperatures and large-scale transport — obtains many features of model water vapour entering the stratosphere. While the two climate model configurations share many attributes, because of their various differences affecting the tropical tropopause layer, this provides confidence that the processes described by the advection-condensation method are the primary controls of H_2O_{strat} typical to many global climate models. Differences in Lagrangian results are associated with the underlying temperature field in each case (more accurately, the field of saturation mixing ratio, which also depends on pressure, is the constraint but is dominated by the temperature field in this region). Both models exhibit a warm and wet bias in the tropical tropopause layer, as well as different spatial patterns of coldest temperatures in the tropical tropopause. These features persist in the Lagrangian results.

Furthermore, the over-efficiency of the Lagrangian dry point method also occurs in the climate models. The advection-condensation method prediction for H_2O_{strat} in ERA-I, UM-UKCA and UM10.4 is too dry by 1.5 ppmv, 1.6 ppmv and 2.0 ppmv respectively.

Compared to transport in ERA-I, both climate models show a larger spread in transit times from Lagrangian dry points to the 83 hPa initialisation level. In an attempt to test the advection-condensation method with transport more similar to the global climate model advection scheme, in section 3.3 a tracer was transported by the UM10.4 advection scheme and subjected to instantaneous dehydration. A number of numerical refinements were needed to resolve the strong vertical gradient changes of the saturation field in the tropical tropopause layer as well as an implemented threshold altitude for a wet troposphere. The difficulty was resolved by substituting the saturation field with its logarithm (plus an offset) in numerical calculations. This affects vertical attenuation of signals in the stratosphere. The vertical attenuation rate agrees with model water vapour when the tracer samples dehydration at a rate within 3–24 hours. This work therefore found subtle details of numerical advection are important to H_2O_{strat} calculations in a climate model.

At the same time, seasonal and latitudinal variability of the model-advected tracer are similar to model water vapour (figures 3.14 and 3.17). The agreement in seasonality and distribution of concentrations in the tropical lower stratosphere is closer than Lagrangian calculations. These results suggest the effects of climate model transport not captured by Lagrangian transport, such as mixing and higher resolution of integration, explain most of the small differences between their estimates of lower stratospheric water vapour in the annual cycle.

Having determined the influence of temperature and large-scale transport on average concentrations of H_2O_{strat}, the impact on the annual cycle from mis-representing sub-seasonal temperature fluctuations was quantified for reanalysis and UM-UKCA (section 3.4). Earlier studies identified some impact without taking account of changes to the timing of Lagrangian dry points (Fueglistaler et al., 2013), and quantified the impact without relating to observations and climate models (Bonazzola and Haynes, 2004).

Kim and Alexander (2015) have found the sub-seasonal temperature fluctuations at the tropical tropopause in the west Pacific Ocean are under-represented in ERA-I. The results of section 3.4 showed that the sub-monthly temperature fluctuations in ERA-I cause a cooling effect of 2.52 K and a drying effect of 1.04 ppmv. This is $\sim$47 % of the Lagrangian prediction using 6 hourly temperatures, identifying the importance of resolving sub-monthly temperature fluctuations accurately in advection-condensation estimates of H_2O_{strat}.

For UM-UKCA, section 3.4 identified smaller sub-monthly temperature fluctuations at Lagrangian dry points (1.7 K) but a larger impact on Lagrangian estimates of H_2O_{strat}, of 1.7 ppmv ($\sim$30 % of the Lagrangian prediction using 6 hourly temperatures). The larger impact is a result of Clausius-Clapeyron scaling. A different structure of sub-monthly temperature fluctuations was also found compared to ERA-I, suggesting under-representation of the associated processes, highlighting one shortcoming of model estimates of H_2O_{strat} that contributes to the climate model wet bias.

Building on the study of the importance of temperature and transport on annual timescales and time averages, chapter 4 tested their roles in the interannual variability of H_2O_{strat}. Section 4.2 compared the deseasonalised monthly mean timeseries of methods to estimate stratospheric water vapour in reanalysis, and the climate models UM-UKCA and UM10.4. These results confirmed that, for the variability in stratospheric water vapour in UM-UKCA and UM10.4, the Lagrangian dry point method explains 84 % and 60 % respectively. This is more than from any of the Eulerian measures of tropical tropopause layer temperatures considered. The model-advected tracer subjected to dehydration in UM10.4 explained 70 % of variability in model water vapour, suggesting that transport scheme differences are responsible for some of the difference in predicted water vapour variability.

Motivated by this, and the study of Hasebe and Noguchi (2016) which had suggested winds were influential in one particular event of the H_2O_{strat} timeseries, the abrupt drop in year 2000, section 4.3 applied a novel method for separating the control of temperatures and transport on interannual variability of the Lagrangian dry point method. In the 11 year series studied in ERA-I reanalysis, this is informative for interannual and seasonal timescales. On interannual scales, agreement was found with the consensus in literature that almost all variability (67–88 %, table 4.2) is due to temperature. What is most interesting from the calculation is that the interannual variability of H_2O_{strat} can be reproduced very closely with any one year of wind fields. The conclusion was particularly clear for the year 2000 drop. Despite this, work also hinted at some variability in transport efficiency across the years studied, particularly 1999 and 2008 show years where winds were more influential. A longer timeseries would be required to determine this further. On seasonal timescales, transport patterns are important, particularly in the summer months.

Repeating these calculations to isolate the control of temperatures and large-scale transport in UM-UKCA reached the same conclusions, pointing to the same proportional control as in ERA-I reanalysis.

At this stage, after temperatures and large-scale transport, the influence of the next most dominant processes was accounted for. The additional information provided in the

context of a global climate model was utilised. In chapter 5, the analysis of complete water budgets confirmed the presence of ice above the final dehydration points identified by the advection-condensation method. The detailed relationship with model convection was reported, suggesting a convective moistening of water vapour in the lower stratosphere.

This information was then used in different ways to rehydrate the simple Lagrangian dry point method. In that sense, it attempted to complete the water budget of the Lagrangian calculation using additional fields. Results showed that ice fields are generally insufficient to rehydrate air parcels to their saturation mixing ratio (section 5.5.2), partly because saturation increases strongly with altitude above the region of final dehydration.

Of the trajectory rehydration methods tested, only one improved both time-mean concentrations and variability of predicted model water vapour (concentration relative to model q increased from 60 % to 92 %, and variability explained increased to 85 %, table 5.2). This approach sublimates all ice encountered along trajectory pathways, testing at every datapoint (6 hourly) and retaining an upper limit of saturation. While this total and instantaneous sublimation is not fully realistic, it complements the simplicity of the instantaneous dehydration approximation. Promisingly, it might also be tested with ice observations.

The results of model-based rehydration of Lagrangian calculations also clarified aspects of a published method which were unclear (Dessler et al., 2016). The conclusion of chapter 5 was that ice concentrations above the tropical tropopause are not always larger than the difference between local humidity and saturation mixing ratio. Therefore, methods that are limited by saturation mixing ratio and test for ice sublimation along trajectories more frequently than the available ice field timeseries will over-count the effect of rehydration.

Finally, having tested the relative roles of temperatures, transport and sublimation, climate forcing scenarios were then conducted in chapter 6. The anticipated changes of a warming and lifting tropopause and stronger Brewer-Dobson circulation were clear in the results of section 6.2. They are reflected in a wetter and quicker water vapour signal propagating through the tropical stratosphere. Events of convective injection of ice tracked the elevated tropopause, and otherwise appeared unchanged (section 6.3.1). However, with higher local saturation mixing ratios, ice sublimated more often (section 6.3.2).

For all ice rehydration methods, the moistening with climate forcing was the same proportionally (for $CO_2\times2$,SST+2 K, they moistened by 44–54 %, and for $CO_2\times4$,SST+4 K by 101–128 %, table 6.1). Furthermore, this proportional increase was similar to the Lagrangian dry point method and to model water vapour ($CO_2\times2$,SST+2 K, respectively wetter by 54 % and 47 %; $CO_2\times4$,SST+4 K, 132 % and 110 %). This leads to two conclusions. First, estimating absolute trends for water vapour is a separate issue to estimating relative

changes. Therefore, the absolute trends reported by Dessler et al. (2016) are not meaningful without knowing the absolute concentrations that their methods report. Secondly, trends in sublimation above the tropical tropopause appear to be constrained by the same saturation limit processes rather than some outside influence such as convective injection.

To clarify, correctly estimating present day concentrations is a matter for detailed parameterisation. Nevertheless, projections of relative change across the 21st century apply separately. The results of this thesis suggest changes to H_2O_{strat} across this century can be treated as observed values around year 2000 ($\sim$3.7 ppmv) plus the percentage changes reported in table 6.1 (44–128 % depending on scenario).

The conclusions of chapters 5 and 6 may also explain the mystery of why corrections for a dry bias take the form of a constant temperature offset (of +3 K, Liu et al. 2010) in calculation of the saturation field. The other ice microphysical processes that are not captured in the simple advection-condensation method, including influence from convective lofting, appear to follow the same Clausius-Clapeyron relationship, because they scale similarly with climate forcing. The horizontal and vertical extent of convective processes may experience saturation limits that are proportional to the Lagrangian dry point. Therefore, applying a positive temperature offset accounts for contributions from a distribution of higher saturation mixing ratios.

Furthermore, the correlation relationships increased with climate forcing in all estimates of model water vapour in the lower stratosphere. This points to a stronger control from temperatures and large-scale transport. Such an influence from temperatures might be expected because the warmer tropical tropopause layer will lead to increased water vapour sensitivity in the Clausius-Clapeyron relation. The fundamental sensitivity of model water vapour concentrations in the stratosphere to climate forcing may be investigated further.

The ideas and results presented in this thesis contribute to current understanding of processes governing water vapour entry to the stratosphere. Many aspects relate directly to model representation of this strong and variable greenhouse gas, offering new insights to improve accuracy of predictions of climate variability, as well as projections across this century.

7.2 Discussion

The overall objective of this thesis has been the study of processes determining stratospheric water vapour. By applying Lagrangian calculations of the advection-condensation method to global climate models, experiments have isolated the role of the key influences of tem-

peratures, transport and ice across various timescales. This discussion will first consider the focus on entry values of H_2O_{strat}, then discuss limitations and implications of the advection-condensation method by considering in turn the potential ways that included processes are mis-represented, and how unaccounted processes may be incorporated. Next, the relevance of results to climate model development and other climate models will be discussed, followed by consideration of the mechanisms underlying the primary processes controlling H_2O_{strat}.

The Lagrangian dry point method (described in section 2.4) was applied throughout this thesis, which considered only the entry values of water vapour entering the tropical lower stratosphere. This directed investigations on the primary source of stratospheric water vapour. Concentrations in the rest of the stratosphere may be considered to be determined from concentrations of the tropical lower stratosphere, with sufficient resolution of advection processes (both large-scale Brewer-Dobson circulation and small-scale mixing) and methane oxidation, which are well represented in chemistry transport models (for example, Poshyvailo et al., 2018). There is also an influence of transport processes on water vapour within the extratropical lower stratosphere which has also been studied separately (Riese et al., 2012).

One limiting aspect is that analysis considers only the trajectories transported to the stratosphere from the troposphere. It has taken no account of other transport contributions in the trajectory set. There are some ways to do so, for example, forward trajectory calculations or assigning some original value to back-trajectories originating in the stratosphere. Water vapour in the stratosphere is generally homogeneous and slightly more humid than immediately above the tropical tropopause. Therefore, for the two examples described, accounting for them is expected to introduce a systematic moistening in the tropical tropopause layer and the stratosphere, thereby raising mean values and reducing interannual variability. This is why the studies in this thesis focus only on comparing observations and models in the tropical lower stratosphere: concentrations in this region are considered to have the strongest control from the processes governing water vapour entry to the stratosphere.

There are multiple physical processes that may have been neglected by analysing the advection-condensation method, potentially raising conclusions into question. Firstly are possible mis-representations in the method. The Lagrangian approach accounts for temperatures and large-scale transport in a particular configuration (for instance, using 6 hourly datapoints and with kinematic or diabatic trajectories). Section 2.4 tested some configuration sensitivities, which were found to provide stable results, and chapters 3 and 4 found that the configuration describes a large portion of H_2O_{strat} variability, providing confidence a representative method was investigated in this thesis.

A second cause to question the advection-condensation method is incomplete representation of temperature and transport effects. For example, all water phase processes (timescale to deposit, and potential sublimation) are not fully accounted for along the air parcel pathway. As raised in chapter 1, a number of earlier studies have investigated these aspects, and they have been found to have a secondary modifying influence. The potential differences in transport (such as small-scale mixing) were considered by the model-advected tracer subject to dehydration in sections 3.3 and 4.2, which found this to be the main cause of differences between the Lagrangian estimate and climate model calculation of H_2O_{strat}. Therefore, transport processes are important to determine H_2O_{strat} variations, and they are fairly well resolved by the Lagrangian calculation.

Another reason for incomplete description of H_2O_{strat} concentrations and variability by the advection-condensation method is the influence of external processes (that is, from outside of an air parcel). Such additional processes include convective injection and sedimentation. These influences may require additional calculations or records along Lagrangian pathways. One approach has been to record the vertical profile of temperatures along Lagrangian pathway calculations (a temperature 'curtain', Jensen and Pfister, 2004, and subsequent publications) to perform more complete microphysical calculations. An alternative approach is used in chapters 5 and 6 where microphysical data (ice and vapour exchange processes) calculated by the global climate model are recorded along the pathway. This separates questions about calculation of the external ice processes from the Lagrangian method. This approach may be useful in studies of observations where ice fields may be estimated and provided to Lagrangian calculations.

One important process not considered for H_2O_{strat} is the effect of methane oxidation. Analysis has focused on the tropical lower stratosphere, where the influence of methane oxidation is arguably negligible (Fueglistaler et al., 2009). Its influence increases with height, as indicated by the UM parameterisation in section 5.2.3. However, it should be noted that the parameterisation is based upon present-day estimates of the stratospheric hydrogen budget. Therefore, trends for water vapour above the lower stratosphere from UM10.4 are not sensitive to potential changes in stratospheric methane. While methane trends are subject to changes human activities, Revell et al. (2016) have studied the range of IPCC projections in a chemistry climate model and found that methane has a relatively small impact on H_2O_{strat} compared to tropical tropopause temperatures.

The conclusions of this thesis also have implications for model development. Impacts on modelled H_2O_{strat} have been quantified for various features, some of which are deficient in global climate models. This includes time-mean temperature bias, sub-monthly temperature

variability, relative control of month-to-month variability by temperatures and winds, ice microphysical processes in the tropical tropopause layer, and projected trends. Improving model representation could then focus on aspects of these. For example, more realistic (increased) sub-monthly temperature variability will reduce the positive bias in stratospheric water vapour concentrations. Development of processes affecting H_2O_{strat} should consider circulation important on seasonal timescales, but not on interannual timescales.

The UM provides one example of a global climate model. UM-UKCA and UM10.4 represent configurations of the UM with contrasting effects on stratospheric water vapour. They differ according to their treatment of atmospheric chemistry (including ozone), tropopause processes and spatial resolution. Therefore, the conclusions of this thesis may be relevant to other, similar, configurations of the UM.

However, the applicability of results to other global climate models was not demonstrated. There are indications of model dependence in climate response in the broad range of tropopause properties seen by Gettelman et al. (2010); Kim et al. (2013). In one particular comparison, lower stratospheric tropical temperatures in UM10.4 did not respond to the climate forcing experiments studied (at 20 km in figure 6.1b), however the same climate forcing experiment with a different model finds a cooling at this level (roughly 60 hPa in figure 1e of Lin et al., 2017). This may also be connected to temperature changes in the tropical tropopause layer, because in the UM10.4 they warm more than in Lin et al. (2017) ($\sim$5 K compared to $\sim$2 K). Extending investigations to other global climate models will determine how general the results of this thesis are.

The conclusions usefully characterise H_2O_{strat} variability in the UM global climate model. These characteristics are sensitive to the configuration of model convection and microphysics schemes, particularly for chapters 5 and 6. Such schemes are extensively parameterised, and have generally been configured to optimise their performance in the climate model, which may not have taken account of tropopause processes. Whether convection and ice microphysics are accurately represented in the tropical tropopause of the UM is important for further study, as they affect budgets of radiation and other trace gases.

The QBOi project has investigated a number of climate models with the same scenarios as investigated here for UM10.4 (Bushell et al., 2019; Holt et al., 2019; Richter et al., 2019). An inter-model comparison of trends in stratospheric water vapour will therefore be possible.

The investigations conducted in this thesis were concerned with quantifying the direct impacts from each of the primary influences on stratospheric water vapour at different timescales. Further understanding may be gained by studying the important processes that directly affect temperatures, transport and convective injection. As mentioned throughout,

tropopause temperatures and the upwelling of the Brewer-Dobson circulation are determined by thermodynamic balance and quasi-periodic phenomena such as QBO, ENSO, MJO and major sudden stratospheric warmings. The impacts of these phenomena on water vapour have so far been studied to varying degrees. Another aspect of indirect study is to examine transport into the stratosphere with trace gas species other than water vapour, for example that have sharp positive gradients (ozone) or a short lifetime after leaving the boundary layer (carbon monoxide). This perspective has been under active study for some time (including Inai et al., 2019; Randel et al., 2007; Riese et al., 2012).

7.3 Outstanding questions for further research

Both the limitations and implications of the investigations in this thesis raise a number of possible developments for further research. These might be divided into furthering the above experiments, and comparing alternative set-ups.

One possible extension to the above experiments might be to develop the microphysical calculations along Lagrangian trajectories, such as applying a finite (non-instant) timescale to vapour deposition, thereby comparing its behaviour with climate model water increments. Similarly, comparing this with instant dehydration at sub-6 hourly timescales will indicate important timescales.

Ideas for alternative set-ups include transport studies. Warm and wet biases can emerge in a climate model due to interpolation errors, especially in a region like the tropical tropopause where gradients are strong and therefore diffused numerically by Eulerian or semi-Lagrangian advection (Hardiman et al., 2015). Fully Lagrangian transport in a global climate model has been shown to improve the representation of quantities close to the tropopause (Stenke et al., 2009, 2008). Essentially, this substitutes numerical diffusion for accuracy. The Lagrangian scheme is not diffusive, however the transformation to Eulerian space for physical schemes introduces an error. This may be tested against an offline Lagrangian transport method.

Alternatively, the numerical diffusion in a semi-Lagrangian scheme may be reduced if the model grid is aligned with the strong gradients. Calculations with vertical levels defined by potential temperature reduce noise from adiabatic processes (as argued for Lagrangian transport calculations by Liu, 2009, and references therein). This theory may be tested in a global climate model for possible reduction of model biases.

The loss of thermodynamic balance appears to be unimportant to the experiment isolating temperature and wind variability (section 4.3), however this could be investigated further. Further work might involve calculating thermal wind balance along co-varying and repeat-

year trajectories, or identifying the strength of eddy heat flux in this region. Another way to highlight that thermodynamic balance is not needed would be to observe dynamical processes. ENSO (and QBO) composites would clarify that dynamical processes are observable in the repeat-temperature and repeat-wind experiments. Some signs of ENSO-related zonal asymmetry emerge for the short 11 year period assessed, but further work is needed to identify a significant signal.

As raised earlier, it might be possible to test the method of complete ice rehydration with global observations. Chapters 5 and 6 suggest an alternative method to Lagrangian (along-trajectory) ice microphysical schemes; the recording of external ice influences as an additional field experienced by Lagrangian pathways. As hypotheses to test, changes in Lagrangian predictions might be anticipated in concentration, variability and isotopic composition (fraction of deuterated water) of water vapour at different levels in the tropical lower stratosphere. This is similar to Dessler et al. (2007), however only one year of global ice observations was available (from MLS, Livesey et al., 2011). In order to create a longer timeseries, they had derived a relationship of convective ice to OLR which was recorded along the trajectory pathway. While the MLS global ice record now spans more than 13 years, no studies have made direct use of such a record as an additional Eulerian field to consider impacts on Lagrangian calculations of H_2O_{strat} variability.

One unreported aspect of the findings in this thesis is the Clausius-Clapeyron scaling of temperature and water vapour. With the tropical tropopause projected to warm in the future, even if the magnitude of temperature variability is unchanged this is expected to raise the sensitivity of H_2O_{strat}. There is evidence of this discussed in section 6.4. The magnitudes of variability of Lagrangian calculations identify the stronger sensitivity of water vapour to tropopause temperature variations. However, analysis of spatial and temporal averages obscure the theoretical relationship. Further study might relate these indirect views of the Clausius-Clapeyron relation with more direct methods such as Lagrangian trajectories and gridpoint value analysis. This is important as increased sensitivity amplifies the impacts on surface climate through stratospheric water vapour.

References

Abalos, M., Legras, B., Ploeger, F., and Randel, W. J. (2015). Evaluating the advective Brewer-Dobson circulation in three reanalyses for the period 1979–2012. *Journal of Geophysical Research: Atmospheres*, 120(15):7534–7554. doi:10.1002/2015JD023182.

Abalos, M., Randel, W. J., and Serrano, E. (2012). Variability in upwelling across the tropical tropopause and correlations with tracers in the lower stratosphere. *Atmospheric Chemistry and Physics*, 12(23):11505–11517. doi:10.5194/acp-12-11505-2012.

Andrews, D. G. (2000). *An Introduction to Atmospheric Physics*. Cambridge University Press, Cambridge, first edition.

Andrews, D. G., Holton, J. R., and Leovy, C. B. (1987). *Middle Atmosphere Dynamics*. Academic Press.

Avery, M. A., Davis, S. M., Rosenlof, K. H., Ye, H., and Dessler, A. E. (2017). Large anomalies in lower stratospheric water vapour and ice during the 2015–2016 El Niño. *Nature Geoscience*, 10(6):405–409. doi:10.1038/ngeo2961.

Baldwin, M. P., Gray, L. J., Dunkerton, T. J., Hamilton, K., Haynes, P. H., Randel, W. J., Holton, J. R., Alexander, M. J., Hirota, I., Horinouchi, T., Jones, D. B. A., Kinnersley, J. S., Marquardt, C., Sato, K., and Takahashi, M. (2001). The quasi-biennial oscillation. *Reviews of Geophysics*, 39(2):179–229. doi:10.1029/1999RG000073.

Bannister, R. N., O'neill, A., Gregory, a. R., and Nissen, K. M. (2004). The role of the south-east Asian monsoon and other seasonal features in creating the 'tape-recorder' signal in the Unified Model. *Quarterly Journal of the Royal Meteorological Society*, 130(599):1531–1554. doi:10.1256/qj.03.106.

Bergman, J. W., Jensen, E. J., Pfister, L., and Yang, Q. (2012). Seasonal differences of vertical-transport efficiency in the tropical tropopause layer: On the interplay between tropical deep convection, large-scale vertical ascent, and horizontal circulations. *Journal of Geophysical Research: Atmospheres*, 117(D5):n/a–n/a. doi:10.1029/2011JD016992.

Bielska, K., Havey, D. K., Scace, G. E., Lisak, D., Harvey, A. H., and Hodges, J. T. (2013). High-accuracy measurements of the vapor pressure of ice referenced to the triple point. *Geophysical Research Letters*, 40(23):6303–6307. doi:10.1002/2013GL058474.

Bonazzola, M. and Haynes, P. H. (2004). A trajectory-based study of the tropical tropopause region. *Journal of Geophysical Research*, 109(D20):D20112. doi:10.1029/2003JD004356.

Boothe, A. C. and Homeyer, C. R. (2017). Global large-scale stratosphere–troposphere exchange in modern reanalyses. *Atmospheric Chemistry and Physics*, 17(9):5537–5559. doi:10.5194/acp-17-5537-2017.

Brasseur, G. P. and Solomon, S. (2006). *Aeronomy of the middle atmosphere: chemistry and physics of the stratosphere and mesosphere*. Springer Science \& Business Media, 3rd edition.

Brewer, A. W. (1949). Evidence for a world circulation provided by the measurements of helium and water vapour distribution in the stratosphere. *Quarterly Journal of the Royal Meteorological Society*, 75(326):351–363. doi:10.1002/qj.49707532603.

Brinkop, S., Dameris, M., Jöckel, P., Garny, H., Lossow, S., and Stiller, G. (2016). The millennium water vapour drop in chemistry–climate model simulations. *Atmospheric Chemistry and Physics*, 16(13):8125–8140. doi:10.5194/acp-16-8125-2016.

Bushell, A. C., Anstey, J. A., Butchart, N., Kawatani, Y., Osprey, S. M., Richter, J. H., Serva, F., Braesicke, P., Cagnazzo, C., Chen, C.-C., Chun, H.-Y., Garcia, R. R., Gray, L. J., Hamilton, K., Kerzenmacher, T., Kim, Y.-H., Lott, F., McLandress, C., Naoe, H., Scinocca, J., Smith, A. K., Stockdale, T. N., Versick, S., Watanabe, S., Yoshida, K., and Yukimoto, S. (2019). Evaluation of the Quasi-Biennial Oscillation in global climate models for the SPARC QBO-initiative. *Quarterly Journal of the Royal Meteorological Society*, In prep.

Butchart, N. (2014). The Brewer-Dobson circulation. *Reviews of Geophysics*, 52(2):157–184. doi:10.1002/2013RG000448.

Butchart, N., Anstey, J. A., Hamilton, K., Osprey, S., McLandress, C., Bushell, A. C., Kawatani, Y., Kim, Y.-H., Lott, F., Scinocca, J., Stockdale, T. N., Andrews, M., Bellprat, O., Braesicke, P., Cagnazzo, C., Chen, C.-C., Chun, H.-Y., Dobrynin, M., Garcia, R. R., Garcia-Serrano, J., Gray, L. J., Holt, L., Kerzenmacher, T., Naoe, H., Pohlmann, H., Richter, J. H., Scaife, A. A., Schenzinger, V., Serva, F., Versick, S., Watanabe, S., Yoshida, K., and Yukimoto, S. (2018). Overview of experiment design and comparison of models participating in phase 1 of the SPARC Quasi-Biennial Oscillation initiative (QBOi). *Geoscientific Model Development*, 11(3):1009–1032. doi:10.5194/gmd-11-1009-2018.

Copernicus Climate Change Service (C3S) (2017). ERA5: Fifth generation of ECMWF atmospheric reanalyses of the global climate. Available at https://cds.climate.copernicus.eu/cdsapp#!/home.

Corti, T., Luo, B. P., de Reus, M., Brunner, D., Cairo, F., Mahoney, M. J., Martucci, G., Matthey, R., Mitev, V., dos Santos, F. H., Schiller, C., Shur, G., Sitnikov, N. M., Spelten, N., Vössing, H. J., Borrmann, S., and Peter, T. (2008). Unprecedented evidence for deep convection hydrating the tropical stratosphere. *Geophysical Research Letters*, 35(10):L10810. doi:10.1029/2008GL033641.

Damadeo, R. P., Zawodny, J. M., Thomason, L. W., and Iyer, N. (2013). SAGE version 7.0 algorithm: application to SAGE II. *Atmospheric Measurement Techniques*, 6(12):3539–3561. doi:10.5194/amt-6-3539-2013.

Danielsen, E. F. (1993). In situ evidence of rapid, vertical, irreversible transport of lower tropospheric air into the lower tropical stratosphere by convective cloud turrets and by larger-scale upwelling in tropical cyclones. *Journal of Geophysical Research: Atmospheres*, 98(D5):8665–8681. doi:10.1029/92JD02954.

Davis, S. M., Hegglin, M. I., Fujiwara, M., Dragani, R., Harada, Y., Kobayashi, C., Long, C., Manney, G. L., Nash, E. R., Potter, G. L., Tegtmeier, S., Wang, T., Wargan, K., and Wright, J. S. (2017). Assessment of upper tropospheric and stratospheric water vapor and ozone in reanalyses as part of S-RIP. *Atmospheric Chemistry and Physics*, 17(20):12743–12778. doi:10.5194/acp-17-12743-2017.

Davis, S. M., Rosenlof, K. H., Hassler, B., Hurst, D. F., Read, W. G., Vömel, H., Selkirk, H., Fujiwara, M., and Damadeo, R. (2016). The Stratospheric Water and Ozone Satellite Homogenized (SWOOSH) database: a long-term database for climate studies. *Earth System Science Data*, 8(2):461–490. doi:10.5194/essd-8-461-2016.

Dee, D. P., Uppala, S. M., Simmons, A. J., Berrisford, P., Poli, P., Kobayashi, S., Andrae, U., Balmaseda, M. A., Balsamo, G., Bauer, P., Bechtold, P., Beljaars, A. C. M., van de Berg, L., Bidlot, J., Bormann, N., Delsol, C., Dragani, R., Fuentes, M., Geer, A. J., Haimberger, L., Healy, S. B., Hersbach, H., Hólm, E. V., Isaksen, L., Kållberg, P., Köhler, M., Matricardi, M., McNally, A. P., Monge-Sanz, B. M., Morcrette, J.-J., Park, B.-K., Peubey, C., de Rosnay, P., Tavolato, C., Thépaut, J.-N., and Vitart, F. (2011). The ERA-Interim reanalysis: configuration and performance of the data assimilation system. *Quarterly Journal of the Royal Meteorological Society*, 137(656):553–597. doi:10.1002/qj.828.

Dessler, A., Ye, H., Wang, T., Schoeberl, M., Oman, L., Douglass, A., Butler, A., Rosenlof, K., Davis, S., and Portmann, R. (2016). Transport of ice into the stratosphere and the humidification of the stratosphere over the 21st century. *Geophysical Research Letters*, 43(5):2323–2329. doi:10.1002/2016GL067991.

Dessler, A. E., Hanisco, T. F., and Fueglistaler, S. (2007). Effects of convective ice lofting on H 2 O and HDO in the tropical tropopause layer. *Journal of Geophysical Research*, 112(D18):D18309. doi:10.1029/2007JD008609.

Dessler, A. E., Schoeberl, M. R., Wang, T., Davis, S. M., and Rosenlof, K. H. (2013). Stratospheric water vapor feedback. *Proceedings of the National Academy of Sciences*, 110(45):18087–18091. doi:10.1073/pnas.1310344110.

Dhomse, S., Weber, M., and Burrows, J. (2008). The relationship between tropospheric wave forcing and tropical lower stratospheric water vapor. *Atmospheric Chemistry and Physics*, 8(3):471–480. doi:10.5194/acp-8-471-2008.

Dion, I.-A., Ricaud, P., Haynes, P., Carminati, F., and Dauhut, T. (2019). Ice injected into the tropopause by deep convection – Part 1: In the austral convective tropics. *Atmospheric Chemistry and Physics*, 19(9):6459–6479. doi:10.5194/acp-19-6459-2019.

Domeisen, D. I., Garfinkel, C. I., and Butler, A. H. (2019). The Teleconnection of El Niño Southern Oscillation to the Stratosphere. *Reviews of Geophysics*, 57(1):5–47. doi:10.1029/2018RG000596.

Eyring, V., Bony, S., Meehl, G. A., Senior, C. A., Stevens, B., Stouffer, R. J., and Taylor, K. E. (2016). Overview of the Coupled Model Intercomparison Project Phase 6 (CMIP6) experimental design and organization. *Geoscientific Model Development*, 9(5):1937–1958. doi:10.5194/gmd-9-1937-2016.

Eyring, V., Shepherd, T. G., and Waugh, D. W. (2010). SPARC CCMVal Report on the Evaluation of Chemistry-Climate Models. Technical report, SPARC. Available at http://www.sparc-climate.org/publications/sparc-reports/.

Forster, P. M. D. F. and Shine, K. P. (1999). Stratospheric water vapour changes as a possible contributor to observed stratospheric cooling. *Geophysical Research Letters*, 26(21):3309–3312. doi:10.1029/1999GL010487.

Fueglistaler, S. (2012). Stepwise changes in stratospheric water vapor? *Journal of Geophysical Research: Atmospheres*, 117(D13302):1–11. doi:10.1029/2012JD017582.

Fueglistaler, S., Bonazzola, M., Haynes, P. H., and Peter, T. (2005). Stratospheric water vapor predicted from the Lagrangian temperature history of air entering the stratosphere in the tropics. *Journal of Geophysical Research*, 110(D8):D08107. doi:10.1029/2004JD005516.

Fueglistaler, S., Dessler, A. E., Dunkerton, T. J., Folkins, I., Fu, Q., and Mote, P. W. (2009). Tropical tropopause layer. *Reviews of Geophysics*, 47(1):RG1004. doi:10.1029/2008RG000267.

Fueglistaler, S. and Haynes, P. H. (2005). Control of interannual and longer-term variability of stratospheric water vapor. *Journal of Geophysical Research*, 110(D24):D24108. doi:10.1029/2005JD006019.

Fueglistaler, S., Haynes, P. H., and Forster, P. M. (2011). The annual cycle in lower stratospheric temperatures revisited. *Atmospheric Chemistry and Physics*, 11(8):3701–3711. doi:10.5194/acp-11-3701-2011.

Fueglistaler, S., Liu, Y., Flannaghan, T., Haynes, P., Dee, D., Read, W., Remsberg, E., Thomason, L., Hurst, D., Lanzante, J., and Bernath, P. (2013). The relation between atmospheric humidity and temperature trends for stratospheric water. *Journal of Geophysical Research: Atmospheres*, 118(2):1052–1074. doi:10.1002/jgrd.50157.

Fueglistaler, S., Liu, Y. S., Flannaghan, T. J., Ploeger, F., and Haynes, P. H. (2014). Departure from Clausius-Clapeyron scaling of water entering the stratosphere in response to changes in tropical upwelling. *Journal of Geophysical Research: Atmospheres*, 119(4):1962–1972. doi:10.1002/2013JD020772.

Garfinkel, C. I., Gordon, A., Oman, L. D., Li, F., Davis, S., and Pawson, S. (2018). Nonlinear response of tropical lower-stratospheric temperature and water vapor to ENSO. *Atmospheric Chemistry and Physics*, 18(7):4597–4615. doi:10.5194/acp-18-4597-2018.

Garfinkel, C. I., Hurwitz, M. M., Oman, L. D., and Waugh, D. W. (2013). Contrasting Effects of Central Pacific and Eastern Pacific El Niño on stratospheric water vapor. *Geophysical Research Letters*, 40(15):4115–4120. doi:10.1002/grl.50677.

Gettelman, A. (2002). Transport of water vapor in the tropical tropopause layer. *Geophysical Research Letters*, 29(1):1009. doi:10.1029/2001GL013818.

Gettelman, A., Hegglin, M. I., Son, S.-W., Kim, J., Fujiwara, M., Birner, T., Kremser, S., Rex, M., Añel, J. a., Akiyoshi, H., Austin, J., Bekki, S., Braesike, P., Brühl, C., Butchart, N., Chipperfield, M., Dameris, M., Dhomse, S., Garny, H., Hardiman, S. C., Jöckel, P., Kinnison, D. E., Lamarque, J. F., Mancini, E., Marchand, M., Michou, M., Morgenstern, O., Pawson, S., Pitari, G., Plummer, D., Pyle, J. a., Rozanov, E., Scinocca, J., Shepherd, T. G., Shibata, K., Smale, D., Teyssèdre, H., and Tian, W. (2010). Multimodel assessment of the upper troposphere and lower stratosphere: Tropics and global trends. *Journal of Geophysical Research*, 115:D00M08. doi:10.1029/2009JD013638.

Gilford, D. M., Solomon, S., and Portmann, R. W. (2016). Radiative Impacts of the 2011 Abrupt Drops in Water Vapor and Ozone in the Tropical Tropopause Layer. *Journal of Climate*, 29(2):595–612. doi:10.1175/JCLI-D-15-0167.1.

Glanville, A. A. and Birner, T. (2017). Role of vertical and horizontal mixing in the tape recorder signal near the tropical tropopause. *Atmospheric Chemistry and Physics*, 17(6):4337–4353. doi:10.5194/acp-17-4337-2017.

Hardiman, S. C., Boutle, I. A., Bushell, A. C., Butchart, N., Cullen, M. J. P., Field, P. R., Furtado, K., Manners, J. C., Milton, S. F., Morcrette, C., O'Connor, F. M., Shipway, B. J., Smith, C., Walters, D. N., Willett, M. R., Williams, K. D., Wood, N., Abraham, N. L., Keeble, J., Maycock, A. C., Thuburn, J., and Woodhouse, M. T. (2015). Processes Controlling Tropical Tropopause Temperature and Stratospheric Water Vapor in Climate Models. *Journal of Climate*, 28(16):6516–6535. doi:10.1175/JCLI-D-15-0075.1.

Harries, J. E., Russell, J. M., Tuck, A. F., Gordley, L. L., Purcell, P., Stone, K., Bevilacqua, R. M., Gunson, M., Nedoluha, G., and Traub, W. A. (1996). Validation of measurements of water vapor from the Halogen Occultation Experiment (HALOE). *Journal of Geophysical Research: Atmospheres*, 101(D6):10205–10216. doi:10.1029/95JD02933.

Hasebe, F. and Noguchi, T. (2016). A Lagrangian description on the troposphere-to-stratosphere transport changes associated with the stratospheric water drop around the year 2000. *Atmospheric Chemistry and Physics*, 16(7):4235–4249. doi:10.5194/acp-16-4235-2016.

Haynes, P. (2005). Stratospheric Dynamics. *Annual Review of Fluid Mechanics*, 37(1):263–293. doi:10.1146/annurev.fluid.37.061903.175710.

Hegglin, M. I., Plummer, D. A., Shepherd, T. G., Scinocca, J. F., Anderson, J., Froidevaux, L., Funke, B., Hurst, D., Rozanov, A., Urban, J., von Clarmann, T., Walker, K. A., Wang, H. J., Tegtmeier, S., and Weigel, K. (2014). Vertical structure of stratospheric water vapour trends derived from merged satellite data. *Nature Geoscience*, 7(10):768–776. doi:10.1038/ngeo2236.

Held, I. M. and Soden, B. J. (2000). Water Vapor Feedback and Global Warming. *Annual Review of Energy and the Environment*, 25(1):441–475. doi:10.1146/annurev.energy.25.1.441.

Holt, L., Lott, F., Garcia, R. R., Kiladis, G. N., Anstey, J., Braesicke, P., Bushell, A. C., Butchart, N., Cagnazzo, C., Chen, C.-C., Chun, H.-Y., Kawatani, Y., Kerzenmacher, T., Kim, Y.-H., McLandress, C., Naoe, H., Osprey, S. M., Richter, J. H., Scaife, A. A., Scinocca, J., Serva, F., Versick, S., Watanabe, S., Yoshida, K., and Yukimoto, S. (2019). An evaluation of tropical waves and wave forcing of the {QBO} in the {QBOi} models. *Quarterly Journal of the Royal Meteorological Society*, 145:—-.

Holton, J. R. and Gettelman, A. (2001). Horizontal transport and the dehydration of the stratosphere. *Geophysical Research Letters*, 28(14):2799–2802. doi:10.1029/2001GL013148.

Hurst, D. F., Oltmans, S. J., Vömel, H., Rosenlof, K. H., Davis, S. M., Ray, E. a., Hall, E. G., and Jordan, A. F. (2011). Stratospheric water vapor trends over Boulder, Colorado: Analysis of the 30 year Boulder record. *Journal of Geophysical Research*, 116(D2):D02306. doi:10.1029/2010JD015065.

Inai, Y., Fujita, R., Machida, T., Matsueda, H., Sawa, Y., Tsuboi, K., Katsumata, K., Morimoto, S., Aoki, S., and Nakazawa, T. (2019). Seasonal characteristics of trace gas transport into the extratropical upper troposphere and lower stratosphere. *Atmospheric Chemistry and Physics*, 19(10):7073–7103. doi:10.5194/acp-19-7073-2019.

Intergovernmental Panel on Climate Change (2013a). Climate change 2013 – the physical science basis: Working group i contribution to the fifth assessment report of the intergovernmental panel on climate change.

Intergovernmental Panel on Climate Change (2013b). Long-term climate change: Projections, commitments and irreversibility. In *Climate Change 2013 – The Physical Science Basis: Working Group I Contribution to the Fifth Assessment Report of the Intergovernmental Panel on Climate Change*, chapter 12, page 1029–1136. Cambridge University Press. doi:10.1017/CBO9781107415324.024.

James, R., Bonazzola, M., Legras, B., Surbled, K., and Fueglistaler, S. (2008). Water vapor transport and dehydration above convective outflow during Asian monsoon. *Geophysical Research Letters*, 35(20):L20810. doi:10.1029/2008GL035441.

Jensen, E. and Pfister, L. (2004). Transport and freeze-drying in the tropical tropopause layer. *Journal of Geophysical Research*, 109(D2):D02207. doi:10.1029/2003JD004022.

Jensen, E. J., Ackerman, A. S., and Smith, J. A. (2007). Can overshooting convection dehydrate the tropical tropopause layer? *Journal of Geophysical Research*, 112(D11):D11209. doi:10.1029/2006JD007943.

Jensen, E. J., Kärcher, B., Ueyama, R., Pfister, L., Bui, T. V., Diskin, G. S., DiGangi, J. P., Woods, S., Lawson, R. P., Froyd, K. D., and Murphy, D. M. (2018). Heterogeneous Ice Nucleation in the Tropical Tropopause Layer. *Journal of Geophysical Research: Atmospheres*, 123(21):12,210–12,227. doi:10.1029/2018JD028949.

Jensen, E. J., Smith, J. B., Pfister, L., Pittman, J. V., Weinstock, E. M., Sayres, D. S., Herman, R. L., Troy, R. F., Rosenlof, K., Thompson, T. L., Fridlind, A. M., Hudson, P. K., Cziczo, D. J., Heymsfield, a. J., Schmitt, C., and Wilson, J. C. (2005). Ice supersaturations exceeding 100% at the cold tropical tropopause: implications for cirrus formation and dehydration. *Atmospheric Chemistry and Physics*, 5(3):851–862. doi:10.5194/acp-5-851-2005.

Jiang, D. and Tian, Z. (2013). East Asian monsoon change for the 21st century: Results of CMIP3 and CMIP5 models. *Chinese Science Bulletin*, 58(12):1427–1435. doi:10.1007/s11434-012-5533-0.

Joseph, B. and Legras, B. (2002). Relation between Kinematic Boundaries, Stirring, and Barriers for the Antarctic Polar Vortex. *Journal of the Atmospheric Sciences*, 59(7):1198–1212. doi:10.1175/1520-0469(2002)059<1198:RBKBSA>2.0.CO;2.

Joshi, M. M. and Shine, K. P. (2003). A GCM Study of Volcanic Eruptions as a Cause of Increased Stratospheric Water Vapor. *Journal of Climate*, 16(21):3525–3534. doi:10.1175/1520-0442(2003)016<3525:AGSOVE>2.0.CO;2.

Kawatani, Y., Lee, J. N., and Hamilton, K. (2014). Interannual Variations of Stratospheric Water Vapor in MLS Observations and Climate Model Simulations. *Journal of the Atmospheric Sciences*, 71(11):4072–4085. doi:10.1175/JAS-D-14-0164.1.

Khaykin, S., Pommereau, J.-P., Korshunov, L., Yushkov, V., Nielsen, J., Larsen, N., Christensen, T., Garnier, A., Lukyanov, A., and Williams, E. (2009). Hydration of the lower stratosphere by ice crystal geysers over land convective systems. *Atmospheric Chemistry and Physics*, 9(6):2275–2287. doi:10.5194/acp-9-2275-2009.

Kim, J., Grise, K. M., and Son, S.-W. (2013). Thermal characteristics of the cold-point tropopause region in CMIP5 models. *Journal of Geophysical Research: Atmospheres*, 118(16):8827–8841. doi:10.1002/jgrd.50649.

Kim, J., Randel, W. J., and Birner, T. (2018). Convectively Driven Tropopause-Level Cooling and Its Influences on Stratospheric Moisture. *Journal of Geophysical Research: Atmospheres*, 123(1):590–606. doi:10.1002/2017JD027080.

Kim, J. and Son, S.-W. (2012). Tropical Cold-Point Tropopause: Climatology, Seasonal Cycle, and Intraseasonal Variability Derived from COSMIC GPS Radio Occultation Measurements. *Journal of Climate*, 25(15):5343–5360. doi:10.1175/JCLI-D-11-00554.1.

Kim, J.-e. and Alexander, M. J. (2015). Direct impacts of waves on tropical cold point tropopause temperature. *Geophysical Research Letters*, 42(5):1584–1592. doi:10.1002/2014GL062737.

Kim, Y.-H., Kiladis, G. N., Albers, J. R., Dias, J., Fujiwara, M., Anstey, J. A., Song, I.-S., Wright, C. J., Kawatani, Y., Lott, F., and Yoo, C. (2019). Comparison of equatorial wave activity in the tropical tropopause layer and stratosphere represented in reanalyses. *Atmospheric Chemistry and Physics*, 19(15):10027–10050. doi:10.5194/acp-19-10027-2019.

Ko, M., Newman, P., Reiman, S., and Strahan, S. (2013). SPARC Report on the Lifetimes of Stratospheric Ozone-Depleting Substances, Their Replacements, and Related Species. Technical report, SPARC. Available at http://www.sparc-climate.org/publications/sparc-reports/sparc-report-no-6/.

Konopka, P., Ploeger, F., Tao, M., and Riese, M. (2016). Zonally resolved impact of ENSO on the stratospheric circulation and water vapor entry values. *Journal of Geophysical Research: Atmospheres*, 121(19):11,486–11,501. doi:10.1002/2015JD024698.

Kremser, S., Wohltmann, I., Rex, M., Langematz, U., Dameris, M., and Kunze, M. (2009). Water vapour transport in the tropical tropopause region in coupled Chemistry-Climate Models and ERA-40 reanalysis data. *Atmospheric Chemistry and Physics*, 9(8):2679–2694. doi:10.5194/acp-9-2679-2009.

Lambert, A., Read, W. G., Livesey, N. J., Santee, M. L., Manney, G. L., Froidevaux, L., Wu, D. L., Schwartz, M. J., Pumphrey, H. C., Jimenez, C., Nedoluha, G. E., Cofield, R. E., Cuddy, D. T., Daffer, W. H., Drouin, B. J., Fuller, R. A., Jarnot, R. F., Knosp, B. W., Pickett, H. M., Perun, V. S., Snyder, W. V., Stek, P. C., Thurstans, R. P., Wagner, P. A., Waters, J. W., Jucks, K. W., Toon, G. C., Stachnik, R. A., Bernath, P. F., Boone, C. D., Walker, K. A., Urban, J., Murtagh, D., Elkins, J. W., and Atlas, E. (2007). Validation of the Aura Microwave Limb Sounder middle atmosphere water vapor and nitrous oxide measurements. *Journal of Geophysical Research*, 112(D24):D24S36. doi:10.1029/2007JD008724.

le Texier, H., Solomon, S., and Garcia, R. R. (1988). The role of molecular hydrogen and methane oxidation in the water vapour budget of the stratosphere. *Quarterly Journal of the Royal Meteorological Society*, 114(480):281–295. doi:10.1002/qj.49711448002.

Lin, P., Paynter, D., Ming, Y., and Ramaswamy, V. (2017). Changes of the Tropical Tropopause Layer under Global Warming. *Journal of Climate*, 30(4):1245–1258. doi:10.1175/JCLI-D-16-0457.1.

Liu, Y. (2009). *Lagrangian Studies of Troposphjere-to-Stratosphere Transport*. PhD thesis, Cambridge.

Liu, Y. S., Fueglistaler, S., and Haynes, P. H. (2010). Advection-condensation paradigm for stratospheric water vapor. *Journal of Geophysical Research: Atmospheres*, 115(D24):1–18. doi:10.1029/2010JD014352.

Livesey, N. J., Read, W. G., Froidevaux, L., Lambert, A., Manney, G. L., Pumphrey, H. C., Santee, M. L., Schwartz, M. J., Wang, S., Cofield, R. E., Cuddy, D. T., Fuller, R. a., Jarnot, R. F., Jiang, J. H., Knosp, B. W., Stek, P. C., Wagner, P. a., and Wu, D. L. (2011). EOS MLS Version 3.3 Level 2 data quality and description document. Technical report, Jet Propulsion Laboratory. Available at http://mls.jpl.nasa.gov/.

Long, C. S., Fujiwara, M., Davis, S., Mitchell, D. M., and Wright, C. J. (2017). Climatology and Interannual Variability of Dynamic Variables in Multiple Reanalyses Evaluated by the SPARC Reanalysis Intercomparison Project (S-RIP). *Atmospheric Chemistry and Physics Discussions*, pages 1–43. doi:10.5194/acp-2017-289.

Lossow, S., Hurst, D. F., Rosenlof, K. H., Stiller, G. P., von Clarmann, T., Brinkop, S., Dameris, M., Jöckel, P., Kinnison, D. E., Plieninger, J., Plummer, D. A., Ploeger, F., Read, W. G., Remsberg, E. E., Russell, J. M., and Tao, M. (2018). Trend differences in lower stratospheric water vapour between Boulder and the zonal mean and their role in understanding fundamental observational discrepancies. *Atmospheric Chemistry and Physics*, 18(11):8331–8351. doi:10.5194/acp-18-8331-2018.

Marti, J. and Mauersberger, K. (1993). A survey and new measurements of ice vapor pressure at temperatures between 170 and 250K. *Geophysical Research Letters*, 20(5):363–366. doi:10.1029/93GL00105.

Maycock, a. C., Shine, K. P., and Joshi, M. M. (2011). The temperature response to stratospheric water vapour changes. *Quarterly Journal of the Royal Meteorological Society*, 137(657):1070–1082. doi:10.1002/qj.822.

Methven, J. (1997). Offline trajectories: Calculation and accuracy. Technical report, University of Reading.

Ming, A., Maycock, A. C., Hitchcock, P., and Haynes, P. (2017). The radiative role of ozone and water vapour in the annual temperature cycle in the tropical tropopause layer. *Atmospheric Chemistry and Physics*, 17(9):5677–5701. doi:10.5194/acp-17-5677-2017.

Morgenstern, O., Braesicke, P., O'Connor, F. M., Bushell, A. C., Johnson, C. E., Osprey, S. M., and Pyle, J. A. (2009). Evaluation of the new UKCA climate-composition model – Part 1: The stratosphere. *Geoscientific Model Development*, 2(1):43–57. doi:10.5194/gmd-2-43-2009.

Morgenstern, O., Hegglin, M. I., Rozanov, E., O'Connor, F. M., Abraham, N. L., Akiyoshi, H., Archibald, A. T., Bekki, S., Butchart, N., Chipperfield, M. P., Deushi, M., Dhomse, S. S., Garcia, R. R., Hardiman, S. C., Horowitz, L. W., Jöckel, P., Josse, B., Kinnison, D., Lin, M., Mancini, E., Manyin, M. E., Marchand, M., Marécal, V., Michou, M., Oman, L. D., Pitari, G., Plummer, D. a., Revell, L. E., Saint-Martin, D., Schofield, R., Stenke, A., Stone, K., Sudo, K., Tanaka, T. Y., Tilmes, S., Yamashita, Y., Yoshida, K., and Zeng, G. (2017). Review of the global models used within phase 1 of the Chemistry–Climate Model Initiative (CCMI). *Geoscientific Model Development*, 10(2):639–671. doi:10.5194/gmd-10-639-2017.

Moss, R. H., Edmonds, J. A., Hibbard, K. A., Manning, M. R., Rose, S. K., van Vuuren, D. P., Carter, T. R., Emori, S., Kainuma, M., Kram, T., Meehl, G. A., Mitchell, J. F. B., Nakicenovic, N., Riahi, K., Smith, S. J., Stouffer, R. J., Thomson, A. M., Weyant, J. P., and Wilbanks, T. J. (2010). The next generation of scenarios for climate change research and assessment. *Nature*, 463(7282):747–756. doi:10.1038/nature08823.

Mote, P. W., Rosenlof, K. H., McIntyre, M. E., Carr, E. S., Gille, J. C., Holton, J. R., Kinnersley, J. S., Pumphrey, H. C., Russell, J. M., and Waters, J. W. (1996). An atmospheric tape recorder: The imprint of tropical tropopause temperatures on stratospheric water vapor. *Journal of Geophysical Research: Atmospheres*, 101(D2):3989–4006. doi:10.1029/95JD03422.

Murphy, D. M. and Koop, T. (2005). Review of the vapour pressures of ice and supercooled water for atmospheric applications. *Quarterly Journal of the Royal Meteorological Society*, 131(608):1539–1565. doi:10.1256/qj.04.94.

Nedoluha, G. E., Bevilacqua, R. M., Hoppel, K. W., Daehler, M., Shettle, E. P., Hornstein, J. H., Fromm, M. D., Lumpe, J. D., and Rosenfield, J. E. (2000). POAM III measurements of dehydration in the Antarctic lower stratosphere. *Geophysical Research Letters*, 27(12):1683–1686. doi:10.1029/1999GL011087.

Niwano, M., Yamazaki, K., and Shiotani, M. (2003). Seasonal and QBO variations of ascent rate in the tropical lower stratosphere as inferred from UARS HALOE trace gas data. *Journal of Geophysical Research: Atmospheres*, 108(D24):n/a–n/a. doi:10.1029/2003JD003871.

Oltmans, S. J., Vömel, H., Hofmann, D. J., Rosenlof, K. H., and Kley, D. (2000). The increase in stratospheric water vapor from balloonborne, frostpoint hygrometer measurements at Washington, D.C., and Boulder, Colorado. *Geophysical Research Letters*, 27(21):3453–3456. doi:10.1029/2000GL012133.

Oman, L., Waugh, D. W., Pawson, S., Stolarski, R. S., and Nielsen, J. E. (2008). Understanding the Changes of Stratospheric Water Vapor in Coupled Chemistry–Climate Model Simulations. *Journal of the Atmospheric Sciences*, 65(10):3278–3291. doi:10.1175/2008JAS2696.1.

Park, M., Randel, W. J., Emmons, L. K., Bernath, P. F., Walker, K. A., and Boone, C. D. (2008). Chemical isolation in the Asian monsoon anticyclone observed in Atmospheric Chemistry Experiment (ACE-FTS) data. *Atmospheric Chemistry and Physics*, 8(3):757–764. doi:10.5194/acp-8-757-2008.

Ploeger, F. and Birner, T. (2016). Seasonal and inter-annual variability of lower stratospheric age of air spectra. *Atmospheric Chemistry and Physics*, 16(15):10195–10213. doi:10.5194/acp-16-10195-2016.

Plumb, R. A. (2002). Stratospheric Transport. *Journal of the Meteorological Society of Japan. Ser. II*, 80(4B):793–809. doi:10.2151/jmsj.80.793.

Poshyvailo, L., Müller, R., Konopka, P., Günther, G., Riese, M., Podglajen, A., and Ploeger, F. (2018). Sensitivities of modelled water vapour in the lower stratosphere: temperature uncertainty, effects of horizontal transport and small-scale mixing. *Atmospheric Chemistry and Physics*, 18(12):8505–8527. doi:10.5194/acp-18-8505-2018.

Press, W. H., Teukolsky, S. A., Vettering, W. T., and Flannery, B. P. (1992). *Numerical recipes in Fortran 77: The are of scientific computing*, volume 1. Cambridge University Press.

Randel, W. J. (2010). Variability and trends in stratospheric temperature and water vapor. In *The Stratosphere: Dynamics, Transport and Chemistry, Geophys. Monogr. Ser*, volume 190, pages 123–135. doi:10.1029/2009GM000870.

Randel, W. J., Garcia, R. R., and Wu, F. (2002). Time-Dependent Upwelling in the Tropical Lower Stratosphere Estimated from the Zonal-Mean Momentum Budget. *Journal of the Atmospheric Sciences*, 59(13):2141–2152. doi:10.1175/1520-0469(2002)059<2141:TDUITT>2.0.CO;2.

Randel, W. J. and Jensen, E. J. (2013). Physical processes in the tropical tropopause layer and their roles in a changing climate. *Nature Geoscience*, 6(3):169–176. doi:10.1038/ngeo1733.

Randel, W. J., Park, M., Wu, F., and Livesey, N. (2007). A Large Annual Cycle in Ozone above the Tropical Tropopause Linked to the Brewer–Dobson Circulation. *Journal of the Atmospheric Sciences*, 64(12):4479–4488. doi:10.1175/2007JAS2409.1.

Randel, W. J., Wu, F., and Ríos, W. R. (2003). Thermal variability of the tropical tropopause region derived from GPS/MET observations. *Journal of Geophysical Research*, 108(D1):4024. doi:10.1029/2002JD002595.

Randel, W. J., Wu, F., Vömel, H., Nedoluha, G. E., and Forster, P. (2006). Decreases in stratospheric water vapor after 2001: Links to changes in the tropical tropopause and the Brewer-Dobson circulation. *Journal of Geophysical Research*, 111(D12):D12312. doi:10.1029/2005JD006744.

Reed, R. J. and Vicek, C. L. (1969). The Annual Temperature Variation in the Lower Tropical Stratosphere. *Journal of the Atmospheric Sciences*, 26(1):163–167. doi:10.1175/1520-0469(1969)026<0163:TATVIT>2.0.CO;2.

Revell, L. E., Stenke, A., Rozanov, E., Ball, W., Lossow, S., and Peter, T. (2016). The role of methane in projections of 21st century stratospheric water vapour. *Atmospheric Chemistry and Physics*, 16(20):13067–13080. doi:10.5194/acp-16-13067-2016.

Richter, J. H., Butchart, N., Kawatani, Y., Bushell, A. C., Holt, L., Anstey, J., Serva, F., Simpson, I. R., Osprey, S. M., Hamilton, K., Braesicke, P., Cagnazzo, C., Chen, C.-C., Garcia, R. R., Gray, L. J., Kerzenmacher, T., Lott, F., McLandress, C., Naoe, H., Scinocca, J., Stockdale, T. N., Watanabe, S., Yoshida, K., and Yukimoto, S. (2019). Response of the quasi-biennial oscillation to a warming climate in global climate models. *Quarterly Journal of the Royal Meteorological Society*, In prep.:—-.

Riese, M., Ploeger, F., Rap, A., Vogel, B., Konopka, P., Dameris, M., and Forster, P. (2012). Impact of uncertainties in atmospheric mixing on simulated UTLS composition and related radiative effects. *Journal of Geophysical Research: Atmospheres*, 117(D16):n/a–n/a. doi:10.1029/2012JD017751.

Rogers, R. R. and Yau, M. K. (1989). *A Short Course in Cloud Physics*. Butterworth-Heinemann, third edition.

Rolf, C., Afchine, A., Spelten, N., and Krämer, M. (2018). Ice particles over the Asian Monsoon: observations during the field campaign StratoClim 2017. In *EGU General Assembly*, page 1860.

Rollins, A. W., Thornberry, T. D., Gao, R. S., Woods, S., Lawson, R. P., Bui, T. P., Jensen, E. J., and Fahey, D. W. (2016). Observational constraints on the efficiency of dehydration mechanisms in the tropical tropopause layer. *Geophysical Research Letters*, 43(6):2912–2918. doi:10.1002/2016GL067972.

Scherllin-Pirscher, B., Randel, W. J., and Kim, J. (2017). Tropical temperature variability and Kelvin-wave activity in the UTLS from GPS RO measurements. *Atmospheric Chemistry and Physics*, 17(2):793–806. doi:10.5194/acp-17-793-2017.

Schoeberl, M. R. and Dessler, A. E. (2011). Dehydration of the stratosphere. *Atmospheric Chemistry and Physics*, 11(16):8433–8446. doi:10.5194/acp-11-8433-2011.

Schoeberl, M. R., Dessler, A. E., and Wang, T. (2012). Simulation of stratospheric water vapor and trends using three reanalyses. *Atmospheric Chemistry and Physics*, 12(14):6475–6487. doi:10.5194/acp-12-6475-2012.

Schoeberl, M. R., Jensen, E. J., Pfister, L., Ueyama, R., Wang, T., Selkirk, H., Avery, M., Thornberry, T., and Dessler, A. E. (2019). Water Vapor, Clouds, and Saturation in the Tropical Tropopause Layer. *Journal of Geophysical Research: Atmospheres*, 124(7):3984–4003. doi:10.1029/2018JD029849.

Schreck, C., Lee, H.-T., and Knapp, K. (2018). HIRS Outgoing Longwave Radiation—Daily Climate Data Record: Application toward Identifying Tropical Subseasonal Variability. *Remote Sensing*, 10(9):1325. doi:10.3390/rs10091325.

Seviour, W. J. M., Butchart, N., and Hardiman, S. C. (2012). The Brewer-Dobson circulation inferred from ERA-Interim. *Quarterly Journal of the Royal Meteorological Society*, 138(665):878–888. doi:10.1002/qj.966.

Sherwood, S. C. and Dessler, A. E. (2000). On the control of stratospheric humidity. *Geophysical Research Letters*, 27(16):2513–2516. doi:10.1029/2000GL011438.

Smalley, K. M., Dessler, A. E., Bekki, S., Deushi, M., Marchand, M., Morgenstern, O., Plummer, D. A., Shibata, K., Yamashita, Y., and Zeng, G. (2017). Contribution of different processes to changes in tropical lower-stratospheric water vapor in chemistry–climate models. *Atmospheric Chemistry and Physics*, 17(13):8031–8044. doi:10.5194/acp-17-8031-2017.

Solomon, S. (1999). Stratospheric ozone depletion: A review of concepts and history. *Reviews of Geophysics*, 37(3):275–316. doi:10.1029/1999RG900008.

Sperber, K. R., Annamalai, H., Kang, I.-S., Kitoh, A., Moise, A., Turner, A., Wang, B., and Zhou, T. (2013). The Asian summer monsoon: an intercomparison of CMIP5 vs. CMIP3 simulations of the late 20th century. *Climate Dynamics*, 41(9-10):2711–2744. doi:10.1007/s00382-012-1607-6.

Stenke, A., Dameris, M., Grewe, V., and Garny, H. (2009). Implications of Lagrangian transport for simulations with a coupled chemistry-climate model. *Atmospheric Chemistry and Physics*, 9(15):5489–5504. doi:10.5194/acp-9-5489-2009.

Stenke, A., Grewe, V., and Ponater, M. (2008). Lagrangian transport of water vapor and cloud water in the ECHAM4 GCM and its impact on the cold bias. *Climate Dynamics*, 31(5):491–506. doi:10.1007/s00382-007-0347-5.

Tao, M., Konopka, P., Ploeger, F., Riese, M., Müller, R., and Volk, C. M. (2015). Impact of stratospheric major warmings and the quasi-biennial oscillation on the variability of stratospheric water vapor. *Geophysical Research Letters*, 42(11):4599–4607. doi:10.1002/2015GL064443.

Tao, M., Konopka, P., Ploeger, F., Yan, X., Wright, J. S., Diallo, M., Fueglistaler, S., and Riese, M. (2019). Multi-timescale variations of modelled stratospheric water vapor derived from three modern reanalysis products. *Atmospheric Chemistry and Physics Discussions*, pages 1–36. doi:10.5194/acp-2019-39.

Taylor, K. E., Stouffer, R. J., and Meehl, G. A. (2012). An Overview of CMIP5 and the Experiment Design. *Bulletin of the American Meteorological Society*, 93(4):485–498. doi:10.1175/BAMS-D-11-00094.1.

Thomason, L. W., Moore, J. R., Pitts, M. C., Zawodny, J. M., and Chiou, E. W. (2010). An evaluation of the SAGE III version 4 aerosol extinction coefficient and water vapor data products. *Atmospheric Chemistry and Physics*, 10(5):2159–2173. doi:10.5194/acp-10-2159-2010.

Thornberry, T. D., Rollins, A. W., Watts, L. A., Gao, R. S., Woods, S., and Bui, T. V. (2017). Insight into the formation processes of high altitude cirrus over the tropical western Pacific during POSIDON. In *American Geophysical Union Fall Meeting*.

Tissier, A.-S. and Legras, B. (2016). Convective sources of trajectories traversing the tropical tropopause layer. *Atmospheric Chemistry and Physics*, 16(5):3383–3398. doi:10.5194/acp-16-3383-2016.

Turner, A. G. and Annamalai, H. (2012). Climate change and the South Asian summer monsoon. *Nature Climate Change*, 2(8):587–595. doi:10.1038/nclimate1495.

Tweedy, O. V., Kramarova, N. A., Strahan, S. E., Newman, P. A., Coy, L., Randel, W. J., Park, M., Waugh, D. W., and Frith, S. M. (2017). Response of Trace Gases to the Disrupted 2015–2016 Quasi-Biennial Oscillation. *Atmospheric Chemistry and Physics Discussions*, (January):1–26. doi:10.5194/acp-2017-76.

Ueyama, R., Jensen, E. J., and Pfister, L. (2018). Convective Influence on the Humidity and Clouds in the Tropical Tropopause Layer During Boreal Summer. *Journal of Geophysical Research: Atmospheres*, pages 1–18. doi:10.1029/2018JD028674.

Ueyama, R., Jensen, E. J., Pfister, L., and Kim, J.-E. (2015). Dynamical, convective, and microphysical control on wintertime distributions of water vapor and clouds in the tropical tropopause layer. *Journal of Geophysical Research: Atmospheres*, 120(19):10,483–10,500. doi:10.1002/2015JD023318.

UMDP26 (2017). UM Documentation Paper 26 – The Large Scale Precipitation Parametrization Scheme. Technical report, UK Met Office.

UMDP29 (2018). UM Documentation Paper 29 – The large scale cloud scheme and saturated specific humidity. Technical report, UK Met Office.

UMDP30 (2015). UM Documentation Papers 30 – The PC2 cloud scheme. Technical report, UK Met Office.

Untch, A., Simmons, A., Hortal, M., and Jakob, C. (1998). Increased stratospheric resolution in the ECMWF forecasting system. *ECMWF Newsletter*, 82(82):2–8.

Urban, J., Lossow, S., Stiller, G., and Read, W. (2014). Another Drop in Water Vapor. *Eos, Transactions American Geophysical Union*, 95(27):245–246. doi:10.1002/2014EO270001.

Virts, K. S. and Wallace, J. M. (2014). Observations of Temperature, Wind, Cirrus, and Trace Gases in the Tropical Tropopause Transition Layer during the MJO*. *Journal of the Atmospheric Sciences*, 71(3):1143–1157. doi:10.1175/JAS-D-13-0178.1.

Vömel, H., Oltmans, S. J., Hofmann, D. J., Deshler, T., and Rosen, J. M. (1995). The evolution of the dehydration in the Antarctic stratospheric vortex. *Journal of Geophysical Research*, 100(D7):13919. doi:10.1029/95JD01000.

von Storch, H. and Zwiers, F. W. (1999). *Statistical Analysis in Climate Research*, volume 95. Cambridge University Press, Cambridge. doi:10.1017/CBO9780511612336.

Wagner, W., Riethmann, T., Feistel, R., and Harvey, A. H. (2011). New Equations for the Sublimation Pressure and Melting Pressure of H2O Ice Ih. *Journal of Physical and Chemical Reference Data*, 40(4):043103. doi:10.1063/1.3657937.

Walters, D., Baran, A. J., Boutle, I., Brooks, M., Earnshaw, P., Edwards, J., Furtado, K., Hill, P., Lock, A., Manners, J., Morcrette, C., Mulcahy, J., Sanchez, C., Smith, C., Stratton, R., Tennant, W., Tomassini, L., Van Weverberg, K., Vosper, S., Willett, M., Browse, J., Bushell, A., Carslaw, K., Dalvi, M., Essery, R., Gedney, N., Hardiman, S., Johnson, B., Johnson, C., Jones, A., Jones, C., Mann, G., Milton, S., Rumbold, H., Sellar, A., Ujiie, M., Whitall, M., Williams, K., and Zerroukat, M. (2019). The Met Office Unified Model Global Atmosphere 7.0/7.1 and JULES Global Land 7.0 configurations. *Geoscientific Model Development*, 12(5):1909–1963. doi:10.5194/gmd-12-1909-2019.

Wilson, D. R., Bushell, A. C., Kerr-Munslow, A. M., Price, J. D., and Morcrette, C. J. (2008). PC2: A prognostic cloud fraction and condensation scheme. I: Scheme description. *Quarterly Journal of the Royal Meteorological Society*, 134(637):2093–2107. doi:10.1002/qj.333.

Wright, J. S., Fu, R., Fueglistaler, S., Liu, Y. S., and Zhang, Y. (2011). The influence of summertime convection over Southeast Asia on water vapor in the tropical stratosphere. *Journal of Geophysical Research*, 116(D12):D12302. doi:10.1029/2010JD015416.

Ye, H., Dessler, A. E., and Yu, W. (2018). Effects of convective ice evaporation on interannual variability of tropical tropopause layer water vapor. *Atmospheric Chemistry and Physics*, 18(7):4425–4437. doi:10.5194/acp-18-4425-2018.

Zerroukat, M. (2010). A simple mass conserving semi-Lagrangian scheme for transport problems. *Journal of Computational Physics*, 229(24):9011–9019. doi:10.1016/j.jcp.2010.08.017.

Zhou, X. L., Geller, M. A., and Zhang, M. (2004). Temperature Fields in the Tropical Tropopause Transition Layer. *Journal of Climate*, 17(15):2901–2908. doi:10.1175/1520-0442(2004)017<2901:TFITTT>2.0.CO;2.